FOUNDATIONS OF TOPOLOGICAL ELECTRODYNAMICS

by

Todd Van Mechelen

A dissertation

Submitted to the Faculty of Purdue University

In Partial Fulfillment of the Requirements for the degree of

Doctor of Philosophy
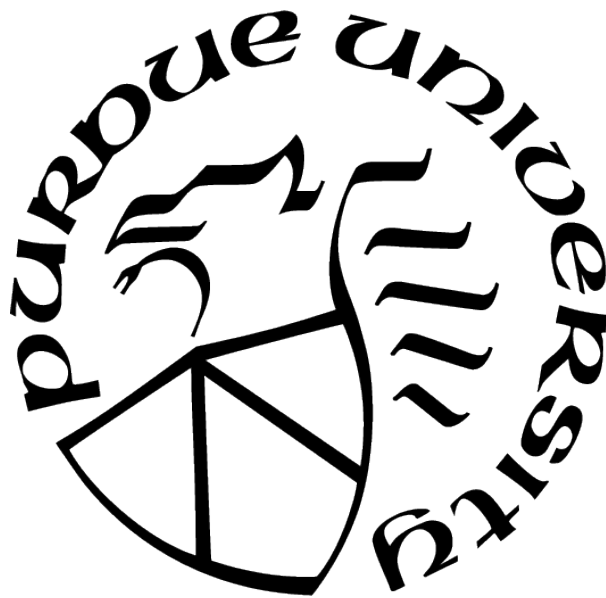
Electrical and Computer Engineering

West Lafayette, Indiana

December 2020

THE PURDUE UNIVERSITY GRADUATE SCHOOL
STATEMENT OF COMMITTEE APPROVAL

Dr. Zubin Jacob, Chair

School of Electrical and Computer Engineering

Dr. Supriyo Datta

School of Electrical and Computer Engineering

Dr. Weng Cho Chew

School of Electrical and Computer Engineering

Dr. Chris H. Greene

Department of Physics and Astronomy

Approved by:

Dr. Dimitrios Peroulis

To my late father who I owe my convictions and my loving mother who I owe the world.

ACKNOWLEDGMENTS

TABLE OF CONTENTS

LIST OF TABLES

LIST OF FIGURES

16

17

Figure   Page

Figure   Page

LIST OF SYMBOLS

$\mathbb{Z}$ set of integers

$\mathbb{R}$ set of real numbers

$\mathbb{C}$ set of complex numbers

$\mathbb{T}^2$ 2-torus

S^2 2-sphere

e elementary charge

m_{e} electron mass

c speed of light

h Planck constant

$\hbar$ reduced Planck constant

m effective mass

n_0 electron concentration

κ Chern-Simons coupling (Chern-Simons mass)

a lattice constant

v_F Fermi velocity

v_s speed of sound

$\mathcal{N}_0$ density of states at the Fermi energy

B biasing magnetic field

B_0 intrinsic magnetic field

τ transport time

ω_c cyclotron frequency

r_c cyclotron radius

ζ bulk viscosity

η shear viscosity

η_H Hall viscosity

ν_0 kinematic shear viscosity

ν kinetic shear viscosity

ν_H kinetic Hall viscosity

D_ν	shear diffusion length
D_H	Hall diffusion length
$\vec{\mathcal{E}}$	electric field
$\vec{\mathcal{B}}$	magnetic field
$\vec{\mathcal{D}}$	electric displacement field
$\vec{\mathcal{H}}$	auxiliary magnetic field
ρ	charge density
$\vec{\mathcal{J}}$	current density
ϕ	electric scalar potential
$\vec{\mathcal{A}}$	magnetic vector potential
$\vec{\mathcal{P}}$	polarization density
$\vec{\mathcal{M}}$	magnetization density
ε	permittivity tensor
χ	electric susceptibility tensor
σ	conductivity tensor
Σ	current-current correlation function
ς	stress-energy tensor
$\vec{r}$	spatial coordinate frame
t	time coordinate
$\vec{k}$	wavevector
ω	angular frequency

ABBREVIATIONS

D	dimensional
QHE	quantum Hall effect
QAHE	quantum anomalous Hall effect
QSHE	quantum spin Hall effect
TKNN	Thouless, Kohomoto, Nightingale and den Nijs
QGEE	quantum gyroelectric effect
MCS	Maxwell-Chern-Simons
NS	Navier-Stokes
FDT	fluctuation-dissipation theorem
GBT	Gauss-Bonnet theorem
BZ	Brillouin zone
IBZ	irreducible Brillouin zone
CRT	crystallographic restriction theorem
irrep	irreducible representation
HSP	high-symmetry point
HSL	high-symmetry line
SML	spin-momentum locking
AM	angular momentum
OAM	orbital angular momentum
SAM	spin angular momentum
MHD	magnetohydrodynamics
BMP	bulk magnetoplasmon
EMP	edge magnetoplasmon
ABC	additional boundary condition
DARPA	Defense Advanced Research Projects Agency
NSF	National Science Foundation

ABSTRACT

Over the last decade, Dirac matter has become one of the most prominent fields of research in contemporary material science due to the incredibly rich physics of the Dirac equation. Notable examples are the Dirac cones in graphene, Weyl points in TaAs, and gapless edge states in Bi_2Te_3. These unique phases of matter are intimately related to the topological structure of Dirac fermions. However, it remains an open question if the topological structure of Maxwell's equations predicts yet new phases of matter. This thesis will conclusively answer this question.

Topological electrodynamics is concerned with the geometry of electromagnetic waves in condensed matter. At the microscopic level, photons couple to the dipole-carrying excitations of a material, such as plasmons and excitons, which hybridize to form new normal modes of the system. The interaction between these bosonic oscillators is the origin of temporal and spatial dispersion in optical response functions like the conductivity tensor. Our main achievement is motivating a global interpretation of these response functions, over all frequencies and wavevectors. This theory led us to the conclusion that there are topological invariants associated with the conductivity tensor itself. In this thesis, we show exactly how to calculate these electromagnetic invariants, in both continuum and lattice theories, to identify unique Maxwellian phases of matter. Magnetohydrodynamic electron fluids in strongly-correlated 2D materials like graphene are the first candidates of this new class of topological phase. The fundamental physical mechanism that gives rise to a topological electromagnetic classification is Hall viscosity η_H which adds a nonlocal component to the Hall conductivity. To study the topological electrodynamics, we propose viscous Maxwell-Chern-Simons theory – a Lagrangian framework that naturally generates the equations of motion, nonlocal Hall response and the boundary conditions. We demonstrate that nonlocal Hall conductivity is the spin-1 photonic equivalent of dispersive mass and induces precession of bulk photonic skyrmions. Nontrivial photonic skyrmions are associated with Dirac monopoles in the bulk momentum space and a singular Berry gauge. A singular gauge occurs when the photonic mass changes sign. Remarkably, the boundary of this medium supports gapless chiral edge states that are spin-1 helically-quantized and satisfy open boundary conditions.

1. INTRODUCTION

Note: For clarity, all 3D vectors will be denoted with a vector arrow $\vec{\mathcal{A}} = (A_x, A_y, A_z)$, while we reserve boldface for 2D vectors $\mathbf{A} = (A_x, A_y)$.

Topology is, generically, the study of quantities that are conserved under continuous deformations. What these particular quantities are and what constitutes a continuous deformation depends on the physical system in question but they all have one thing in common: there is a topological property that is invariant under these deformations and it usually takes the form of a discrete number. In physics this is known as a topological invariant or topological quantum number.

A customary application of topology is to consider the donut. If we do not tear the donut or glue parts of the donut together, the number of holes cannot change. There is only one. However, we can "continuously deform" the donut by stretching, bending, twisting all we like until it looks more like a teacup. Topologically, the donut and the teacup are identical because they possess the same number of holes. The precise mathematical formulation of this statement is known as the Gauss-Bonnet theorem (GBT) [1]. The GBT was one of the original topological theorems derived in differential geometry and is remarkably elegant,

$$4\pi(1 - g) = \int_M K dA. \tag{1.1}$$

K is the Gaussian curvature of the surface manifold M and dA is the differential area of this manifold over which the integral is performed. The genus g is a topological invariant equal to the number of holes of the object [Fig. 1.1]. Calculating the integral produces

$$g = 0 \qquad\qquad g = 1 \qquad\qquad g = 2$$
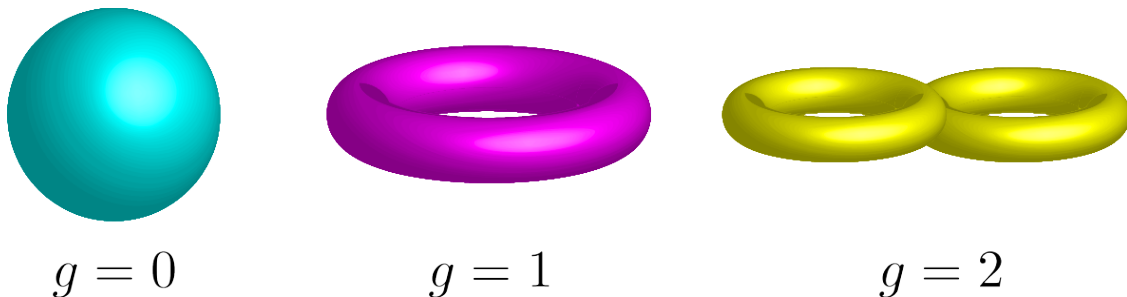
Figure 1.1. Genus (number of holes) of various geometric objects.

$g = 1$ for both the donut and the teacup. Like many topological theorems, the GBT links a local quantity K, with a global quantity g, through an integral equation. No matter how much the curvature is changed at any point on the surface, it must always integrate to the same quantity. This is a very powerful and somewhat surprising statement. It is even more surprising that such a quantity can be found in ordinary linear response measurements like the Hall conductivity.

1.1   Quantum Hall effect

The Hall effect was discovered by Edwin Hall in 1879 [2]. Classically, the Hall effect arises from the Lorentz force acting on an electrical current in the presence of a magnetic field. The magnetic field generates a force perpendicular to the electron's motion which causes the trajectory to bend. Since positive and negative charge carriers bend in opposing directions, there is a build up of positive and negative charge at opposite walls of the sample. This generates a potential known as the Hall voltage V_H. The proportionality of the Hall voltage to the transverse current is the Hall resistance. Astonishingly, the Hall resistivity $\rho_{xy} = B/n_0 e$, or the Hall conductivity $\sigma_{xy} = \rho_{xy}^{-1}$, is independent of material dimensions and is therefore a very useful means to determine the electron density n_0 or the magnetic field B. The Hall coefficient $R_H = 1/n_0 e$ is an intrinsic material quantity and gives the slope of the Hall resistivity ρ_{xy} vs. magnetic field B.

The classical Hall effect remains valid for relatively weak magnetic fields and was a standard laboratory tool for decades. However, in 1980, one hundred years later, Klaus von Klitzing discovered that qualitatively different behavior occurs in strong magnetic fields and very low temperatures [3]. The Hall conductivity plateaus at integer values of the conductance quantum,

$$\sigma_{xy} = C\frac{e^2}{h}, \qquad C \in \mathbb{Z}. \tag{1.2}$$

h is the Planck constant and C is an integer. The quantization of σ_{xy} is incredibly robust and has been measured to better than one part in a billion even in relatively dirty samples [Fig. 1.2]. This is the quantum Hall effect (QHE) and it has become an electrical resistance standard due to its precision measurement of the conductance quantum e^2/h and the fine
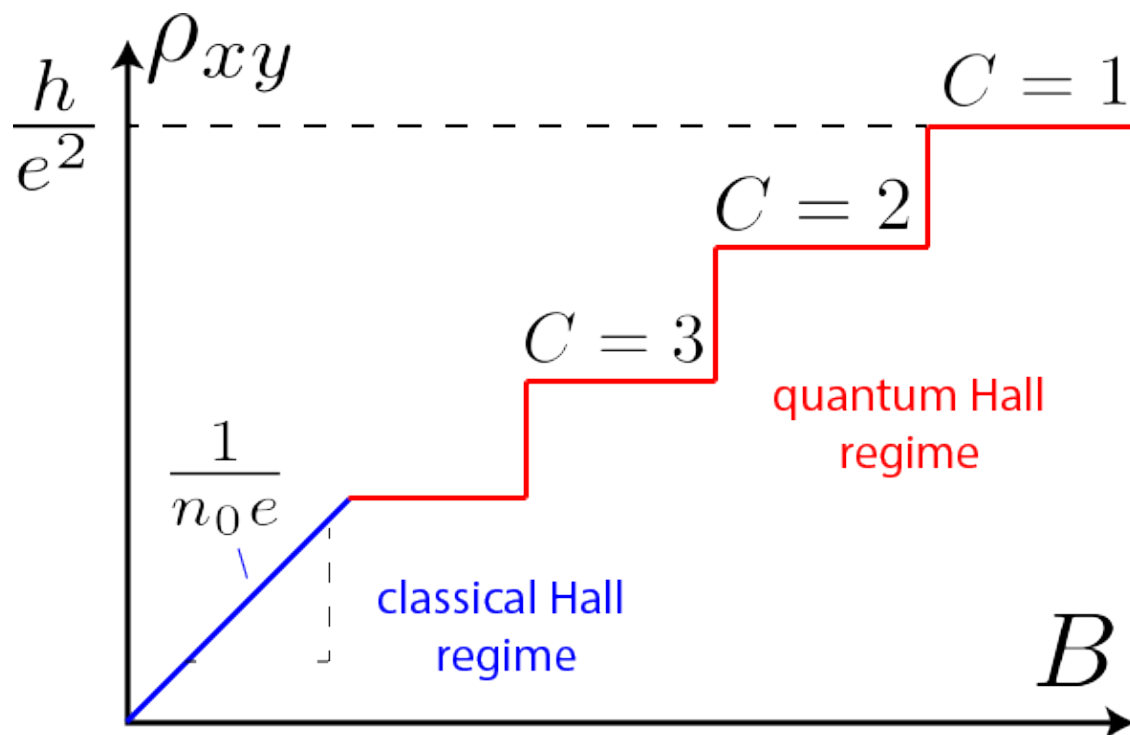
Figure 1.2. Hall resistivity ρ_{xy} as a function of the applied magnetic field B. In the classical regime $B \lesssim 1$ T, the slope is equal to the Hall coefficient $R_H = 1/n_0 e$. In the quantum regime, the Hall resistivity plateaus at discrete values of the resistance quantum $\rho_{xy} = h/Ce^2$, where $C \in \mathbb{Z}$ is an integer.

structure constant [4]. Although there are a few equivalent explanations of the QHE, such as gauge invariance [5] and Landau quantization [6], the one we are most interested in is the topological interpretation.

1.1.1 Chern number (TKNN invariant)

Thouless, Kohomoto, Nightingale and den Nijs (TKNN) showed that the Hall conductivity is proportional to a topological invariant [7]. Using the Kubo formula and some clever mathematical manipulations, one can show that C is in fact the Chern number, also known as the TKNN invariant,

$$2\pi C = \sum_\alpha \int_{\mathbb{T}^2} F_{\alpha\mathbf{k}} d^2\mathbf{k}, \qquad F_{\alpha\mathbf{k}} = -\mathrm{i}\left[\langle\partial_x u_{\alpha\mathbf{k}}|\partial_y u_{\alpha\mathbf{k}}\rangle - \langle\partial_y u_{\alpha\mathbf{k}}|\partial_x u_{\alpha\mathbf{k}}\rangle\right]. \qquad (1.3)$$

$|u_{n\mathbf{k}}\rangle = \mathrm{e}^{-\mathrm{i}\mathbf{k}\cdot\mathbf{r}}|\psi_{n\mathbf{k}}\rangle$ are the cell-periodic wave functions and α runs over all the filled bands. The Fermi energy μ lies in the band gap such that all bands $E_{n\mathbf{k}} < \mu$ are completely filled. The derivatives $\partial_i = \partial/\partial k_i$ are with respect to the momentum coordinate. Equation (1.3) has an unmistakably similar form as the GBT theorem [Eq. (1.1)] with a few minor caveats. In this case, F_n is the Berry curvature of a band n and the integral is performed over the momentum space manifold $\mathbf{k} \in \mathbb{T}^2$. In two spatial dimensions, the Brillouin zone (BZ) is equivalent to a torus due to the periodic boundary conditions. It must be noted that F is *not* the same as the Gaussian curvature of the manifold – it is slightly more abstract. The Berry curvature F is associated with the phase (U(1) gauge) of the wave function.

1.1.2 Berry phase

The astute reader may have noticed that the Berry curvature F can be expressed as the curl of a vector potential $\mathbf{A}$, known as the Berry connection,

$$\mathbf{A}_{\mathbf{k}} = -\mathrm{i}\langle u_{\mathbf{k}}|\partial_{\mathbf{k}} u_{\mathbf{k}}\rangle, \qquad F_{\mathbf{k}} = \partial_x A_y - \partial_y A_x. \qquad (1.4)$$

There is a clear analogy with electromagnetism as F takes the same form as the out-of-plane magnetic field B, but in momentum space. As a consequence of Dirac quantization [8], the

Chern number C therefore counts the number of "magnetic monopoles" in the solid-state band structure. Although magnetic monopoles have never been found in real space, there is conclusive evidence that they can exist in momentum space. This monopole argument will be made more precise in Ch. 4, as well as the connection to topological electrodynamics, but it suffices to prove that C must be quantized due to the single-valuedness of the wave function.

The Berry connection $\mathbf{A}$ is not gauge invariant and is therefore not observable because any arbitrary choice in U(1) gauge takes us to,

$$|u_\mathbf{k}\rangle \to e^{i\phi_\mathbf{k}}|u_\mathbf{k}\rangle, \qquad \mathbf{A}_\mathbf{k} \to \mathbf{A}_\mathbf{k} + \partial_\mathbf{k}\phi_\mathbf{k}. \tag{1.5}$$

However, the line integral around any closed path P is gauge invariant and determines the Berry phase $e^{i\gamma}$ accumulated from this cyclic evolution [9],

$$\gamma(P) = \oint_P \mathbf{A}_\mathbf{k} \cdot d\mathbf{k} = \int_M F_\mathbf{k} d^2\mathbf{k}. \tag{1.6}$$

The Berry phase is a geometric phase because it only depends on the path traversed in momentum space, not the rate the path is traversed. Utilizing Stoke's theorem, the Berry phase is equivalent to the flux of Berry curvature F through the surface manifold M that is bounded by P. Now we choose a path P that encloses the entire BZ such that the surface is the torus $M = \mathbb{T}^2$. Due to periodic boundary conditions, the evolution of this path is equivalent to translating to another BZ $|\psi_{\mathbf{k}+\mathbf{g}}\rangle = |\psi_\mathbf{k}\rangle$. Hence, the Berry phase around this path must come in integer multiples of 2π for the wave function to be single-valued,

$$\gamma(P) = \oint_P \mathbf{A}_\mathbf{k} \cdot d\mathbf{k} = \int_{\mathbb{T}^2} F_\mathbf{k} d^2\mathbf{k} = 2\pi C, \tag{1.7}$$

where $C \in \mathbb{Z}$ is the Chern number (TKNN invariant). The topological quantization of C is incredibly robust as it does not depend on any special properties or configurations of the system. It is fairly straightforward to show that all perturbations to the Hamiltonian (aka. continuous deformations) leave the Chern number in Eq. (1.7) invariant [10]. Even in relativity dirty samples, with moderate disorder, the Hall conductivity remains quantized at
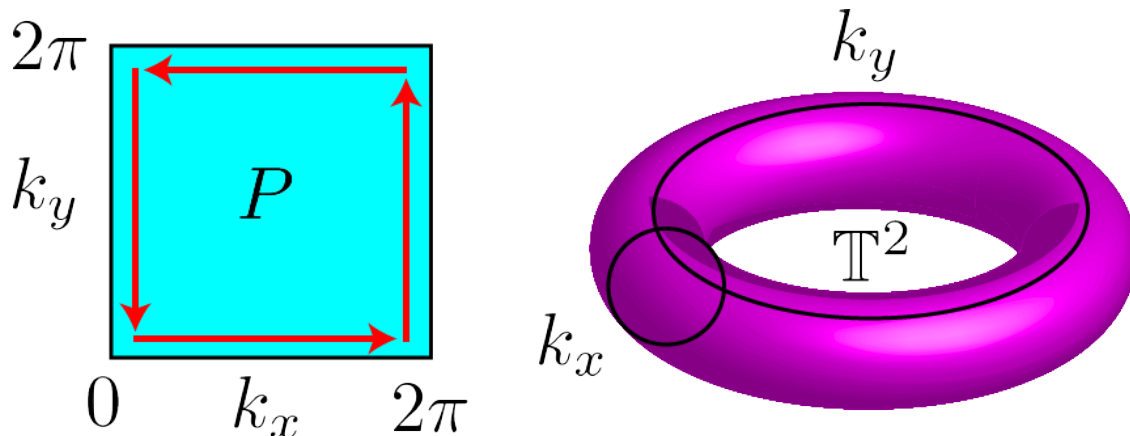
Figure 1.3. Proof of Chern quantization for a rectangular lattice. The line integral around the path P encloses the entire Brillouin zone (BZ), which is equal to the total Berry flux through the torus $\mathbb{T}^2$. The Berry phase around this path must come in 2π multiples of the Chern number $\gamma(P) = 2\pi C$.

the plateaus. A Landau quantization argument could never explain this behavior because it assumes there is no atomic potential, such that the energy spectrum is flat and massively degenerate. This is the power of topology and why it has pervaded every realm of condensed matter physics.

1.2 Quantum anomalous Hall effect

Historically, the Chern number C was associated with different quantum Hall states in the presence of an external magnetic field B. Increasing the strength of the magnetic field takes the electron through successive topological phase transitions which are exemplified in the integer plateaus of the Hall conductivity [Fig. 1.2]. However, not long after the discovery of the QHE, a few brilliant physicists realized that topology is not predicated on the existence of a magnetic field. Topology is an intrinsic property of matter itself. Indeed, the definition of the Chern number [Eq. (1.7)] makes no mention of a magnetic field and is still a relevant quantity in its absence $B = 0$. Haldane would be the first to demonstrate these unique topological states of matter with nonzero Chern number $C \neq 0$ [11]. Such exotic materials are aptly named Chern insulators.

An intriguing repercussion of the Chern insulator is that the Hall conductivity is quantized in units of the conductance quantum $\sigma_{xy} = Ce^2/h$ with no external magnetic field. Charge transport is permitted on the boundary of the material but forbidden in the bulk. A finite Hall voltage V_H and dissipationless edge currents are generated naturally by the material, usually from a combination of magnetic polarization and spin-orbit coupling [12]. This phenomenon is known as the quantum anomalous Hall effect (QAHE) because it was originally associated with the parity anomaly in condensed matter. We will analyze the Haldane model extensively in Sec. 1.2.1 to understand the fundamental physics of a Chern insulator and the origin of nontrivial topology. This procedure will provide us with valuable insight when we translate these ideas to electromagnetism.

1.2.1 Chern insulator: the Haldane model

The question asked by Haldane in 1988 was: can the Chern number be nonzero $C \neq 0$ if there is no magnetic field $B = 0$? The answer is yes – at least no net magnetic field. His proposal would be the first realization of a new phase of matter, the Chern insulator. That is, an isolated 2D solid-state system with a nontrivial topological invariant and a quantized Hall conductivity. Although it would take nearly thirty years to achieve the Haldane model experimentally [13], it revolutionized our understanding of matter. Topological phases cannot be explained by Landau theory as there is no symmetry breaking at a phase transition. A topological phase is a type of quantum phase, which are states of matter at absolute zero. Contrary to classical thermodynamic phase transitions, quantum phase transitions are only accessible by varying a physical parameter at zero temperature. We will see exactly how this manifests in the Haldane model.

The idea was fairly simple but ingenious. We start with graphene which is known to host Dirac fermions [14]. Graphene is comprised of a single layer of carbon atoms arranged in a honeycomb lattice. The honeycomb lattice can be decomposed into a superposition of two triangular sublattices A and B, which is illustrated in Fig. 1.4. In the tight-binding model, we assume the electrons are localized to the carbon atoms but can can hop between neighboring
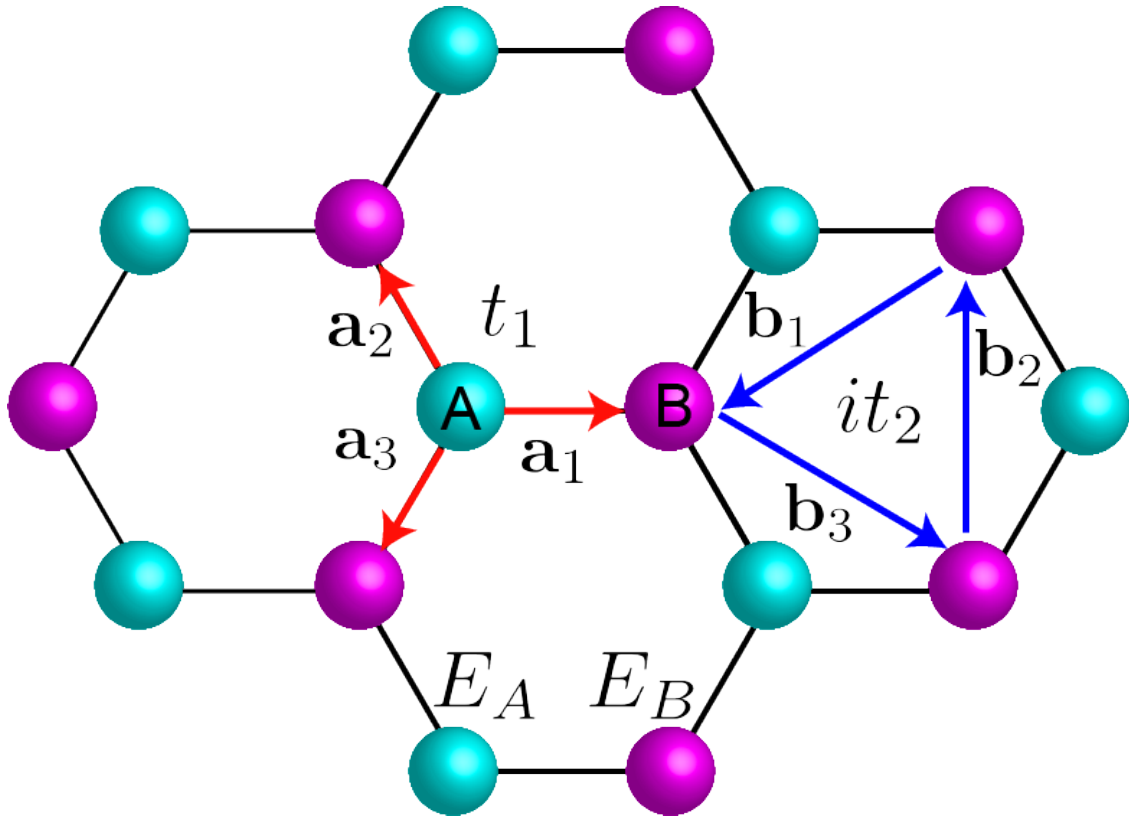
Figure 1.4. The Haldane model of graphene. The honeycomb lattice has two sublattices denoted A and B. E_A and E_B are the on site energies at A and B respectively. t_1 and t_2 are the nearest and next-nearest-neighbor (NNN) hopping amplitudes. The NNN hopping breaks time-reversal symmetry and therefore has a sense of chirality. Clockwise and counterclockwise hopping are not equivalent.

sites through overlapping p_z orbitals. Therefore, we can construct a tight-binding basis in the 2-atom unit cell,

$$u_{\mathbf{k}} = \begin{bmatrix} u_A \\ u_B \end{bmatrix}, \qquad H_{\mathbf{k}} u_{\mathbf{k}} = E_{\mathbf{k}} u_{\mathbf{k}}. \tag{1.8}$$

u_A and u_B are the amplitudes on sites A and B respectively, and $u_{\mathbf{k}}$ satisfies the Bloch equation. For nearest-neighbor hopping, the Bloch Hamiltonian can be expressed as,

$$H_{\mathbf{k}} = \begin{bmatrix} 0 & h_{\mathbf{k}}^* \\ h_{\mathbf{k}} & 0 \end{bmatrix}, \qquad h_{\mathbf{k}} = t_1 \sum_{i=1}^{3} e^{i\mathbf{k}\cdot\mathbf{a}_i}, \tag{1.9}$$

where t_1 is the hopping amplitude and $\mathbf{a}_i$ are the vectors connecting nearest-neighbors. Utilizing a set of Pauli matrices $\vec{\sigma} = (\sigma_x, \sigma_y, \sigma_z)$, the Hamiltonian can be decomposed as,

$$H_{\mathbf{k}} = t_1 \sum_i \left(\sigma_x \cos \mathbf{k} \cdot \mathbf{a}_i + \sigma_y \sin \mathbf{k} \cdot \mathbf{a}_i \right), \qquad E_{\mathbf{k}} = \pm |h_{\mathbf{k}}|. \tag{1.10}$$

We obtain the famous two-band dispersion of graphene which is plotted in Fig. 1.5. The honeycomb lattice possesses three-fold rotational symmetry which has high-symmetry points (HSPs) at $\mathbf{\Gamma} = (0,0)$ and $\mathbf{K}^{\pm} = (2\pi/a)(1, \pm 1/\sqrt{3})/3$. Graphene specifically has so-called Dirac points where the two bands intersect $E_{\mathbf{K}^{\pm}} = 0$. Performing a small momentum expansion around these points we obtain 2D massless Dirac fermions (Weyl fermions),

$$H(\mathbf{K}^{\pm} + \mathbf{q}) = \hbar v_F (q_x \sigma_x \pm q_y \sigma_y). \tag{1.11}$$

$v_F = t_1 a/\hbar$ is the Fermi velocity and $a = |\mathbf{a}_i|$ is the length of the nearest-neighbor vector.

1.2.2 Discrete symmetries

The degeneracy at the Dirac points is protected by the combination of two symmetries: inversion and time-reversal symmetry. Since the carbon atoms at sites A and B are identical, an exchange of these two sites is an inversion symmetry,

$$\sigma_x H(-\mathbf{k}) \sigma_x = H(\mathbf{k}). \tag{1.12}$$

(a) $M = t_2 = 0$

(b) $M = t_1/2$ $t_2 = 0$
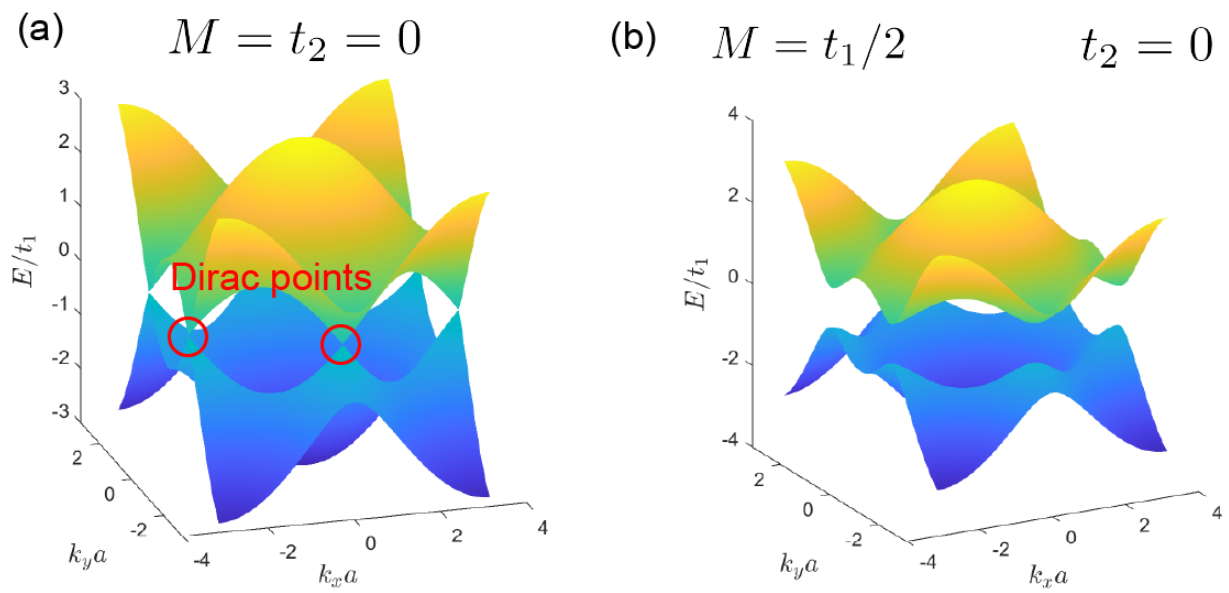
Dirac points

Figure 1.5. Dispersion $E_\mathbf{k}$ of the Haldane model of graphene for various mass parameters M and t_2. (a) Dirac points occur at the HSPs $\mathbf{K}^\pm$ in the absence of mass $M = t_2 = 0$. (b) A gap is opened when inversion symmetry is broken $M \neq 0$.

Time-reversal symmetry is anti-unitary as it involves complex conjugation. It implies the reverse process is identical,

$$H^*(-\mathbf{k}) = H(\mathbf{k}). \tag{1.13}$$

Graphene also has an approximate sublattice symmetry,

$$\sigma_z H(\mathbf{k})\sigma_z = -H(\mathbf{k}). \tag{1.14}$$

To realize topological phases in graphene, we need to break both time-reversal [Eq. (1.13)] and sublattice [Eq. (1.14)] symmetry [15]. Technically, inversion symmetry does not need to be broken but it will be useful in our theoretical exercise.

1.2.3 Breaking symmetries

Topological phases of matter are generally considered insulators and therefore the existence of a band gap is essential. The easiest way to open a band gap is to break inversion symmetry which can be done by making A and B lattice sites different atoms. The difference in the onsite energies defines an effective mass $E_A - E_B = 2M$. In the tight-binding picture, the Hamiltonian becomes,

$$H_{\mathbf{k}} = t_1 \sum_i \left(\sigma_x \cos \mathbf{k} \cdot \mathbf{a}_i + \sigma_y \sin \mathbf{k} \cdot \mathbf{a}_i \right) + M\sigma_z, \qquad E_{\mathbf{k}} = \pm\sqrt{|h_{\mathbf{k}}|^2 + M^2}. \tag{1.15}$$

The effective mass M creates a band gap and we assume the Fermi energy μ lies within this band gap, such that the lowest energy state is completely filled. However, the system is still topologically trivial because time-reversal symmetry is still present. The Berry curvature is odd $F(-\mathbf{k}) = -F(\mathbf{k})$ which implies the integral vanishes $2\pi C = \int F(\mathbf{k})d^2\mathbf{k} = 0$. To understand why this is the case in the Haldane model, we expand around the HSPs $\mathbf{K}^{\pm}$ once again,

$$H(\mathbf{K}^{\pm} + \mathbf{q}) = \hbar v_F(q_x\sigma_x \pm q_y\sigma_y) + M\sigma_z. \tag{1.16}$$

The 2D Dirac fermions have gained mass and therefore the spectrum is gapped. However, the masses at $\mathbf{K}^{\pm}$ are identical due to time-reversal symmetry $M_{K+} = M_{K-} = M$. Calculating the Chern number of the lower energy band, we find that,

$$C = \frac{1}{2}[\mathrm{sgn}(M_{K+}) - \mathrm{sgn}(M_{K-})]. \tag{1.17}$$

Clearly the phase is trivial $C = 0$ when $\mathrm{sgn}(M_{K+}) = \mathrm{sgn}(M_{K-})$. Haldane surmised that if the signs of the mass are different at the two HSPs, it is possible to achieve nontrivial $C \neq 0$ topological phases.

The final and most important step was to consider imaginary next-nearest-neighbor (NNN) hopping, which can be thought of as a staggered magnetic flux arising from some form of magnetic ordering. This breaks time-reversal symmetry because clockwise and counterclockwise hopping are not equivalent $(it_2)^* \neq it_2$. We obtain the complete Haldane model of graphene,

$$H_{\mathbf{k}} = t_1 \sum_i \left(\sigma_x \cos \mathbf{k} \cdot \mathbf{a}_i + \sigma_y \sin \mathbf{k} \cdot \mathbf{a}_i \right) + M\sigma_z + 2t_2\sigma_z \sum_i \sin \mathbf{k} \cdot \mathbf{b}_i. \tag{1.18}$$

$\mathbf{b}_i$ are the NNN vectors. With the time-reversal breaking hopping $t_2 \neq 0$, it is now possible to have different signs of the mass at the two HSPs,

$$M_{K\pm} = M \pm 3\sqrt{3}t_2. \tag{1.19}$$

Indeed, there are regimes where $\mathrm{sgn}(M_{K+}) \neq \mathrm{sgn}(M_{K-})$ and the Chern number is nonzero $C \neq 0$. These topological regimes are materialized when $|M| < 3\sqrt{3}|t_2|$. The truly remarkable consequence is that the Hall conductivity is quantized $\sigma_{xy} = Ce^2/h$ in the absence of a magnetic field. Although the material is insulating in the bulk, there is a dissipationless chiral current on the edge. Interestingly, the topological phase transitions occur at points of accidental degeneracy (Dirac points) where the bands intersect one another. Here, the Berry curvature is singular and indicates a discontinuous deformation of the wave function. For the Haldane model, these Dirac points can reappear whenever a mass passes through zero
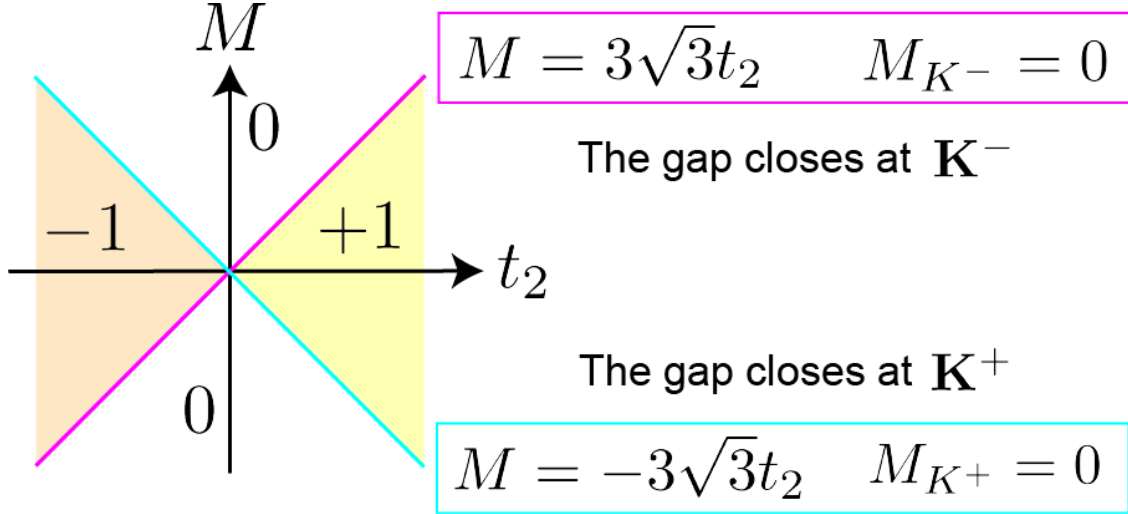
Figure 1.6. Topological phase diagram for the Haldane model of graphene at zero temperature. The plot is of the Chern number C for various mass parameters M and t_2. The magenta and cyan lines denote the phase transition lines where the Chern number changes discontinuously. These topological phase transitions at Dirac points (accidental degeneracies) where the band gap closes.

$M_{K\pm} = 0$. The topological phase diagram of the Haldane model Chern insulator is shown in Fig. 1.6.

1.3 Topological electrodynamics

Since the dawn of the Chern insulator, a plethora of topological phases in condensed matter have been proposed [16]. Most notably, it spawned the field of topological insulators [17] which are the time-reversal symmetric counterparts to the Chern insulator. Topological insulators are a fermionic phase and have become one of the most active research areas in condensed matter physics because they exist in both 2D and 3D. There is expected to be many naturally occurring topological insulators which has made them incredibly enticing for device applications. Nevertheless, all known topological phases of matter have focused on the fermionic states – the topology of the electronic wave function. The main goal of this thesis is to motivate a topological interpretation of the electromagnetic field and consider the bosonic states of matter.

The principal idea behind topological electrodynamics is to analyze the electromagnetic fields through the lens of topology, the same way we analyze the electron wave function. We want to systematically dissect the properties in electromagnetism that are conserved under continuous deformations. Generally, these constitute the topological quantities of the electric $\vec{\mathcal{E}}$ and magnetic $\vec{\mathcal{H}}$ fields, but also the polarization $\vec{\mathcal{P}}$ and magnetization $\vec{\mathcal{M}}$ densities. In the photonic crystal and metamaterials literature, this area of research is called topological photonics [18] as it mostly concerns free photons. Here, the densities $\vec{\mathcal{P}}$ and $\vec{\mathcal{M}}$ are strictly linear functions of the fields $\vec{\mathcal{E}}$ and $\vec{\mathcal{H}}$. In condensed matter systems we are also interested in dipole-carrying excitations like plasmons, excitons, magnons and phonons as they can couple strongly to the photon to form quasiparticles (polaritons). Here, the densities $\vec{\mathcal{P}}$ and $\vec{\mathcal{M}}$ are also functions of the temporal and spatial derivatives of $\vec{\mathcal{E}}$ and $\vec{\mathcal{H}}$. Polaritons become the new normal modes of a material and these electromagnetic states can possess nontrivial topology – this is the main underpinning of topological electromagnetic phases of matter. For conciseness, topological electrodynamics is the umbrella that refers to all topological phenomena in electromagnetism, whether it be in photonic crystals or condensed matter. A comparison is provided in Fig. 1.7.

By the advent of topological electrodynamics, the condensed matter community had mapped out all single-particle topological field theories in every dimension and symmetry class. This is known as the ten-fold way as there are generically ten symmetry classes that make up all possible Hamiltonians [15]. The symmetry classes are related to the species of particle, fermion or boson, in the presence or absence of some discrete symmetries. Since electromagnetism is a real-valued vector (bosonic) field theory it technically belongs to symmetry class D. As a result, an electromagnetic topological invariant is an integer $\mathbb{Z}$ and only exists in 2D when time-reversal symmetry is broken. A bosonic counterpart to the topological insulator does not exist. This significantly narrows the number of topological electromagnetic materials at our disposal but fortunately 2D materials like graphene are of considerable interest. Note that the electromagnetic invariant is analogous to the Chern number, but is a measure of the Berry phase of the photon/polariton field, not the electron wave function.

1.3.1 Topological photonics

Coincidentally, Haldane also pioneered topological photonics and is attributed with the first conceptual propositions for both electronic and photonic Chern insulators [19], [20]. A photonic Chern insulator possesses a nontrivial photonic Chern number, which is calculated from the Berry phase of the electric $\vec{\mathcal{E}}$ and magnetic $\vec{\mathcal{H}}$ fields,

$$\mathbf{A_k} = -\mathrm{i}\langle\vec{\mathcal{D}}_\mathbf{k}|\partial_\mathbf{k}\vec{\mathcal{E}}_\mathbf{k}\rangle - \mathrm{i}\langle\vec{\mathcal{B}}_\mathbf{k}|\partial_\mathbf{k}\vec{\mathcal{H}}_\mathbf{k}\rangle, \qquad F_\mathbf{k} = \partial_x A_y - \partial_y A_x. \tag{1.20}$$

Note that Eq. (1.20) only holds in a non-interacting free-field theory. The Berry phase in an interacting theory is significantly more complicated. As we know from the TKNN invariant [Eq. (1.3)], a closed momentum manifold M is essential to guarantee Chern number quantization,

$$2\pi C = \int_M F_\mathbf{k} d^2\mathbf{k}, \qquad C \in \mathbb{Z}. \tag{1.21}$$

Raghu and Haldane utilized a gyrotropic photonic crystal to achieve their nontrivial topology which places photons on the torus $M = \mathbb{T}^2$. The proof of Chern quantization in Eq. (1.7) applies equally well for photons and is a consequence of the single-valuedness of the electromagnetic field.

Photonic crystals are macroscopically engineered lattices that facilitate unique control over light propagation [21]. Dielectric scatterers and resonators are arranged in a periodic structure to form a lattice where electromagnetic waves can interfere with themselves. Since the lattice is designed to match the wavelength of a free photon, the normal modes of the system generate a photonic band structure. This band structure can possess spectral gaps that forbid photon propagation just like insulators forbid electron propagation. Note though, the operating regime of a photonic crystal is usually far detuned from any dipolar oscillations of the constituent materials. Thus, the photon can be treated as a non-interacting free-field theory [22]. This essentially means there is no temporal or spatial dispersion – the materials respond instantaneously and point-like.

The procedure to create a topological photonic band structure was similar to Haldane's original proposal in graphene. His photonic crystal was designed using time-reversal break-

ing magneto-optic media, also known as Faraday-effect or gyrotropic media, in a hexagon formation. Breaking time-reversal and inversion symmetry creates a spectral gap at the Dirac points due to the generation of an effective mass. For certain parameters, the Dirac Hamiltonian acquires a mass that changes sign at different HSPs and is therefore topologically nontrivial. Although the photonic Chern number is nonzero, there is no quantized observable like the Hall conductivity. The primary feature of a topological photonic system is chiral edge states at the boundary that span the entire photonic band gap.

Shortly after the theoretical proposal of a topological photonic crystal, a similar platform was demonstrated experimentally by Joannopoulos and Soljacic [23]. Their microwave crystal utilized ferrite rods surrounded by air to generate a topologically nontrivial photonic band structure. The main result was direct observation of unidirectional backscatter-immune topological electromagnetic states at the boundary of the photonic crystal. Electromagnetic waves propagate in a singular direction and around sharp defects because no backward propagating mode exists to scatter into. Since these achievements, there has been a veritable explosion of research in topological photonics. Most of the intense interest is focused on utilizing robust photonic pathways for applications and discovering other exotic topological phenomena [24].

Nevertheless, the question posed in this thesis is can topological electromagnetic phases exist as a *state of matter*? That is, can real atomic crystals like graphene be intrinsically topological with respect to the photon, without the need for macroscopic engineering? The answer is a resounding yes and there are two reasons why this is an important pursuit. Firstly, from a fundamental science perspective, it means there are new quantum phases of matter that are intrinsically bosonic and cannot be explained by electronic band theory or many-body theory. Second, from a technological standpoint, this would miniaturize current photonics platforms by orders of magnitude since the length scales are comparable to the atomic lattice constant.

1.3.2 Topological electromagnetic phases of matter

The key idea behind my work is to substitute the photonic crystal with the atomic crystal [Fig. 1.7]. Since real materials are periodic, a photon propagating in the solid-state innately
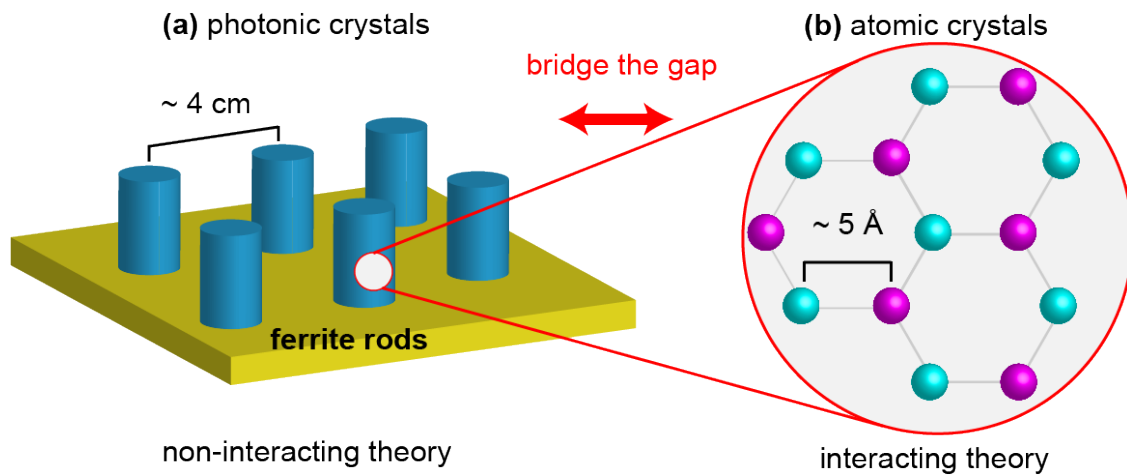
Figure 1.7. Comparison of (a) photonic crystals and (b) atomic crystals. The goal of topological electrodynamics is to bridge the gap between photonic crystals and condensed matter systems. (a) Topological photonics is usually explained by a non-interacting free-field theory as there are no dipole-carrying excitations. Here, topology is generated by wave interference from dielectric scatterers and resonators. (b) Topological electromagnetic phases is necessarily an interacting theory as there are many dipole-carrying excitations. In this case, the material itself is topological and pertains to unique quantum phases of matter.

lives within the Brillouin zone (on the torus), at least at the microscopic level. Hence, a naturally occurring electromagnetic topological invariant (photonic Chern number) exists but it requires an atomic theory. The photon momentum must be defined to the edges of the BZ as this is necessary to ensure Chern quantization. The uniquely difficult problem in the atomic theory is that the crystal is both temporally and spatially dispersive. How this physically manifests will be discussed below. We also require some form of nonreciprocity which is usually generated from an external magnetic field B. We leave the rigorous definition of these electromagnetic topological invariants to the following chapters since they are very involved. Here, we outline the many hurdles that need to be overcome to achieve nontrivial topology in condensed matter.

One difficulty that is immediately encountered in nonreciprocal electromagnetism is temporal dispersion – the frequency dependence of optical response. Temporal dispersion is ultimately connected to some electric or magnetic dipole-carrying excitation and cannot be avoided as it is impossible to break time-reversal symmetry without dispersion. In photonic crystals one can get around this problem by detuning far from the resonance, such that the effect of dispersion is negligible. However, in condensed matter, these excitations are components of the natural modes of the material – the polaritons. We call this an interacting theory because there are extra degrees of freedom in the system that cannot be ignored. The relevant particles are not simply photons but hybrid quasiparticles such as plasmon-, exciton- or phonon-polaritons. To understand topological electromagnetic phases of matter, we need to carefully quantify these complex coupled oscillators.

When dealing with nanophotonic structures we also run into spatial dispersion. Spatial dispersion, or nonlocality, is associated with the wavevector dependence of optical response and accounts for the spreading of the interaction over a finite length. These effects are significant on microscopic length scales and therefore must enter the atomic field theory. Nonlocality has generally been ignored in photonics because it is rather cumbersome and the boundary physics is incredibly complicated. The conventional wisdom would suggest that nonlocality contributes relatively small perturbations to optics and is therefore negligible. However, topological electromagnetic phases of matter *require* spatial dispersion and there is qualitatively new phenomena when both nonlocality and nonreciprocity are present.
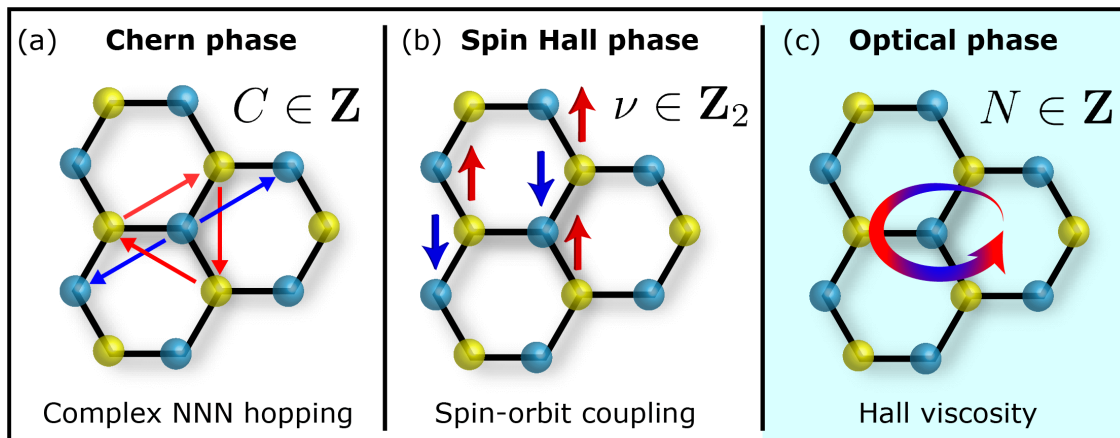
Figure 1.8. Topological phases of graphene. (a) The Chern phase $C \in \mathbb{Z}$ arises from complex next-nearest-neighbor (NNN) hopping. (b) The quantum spin Hall phase $\nu \in \mathbb{Z}_2$ is due to spin-orbit coupling (topological insulator). (c) The optical phase $N \in \mathbb{Z}$ is a consequence of Hall viscosity η_H. These three phases can be identified as the Chern insulator, quantum spin Hall insulator and viscous Hall insulator respectively.

Fundamentally, these effects cannot be regarded as perturbations as they have topological implications and contribute to the overall Berry phase.

1.3.3   Magnetohydrodynamics and Hall viscosity

Many of the physical systems proposed in this thesis take inspiration from the Haldane model – a change in sign of a mass parameter indicates nontrivial topology. Perhaps unsurprisingly, this change in sign of a "photonic mass" cannot occur without nonlocality. Our main theoretical tool to study such problems is magnetohydrodynamics (MHD) which characterizes viscous electron fluids in the presence of strong magnetic fields. For time-varying waves, MHD describes the viscous plasma oscillations (plasmons) of the electron fluid. Plasmons couple to photons to generate the new quasiparticles of the system – plasmon-polaritons. In specific hydrodynamic regimes, these quasiparticles can be topologically nontrivial and the fundamental physical mechanism is due to an intriguing nonlocal effect known as Hall viscosity [see Fig. 1.8].

Viscosity inherently entails nonlocality as there is diffusion of the fluid. This emerges from the stress-strain response of a deformable body – a gradient in the velocity field generates

a stress. In two dimensions, the stress tensor ς_{ij} can be expressed in terms of the rank-four viscosity tensor $\eta_{ij,kl}$ and the velocity gradient (strain-rate) tensor $(\partial^i v^j + \partial^j v^i)/2$,

$$\varsigma_{ij} = \frac{1}{2}\eta_{ij,kl}(\partial^k v^l + \partial^l v^k). \tag{1.22}$$

Repeated spatial indices $(i = x, y)$ implies summation. Viscosity is a measure of a fluid's resistance to deformation. In a 2D isotropic fluid, there are three possible contributions to the viscosity tensor,

$$\eta_{ij,kl} = \zeta\delta_{ij}\delta_{kl} + \eta(\delta_{ik}\delta_{jl} + \delta_{il}\delta_{jk} - \delta_{ij}\delta_{kl}) - \eta_H(\delta_{jk}\epsilon_{il} - \delta_{il}\epsilon_{kj}). \tag{1.23}$$

ζ and η are the bulk and shear viscosities respectively, which govern dissipation due to compression and shearing. From the second law of thermodynamics, $\zeta \geq 0$ and $\eta \geq 0$ must always be positive to ensure lossy fluid flow. One additional viscous component is permitted in parity and time-reversal breaking fluids – the so-called Hall viscosity η_H. Hall viscosity, also known as odd viscosity in fluid mechanics, can be either positive or negative as it is dissipationless. The effect of η_H is to generate a diffusive force perpendicular to the fluid's motion which may repel or reinforce an external magnetic field B. Hall viscosity has gained considerable attention recently due to multiple experimental observations of hydrodynamic electron fluids [25]. The hydrodynamic regime occurs in very clean, strongly-correlated systems, which has only been made possible due to isolation of high-grade materials like graphene.

The Hall viscosity enters electromagnetism through conventional continuum mechanics. Since the current density $\mathbf{J} = -en_0\mathbf{v}$ is directly proportional to the velocity field, the divergence of the stress tensor $\boldsymbol{\nabla} \cdot \varsigma$ imparts a type of Lorentz force on a stream of electrons. Linearizing the Navier-Stokes (NS) equation around its equilibrium state and assuming a zero temperature quantum limit $\zeta = \eta = 0$, we obtain the MHD model of a viscous quantum Hall fluid,

$$\partial_t \mathbf{J} = -v_s^2\boldsymbol{\nabla}\rho - (\omega_c + \nu_H\boldsymbol{\nabla}^2)\mathbf{J} \times \hat{z} + \frac{e^2 n_0}{m}\mathbf{E}. \tag{1.24}$$

48

APPLIES UNIVERSALLY

Cyclotron orbits — 2D electron fluid — Landau levels

weak field regime   strong field regime
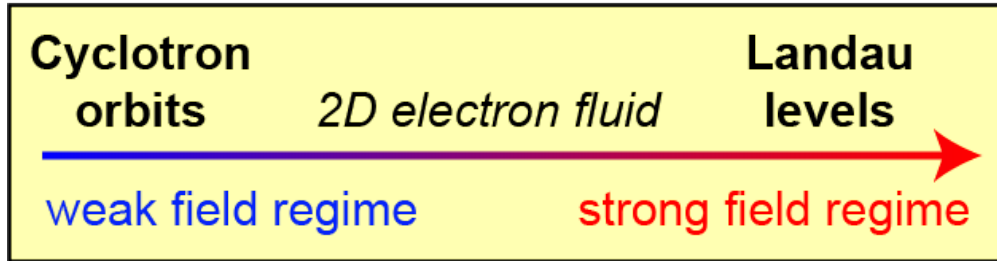
Hall conductivity: σ_{xy} Hall viscosity: η_H

EM theory	$\mathrm{sgn}(\sigma_{xy})$	$\mathrm{sgn}(\eta_H)$
trivial gap open	$+$	$-$
	$-$	$+$
nontrivial gap closed by edge states	$+$	$+$
	$-$	$-$

Figure 1.9. The main result of an electromagnetic (EM) theory of magneto-hydrodynamics is that the relative sign of the Hall conductivity σ_{xy} and the the Hall viscosity η_H predicts a new quantum phase of matter. When the relative signs are the same, Hall viscosity repels external magnetic fields and the EM theory is topologically nontrivial.

Table 1.1. Summary of the 2+1D topological phases in graphene. The charge C and spin ν phases are defined at zero photon energy and momentum $\omega = k = 0$. The optical N-phases are defined for dynamical electromagnetic (EM) fields, $\omega \neq k \neq 0$.

Quanta	(a) Charge	(b) Spin	(c) Polarization
Class	A	AII	D
Invariant	$C \in \mathbb{Z}$	$\nu \in \mathbb{Z}_2$	$N \in \mathbb{Z}$
Mechanism	NNN hopping	Spin-orbit coupling	Hall viscosity
Observable	$\sigma_{xy} = Ce^2/h$	$\sigma_{xy}^s = \nu e/2\pi$	B-field repulsion
EM field	$\omega = k = 0$		$\omega \neq k \neq 0$

Combining Eq. (1.24) with the continuity equation $\partial_t \rho + \boldsymbol{\nabla} \cdot \mathbf{J} = 0$ completely specifies the charge and current densities with appropriate boundary conditions. v_s is the speed of sound, $\omega_c = eB/cm$ is the cyclotron frequency and $\nu_H = \eta_H/mn_0$ is the kinetic Hall viscosity. m being the effective mass. This model has been remarkably successful explaining experimental observations of Hall viscosity in graphene.

The topology can be surmised by considering the combined effect of ω_c and ν_H in the bulk momentum space. The cyclotron motion ω_c creates a spectral gap in the plasmon dispersion and is formally equivalent to a Dirac mass. Hall viscosity ν_H makes this Dirac mass momentum dependent $\omega_c \rightarrow \omega_c - \nu_H k^2$, which means it can change sign within the dispersion. Clearly a sign change is only possible in the repulsive regime $\omega_c \nu_H > 0$ which denotes the nontrivial phase. The most important outcome of MHD is that the electromagnetic theory is topological for specific signs of the Hall conductivity and Hall viscosity which is illustrated in Fig. 1.9. It should be emphasized that this unique quantum phase of matter is defined through the topology of electromagnetism. Table 1.1 summarizes the three topological phases in 2D materials and their relevant quanta.

1.4 Outline of thesis

This thesis follows an article-based format where each chapter is composed of a self-contained publication. In some cases, the terminology changes between chapters due to transitioning between photonics and condensed matter communities. For instance, the effect of Hall viscosity is often referred to as nonlocal gyrotropy or nonlocal Hall conductivity. In

earlier papers, this type of response was argued purely from a mathematical basis but we would ultimately link it to an important physical mechanism in strongly-correlated electron fluids. My work is entirely theoretical and combines topology with the classical electromagnetic field theory of condensed matter for the first time. However, the content should be accessible to readers with a graduate background in electromagnetism. I have tried to provide a thorough review and detailed derivations of all the results which can be found in the supplementary information of each article. These have been included in the appendices for reference. Below we summarize the key contributions of each paper.

Chapter 2 is a rigorous study of evanescent waves in traditional nanophotonic systems, such as total internal reflection, surface plasmon polaritons and optical fibers. This work utilizes only classical electromagnetism but forms the necessary stepping stone for the fully topological field theory developed in later chapters. The main achievement of this paper is the proof that transverse spin-momentum locking (SML) is an inherent property of evanescent electromagnetic waves. In these cases, photonic SML is connected to causality requirements on passive media and does not possess a robust topological interpretation like the QSHE for electrons. Nevertheless, we show that SML can be utilized for remarkably precise control of photonic pathways that are polarization dependent. By coupling circular dipoles to the near-field of optical fibers, we can achieve near 100% transmission in a single direction.

Chapter 3 is our first foray into topological electromagnetism. From first principles, we derive the effective Hamiltonian governing the dynamics of the polaritons, which generates the normal modes of the condensed matter system. We then identify the essential topological criteria for continuum photonic media and the role of spin-1 quantization in topological phases. The most significant result is that both temporal and spatial dispersion are necessary to define a topological electromagnetic phase of matter. To conclude the chapter, we propose the simplest realization of a naturally occurring photonic Chern insulator, which arises from nonlocal Hall conductivity (Hall viscosity). At the boundary of the material, we uncover gapless chiral photonic edge states that are immune to back-scattering. This has been dubbed the quantum gyroelectric effect (QGEE) because the edge state is completely insensitive to the contacting medium. A major accomplishment of this boundary theory is proving that the edge state satisfies open boundary conditions which has never been demon-

strated in any photonics platform. It is important to note that fundamental symmetries of field theory such as U(1) gauge symmetry and SO(3) spin symmetry are captured by our theoretical framework. In this regard, the Maxwell Hamiltonian presents an entirely new approach to classical electromagnetic fields interacting with condensed matter. The topological quantization arises due to the spin-1 nature of the theory and is fundamentally different from the conventional Hamiltonian defined in quantum optics.

Chapter 4 provides a detailed analysis of the photonic Chern insulator proposed in Ch. 3 by comparing it with its supersymmetric partner – the electronic Chern insulator. At low frequency, Hall conductivity plays the role of photonic mass as there is a one-to-one correspondence with the Dirac equation. Here, we show that the electromagnetic field possesses a spin-1 skyrmion in momentum space. The precession of photon spin is a direct result of Hall viscosity and is ultimately tied to the presence of Dirac monopoles and strings in the Berry gauge. These photonic Dirac monopoles are integer quantized due to the spin-1 nature of the photon. Importantly, we show that this phenomenon of gauge discontinuity in the photonic eigenmodes fundamentally requires nonlocal gyrotropy.

Chapter 5 presents the lattice generalization of the continuum theory in Ch. 3. Here, we derive the complete atomic theory of the polaritonic Bloch modes, for all momenta in the Brillouin zone, and show that an electromagnetic topological invariant is rigorously defined. We also uncover important properties of the topology that are connected to the underlying point group symmetries of the lattice. The irreducible representation (irrep) of the photon at high-symmetry points places restrictions on the photonic Chern number. These restrictions amount to distinct classes of symmetry-protected topological phases. Crucially, symmetry-protected phases in electromagnetism are bosonic because the representations must be single-valued. Fermions on the other hand have double-valued representations and represent an entirely different class of symmetry-protected phase.

In Chapter 6 we delve deeper into this concept of photonic mass and engineer interfaces that host robust unidirectional electromagnetic edge states. At fixed frequency, it is revealed that gyrotopy plays exactly the role of a photonic mass. The interface of two materials with opposite gyrotopy is therefore the photonic equivalent of Jackiw-Rebbi modes. It is proven that as long as gyrotropy changes sign across the interface, an edge state must exist and is

immune to perturbations. Additionally, we study the polarization properties of these edge modes which reveals longitudinal SML that is helically-quantized. Quantization of these unidirectional Maxwellian spin waves has a topological origin. This should be contrasted with transverse SML in traditional surface waves which is not quantized and has no topological interpretation (see Ch. 2).

Chapter 7 completes the discussion on topological electrodynamics. This chapter is a milestone because we propose the first Lagrangian formulation of a topological electromagnetic phase. It is now possible to canonically quantize topological photons which has been inaccessible in electromagnetism until now. Interestingly, the effective field theory we propose is a combination of Hall viscosity with Maxwell-Chern-Simons (MCS) theory – aptly named viscous MCS theory. Minimization of the viscous MCS action generates the equations of motion of the photonic Chern insulator (see Ch. 4). It also supplies the topological boundary conditions that minimize the surface variation, guaranteeing that the gapless photonic edge states cost zero energy.

Lastly, the summary Chapter 8 reviews the material presented in this thesis and provides some concluding remarks on the future outlook of topological electrodynamics.

2. UNIVERSAL SPIN-MOMENTUM LOCKING OF EVANESCENT WAVES

From [T. V. Mechelen and Z. Jacob, "Universal spin-momentum locking of evanescent waves," *Optica*, vol. 3, no. 2, pp. 118–126, Feb. 2016]. © 2020 Optical Society of America. [26]

We show the existence of an inherent property of evanescent electromagnetic waves: spin-momentum locking, where the direction of momentum fundamentally locks the polarization of the wave. We trace the ultimate origin of this phenomenon to complex dispersion and causality requirements on evanescent waves. We demonstrate that every case of evanescent waves in total internal reflection, surface states and optical fibers/waveguides possesses this intrinsic spin-momentum locking. We also introduce a universal right-handed triplet consisting of momentum, decay and spin for evanescent waves. We derive the Stokes parameters for evanescent waves which reveal an intriguing result – every fast decaying evanescent wave is inherently circularly polarized with its handedness tied to the direction of propagation. We also show the existence of a fundamental angle associated with total internal reflection (TIR) such that propagating waves locally inherit perfect circular polarized characteristics from the evanescent wave. This circular TIR condition occurs if and only if the ratio of permittivities of the two dielectric media exceeds the golden ratio. Our work leads to a unified understanding of this spin-momentum locking in various nanophotonic experiments and sheds light on the electromagnetic analogy with the quantum spin-Hall state for electrons.

2.1 Introduction

An important signature of the recently discovered quantum spin-Hall (QSH) state of matter is the existence of electronic surface states which are robust to disorder (non-magnetic impurities) [27], [28]. This property arises since the spin of the electron is intrinsically locked to the direction of propagation (momentum) and the electrons cannot backscatter unless there is a spin-flip [29]. Intriguingly, recent experiments have explored an analogous phenomenon in photonics showing polarization dependent directional propagation of optical

modes in spontaneously emitted as well as scattered light [30]–[35]. For example, experiments have shown that spontaneous emission from atomic transitions is preferentially uni-directed along a fiber depending on the magnetic quantum number of the excited state [36]. On the other hand, surface plasmon polaritons excited with circularly polarized light have also demonstrated unidirectional propagation [37], [38]. One common thread in these experiments is the evanescent wave which leads to a clear hint that the effect is tied to fundamental properties of decaying waves and not the details of the nanophotonic structures. A quantum field theoretic treatment has also recently shed light on the interesting spin properties of evanescent waves [39], [40]. However, there is an urgent need for a unified theory about the inherent origin of this effect and its underlying connection to experiments. In analogy with the behavior of electrons in the quantum spin-Hall effect, we call this phenomenon "spin-momentum locking".

In this paper, our central contribution is the proof that spin-momentum locking is universal behavior for electromagnetic waves which stems from the complex dispersion relation of evanescent waves and fundamental causality requirements. We introduce a universal triplet consisting of momentum, decay and spin of evanescent waves. We show that the Stokes parameters for an evanescent wave unambiguously reveals that every fast decaying evanescent wave is inherently circularly polarized irrespective of how it originates. Furthermore, this inherent handedness (spin) is locked to the direction of propagation (momentum). This information hidden in the Stokes parameters has been overlooked till date and is in stark contrast to the existing knowledge on propagating waves. The universality of this phenomenon is revealed by analyzing, in detail, the cases corresponding to a) total internal reflection (TIR) b) waveguides c) optical fibers d) surface electromagnetic waves. We also show the existence of a unique criterion in TIR ("golden ratio condition") at which propagating light is locally circularly polarized on total internal reflection. This effect can be used to verify our theory in near-field optical experiments. Lastly, we provide detailed insight on how spontaneous emission from a quantum emitter can couple to spin-momentum locked states in optical fibers. Our work explains various experimental observations and should open up future ways of exploiting this universal spin-momentum locking for practical applications.

2.2 Evanescent waves

2.2.1 Complex dispersion relation

We first construct a general basis vector for evanescent waves independent of origin which reveals a universal electromagnetic right handed triplet consisting of momentum, decay and spin. The wavevector of an evanescent plane wave necessarily has to be complex and can be written in a general form as $\vec{k} = \vec{\kappa} + i\vec{\eta}$. Here, $\vec{\eta}$ is the imaginary part of $\vec{k}$ and is related to the decay while $\vec{\kappa}$ is the real part related to phase propagation (momentum). Starting from the dispersion relation obtained using Maxwell's equations in free space, we have,

$$\vec{k} \cdot \vec{k} = k_0{}^2 \tag{2.1}$$

which implies, since $k_0 = \omega/c$ is purely real, that the two components of $\vec{k}$ must satisfy,

$$\kappa^2 - \eta^2 = k_0{}^2 \tag{2.2a}$$

$$\vec{\kappa} \cdot \vec{\eta} = 0. \tag{2.2b}$$

We note here that for complex wavevector $\vec{k}$, the absolute value is given by $|\vec{k}|^2 = \vec{k} \cdot \vec{k}^*$ which is different from the factor $\vec{k} \cdot \vec{k}$ that enters the dispersion relation of plane waves in vacuum. These two terms are not equivalent for evanescent waves. From Eq. (2.2b), we make an important observation: the complex dispersion relation in free space necessarily requires that $\vec{\kappa}$ and $\vec{\eta}$ be orthogonal. This implies that the phase propagation of an evanescent wave (momentum) is perpendicular to its direction of decay. Furthermore, these orthogonal phase propagation and decay vectors always have a phase difference between them (factor of i $= \sqrt{-1}$) which are imprinted on orthogonal components of the electromagnetic field vectors through the transversality condition ($\vec{k} \cdot \vec{\mathcal{E}} = 0$). We will show now that this is the intuitive reason for the inherent handedness (spin) of the evanescent wave.

Like propagating plane waves, evanescent waves can have two orthogonal field polarizations which we denote by $\hat{s}$ and $\hat{p}$ unit vectors. $\hat{s}$ is defined to have an electric field perpendicular to the plane formed by the propagation vector ($\vec{\kappa}$) and decay vector ($\vec{\eta}$) while

the electric field vector lies in the plane for $\hat{p}$. Without any loss of generality, an elegant choice of basis can be made to represent these unit vectors uniquely in terms of the evanescent wave wavevector. Our choice of basis is the triplet $\{\vec{\kappa}, \vec{\eta}, \vec{\kappa} \times \vec{\eta}\}$. We emphasize that this choice of basis alone fulfils the transversality condition imposed on electromagnetic waves in vacuum ($\vec{k} \cdot \vec{\mathcal{E}} = 0$) and therefore is *coordinate-independent*.

By defining $\hat{s}$ and $\hat{p}$ as,

$$\hat{s} = \frac{\vec{\kappa} \times \vec{\eta}}{|\vec{\kappa} \times \vec{\eta}|} = i\frac{\vec{k} \times \vec{k}^*}{|\vec{k} \times \vec{k}^*|} \tag{2.3a}$$

$$\hat{p} = \frac{\vec{k} \times \hat{s}}{|\vec{k}|} = i\frac{\vec{k} \times (\vec{k} \times \vec{k}^*)}{|\vec{k}||\vec{k} \times \vec{k}^*|} \tag{2.3b}$$

$$\vec{k} \cdot \hat{s} = \vec{k} \cdot \hat{p} = \hat{s} \cdot \hat{p} = 0 \tag{2.3c}$$

we express the evanescent field polarization entirely in terms of its momentum ($\vec{k}$). This form is robust enough that it can also be generalized to lossy media when $\vec{\kappa}$ and $\vec{\eta}$ are non-orthogonal. We emphasize that this unique form of evanescent wave basis vectors is universal and reduces to the case of plane wave basis vectors when $\eta \to 0$. A proof is given in the supplementary information.

The above representation reveals important aspects about the intrinsic "spin" of an evanescent wave. We define this intrinsic "spin" to be the inherent handedness (left/right circular/elliptical polarization) of the field basis vector. We rigorously justify this in the next section but make a note that electric fields in any specific scenario can be represented using these basis vectors. Hence, properties of field basis vectors will always be manifested in the electric and magnetic fields.

Note first that $\hat{s}$ is purely real so the orthogonal components comprising the field vector will be in phase. Thus evanescent waves with electric field vector field perpendicular to the plane formed by the decay vector and propagation vector will show no interesting polarization characteristics. However, the $\hat{p}$ field basis vector is now complex. Using the properties from Eq. (2.2) and a bit of manipulation we obtain,

$$\hat{p} = i\left[\frac{\eta}{|\vec{k}|}\left(\frac{\vec{\kappa}}{\kappa}\right) + i\frac{\kappa}{|\vec{k}|}\left(\frac{\vec{\eta}}{\eta}\right)\right] \tag{2.4}$$
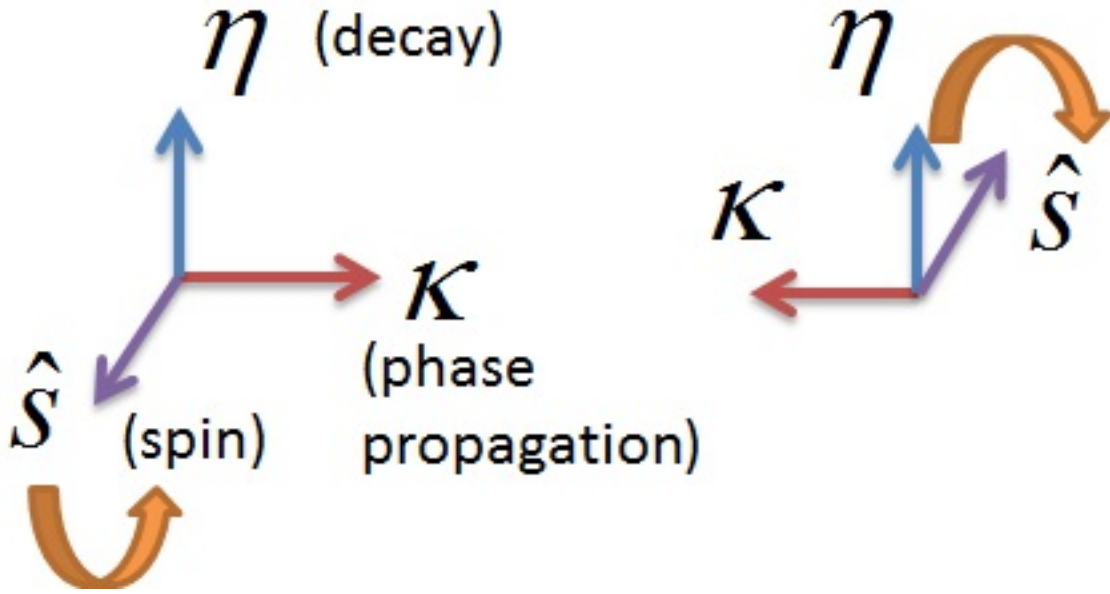
Figure 2.1. Our result shows a fundamental right handed triplet formed by momentum, decay and spin for evanescent waves. Note the locked triplets for waves propagating in two opposite directions. As we can see, the direction of the spin $\hat{s}$ flips for the two cases. It is important to note that in general there are four degenerate solutions but two of these correspond to growing evanescent waves which are forbidden due to causality. This explains why the left handed triplet is not allowed and the phenomenon of spin-momentum locking is universal to evanescent waves.

where we can clearly see that the $\hat{p}$-polarization is just a linear combination of $\vec{\kappa}$ and $\vec{\eta}$ unit vectors with an in-built phase difference between the orthogonal components. This immediately implies that there will be an inherent elliptical polarization imparted to the field.

2.2.2 Stokes parameters

We now extend the concept of Stokes parameters [41] beyond propagating waves to fully characterize this interesting $\hat{p}$-polarization state of an evanescent wave. Complex $\hat{p}$ is expressed as a linear combination of two basis vectors which motivates us to consider spin-$\frac{1}{2}$

operators. The Stokes parameters of an evanescent wave can be written as the expectation values of the Pauli matrices and carries non-trivial information;

$$S_0 = \langle \hat{p}|1|\hat{p}\rangle = 1 \tag{2.5a}$$

$$S_1 = \langle \hat{p}|\sigma_z|\hat{p}\rangle = \frac{k_0{}^2}{|\vec{k}|^2} \tag{2.5b}$$

$$S_2 = \langle \hat{p}|\sigma_x|\hat{p}\rangle = 0 \tag{2.5c}$$

$$S_3{}^\pm = \langle \hat{p}|\sigma_y|\hat{p}\rangle = \pm 2\frac{\kappa\eta}{|\vec{k}|^2}. \tag{2.5d}$$

S_1 and S_3 quantify the amount of spin, i.e. the degree of linear and circular polarized character of an electromagnetic wave. Here, $\pm$ denotes the two directions of the phase propagation possible for the evanescent wave. We see that the polarization state of the field basis vector $\hat{p}$ is dependent only on the complex components of the wavevector while the actual electric and magnetic field elements are irrelevant in this instance. This means that there will be a certain degree of elliptical polarization *intrinsic* to the electromagnetic field which is determined entirely by the real and imaginary components of the momentum ($\vec{k}$). In this sense, there will be inherent "spin" associated with the evanescent wave since the unique basis vector $\hat{p}$ itself imparts handedness to the wave.

Note, the $\hat{s}$ vector can now be interpreted as the "spin direction" since it signifies the handedness of the electric field with $\hat{p}$-polarization. This spin vector ($\hat{s}$) is orthogonal to both $\vec{\kappa}$ and $\vec{\eta}$ which constitute the basis of $\hat{p}$. Furthermore, the transformation $\vec{\kappa} \to -\vec{\kappa}$, for fixed decay direction ($\vec{\eta}$), changes the handedness of $\hat{p}$ (sign(S_3)). This also flips the direction of $\hat{s}$ which is consistent with an opposite direction of spin. This shows that the spin is fundamentally locked to the direction of propagation (momentum). The diagram in Fig. (2.1) shows the construction of a fundamentally locked triplet for evanescent waves formed by the phase propagation vector ($\vec{\kappa}$), decay vector ($\vec{\eta}$) and spin ($\hat{s}$).
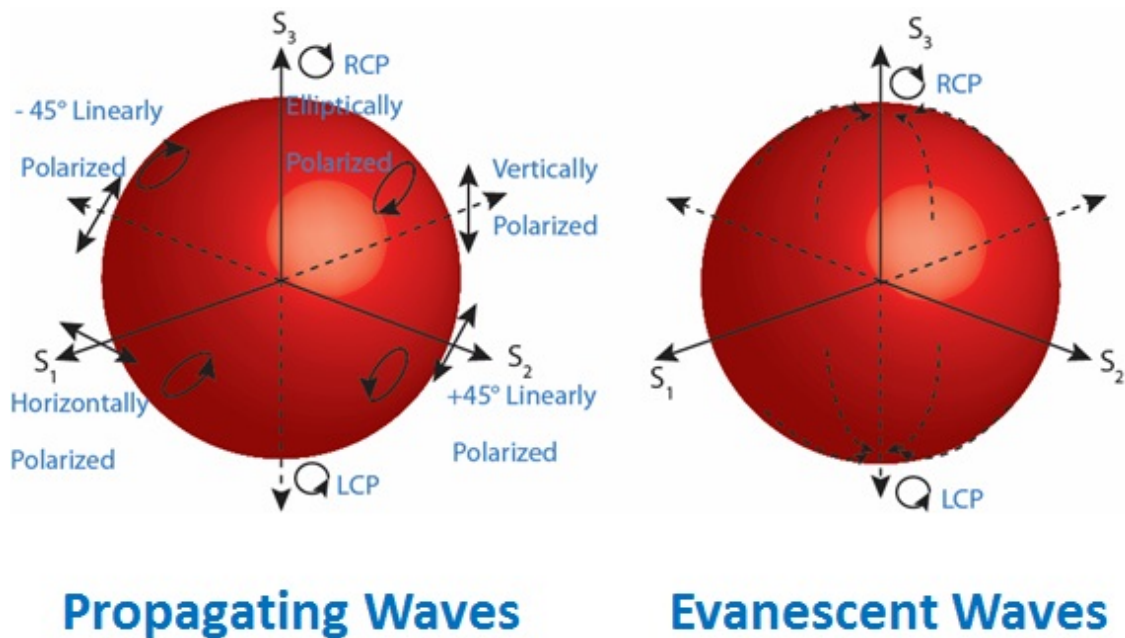
Figure 2.2. Poincaré spheres for propagating waves and evanescent waves. Propagating waves can have any arbitrary polarization state for a given phase velocity. However, all fast decaying evanescent waves are circularly polarized and lie on the south or north pole of the Poincaré sphere ($S_3 = \pm 1$). Furthermore, the choice between these two points is locked to the direction of momentum ($\pm \vec{\kappa}$).

2.2.3 Inherent polarization

In this section, we prove that every fast decaying evanescent wave is inherently circularly polarized and its handedness is tied to the direction of phase propagation (momentum). We consider the case of an evanescent wave with very high momentum such that $\kappa \gg k_0$. The dispersion relation then implies $\kappa \approx \eta$ and the wave decays on a length scale much smaller than the wavelength. Simplifying the expression for the $\hat{p}$-polarized basis vector,

$$\hat{p} \rightarrow \frac{\mathrm{i}}{\sqrt{2}} \left[\left(\frac{\vec{\kappa}}{\kappa} \right) + \mathrm{i} \left(\frac{\vec{\eta}}{\eta} \right) \right] \tag{2.6a}$$

$$S_1 \rightarrow 0 \tag{2.6b}$$

$$S_3{}^{\pm} \rightarrow \pm 1 \tag{2.6c}$$

which we can clearly see is a state of circular polarization.

The above result implies that every fast decaying evanescent wave lies on the north or south pole of the Poincaré sphere while propagating waves can lie anywhere on the Poincaré sphere. Furthermore, the choice of the south and north pole ($S_3 = \pm 1$) is dictated by the direction of the phase velocity ($\pm \vec{\kappa}$). Thus spin-momentum locking is a fundamental property of evanescent waves. To visually illustrate these polarization states, we compare the Poincaré spheres of propagating and evanescent waves in Fig. (2.2).

2.3 Spin-momentum locking from causality

The "spin-locking" characteristic of evanescent waves comes from the fact that $\vec{\kappa}$ and $\vec{\eta}$ are inherently orthogonal as dictated by the complex dispersion (Eq. (2.2)). Simultaneously, the unit field vector $\hat{p}$ which is related to the wavevector possesses a $\pi/2$ phase difference between its orthogonal components. This phase is not an artifact of some particular combination of polarization vectors but is embedded into the vector field itself to guarantee that the transverse condition ($\vec{k} \cdot \vec{\mathcal{E}} = 0$) is satisfied.

Ultimately, evanescent waves require some sort of boundary condition to exist in a region of space, which usually involves a symmetry breaking or a change in material parameters. For an arbitrary plane wave ($\propto \exp(\mathrm{i}\vec{k} \cdot \vec{r}) = \exp(\mathrm{i}\vec{\kappa} \cdot \vec{r}) \exp(-\vec{\eta} \cdot \vec{r})$), this boundary condition,

in general, opens up 2 possible propagation directions $\pm\vec{\kappa}$, and 2 decay/growth directions $\pm\vec{\eta}$ which allows up to 4 degenerate solutions. However, we know immediately that only one of the $\vec{\eta}$ solutions can exist because the wave must be finite in the region of space that includes infinity, i.e. it must decay away from the boundary towards infinity. Exponential growth in a passive medium is non-physical because it would require a non-causal solution to the boundary condition. For planar interfaces, the branch cut for the complex wavevector ($\vec{k}$) is chosen based on the direction of the decay of the evanescent wave, which occurs along the normal to the interface. Note the branch cut corresponding to growing evanescent waves is discarded for passive media.

This causality requirement leads to the fact that the handedness or "spin" of the evanescent waves is now determined and locked to the propagation direction (the momentum). This is because while the decay vector ($\vec{\eta}$) cannot change, the wave is free to propagate in both directions ($\pm\vec{\kappa}$), flipping the handedness of $\hat{p}$. In other words, the set of allowed evanescent waves only consists of 2 possibilities due to this condition. One with positive momentum $+\vec{\kappa}$ and positive spin direction $+\hat{s}$ and the other with negative momentum $-\vec{\kappa}$ and negative spin direction $-\hat{s}$. Hence, causality and transversality (or complex dispersion) can be considered to be the fundamental origin of the universal spin-momentum locking of evanescent waves (see Fig. (2.1)).

2.4 Universal behavior

In this section, we show that evanescent waves possess this spin-momentum locking in various scenarios. It becomes imperative to revisit fundamental concepts of total internal reflection and waveguide modes to prove that evanescent waves indeed possess a property which has been overlooked. To analyze these textbook phenomena, we introduce the concept of a local handedness for inhomogeneous fields. We specifically plot the spatial distribution of the Stokes parameter (S_3) which depends on the local electric fields and sheds light on the local handedness (polarization state) of the fields. We note that our approach is different but equivalent to the historic concept of the light beam tensor introduced by Fedorov [42] and the recently developed concept of the spin density [40], [43], [44].

2.4.1 Circular total internal reflection (golden ratio condition)

The simplest case where such a phenomenon can occur is when evanescent waves are generated at total internal reflection (TIR). We consider a wave $\hat{p}$-polarized in the $\hat{x}$-$\hat{z}$ plane (TM) travelling from glass with index $n_1 = \sqrt{\varepsilon_1}$ into medium 2 with index $n_2 = \sqrt{\varepsilon_2}$ where we require $\varepsilon_1 > \varepsilon_2$ for evanescent waves to be supported. The electric fields generated during TIR are well known and are depicted by white arrows in Fig. (2.3). However, when overlaid against the local handedness of the field an intriguing phenomenon comes to light – the direction of propagation of the wave alters the relative handedness of the evanescent field. The false colors in the same figures depict the spatial distribution of the normalized Stokes parameter (S_3) and quantifies the polarization state of the field at each point. In region 2, it is evident that the evanescent wave possesses similar handedness at every point (orange region). Furthermore, comparing the counter-propagating cases between Fig. (2.3) we clearly see that the polarization state of the evanescent wave is reversed and the Stokes parameter changes sign. The insets of Fig. (2.3) elucidate this spin-momentum locking phenomenon for TIR.

We now show that the propagating waves inherit handedness from the evanescent waves due to boundary conditions at the interface. The phase between the perpendicular and parallel components of an arbitrary ($\hat{p}$-polarized) electric field in region 1, interfaced with an evanescent wave in region 2 must satisfy

$$\left[\frac{E_\perp}{E_\parallel}\right]_1 = \pm\mathrm{i}\frac{\varepsilon_2}{\varepsilon_1}\left[\frac{\kappa}{\eta}\right]_2 \qquad @\text{interface} \qquad (2.7)$$

where the $\pm$ indicates oppositely travelling evanescent waves and the subscripts designate the field components in their respective material regions. It should be stressed that this only applies *locally* at the interface. However, this could have interesting consequences for near-field optics since it implies that there is a preferential handedness depending on the direction of propagation when we couple to evanescent waves. We make the important observation that perfect circular polarization is enforced (locally) in region 1 when

$$\frac{\varepsilon_1}{\varepsilon_2} = \left[\frac{\kappa}{\eta}\right]_2. \qquad (2.8)$$

We can now solve for the momentum and decay of the evanescent wave which achieves this circular total internal reflection. They are

$$\kappa_2 = \varepsilon_1 \sqrt{\frac{\varepsilon_2}{\varepsilon_1{}^2 - \varepsilon_2{}^2}} k_0 \tag{2.9}$$

and

$$\eta_2 = \varepsilon_2 \sqrt{\frac{\varepsilon_2}{\varepsilon_1{}^2 - \varepsilon_2{}^2}} k_0. \tag{2.10}$$

In the case of TIR, this local circular polarization is generated in region 1 because there is a phase shift imparted to the reflected wave and the interference with the incident wave causes the combined field to be locally handed. Lastly, we need to determine the angle of incidence of the propagating wave that is required to accomplish this circular TIR condition. Using Snell's law, it can be shown that the CTIR angle of incidence $\theta_1 = \theta_{\mathrm{CTIR}}$ is,

$$\sin(\theta_{\mathrm{CTIR}}) = 1/\sqrt{\varepsilon_1/\varepsilon_2 - \varepsilon_2/\varepsilon_1}. \tag{2.11}$$

We note that in this instance, θ_{CTIR} must necessarily be real which requires that the denominator be greater than 1. Therefore, there is an interesting limiting condition for local CTIR to exist which is when $\theta_{\mathrm{CTIR}} \to \pi/2$ (i.e. when the propagating wave in region 1 is parallel to the interface). This is equivalent to the limit when

$$\left[\frac{\varepsilon_1}{\varepsilon_2}\right]_{\mathrm{GR}} = \frac{1}{2}(1 + \sqrt{5}) \approx 1.618 \tag{2.12}$$

which is the *minimum* allowable ratio of the permittivities for CTIR to occur, and curiously, it can also be identified as the golden ratio [45]. We term this the "golden ratio condition" for local circularly polarized total internal reflection.

This induced CTIR in region 1 is visible clearly in Fig. (2.3). Note our choice of refractive indices satisfies $\varepsilon_1/\varepsilon_2 = 4 > [\varepsilon_1/\varepsilon_2]_{\mathrm{GR}}$. The angle given by our analytical expression in Eq. (2.11) is $\theta_{\mathrm{CTIR}} = 31.09º$ and we have plotted the fields for this incident angle. Close to the interface in region 1, the Stokes parameter takes the maximal values of $S_3 = \pm 1$ (red and blue regions). Thus the fields are perfectly circular polarized close to the interface
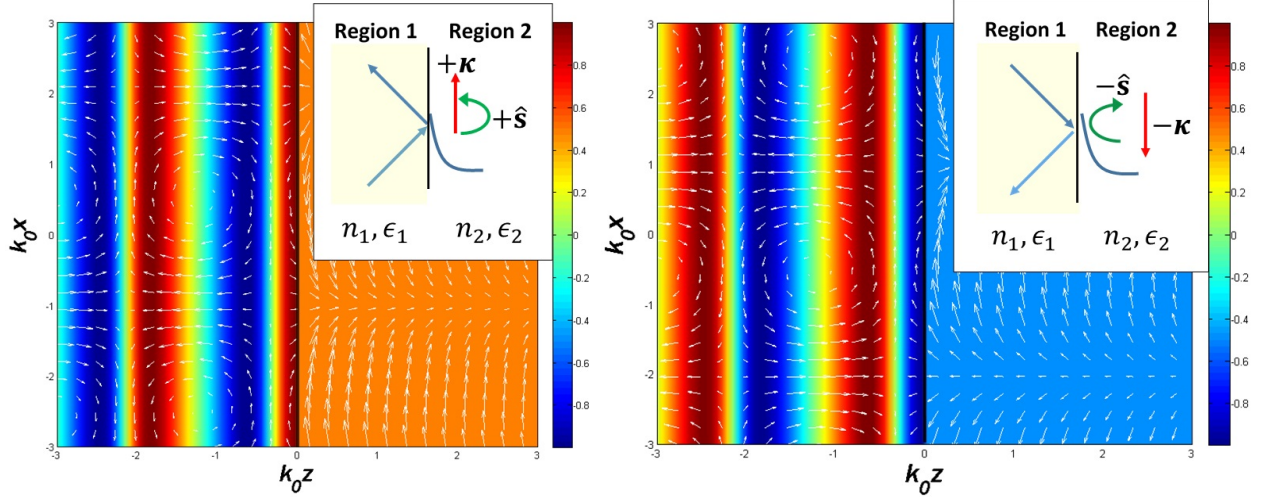
Figure 2.3. Left: CTIR at interface between glass with $n_1 = 2$ and air with $n_2 = 1$ at the θ_{CTIR} condition. For waves travelling in the $+x$ direction, the evanescent wave in region 2 has right handed spin-momentum locking (inset). Note the wave in medium 1 has perfect circular polarization characteristics close to the interface at this angle of incidence. The overlaid false color plot is the spatial distribution of the normalized Stokes parameter (S_3) which characterizes the handedness of the wave (degree of circular polarization) from -1 to 1 at each point. Right: CTIR at interface between glass with $n_1 = 2$ and air with $n_2 = 1$ at the θ_{CTIR} condition. For waves travelling in the $-x$ direction, the evanescent wave in region 2 has left handed spin-momentum locking (inset). The plot illustrates that the evanescent wave spin has the opposite sign as compared to the previous case because the momentum and spin are locked.

specifically for this angle of incidence. Although phase propagation normal to the interface ($\hat{z}$) will alter the degree of this polarization, the *relative* handedness between forward and backward propagating waves is maintained. This can be seen from the blue and red contours in region 1, where rotation of the electric field vectors is reversed at every point in space – which is in agreement of differing signs of S_3.

2.4.2 Waveguides

Interesting spin-locking phenomena also occur when we consider confined light in waveguides and optical fibres. The confinement of light necessarily requires evanescent waves to be present which implies that there will be handedness imparted on the waveguide and fibre

modes through the boundary conditions. For planar waveguides, there are even and odd solutions and the $\hat{p}$-polarized electric field components (TM modes) inside the waveguide are proportional to

$$\vec{\mathcal{E}} \propto \left[k_z \left\{ \begin{array}{c} \sin(k_z z) \\ -\cos(k_z z) \end{array} \right\} \hat{x} + \mathrm{i} k_x \left\{ \begin{array}{c} \cos(k_z z) \\ \sin(k_z z) \end{array} \right\} \hat{z} \right] \mathrm{e}^{\mathrm{i} k_x x} \tag{2.13}$$

where the array inside the braces indicates the two separate solutions. Note that the electric field components along the x- and z-axis have a phase difference between them dictated solely by the boundary conditions that maintain the transversality of the field. If we consider a wave propagating in the opposite direction, i.e. change $k_x \rightarrow -k_x$ the wave changes handedness. We see that there is spin-momentum locking in waveguides since k_x now constitutes the momentum and also controls the relative phase between the orthogonal field components. The electric field vector plots in Fig. (2.4) are overlaid on the spatial distribution of the S_3 Stokes parameters (false color plot) to illustrate the different spin (handedness) between two oppositely propagating waveguide modes. We note that a similar explanation can be extended to the case of metamaterials [33]. This is discussed briefly in the supplementary information and a detailed derivation will be presented elsewhere.

2.4.3 Optical fibres

We now show that spin-momentum locking in optical fibres is the fundamental origin of recent experimental observations where scattered light and spontaneous emission was directed preferentially along the fiber [31], [36]. The HE$_{11}$ fundamental mode operation is the most important case so we quantify its degree of polarization. To characterize our fibre mode we consider weakly guided waves, $\Delta = (n_1{}^2 - n_2{}^2)/(2n_1{}^2) \approx (n_1 - n_2)/n_1 \ll 1$ with a numerical aperture, $\mathrm{NA} = \sqrt{n_1{}^2 - n_2{}^2} \approx n_1\sqrt{2\Delta}$. For single mode HE$_{11}$ operation, we require that $\mathrm{V} = 2\pi(a/\lambda_0)\mathrm{NA} = \sigma_1\sqrt{2\Delta} < 2.405$, where a is the radius of the fibre and $\sigma_1 = k_1 a = 2n_1\pi(a/\lambda_0)$ is the scaling parameter inside the core.

The HE$_{11}$ is doubly degenerate in that we have two counter-rotating angular momentum modes in the plane perpendicular to the fiber-optic axis. We denote the electric and magnetic fields as $\vec{\mathcal{E}}_m$ and $\vec{\mathcal{H}}_m$ respectively where the subscripts denote $m = +1$ or $m = -1$. In the circular basis we define unit vectors $\hat{e}_m = (\hat{r} + im\hat{\phi})/\sqrt{2}$ and clearly $\hat{e}_\pm^* = \hat{e}_\mp$. With a
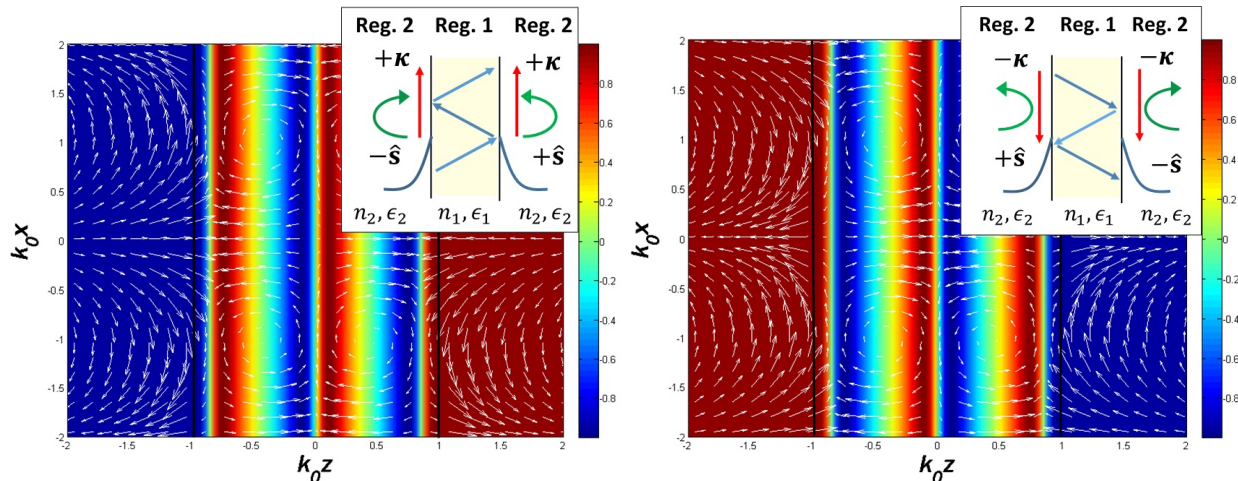
Figure 2.4. Left: Waveguide mode at interface between glass with $n_1 = 4$ and air with $n_2 = 1$. The width of the waveguide is $2k_0d = 2$. For waveguide modes travelling in the $+x$ direction, the evanescent waves in region 2 lock the handedness (locally) to $+\hat{s}$ at $k_0z = 1$ and $-\hat{s}$ at $k_0z = -1$. The false color plot shows the spatial distribution of the normalized Stokes parameter (S_3) from -1 to 1 for the waveguide and illustrates the intrinsic handedness of the evanescent waves. Furthermore, on comparison with the counter-propagating waveguide mode, we see that the handedness is reversed. Right: Waveguide mode at interface between glass with $n_1 = 4$ and air with $n_2 = 1$. The width of the waveguide is $2k_0d = 2$. For waveguide modes travelling in the $-x$ direction, the evanescent waves in region 2 lock the handedness (locally) to $-\hat{s}$ at $k_0z = 1$ and $+\hat{s}$ at $k_0z = -1$.

propagation factor of $\exp\left[i(\beta z/a - \omega t)\right]$ omitted, the electric and magnetic fields can then be written as,

$$\vec{\mathcal{E}}_m = E_0[\sqrt{2}\beta J_0(\mathrm{X}r/a)\hat{e}_m + i\mathrm{X}J_1(\mathrm{X}r/a)\hat{z}]e^{im\phi} \tag{2.14a}$$

$$\vec{\mathcal{H}}_m = -imH_0[\sqrt{2}(\sigma_1)^2 J_0(\mathrm{X}r/a)\hat{e}_m + i\beta\mathrm{X}J_1(\mathrm{X}r/a)\hat{z}]e^{im\phi} \tag{2.14b}$$

for fields inside the fibre when $r < a$, where $H_0 = E_0/(\omega\mu_0 a)$ and

$$\vec{\mathcal{E}}_m = \mathcal{N}E_0[\sqrt{2}\beta K_0(\mathrm{Y}r/a)\hat{e}_m + i\mathrm{Y}K_1(\mathrm{Y}r/a)\hat{z}]e^{im\phi} \tag{2.15a}$$

$$\vec{\mathcal{H}}_m = -im\mathcal{N}H_0[\sqrt{2}(\sigma_2)^2 K_0(\mathrm{Y}r/a)\hat{e}_m + i\beta\mathrm{Y}K_1(\mathrm{Y}r/a)\hat{z}]e^{im\phi} \tag{2.15b}$$

outside the fibre when $r > a$ and $\mathcal{N} = (\mathrm{X}/\mathrm{Y})J_1(\mathrm{X})/K_1(\mathrm{Y})$. J_n and K_n are the Bessel and Modified Bessel functions of order n respectively. The normalized propagation constants are defined as, $|\beta| = \sqrt{(\sigma_1)^2 - \mathrm{X}^2} = \sqrt{(\sigma_2)^2 + \mathrm{Y}^2}$ and $\mathrm{V}^2 = \mathrm{X}^2 + \mathrm{Y}^2$. The components of the $\vec{\mathcal{E}}_m$ and $\vec{\mathcal{H}}_m$ fields have identical forms (up to a proportionality constant) so we concentrate on the electric type.

The above equations are commonplace in textbooks on fiber optics. However, the differentiation between the angular momentum and spin components of the HE_{11} mode has not been done before. This can be done unambiguously by extending our concept of local handedness of a wave to three dimensions. We consider the Stokes parameter (S_3) which characterizes circular polarization. However, for the optical fiber, it has to be evaluated for three dimensional fields by considering pairs of orthogonal directions. This leads to Stokes parameters S_3^z and S_3^ϕ which can be interpreted as local circular polarization of the field with handedness along the $\hat{z}$ direction or $\hat{\phi}$ direction. We concentrate on the field components inside the core when $r < a$, but similar expressions hold for $r > a$ where the Bessel functions are substituted with the Modified Bessel functions.

For the two $m = \pm 1$ angular momentum modes, the S_3^z Stokes parameter evaluated with electric field components orthogonal to the propagation $\hat{z}$ direction is

$$(I_{AM})_m = 2m|E_0|^2\beta^2 J_0^2(\mathrm{X}r/a) \tag{2.16}$$

which we denote as the angular momentum intensity. The handedness of this angular momentum is either positive or negative for the $m = \pm 1$ modes. This is valid even if we change the sign of the propagation constant, i.e. if the HE_{11} mode moves along $-\hat{z}$. Thus, both forward and backward propagating waves can have either positive or negative angular momentum as is expected.

However, a fundamental and intriguing asymmetry is noticed for the S_3^ϕ Stokes parameter evaluated using electric field components orthogonal to $\hat{\phi}$. It is given by the expression

$$(I_S)_m = \mathrm{sign}(\beta)2|E_0|^2|\beta|\mathrm{X}J_0(\mathrm{X}r/a)J_1(\mathrm{X}r/a) \tag{2.17}$$

which we denote as the spin polarization intensity. The direction of this "spin" is in the unique $\hat{\phi}$ direction and is seen to be independent of the sign of the angular momentum. Furthermore, it is also locked to the momentum β since $\mathrm{sign}(\beta) = \pm 1$ leading to fundamentally different behavior of forward and backward propagating HE_{11} modes along the fiber. For forward momentum $\mathrm{sign}(\beta) = +1$ we have $+\hat{\phi}$ transverse spin and for $\mathrm{sign}(\beta) = -1$ we have $-\hat{\phi}$ regardless of which angular momentum mode we are considering. Therefore, instead of four degenerate solutions, only two are allowed.

We emphasize once again that the spin-momentum locking arises from the fact that growing solutions for evanescent waves outside the optical fiber are discarded. These growing solutions have the opposite spin direction for a given propagation direction. (Sec. 2.3). This shows we have spin-momentum locking even in standard optical fibres which is directly linked to the evanescent fields necessary for confinement. Strictly speaking, we enforced spin-momentum locking from the outset by only permitting K_n type Modified Bessel functions and discarding the I_n type – since they exponentially grow as r increases. This causality requirement with regards to fiber modes is the precise reason that we have handedness imparted to the optical fiber.

The total electric field intensity is a sum of linear, angular momentum and spin intensities which arises from the properties of Stokes parameters $(S_0{}^2 = S_1{}^2 + S_2{}^2 + S_3{}^2)$. We thus have $I_E{}^2 = I_{AM}{}^2 + I_S{}^2 + I_L{}^2$ where $I_E = |\vec{\mathcal{E}}|^2 = 2|E_0|^2\beta^2 J_0{}^2 + |E_0|^2\mathrm{X}^2 J_1{}^2$ is the total intensity of the electric field. Here, the linear polarization intensity is defined as $I_L = |E_0|^2\mathrm{X}^2 J_1{}^2$, arising

due to the electric field component in the $\hat{z}$ direction. We can now analyze the fractional field intensity residing in the angular momentum, spin or linear polarization components. The normalized polarization intensities for a weakly-guiding optical fibre are shown in the plot of Fig. (2.6). We also include a field vector plot in Fig. (2.5) to help visualize the transverse spin component in the HE_{11} mode.

2.4.4 Directional quantum emitter coupling

All that being said, this intriguing symmetry breaking could be exploited for applications in the field of quantum photonics. One recent experiment has utilized cold atoms near optical fibers to demonstrate directional waveguiding of spin-polarized spontaneous emission [36]. We show how this phenomenon is related to spin-momentum locking of the HE_{11} mode. Note, our results can be expanded to an isotropic scatterer with circularly polarized incident light or a chiral scatterer with linearly polarized incident light.

Let us consider a left and right handed circularly polarized source that has both electric and magnetic moments. Following the semiclassical theory of spontaneous emission [46]–[48], we approximate this chiral source to be

$$
\begin{bmatrix} \vec{J}_{\mathrm{E}}(\vec{r}) \\ \vec{J}_{\mathrm{H}}(\vec{r}) \end{bmatrix}_{\pm} = -\mathrm{i}\omega\delta^3(\vec{r}-\vec{r}_0) \begin{bmatrix} \vec{p} \\ \vec{m} \end{bmatrix} = -\mathrm{i}\omega\delta^3(\vec{r}-\vec{r}_0) \begin{bmatrix} p_0 \\ -\mathrm{i}m_0 \end{bmatrix} \hat{e}_{\pm}\mathrm{e}^{\pm\mathrm{i}\phi} \tag{2.18}
$$

where the $\pm$ indicates left or right handed circular polarization in the cylindrical coordinate basis of the optical fiber. The coupling strength (energy of interaction) into one of the HE_{11} modes is then proportional to $A_m \propto \mathrm{i}\omega[\vec{p}^* \cdot \vec{\mathcal{E}}_m(\vec{r}_0) + \vec{m}^* \cdot \vec{\mathcal{H}}_m(\vec{r}_0)]$. Plugging in for $\vec{r}_0 = \vec{0}$ it can be shown that the magnitude of the coupling strength ($|A_m|^2$) for each $m = \pm 1$ mode is equal to

$$
|A_m|^2 = C_1 \left| \mathrm{sign}(\beta)|\beta|\omega p_0 + m\frac{(\sigma_1)^2 m_0}{\mu_0 a} \right|^2 \tag{2.19}
$$

where C_1 is some positive proportionality constant. The angular momentum quantum number $m = \pm 1$ should not be confused with the magnitude of the magnetic dipole $|\vec{m}| = m_0$. Also note, that the time averaged power along the fiber axis for each mode is proportional to $P_m \propto |A_m|^2$.
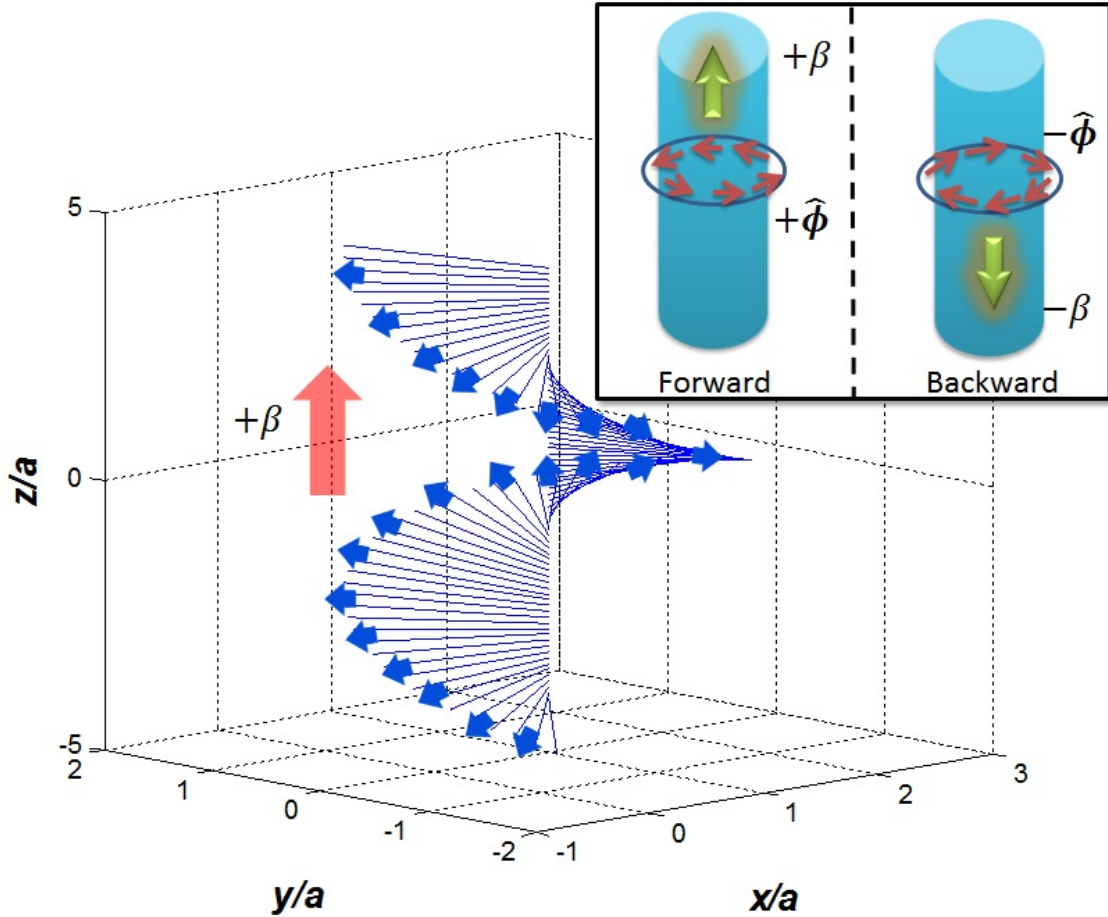
Figure 2.5. The evolution of the polarization vector as it propagates in an optical fibre with V = 1.5 and $\Delta = 0.1$. We display the electric field at a single point at $r = a$ in the $m = +1$ HE_{11} mode to demonstrate the transverse spin near the core-cladding region. As we can see, the electric field rotates in the z-plane as well as in the x-y plane, hence there is a spin component directed around $\hat{\phi}$ (inset). Out of four possible degenerate solutions, only two are allowed because of the decaying condition on evanescent waves outside the core. Consequently, the HE_{11} mode of the optical fiber has spin-momentum locking.
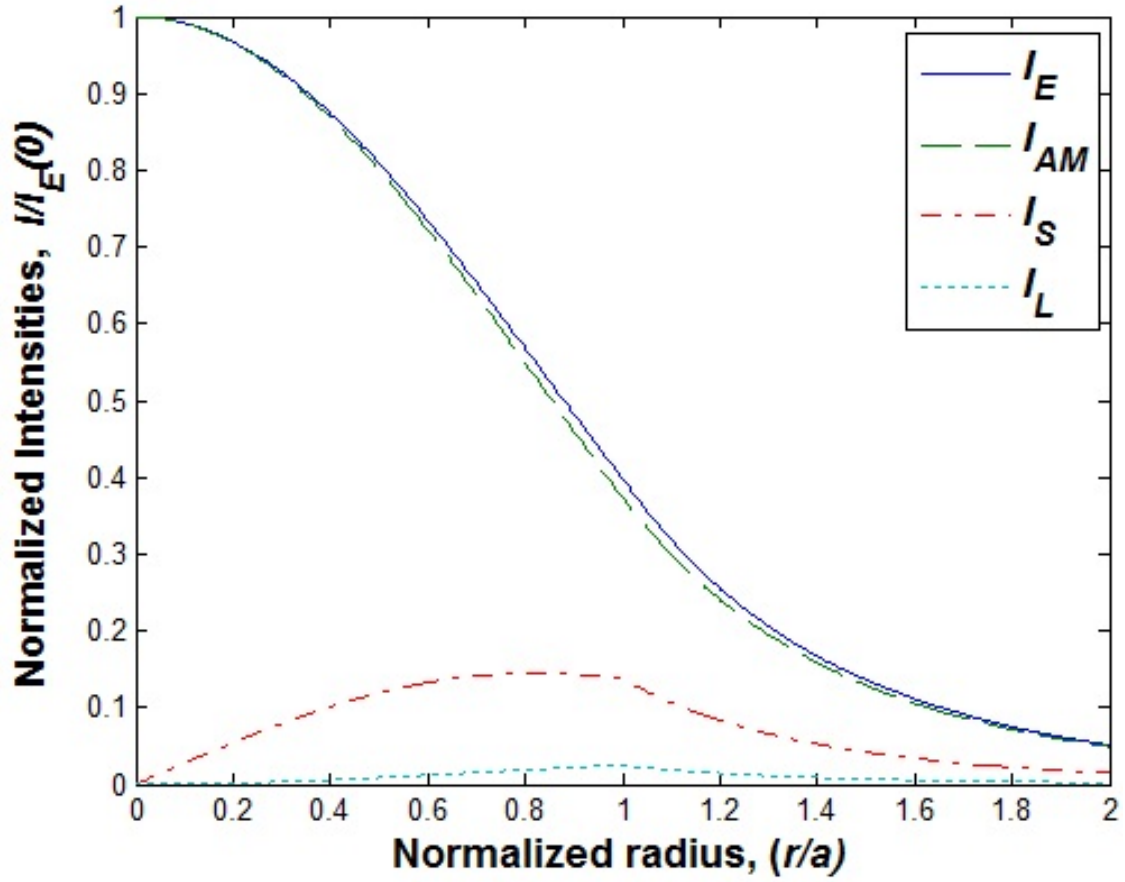
Figure 2.6. Normalized HE_{11} polarization intensities ($I/I_E(0)$) for an optical fibre of V = 1.5 and $\Delta = 0.1$. We see that the majority of field is concentrated in the I_{AM} angular momentum component but there is a significant component of spin intensity (I_S) in the $\hat{\phi}$ direction near the core-cladding interface at $r = a$.

We notice the striking fact that this coupling factor of the chiral emitter into the HE$_{11}$ mode is direction dependent. Hence, we will have asymmetrical power emitted in differing directions along the fiber. The + polarization chiral emitter couples only into the $m = +1$ mode and emits most strongly in the forward propagating sign$(\beta) = +1$ direction while being weaker for backward propagation sign$(\beta) = -1$. Conversely, the − polarization chiral emitter couples only into the $m = -1$ mode and emits more strongly in the sign$(\beta) = -1$ direction rather than sign$(\beta) = +1$. This means we can control the directional propagation of waves *and* the specific angular momentum mode ($m = \pm 1$) we couple into by choosing either left or right handed chiral emitters. This effect is maximal when the electric and magnetic dipole moments are tuned to have $|\beta|\omega p_0 = \frac{(\sigma_1)^2}{\mu_0 a} m_0$. For weakly guided waves, $|\beta| \approx \sigma_1$, and it can be shown that maximal coupling will occur when $m_0 \approx Z_1 p_0$ where $Z_1 = Z_0/n_1 = \sqrt{\mu_0/\varepsilon_1 \varepsilon_0}$ is the wave impedance inside the fibre.

We now propose an approach to couple strictly to the transverse spin components of the electric field with a transversely polarized electric source. This can have the advantage of not requiring magnetic dipoles or chirality. We achieve this by tuning the phase difference between two orthogonally oriented point dipole emitters $\vec{p} = p_x \hat{x} + i p_z \hat{z}$. This emitter is placed at the location $\vec{r}_0 = a\hat{x}$ where the spin intensity is maximum (see Sec. 2.4.3). The transverse spin is unchanged between angular momentum modes so they will both contribute to the propagation of the wave. The transverse coupling strength for both $m = \pm 1$ is equal to

$$|A_m|^2 = C_2 \omega^2 \left| \text{sign}(\beta)|\beta|J_0(\text{X})p_x + \text{X}J_1(\text{X})p_z \right|^2 \tag{2.20}$$

where C_2 is another positive proportionality constant. We see again that there is dominance of the wave to be in the sign$(\beta) = +1$ direction compared to the sign$(\beta) = -1$. The asymmetry in coupling between the two directions is maximal when the dipole strengths are adjusted to have $|\beta|J_0(\text{X})p_x = \text{X}J_1(\text{X})p_z$. We illustrate these two unique quantum emitter couplings in Fig. (2.7) and their orientation in the optical fiber.
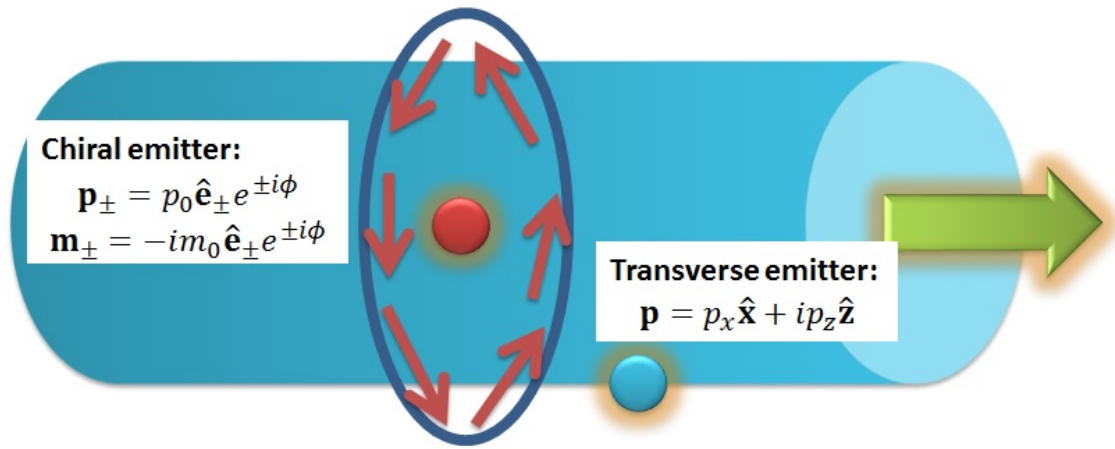
Figure 2.7. Chiral emitter placed at $\vec{r}_0 = \vec{0}$ and transverse emitter placed at $\vec{r}_0 = a\hat{x}$ inside the optical fibre. The intrinsic chirality of the HE_{11} mode opens possibilities for spin-controlled quantum photonics. We emphasize that this intrinsic chirality is universal and arises from the evanescent waves outside the core.

2.4.5 Surface states

The last example is that of surface electromagnetic waves such as Zenneck waves [49], Dyakonov waves [50] and surface plasmon-polaritons (SPPs) which exist at the interface of two materials. The necessarily evanescent nature of the electromagnetic field will introduce very clear spin-momentum locking in all these waves. We emphasize that such polarization dependent transport has been observed for the particular case of surface plasmon polaritons [32], [37], [38], [40] but the universality and fundamental origin of the phenomenon has never been pointed out.

Note that surface waves are evanescent in both regions (see Fig. (2.8)) and hence will have *global* spin-locking where the handedness of the wave will be invariant in each of the half-spaces. We explain this by taking the example of surface plasmon polaritons which exist at the interface of a metal and dielectric. Region 1 ($-z$) is metallic having a relative permittivity $\varepsilon_1 < 0$ and the dielectric in region 2 ($+z$) has a relative permittivity $\varepsilon_2 > 1$. This results in the familiar dispersion relation $\kappa = k_0\sqrt{\varepsilon_1\varepsilon_2/(\varepsilon_1 + \varepsilon_2)}$.

We can now fully quantify the evanescent spin in terms of the permittivities. Utilizing the expression for the circular Stokes parameters (S_3) derived in Eq. (2.5) this leads to

$$- (S_3)_1 = (S_3)_2 = 2\frac{\sqrt{|\varepsilon_1|\varepsilon_2}}{|\varepsilon_1| + \varepsilon_2} \tag{2.21}$$

where $(S_3)_1$ and $(S_3)_2$ are the $\hat{p}$-polarization Stokes parameters in region 1 and 2 respectively and we are assuming the permittivities are purely real in this instance. As we can see, as $|\varepsilon_1| \to \varepsilon_2$, the momentum $\kappa \to \infty$ and the spin approaches perfect circular polarization $-(S_3)_1 = (S_3)_2 \to 1$, as expected. Also to reiterate, the spin-momentum locking of evanescent waves means these spins are flipped when the wave is propagating in the opposite direction. To help visualize these phenomena, the electric field vector plot for an SPP is displayed in Fig. (2.8) along with the "full" SPP dispersion relation that includes the handedness of the spin (in the dielectric region). Our approach provides an intuitive explanation of this phenomenon observed in recent experiments where chiral emitters or near-field
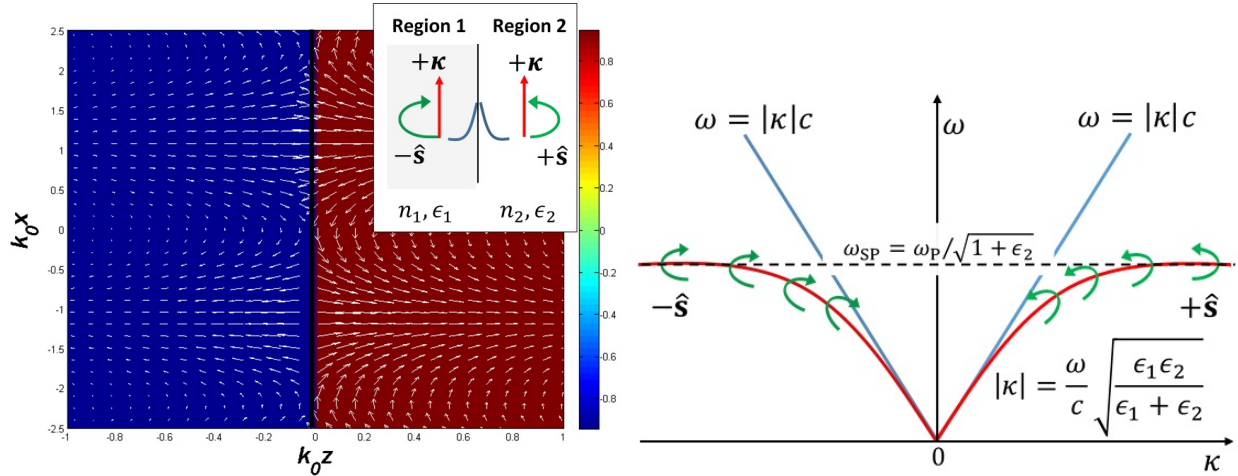
Figure 2.8. Left: All electromagnetic surface waves will show spin-momentum locking. We depict here an SPP excitation between metal with $\varepsilon_1 = -2$ and air with $\varepsilon_2 = 1$ propagating in the $+x$ direction. The vector plot overlaid on the spatial distribution of the Stokes parameter (S_3) illustrates the inherent handedness of the two evanescent waves and how they couple with counter rotating spins. Right: SPP dispersion relation that also includes the handedness of the evanescent spin (in the dielectric region). As the momentum κ increases, the SPP spin approaches perfect circular polarization (SPP resonance).

interference from electric and magnetic dipoles lead to unidirectional SPP propagation [32], [37], [38], [48].

2.5 Conclusion

In conclusion, we have shown that evanescent waves possess inherent local handedness (spin) which is tied to their phase velocity (momentum). We have proven this spin-momentum locking is universal behavior since it arises due to causality and the complex dispersion relation of evanescent waves. It is interesting to note that recent work on topological photonics [18], [51]–[53] has shed light on the existence of surface states immune to disorder and our work will surely lead to a better understanding of those surface states as well. The QSH surface state has electrons with spins locked to their direction of propagation but only occurs on the surface (interface) of materials with spin-orbit coupling (eg: HgTe quantum wells). The electromagnetic surface state curiously always possesses this prop-

erty irrespective of the nature of the material. This warrants a deeper investigation and simultaneously opens up possibilities for practical applications.

See Supplemental Material for supporting content.

3. QUANTUM GYROELECTRIC EFFECT: PHOTON SPIN-1 QUANTIZATION IN CONTINUUM TOPOLOGICAL BOSONIC PHASES

Topological phases of matter arise in distinct fermionic and bosonic flavors. The fundamental differences between them are encapsulated in their rotational symmetries – the spin. Although spin quantization is routinely encountered in fermionic topological edge states, analogous quantization for bosons has proven elusive. To this end, we develop the complete electromagnetic continuum theory characterizing 2+1D topological bosons, taking into account their intrinsic spin and orbital angular momentum degrees of freedom. We demonstrate that spatiotemporal dispersion (momentum and frequency dependence of linear response) captures the matter-mediated interactions between bosons and is a necessary ingredient for topological phases. We prove that the bulk topology of these 2+1D phases is manifested in transverse spin-1 quantization of the photon. From this insight, we predict two unique bosonic phases – one with even parity $C = \pm 2$ and one with odd $C = \pm 1$. To understand the even parity phase $C = \pm 2$, we introduce an exactly solvable model utilizing nonlocal optical Hall conductivity and reveal a single gapless photon at the edge. This unidirectional photon is spin-1 helically quantized, immune to backscattering, defects, and exists at the boundary of the $C = \pm 2$ bosonic phase and any interface – even vacuum. The contrasting phenomena of transverse quantization in the bulk, but longitudinal (helical) quantization on the edge is addressed as the quantum gyroelectric effect (QGEE). We also validate our bosonic Maxwell theory by direct comparison with the supersymmetric Dirac theory of fermions. To accelerate the discovery of such bosonic phases, we suggest two new probes of topological matter with broken time-reversal symmetry: momentum-resolved electron energy loss spectroscopy and cold atom near-field measurement of nonlocal optical Hall conductivity.

3.1 Introduction

Initial observations of topological phases of matter surfaced with the quantum Hall effect (QHE), a discovery which revealed that the transverse conductivity $\sigma_H = ne^2/h$ is naturally quantized [3], [5], [7]. e is the elementary charge of the electron and h is the Planck constant. Here, $n \in \mathbb{Z}$ is the electronic Chern number and represents a global topological invariant. Being a global property of the bulk electronic band structure, it is insensitive to disorder within the material. Yet, in terms of the photon with frequency ω and momentum k,

$$\sigma_H(0,0) = n\frac{e^2}{h}, \tag{3.1}$$

only describes the local static response $\omega = k = 0$ and contains no information of the high-frequency $\omega > 0$, short-wavelength $k > 0$ behavior of the electromagnetic field. The AC dynamical equivalent $\sigma_H(\omega, 0)$ of the conventional DC conductivity $\sigma_H(0,0)$ is known as the optical Hall conductivity. It is measured using the Faraday rotation angle (gyrotropic response) and has shown plateau-like behavior up to THz frequencies [55]. The purpose of this paper is to unravel the global topological properties of the photon and the role of spin-1 quantization in the generalized optical Hall conductivity $\sigma_H(\omega, k)$.

Conventionally, topological materials have focused on fermionic behavior, which display spin-½ polarized edge states and integer quantization of the Hall conductivity [27], [28]. However, spin-1 bosonic phases with broken time-reversal symmetry (TRS) have recently been proposed [56]–[63] and correspond to even integer Hall quantization. Pioneering research in topological photonics has mimicked the fermionic behavior using carefully structured pseudo-spin-½ photonic crystals [64]–[67]. A few striking examples are gyrotropic photonic crystals [23], [68], [69], Floquet topological insulators [52] and bianisotropic metamaterials [51], [70], [71] which support chiral photonic edge states. Similar pseudo-spin approaches utilizing Haldane models on honeycomb lattices have led to Chern insulators [19]. These are quantum Hall phases but with zero field – realized in photonic crystals, circuit QED [72] and cold atom systems [73]. Important work has also developed Chern invariants for continuous photonic media with broken TRS [74]–[77]. Nevertheless, the discovery of true spin-1 quantized phases has remained an open problem, as well as the connection between

bosonic and photonic topologies. We solve both these problems simultaneously which can open interesting avenues for condensed matter physics and photonics.

The essential difference between fermions and bosons is revealed in their half-integer vs. integer spins. This difference is directly reflected in single-particle geometric phases [78], [79] and arises from their rotational symmetries ($\mathcal{R}$). Under cyclic revolution, a fermion returns out of phase with itself $\mathcal{R}(2\pi) = -1$, meaning topological monopoles exhibit half-integer quantization. Conversely, bosons return in phase under the same rotation $\mathcal{R}(2\pi) = +1$, signaling integer monopoles in the band structure. Due to this critical distinction, fermions and bosons constitute different topological classes which are incommensurable with one another. Although a host of naturally occurring fermionic phases have been discovered [80], no bosonic equivalent has been found till date. In this paper, we develop the theory of TRS broken bosonic phases for light to accelerate their discovery.

We put forth the complete microscopic continuum theory describing all 2+1D bosonic phases of the photon. We account for the inherent spin-1 symmetries of the electromagnetic field such that the bosonic properties emerge naturally. This marks a distinct departure from previous attempts at building topological field theories for the photon. We reveal that the signature of these topological bosonic phases is bulk transverse spin quantization [26], [81]– [83] – in stark contrast to conventional photonic media where transverse spin is a continuous classical number. From very general symmetry arguments, we predict two unique photonic phases, with even $C = \pm 2$ or odd $C = \pm 1$ parity.

We show the fundamental necessity of spatiotemporal dispersion (momentum and frequency dependence of linear response) to define global topological invariants in continuum phases of matter. Spatiotemporal dispersion is a natural consequence of matter-mediated interactions between bosonic fields. We introduce an exactly solvable model, exploiting nonlocal optical Hall conductivity $\sigma_H(\omega, k)$, to unravel the topological physics of the even parity phase $C = \pm 2$. This phase has been predicted in interacting bosonic systems and corresponds to a single gapless photon at the edge. The unidirectional photon exists at the boundary of the nontrivial gyrotropic medium and arbitrary material interface, unlike any previously known edge states in electromagnetism. It hosts many intriguing optical properties, such as spin-1 helical quantization, anomalous displacement currents and robustness to

disorder. We address the contrasting phenomena of transverse quantization in the bulk and longitudinal (helical) quantization at the edge as the quantum gyroelectric effect (QGEE). To rigorously validate our bosonic predictions, we directly compare this model to its supersymmetric Dirac theory [84]–[86], highlighting the striking similarities, but important differences, between spin-1 and spin-½ topologies. Finally, we suggest experimental probes to search for these new bosonic phases of matter.

This article is organized as follows. In Sec. 3.2 we analyze the linear response theory of 2+1D electromagnetism and derive the regularized continuum Hamiltonian with broken TRS. In Sec. 3.3 we study the rotational symmetries of this Hamiltonian and discuss the physical implications of orbital, spin and total angular momentum of the collective light-matter excitations. The following Sec. 3.4 relates integer spin directly to the Chern number and all topological bosonic phases of the photon are found. Using an exactly solvable model, the even parity bosonic phase $C = \pm 2$ is examined extensively. Sec. 3.5 validates our predictions by directly comparing the Maxwell model to its supersymmetric Dirac theory. This procedure highlights the correspondence between traditional fermionic phases and even parity bosonic phases, while also elucidating the fundamental role of spin. Sec. 3.6 presents our conclusions and a discussion of how to search for bosonic phases in gyrotropic plasmas and quantum wells. We anticipate the development of new experimental tools to probe the signatures of these spin-1 quantized photonic edge states.

The focus of this paper is TRS broken topological bosonic phases which possess unidirectional edge states. As mentioned above, this is fundamentally related to optical Hall conductivity and gyrotropy in matter. However, TRS protected bosonic phases are also possible and show counter-propagating edge states [63]. This arises from antisymmetric magnetoelectricity as opposed to gyrotropy. The hallmark of both these bosonic phases is longitudinal spin-1 quantization at the edge. These topologically protected edge states are emergent massless photons with massive-like photons in the bulk material. The rigorous validity of these topological bosonic phases follows from supersymmetric Dirac theory and constitutes a one-to-one mapping to the continuum fermionic phase. This direct analogy between Dirac-fermions and Maxwell-bosons fundamentally requires spatiotemporal dispersion, which has not been previously tackled in electromagnetic topological field theories.
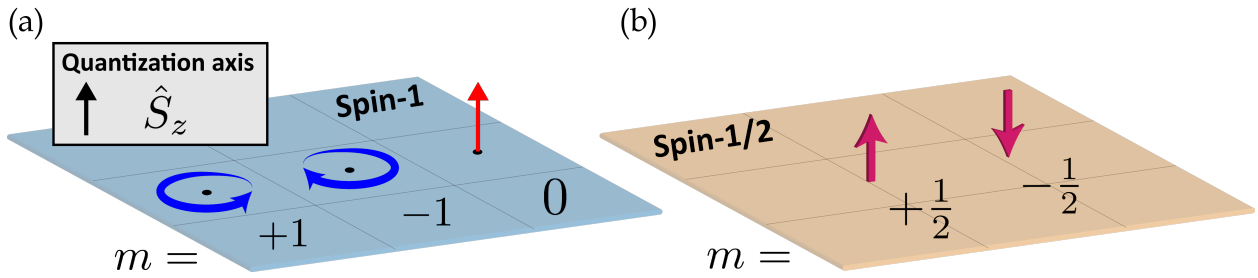
Figure 3.1. Our work emphasizes the fundamental differences between 2+1D topological materials for Maxwell-bosons and Dirac-fermions, which are characterized by their bulk spin quantum numbers. In 2D, the quantization axis is along z as all rotations occur in the x-y plane. Both (a) photonic and (b) electronic topologies are connected to $\hat{S}_z$ quantization at certain high-symmetry $\mathbf{k}$ points in the bulk material. The distinction lies in their rotational symmetries ($\mathcal{R}$). Photons are bosonic particles and respect spin-1 statistics $\mathcal{R}(2\pi) = +1$, which possess integer spin projections $m = \pm 1, 0$. Conversely, electrons are fermionic particles and respect spin-½ statistics $\mathcal{R}(2\pi) = -1$, which possess half-integer spin projections $m = \pm 1/2$. This changes the interpretation of topological invariants and the observable phenomena of different particles.

3.2 Continuum topological photonics

3.2.1 2+1D electrodynamics

In two spatial dimensions and one temporal dimension, the propagation of charge is restricted to the x-y plane. This limits the degrees of freedom of both the electromagnetic field and the induced response of a material [Fig. 3.2a]. Therefore, we focus on strictly transverse-magnetic (TM) waves, meaning there are only 3 unique components of the field. From first principles [App. B.1], we derive the corresponding wave equation of the 2D photon coupled to matter,

$$\mathcal{H}_0(\mathbf{k})f = \omega\mathcal{M}(\omega, \mathbf{k})f, \qquad f = \begin{bmatrix} E_x \\ E_y \\ H_z \end{bmatrix}, \tag{3.2}$$

where f is the TM polarization state (wavefunction) of the electromagnetic field. In the absence of matter, $\mathcal{H}_0(\mathbf{k})$ are the vacuum Maxwell equations in momentum space,

$$\mathcal{H}_0(\mathbf{k}) = k_x\hat{S}_x + k_y\hat{S}_y = \begin{bmatrix} 0 & 0 & -k_y \\ 0 & 0 & k_x \\ -k_y & k_x & 0 \end{bmatrix}. \tag{3.3}$$

Notice that $\mathcal{H}_0(\mathbf{k}) = \mathbf{k}\cdot\mathbf{S}$ represents optical helicity, i.e. the projection of momentum $\mathbf{k}$ onto the spin $\mathbf{S}$. We identify these spin-1 operators $\hat{S}_x$ and $\hat{S}_y$ that satisfy the angular momentum algebra $[\hat{S}_x, \hat{S}_y] = \mathrm{i}\hat{S}_z$,

$$\hat{S}_x = \begin{bmatrix} 0 & 0 & 0 \\ 0 & 0 & 1 \\ 0 & 1 & 0 \end{bmatrix}, \qquad \hat{S}_y = \begin{bmatrix} 0 & 0 & -1 \\ 0 & 0 & 0 \\ -1 & 0 & 0 \end{bmatrix}, \qquad \hat{S}_z = \begin{bmatrix} 0 & -\mathrm{i} & 0 \\ \mathrm{i} & 0 & 0 \\ 0 & 0 & 0 \end{bmatrix}. \tag{3.4}$$

Here, $(\hat{S}_z)_{ij} = -\mathrm{i}\epsilon_{ijz}$ is the generator of rotations in the x-y plane and is represented by the antisymmetric matrix. $\hat{S}_z$ will be foundational when discussing spin-1 symmetries in 2D.

The linear response function of the 2D material $\mathcal{M}$ is dependent on continuous variables ω and $\mathbf{k}$,

$$\mathcal{M}(\omega, \mathbf{k}) = \begin{bmatrix} \varepsilon_{xx} & \varepsilon_{xy} & \chi_x \\ \varepsilon_{xy}^* & \varepsilon_{yy} & \chi_y \\ \chi_x^* & \chi_y^* & \mu \end{bmatrix}, \qquad \begin{aligned} D_i &= \varepsilon_{ij} E^j + \chi_i H_z, \\[1em] B_z &= \chi_i^* E^i + \mu H_z, \end{aligned} \tag{3.5}$$

which compactly represents the constitutive relations. We include all possible material responses as a generalization – for instance magnetoelectricity χ_i and birefringence in ε_{ij}. However, based on symmetry constraints, we will show that only certain parameters of $\mathcal{M}$ are important in the topological classification.

3.2.2 Continuum response function

Alas, Eq. (3.2) poses a problem; it does not represent a proper first-order in time Hamiltonian since the response function $\mathcal{M}(\omega, \mathbf{k})$ is dependent on its own eigenvalue. Nevertheless, we can prove that it is derived from a first-order Hamiltonian by exploiting stringent symmetry properties. We demand Hermiticity $\mathcal{M} = \mathcal{M}^\dagger$ such that the response is lossless. We also require positive definiteness $\bar{\mathcal{M}} = \partial_\omega(\omega \mathcal{M}) > 0$ to ensure the energy density is non-negative and admits proper normalization $f^\dagger \bar{\mathcal{M}} f > 0$. The response must be causal (Kramers-Kronig) and obey the reality condition $\mathcal{M}(\omega, \mathbf{k}) = \mathcal{M}^*(-\omega, -\mathbf{k})$, guaranteeing the electromagnetic fields are real-valued [87]. Two additional constraints should also be considered for realistic materials. Stability at static equilibrium $\mathcal{M}(0, \mathbf{k}) = \bar{\mathcal{M}}(0, \mathbf{k}) > 0$, and the ultraviolet limit $\lim_{\omega \to \infty} \mathcal{M}(\omega, \mathbf{k}) = \mathbb{1}_3$. Here, $\mathbb{1}_3$ is the 3×3 identity matrix and the limit implies transparency at high-frequency $\omega \to \infty$, as the material cannot respond to sufficiently fast temporal oscillations.

Combining all the above criteria, we find that the response function can always be decomposed as a discrete summation of oscillators [19], [74], [88],

$$\mathcal{M}(\omega, \mathbf{k}) = \mathbb{1}_3 - \sum_\alpha \frac{\mathcal{C}_{\alpha\mathbf{k}}^\dagger \mathcal{C}_{\alpha\mathbf{k}}}{\omega_{\alpha\mathbf{k}}(\omega - \omega_{\alpha\mathbf{k}})}. \tag{3.6}$$

α labels any arbitrary bosonic excitation in the material, such as an exciton or phonon, which couples linearly to the electromagnetic fields via the 3×3 tensor $\mathcal{C}_{\alpha\mathbf{k}}$. $\omega_{\alpha\mathbf{k}}$ is the resonant

84

energy of the oscillator and corresponds to a first-order pole of the response function. Note both $\mathcal{C}_{\alpha\mathbf{k}}$ and $\omega_{\alpha\mathbf{k}}$ are in general $\mathbf{k}$ dependent. We emphasize that the response function is consistent with previous work on gyrotropic plasmas [89], [90]. However, our key advance is that the tensors $\mathcal{C}_{\alpha\mathbf{k}}$, characterizing the collective light-matter excitations, carry information of spin and orbital angular momentum.

3.2.3 Continuum Hamiltonian

A detailed derivation of the continuum electromagnetic Hamiltonian $H(\mathbf{k})$ is presented in App. B.2. To accomplish this, we expand the response function $\mathcal{M}(\omega, \mathbf{k})$ in terms of 3-component matter oscillators ψ_α. These represent internal polarization and magnetization modes of the material,

$$\psi_\alpha = \frac{\mathcal{C}_{\alpha\mathbf{k}}f}{\omega - \omega_{\alpha\mathbf{k}}}, \qquad \omega\psi_\alpha = \omega_{\alpha\mathbf{k}}\psi_\alpha + \mathcal{C}_{\alpha\mathbf{k}}f. \tag{3.7}$$

We now define u as the generalized state vector of the electromagnetic problem, accounting for the photon f and all possible internal excitations ψ_α,

$$H(\mathbf{k})u = \omega u, \qquad u = \begin{bmatrix} f & \psi_1 & \psi_2 & \dots \end{bmatrix}^\mathsf{T}, \tag{3.8}$$

which satisfies a first-order Hamiltonian wave equation. Notice that contraction of u naturally reproduces the energy density upon summation over all degrees of freedom $u^\dagger u = f^\dagger \bar{\mathcal{M}} f$, with $\bar{\mathcal{M}} = \partial_\omega(\omega\mathcal{M}) > 0$ always positive definite. The continuum Hamiltonian $H(\mathbf{k})$ acting on u is given concisely as,

$$H(\mathbf{k}) = \begin{bmatrix} \mathcal{H}_0(\mathbf{k}) + \sum_\alpha \omega_{\alpha\mathbf{k}}^{-1} \mathcal{C}_{\alpha\mathbf{k}}^\dagger \mathcal{C}_{\alpha\mathbf{k}} & \mathcal{C}_{1\mathbf{k}}^\dagger & \mathcal{C}_{2\mathbf{k}}^\dagger & \dots \\ \mathcal{C}_{1\mathbf{k}} & \omega_{1\mathbf{k}} & 0 & \dots \\ \mathcal{C}_{2\mathbf{k}} & 0 & \omega_{2\mathbf{k}} & \dots \\ \vdots & \vdots & \vdots & \ddots \end{bmatrix}. \tag{3.9}$$

This eigenvalue problem generates the complete spectrum of quasiparticle eigenstates,

$$H_{\mathbf{k}} u_{n\mathbf{k}} = \omega_{n\mathbf{k}} u_{n\mathbf{k}}, \tag{3.10}$$

and the eigenstates are normalized to the energy density $u_{n\mathbf{k}}^{\dagger} u_{n\mathbf{k}} = f_{n\mathbf{k}}^{\dagger} \bar{\mathcal{M}}(\omega_{n\mathbf{k}}, \mathbf{k}) f_{n\mathbf{k}} = 1$. Moreover, the eigenenergies $\omega_{n\mathbf{k}}$ are the n nontrivial roots of the characteristic equation,

$$\det \left[\mathcal{H}_0(\mathbf{k}) - \omega \mathcal{M}(\omega, \mathbf{k}) \right] = 0, \qquad \omega = \omega_n(\mathbf{k}), \tag{3.11}$$

proving that the response function $\mathcal{M}(\omega, \mathbf{k})$ is derived from a first-order Hamiltonian $H(\mathbf{k})$.

3.2.4 Continuum regularization (one-point compactification)

Our goal is to develop a continuum topological theory that accounts for both spatiotemporal dispersion and the inherent bosonic properties of light. Due to the unbounded nature of the momentum space $\mathbb{R}^2$, continuum Chern numbers are usually ill-defined. Nevertheless, as long as the system is properly regularized, continuum field theories are possible and can be incredibly powerful tools to study long wavelength topological physics [91]–[93]. A necessary condition is one-point compactification of the momentum space [1], [15], [94], which governs the high-k asymptotic behavior of the Hamiltonian. This requirement is well understood in condensed matter and demands the Hamiltonian approach a directionally independent value,

$$\lim_{k \to \infty} H(\mathbf{k}) \to H(k), \tag{3.12}$$

where $k = \sqrt{\mathbf{k} \cdot \mathbf{k}}$ is the magnitude of the wavevector. In this way, all limits at infinity are mapped into the same point and satisfy a "periodic" boundary condition. The momentum space is closed and topologically equivalent to the Riemann sphere $\mathbb{R}^2 \simeq S^2$ [Fig. 3.2b]. Hence, Chern numbers are quantized. A rigorous proof is presented in App. B.3.

This constraint has important implications in continuum photonic media. Since Maxwell's equations are strictly first-order in spatial derivatives [Eq. (3.3)], one-point compactification can only be satisfied by introducing nonlocality [95], [96]. Nonlocality (or spatial dispersion) is the momentum dependence of linear response – commonly ignored in photonics problems,
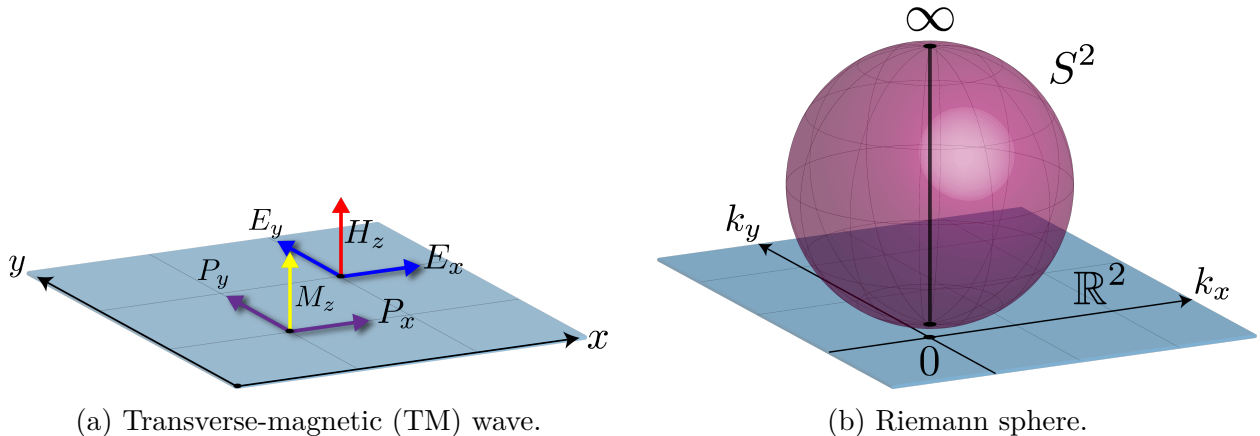
(a) Transverse-magnetic (TM) wave.

(b) Riemann sphere.

Figure 3.2. (a) Only transverse-magnetic (TM) waves propagate as charge is restricted to the x-y plane (blue and red arrows denote the fields). This limits the degrees of freedom of both the electromagnetic field and the induced response of a material. Electromagnetic polarization and magnetization response in a 2D material is shown with the purple and yellow arrows. The electric and magnetic displacement fields are the linear superposition of $D_i = P_i + E_i$ and $B_z = M_z + H_z$. Our focus in this paper is gyrotropic media which correspond to optical (dynamical) Hall conductivity. (b) One-point compactification of the momentum space $\mathbb{R}^2 \simeq S^2$ over which the topological quantum numbers are defined. When the Hamiltonian is properly regularized, the planar $\mathbf{k}$-space is topologically equivalent to the bounded Riemann sphere. $k_p = 0$ and $k_p = \infty$ are the rotationally invariant (high-symmetry) points on the sphere, passing through the z-axis. This procedure is necessary to ensure Chern quantization in continuum topological field theories and fundamentally requires nonlocal photonic media.

DC transport measurements, as well as Faraday rotation experiments. However, we strongly emphasize that the high-k behavior cannot be neglected even in the long wavelength continuum theory. These deep sub-wavelength components encode global information of the fields and are essential to properly describe the topological physics. By exploiting rotational symmetry, we will show that the asymptotic behavior of the Hamiltonian $H(\mathbf{k})$ and by extension, the response function $\mathcal{M}(\omega, \mathbf{k})$, is naturally regularized and predicts new bosonic phases of matter.

3.3 Rotational symmetry

3.3.1 Definition of orbital, spin and total angular momentum

If the two dimensional crystal has a center (at least 3-fold cyclic [97], [98]), the continuum Hamiltonian is rotationally symmetric about z,

$$\mathcal{R}^{-1}H(\mathcal{R}\mathbf{k})\mathcal{R} = H(\mathbf{k}), \qquad \mathcal{R}(2\pi) = \mathbb{1}_3, \tag{3.13}$$

and the eigenenergies $\omega = \omega_n(k)$ depend only on the magnitude of k. Note that $\mathcal{R}$ is diagonal in u, meaning the photon and each oscillator is rotated individually, $f \to \mathcal{R}f$ and $\psi_\alpha \to \mathcal{R}\psi_\alpha$. In this case $\mathcal{R}(\theta)$ is a continuous rotation,

$$\mathcal{R}(\theta) = \exp\left[\mathrm{i}\theta\hat{S}_z\right] = \begin{bmatrix} \cos\theta & \sin\theta & 0 \\ -\sin\theta & \cos\theta & 0 \\ 0 & 0 & 1 \end{bmatrix}, \tag{3.14}$$

and can be expressed as the exponential of the spin-1 generator $(\hat{S}_z)_{ij} = -\mathrm{i}\epsilon_{ijz}$. This represents an element of SO(3) in the subspace of $\mathbb{R}^2$ [99], as all rotations occur in the x-y plane. We stress that the vector representation is bosonic, meaning the quasiparticles return in phase under cyclic revolution $\mathcal{R}(2\pi) = \mathbb{1}_3$.

Since the Hamiltonian possesses a continuous rotational symmetry, the total angular momentum (TAM) is conserved,

$$[\hat{J}_z, H(\mathbf{k})] = 0, \qquad \hat{J}_z = \hat{L}_z + \hat{S}_z. \tag{3.15}$$

Eq. (3.13) and (3.15) are equivalent statements in this context. Here, $\hat{L}_z$ is the orbital angular momentum (OAM) operator in 2D $\mathbf{k}$-space and can be expressed in polar coordinates as,

$$\hat{L}_z = -\mathrm{i}k_x\frac{\partial}{\partial k_y} + \mathrm{i}k_y\frac{\partial}{\partial k_x} = -\mathrm{i}\partial_\phi. \tag{3.16}$$

Eigenstates of the OAM are well known and represent quantized azimuthal charges,

$$\hat{L}_z |l\rangle = l|l\rangle, \qquad |l\rangle = \exp(\mathrm{i}l\phi), \tag{3.17}$$

where $l \in \mathbb{Z}$ is any integer. Conversely, eigenstates of the spin angular momentum (SAM) represent states of quantized polarization, transverse to the x-y plane,

$$\hat{S}_z \vec{e} = m\vec{e}. \tag{3.18}$$

The matrix form of $\hat{S}_z$ is given in Eq. (3.4). For photons, the spin is an integer $m = \pm 1, 0$ and takes one of three discrete values. First, we have the $m = \pm 1$ spin states,

$$\vec{e}_\pm = \frac{1}{\sqrt{2}} \begin{bmatrix} 1 \\ \pm \mathrm{i} \\ 0 \end{bmatrix}, \qquad \hat{S}_z \vec{e}_\pm = \pm \vec{e}_\pm. \tag{3.19}$$

$\vec{e}_\pm$ are resonant electric ($H_z = 0$) counter-rotating states. Secondly, we have the $m = 0$ spin state, which is resonant magnetic ($E_i = 0$) and irrotational,

$$\vec{e}_0 = \begin{bmatrix} 0 \\ 0 \\ 1 \end{bmatrix}, \qquad \hat{S}_z \vec{e}_0 = 0. \tag{3.20}$$

A visualization of the quantized spin-1 states is displayed in Fig. 3.1(a) and this is compared to quantized spin-½ states in Fig. 3.1(b). In Sec. 3.4, we will prove that these spin quantized eigenstates naturally arise at high-symmetry $\mathbf{k}$ points in 2+1D bosonic phases.

3.3.2 High-symmetry points and gauge singularities

At an arbitrary momentum $\mathbf{k}$, the quasiparticles $u_{n\mathbf{k}}$ are not eigenstates of $\hat{L}_z$ or $\hat{S}_z$. Instead, they are eigenstates of the total angular momentum $\hat{J}_z = \hat{L}_z + \hat{S}_z$,

$$\hat{J}_z u_{n\mathbf{k}} = j_n u_{n\mathbf{k}}, \qquad j_n \in \mathbb{Z}, \tag{3.21}$$

where j_n is an integer for bosons. Since $\hat{J}_z$ is a differential operator, the choice of j_n represents a particular Berry gauge for the eigenstates. This gauge is single-valued for all $\mathbf{k}$ with the possible exception of two points, $k_p = 0$ and $k_p = \infty$. These are called high-symmetry points (HSPs). At these specific momenta, the Hamiltonian is rotationally invariant [100],

$$\mathcal{R}^{-1} H(k_p) \mathcal{R} = H(k_p), \qquad [\hat{S}_z, H(k_p)] = 0, \tag{3.22}$$

which follows immediately from Eq. (3.13) and (3.15). In the continuum theory, $k_p = 0$ is a HSP because the origin always rotates into itself. Owing to one-point compactification [Eq. (3.12)], $k_p = \infty$ is also a HSP. This is clear by direct inspection of the Riemann sphere in Fig. 3.2b. A rotation in the plane of $\mathbb{R}^2$ rotates S^2 about its axis, keeping both $k_p = 0$ and $k_p = \infty$ fixed. Invariance at $k_p = \infty$ is therefore imperative to describe continuum topological theories.

At HSPs the SAM of any eigenstate $u_{n\mathbf{k}}$ is quantized and this is guaranteed by symmetry [Eq. (3.22)]. Still, the Berry gauge may be multi-valued here due to the OAM – known as a phase singularity [101],

$$\lim_{k \to k_p} u_n(\mathbf{k}) \to u_n(k_p) \exp\left[i l_n(k_p)\phi\right], \tag{3.23}$$

$$\hat{S}_z u_n(k_p) = m_n(k_p) u_n(k_p), \tag{3.24}$$

where $j_n = l_n(k_p) + m_n(k_p)$ at HSPs. We come to an important revelation from Eq. (3.23). If the spin does not change within the eigenstate dispersion $m_n(0) = m_n(\infty)$, we can remove the phase singularity at both points simultaneously $l_n(0) = l_n(\infty) = 0$, such that the Berry gauge $j_n = m_n(0) = m_n(\infty)$ is single-valued for all $\mathbf{k}$.

However, if the spin changes within the dispersion $m_n(0) \neq m_n(\infty)$, this procedure is impossible. The Berry gauge is always multi-valued because the singularity $l_n(k_p) \neq 0$ cannot be resolved at $k_p = 0$ and $k_p = \infty$ simultaneously. This is a nontrivial topology. The physical interpretation is simple but profound; since the TAM is conserved for each eigenstate $\Delta j_n = 0$, the OAM $\Delta l_n = l_n(\infty) - l_n(0) \neq 0$ must change to compensate for the SAM,

$$\Delta l_n = -\Delta m_n = m_n(0) - m_n(\infty). \tag{3.25}$$

We will now prove that Eq. (3.25) fundamentally defines the Chern classification of 2+1D bosonic phases.

3.4 Continuum topological bosonic phases

3.4.1 Continuum photonic Chern number

Utilizing the eigenstates of the Hamiltonian in Eq. (3.10); we obtain the Berry connection by varying a quasiparticle with respect to the momentum,

$$\mathbf{A}_n(\mathbf{k}) = -\mathrm{i} u_{n\mathbf{k}}^\dagger \partial_{\mathbf{k}} u_{n\mathbf{k}}. \tag{3.26}$$

Applying the curl produces the gauge invariant Berry curvature $F_n(\mathbf{k}) = \hat{z} \cdot [\partial_{\mathbf{k}} \times \mathbf{A}_n(\mathbf{k})]$. The Chern number C_n is a global topological invariant and is traditionally found by integrating F_n over the 2D Brillouin zone – i.e. the torus $\mathbb{T}^2 = S^1 \times S^1$. For continuum theories, we integrate over the entire 2D momentum space $\mathbb{R}^2$,

$$C_n = \frac{1}{2\pi} \iint_{\mathbb{R}^2} F_n(\mathbf{k}) \, d^2\mathbf{k}. \tag{3.27}$$

When properly regularized, the planar manifold is topologically equivalent to the Riemann sphere $\mathbb{R}^2 \simeq S^2$ and the Chern number is quantized [App. B.3].

Although photonic Chern numbers have been defined, neither the high-k behavior nor the inherent bosonic properties have been addressed. With this in mind, we return to the Berry connection $\mathbf{A}_n$ in polar coordinates $\partial_{\mathbf{k}} = \hat{k}\partial_k + \hat{\phi}\partial_\phi$,

$$\mathbf{A}_n(\mathbf{k}) = \hat{k} A_n^k(k) + \hat{\phi} A_n^\phi(k). \tag{3.28}$$

Due to rotational symmetry, the polar components of $\mathbf{A}_n$ depend only on k. Furthermore, we can connect the Berry potential A_n^ϕ directly to the OAM,

$$A_n^\phi(k) = -\mathrm{i} u_{n\mathbf{k}}^\dagger \partial_\phi u_{n\mathbf{k}} = \langle \hat{L}_z \rangle_n. \tag{3.29}$$

Here, $\langle \hat{L}_z \rangle_n$ is the expectation value of the OAM for the nth eigenstate. This corresponds to a Berry curvature F_n of,

$$F_n(k) = \partial_k \langle \hat{L}_z \rangle_n. \tag{3.30}$$

When integrating over all momenta $d^2\mathbf{k} = dk d\phi$, we find that the continuum Chern number C_n is determined solely by the phase singularities at HSPs,

$$C_n = \int_0^\infty dk \ \partial_k \langle \hat{L}_z \rangle_n = \langle \hat{L}_z \rangle_n|_0^\infty = \Delta l_n, \tag{3.31}$$

precisely the change in OAM. Substituting for $\Delta l_n = -\Delta m_n$ in Eq. (3.25), we attain an elegant expression for the Chern number,

$$C_n = \Delta l_n = m_n(0) - m_n(\infty). \tag{3.32}$$

Eq. (3.32) is one of the central results of this paper and is valid for both fermionic and bosonic representations. Essential differences between the two are immediately apparent.

For a spin-½ electron, quanta take one of two half-integer values $m_n = \pm\frac{1}{2}$. Consequently, we find only one truly distinct fermionic phase,

$$\text{fermion}: \qquad C_n = \pm 1, 0. \tag{3.33}$$

However, for the spin-1 photon, quanta take three integer values $m_n = \pm 1, 0$. We discover two unique bosonic phases,

$$\text{boson}: \qquad C_n = \pm 2, \pm 1, 0. \tag{3.34}$$

One with even parity $C_n = \pm 2$ and one with odd $C_n = \pm 1$. Even parity corresponds to a change from $m_n(0) = \pm 1$ to $m_n(\infty) = \mp 1$ at HSPs. This phase is familiar in interacting bosonic systems and is identified with a single gapless boson at the edge [57]–[62] – not two as we might expect from fermionic Chern number arguments. Odd parity bosonic phases are quite exotic in this regard [102], [103]. This phase corresponds to a change from $m_n(0) = \{0, \pm 1\}$ to $m_n(\infty) = \{\pm 1, 0\}$ at HSPs.

3.4.2 Nonlocal regularization of the response function

We now derive the asymptotic behavior of the Hamiltonian $H(\mathbf{k})$ to ensure the continuum theory is properly regularized at $k \to \infty$. This will help us discover the precise form of the response function $\mathcal{M}(\omega, \mathbf{k})$ and the order of nonlocality necessary to describe a topological field theory. Nonlocality plays two equally important roles in this context – it distinguishes between trivial and nontrivial phases. If high-k components are ignored, it is impossible to define either of these phases in the continuum.

From Eq. (3.6) and (3.9), rotational symmetry implies the coupling tensors obey,

$$\mathcal{R}^{-1}\mathcal{C}_\alpha(\mathcal{R}\mathbf{k})\mathcal{R} = \mathcal{C}_\alpha(\mathbf{k}), \tag{3.35}$$

and the oscillator resonances $\omega_\alpha(k)$ depend only on k. We find the exact expression of $\mathcal{C}_\alpha(\mathbf{k})$,

$$\mathcal{C}_\alpha(\mathbf{k}) = c_\alpha(k)\mathbf{k} \otimes \mathbf{k} + d_\alpha(k)\mathbf{k} \cdot \mathbf{S} + \mathcal{G}_\alpha(k), \tag{3.36}$$

where $c_\alpha(k)$ and $d_\alpha(k)$ are scalars. It is easy to check that the tensors also commute with $[\hat{J}_z, \mathcal{C}_\alpha(\mathbf{k})] = 0$, conserving TAM. $c_\alpha(k)$ introduces a nonlocal birefringence in ε_{ij} and $d_\alpha(k)$ is a type of nonlocal magnetoelectricity χ_i. Both terms are permitted by symmetry but neither is important, as all contributions besides $\mathcal{G}_\alpha(k)$ vanish identically at $k_p = 0$ and $k_p = \infty$. This is because $\mathcal{G}_\alpha(k)$ is the only rotationally invariant component of $\mathcal{C}_\alpha(\mathbf{k})$, which defines the topology,

$$\mathcal{R}^{-1}\mathcal{G}_\alpha(k)\mathcal{R} = \mathcal{G}_\alpha(k), \qquad [\hat{S}_z, \mathcal{G}_\alpha(k)] = 0. \tag{3.37}$$

The Hamiltonian in Eq. (3.9) takes the following form at HSPs,

$$H(k_p) = \begin{bmatrix} \sum_\alpha \omega_{\alpha k_p}^{-1} \mathcal{G}_{\alpha k_p}^\dagger \mathcal{G}_{\alpha k_p} & \mathcal{G}_{1k_p}^\dagger & \mathcal{G}_{2k_p}^\dagger & \cdots \\ \mathcal{G}_{1k_p} & \omega_{1k_p} & 0 & \cdots \\ \mathcal{G}_{2k_p} & 0 & \omega_{2k_p} & \cdots \\ \vdots & \vdots & \vdots & \ddots \end{bmatrix}. \tag{3.38}$$

Notice the vacuum Maxwell equations $\mathcal{H}_0(\mathbf{k})$ play no role in either limit; the Hamiltonian is governed entirely by the material response at HSPs. Nevertheless, this imposes pivotal stipulations on the asymptotic behavior. The largest powers in k must arise from $\mathcal{G}_{\alpha k}$ as these terms dominate at exceedingly large momentum $k \to \infty$. Consequently, $\mathcal{G}_{\alpha k}$ and $\omega_{\alpha k}$ require quadratic nonlocality $\propto k^2$ at minimum, since the vacuum fields $\mathcal{H}_0(\mathbf{k})$, which are linear in $\mathbf{k}$, must be outpaced in the $k \to \infty$ limit.

By extension of Eq. (3.38), the response function is regularized and rotationally invariant at HSPs,

$$[\hat{S}_z, \mathcal{M}(\omega, k_p)] = 0. \tag{3.39}$$

Upon summation over all oscillators describing the linear response, $\mathcal{M}$ takes a remarkably simple form,

$$\mathcal{M}(\omega, k_p) = \mathbb{1}_3 - \sum_\alpha \frac{\mathcal{G}^\dagger_{\alpha k_p} \mathcal{G}_{\alpha k_p}}{\omega_{\alpha k_p} \left(\omega - \omega_{\alpha k_p}\right)} = \begin{bmatrix} \varepsilon & ig & 0 \\ -ig & \varepsilon & 0 \\ 0 & 0 & \mu \end{bmatrix}, \tag{3.40}$$

where all parameters are evaluated at k_p. Here, ε and μ are the conventional scalar permittivity and permeability of a 2D material. g is a generalized gyrotropic coupling which breaks both parity and time-reversal symmetry.

Although the condition at $k_p = \infty$ is a mathematical requisite, it makes perfect sense physically when we acknowledge that the continuum theory is simply an approximation of the underlying crystal lattice. In reality, the momentum can never reach arbitrarily large values. As the momentum approaches the scale of the lattice constant $ka \approx \pi$, the wave approaches a Bragg condition. These are HSPs in the reciprocal lattice [97]–[100] so the continuum theory must encode this behavior. Accordingly, the $k \to \infty$ limit should be interpreted as a Bragg resonance.

3.4.3 Transverse spin quantization of the photon

We go one step further to uncover the precise origin of the spin-1 eigenvalues $m_n(k_p)$, the spin states $\vec{e}$, and their relation to the response function $\mathcal{M}$. At HSPs, the SAM expectation value is represented as,

$$\langle \hat{S}_z \rangle_n = m_n(k_p) = u_n^\dagger(k_p) \hat{S}_z u_n(k_p). \tag{3.41}$$

Using Eq. (3.7) and (3.37), this can be simplified to yield,

$$m_n(k_p) = f_n^\dagger(k_p) \bar{\mathcal{M}}(\omega_n(k_p), k_p) \hat{S}_z f_n(k_p). \tag{3.42}$$

We note that precisely at HSPs, the quantum of spin $m_n(k_p)$ is determined entirely by the photonic component $f_n(k_p)$ of the eigenmode $u_n(k_p)$ – but not the coordinates of the matter oscillations ψ_α. Utilizing the normalization condition $f_n^\dagger(k_p) \bar{\mathcal{M}}(\omega_n(k_p), k_p) f_n(k_p) = 1$, Eq. (3.42) leads to,

$$\hat{S}_z f_n(k_p) = m_n(k_p) f_n(k_p). \tag{3.43}$$

This indicates that the electromagnetic wavefunction f must be a spin state $f_n(k_p) \propto \vec{e}$ at HSPs [Eq. (3.18)].

Our problem reduces to finding the eigenstates of the photon at HSPs and directly evaluating their spin eigenvalues. We return to the characteristic equation in Eq. (3.11), which defines the photonic wavefunction f. As $k \to 0$, the vacuum equations vanish identically $\mathcal{H}_0(\mathbf{k}) \to 0$. Moreover, the response function is regularized and includes quadratic nonlocality $\propto k^2$ at minimum. As $k \to \infty$, the vacuum fields do not contribute $\mathcal{H}_0(\mathbf{k}) \to 0$. Therefore, a nontrivial solution exists $\omega_n(k_p) \neq 0$ if and only if it satisfies,

$$\det\left[\mathcal{M}(\omega_n(k_p), k_p)\right] = 0. \tag{3.44}$$

Eq. (3.44) represents the threshold condition at $k_p = 0$ and the Bragg condition at $k_p = \infty$ for any particular eigenstate n. To allow for nontrivial solutions $\mathcal{M}f = 0$ in Eq. (3.40), one of three possible conditions must be fulfilled,

$$\frac{g(\omega_n(k_p), k_p)}{\varepsilon(\omega_n(k_p), k_p)} = \pm 1, \qquad \text{or} \qquad \mu(\omega_n(k_p), k_p) = 0. \tag{3.45}$$

We see that the photonic wavefunction is clearly a spin-1 eigenstate $f_n(k_p) \propto \vec{e}$ at HSPs. The gyrotropic constraint gives us counter-rotating spin states $\hat{S}_z \vec{e}_\pm = \pm \vec{e}_\pm$ with eigenvalues $m_n(k_p) = \pm 1$, while the magnetic constraint gives us the irrotational spin state $\hat{S}_z \vec{e}_0 = 0$ with eigenvalue $m_n(k_p) = 0$. Physically, these conditions at HSPs correspond to gyrotropic or magnetic plasmon resonances in the bulk 2D material. In a lattice theory, the resonance at $k_p = 0$ describes the response at the Γ point, while $k_p = \infty$ describes the behavior near the edges of the Brillouin zone.

The meaning behind each topological bosonic phase is now revealed. In the even parity phase $C_n = \pm 2$, a gyrotropic mode dominates but the handedness of the plasmon changes at HSPs, $g/\varepsilon = \pm 1 \to \mp 1$. If the handedness does not change as $k \to \infty$, the phase is trivial $C_n = 0$. The odd parity phase $C_n = \pm 1$ is very different however. Instead, the mode changes from a magnetic plasmon $\mu = 0$ to a gyrotropic plasmon $g/\varepsilon = \pm 1$ at HSPs. In the following sections, we restrict our discussion to the even parity phase $C_n = \pm 2$. The odd parity phase $C_n = \pm 1$ is significantly more complicated and will be dedicated to a future paper.

3.4.4 Even parity bosonic phase: $C = \pm 2$

We adopt an exactly solvable model to unravel the low energy topological physics of this phase. We let the response function be rotationally invariant $[\hat{S}_z, \mathcal{M}(\omega, k)] = 0$ at all momenta, while also assuming $\varepsilon = \text{const.} > 1$ is dielectric and the response is nonmagnetic $\mu = 1$. In this case, all the physics is captured by the gyrotropic coefficient g, which is the high-frequency analog of the DC Hall conductivity,

$$g(\omega, k) = \frac{\sigma_H(k)}{\omega}, \qquad \sigma_H(k) = \sigma_0 - \sigma_2(ka)^2. \tag{3.46}$$
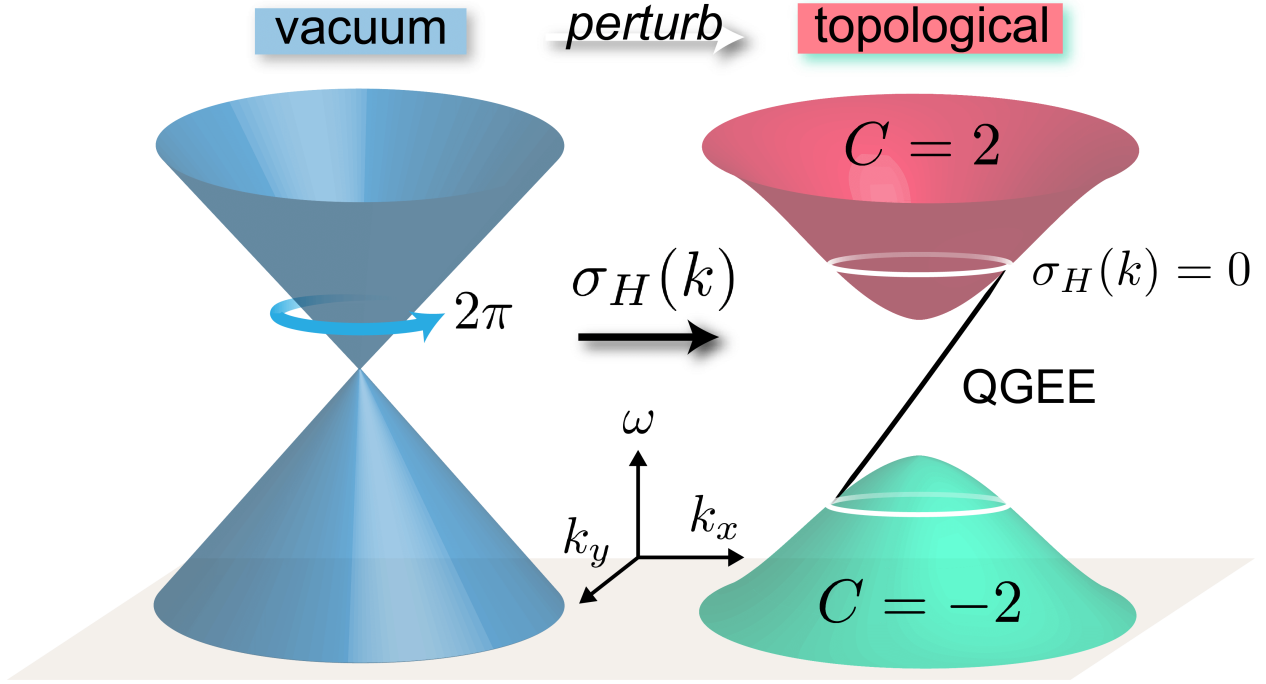
Figure 3.3. Schematic of the exactly solvable topological model. In vacuum, Maxwell's equations can be written in the form $\mathcal{H}_0(\mathbf{k}) = \mathbf{k} \cdot \mathbf{S}$, which captures both the spin-1 behavior and linear dispersion of the massless photon. The gyrotropic medium perturbs the linear dispersion and induces a bulk bandgap near zero frequency. In this case, the perturbation is a nonlocal Hall conductivity $\sigma_H(k) = \sigma_0 - \sigma_2(ka)^2$, which behaves identically to the effective mass of the Dirac equation. If $\sigma_H(k) = 0$ passes through zero at some finite momentum, the medium is topological. The nontrivial phase $C = 2$ corresponds to a gapless unidirectional photon at the boundary, dubbed the quantum gyroelectric effect (QGEE). We strongly emphasize that this model is validated by direct comparison with the supersymmetric Dirac theory for continuum fermions.

$\sigma_H(k)$ is a nonlocal Hall conductivity [104]. σ_0 is the static response and σ_2 characterizes the momentum dependence (scaled to the lattice constant a). At low energy $\omega \to 0$, this is the only admissible form of $g \neq 0$ [89], [90]. Due to the reality of the electromagnetic field $\mathcal{M}^*(-\omega, k) = \mathcal{M}(\omega, k)$, gyrotropy must always be odd in frequency $g(-\omega, k) = -g(\omega, k)$. This means a first-order pole at $\omega = 0$ is permissible and corresponds to nonzero Hall conductivity $\omega g(\omega, k) = \sigma_H(k) \neq 0$. The energy density is positive definite $\bar{\mathcal{M}} = \partial_\omega(\omega\mathcal{M}) = \text{diag}[\varepsilon, \varepsilon, 1] > 0$ and nonsingular at $\omega = 0$.

We highlight important aspects of our model and the connections to experimentally measured gyrotropic responses. Firstly, we deal with Hermitian systems so the imaginary part of the dielectric permittivity is zero $\text{Im}\,[\varepsilon] = \sigma/\omega = 0$. Therefore, no dissipative currents exist in this system and the gyrotropic coefficient is related only to a dissipationless Hall current. Experimentally measured variables connecting to the gyrotropic coefficient, such as Verdet constants, are highly frequency dependent and this is consistent with our model. Furthermore, the zero frequency behavior of the gyrotropic coefficient $g = \sigma_H/\omega$ is in agreement with first-order poles in standard models of conductivity $\text{Im}\,[\varepsilon] = \sigma/\omega$.

Remarkably, the quadratic spatial correction to σ_H is sufficient to describe a topological photonic phase and the continuum theory is regularized at $k \to \infty$. The interpretation is particularly simple in this context. At long wavelengths $\sigma_H(k \to 0) \to \sigma_0$, the Hall conductivity induces circulating currents of a specific handedness (clockwise or counter-clockwise), but at short wavelengths $\sigma_H(k \to \infty) \to -\sigma_2(ka)^2$, the handedness can reverse directions. We will show that when σ_H switches sign, the phase is nontrivial.

3.4.5 Bulk (bosonic Chern insulator)

In vacuum, the photon is massless and therefore linearly dispersing $\omega = k$. This is the photonic (spin-1) equivalent of a Dirac point and arises naturally from Maxwell's equations $\mathcal{H}_0(\mathbf{k}) = \mathbf{k} \cdot \mathbf{S} = k_x \hat{S}_x + k_y \hat{S}_y$, as mentioned in Sec. 3.2. By introducing the Hall conductivity, the linear dispersion of bulk waves fundamentally changes – a gap is formed at zero frequency $\omega = 0$,

$$\varepsilon\omega^2(k) = k^2 + \frac{\sigma_H^2(k)}{\varepsilon}, \tag{3.47}$$

where σ_H acts identically to an effective photon mass [84], [85]. ε governs the effective speed of light. A schematic of the vacuum and bulk dispersion is displayed in Fig. 3.3.

There is only one positive frequency $\omega > 0$ eigenstate associated with this system and is expressed in polar coordinates as,

$$f_{\mathbf{k}} = \begin{bmatrix} E_x \\ E_y \\ H_z \end{bmatrix} = \frac{1}{\sqrt{2\varepsilon}} \left(\frac{\sigma_H}{\varepsilon\omega}\hat{k} + i\hat{\phi} + i\frac{k}{\omega}\hat{z} \right) e^{i\phi}. \tag{3.48}$$

$f_{\mathbf{k}}$ is normalized to the energy density $1 = f_{\mathbf{k}}^{\dagger}\bar{\mathcal{M}}f_{\mathbf{k}}$ and is written in a fixed Berry gauge defined by the TAM $\hat{J}_z f_{\mathbf{k}} = f_{\mathbf{k}}$. We now show that the photon in this eigenstate exhibits transverse spin quantization at HSPs, which is independent of the chosen Berry gauge. From Eq. (3.48) above, we have $\hat{S}_z f(k_p) = m(k_p)f(k_p)$ at the plasmon resonances,

$$m(k_p) = \frac{g(\omega(k_p), k_p)}{\varepsilon(\omega(k_p), k_p)} = \frac{\sigma_H(k_p)}{\varepsilon\omega(k_p)} = \text{sgn}[\sigma_H(k_p)]. \tag{3.49}$$

Since ε is a constant, the eigenvalues are determined solely by the long and short wavelength behavior of the Hall conductivity, $m(0) = \text{sgn}[\sigma_0]$ and $m(\infty) = -\text{sgn}[\sigma_2]$, giving a Chern number of,

$$C = m(0) - m(\infty) = \text{sgn}[\sigma_0] + \text{sgn}[\sigma_2]. \tag{3.50}$$

A nontrivial phase corresponds to $\sigma_0\sigma_2 > 0$, which can be $C = \pm 2$ depending on the signs of σ_0 and σ_2. This is the simplest realization of a bosonic Chern insulator [13]. It is equally important to note that $\sigma_0\sigma_2 < 0$ corresponds to a trivial phase $C = 0$. Distinguishing between trivial $C = 0$ and nontrivial $C = \pm 2$ phases is only possible by incorporating nonlocality $\sigma_2 \neq 0$. A topological phase diagram of this system is presented in Fig. 3.4a.

In the nontrivial phase, there is a point where the Hall conductivity $\sigma_H(k) = 0$ passes through zero – precisely at $ka = \sqrt{\sigma_0/\sigma_2}$. The zero must occur for the spin to change handedness and can only be removed by a topological phase transition. This also puts an approximate bound on the Hall parameters. As long as $\sqrt{\sigma_0/\sigma_2} \ll \pi$ the continuum theory is valid and the zero occurs within the Brillouin zone. As an aside, we note the negative

(a) Phase diagram.

(b) Band diagram.
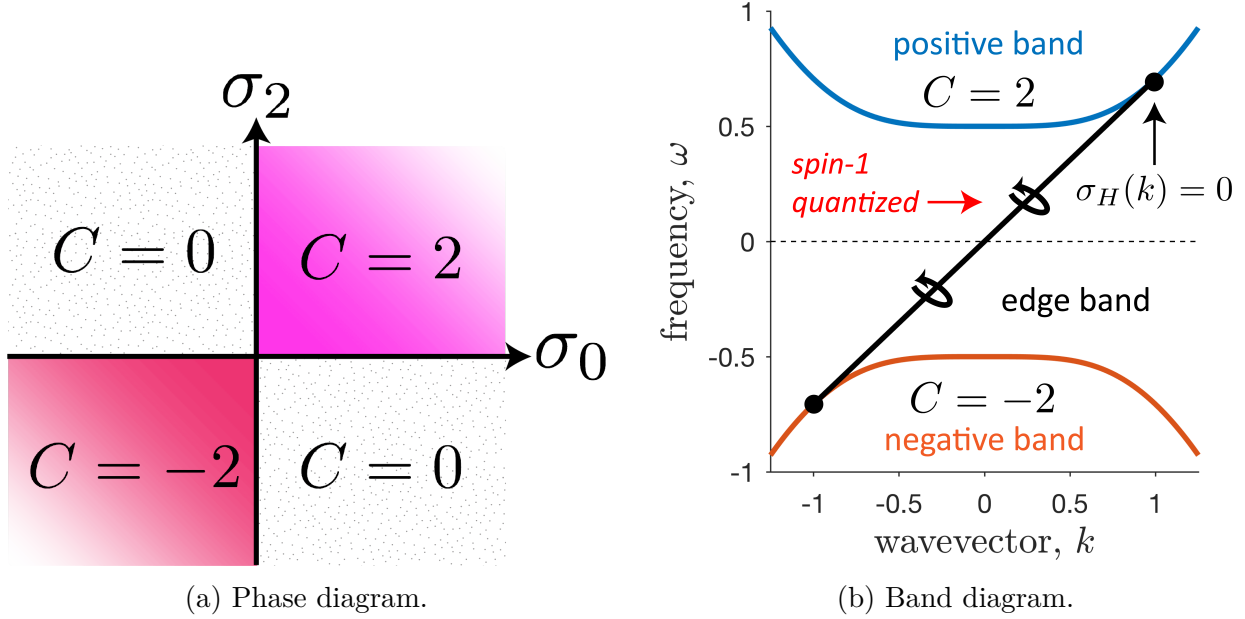
Figure 3.4. (a) Topological phase diagram of the nonlocal Hall model $\sigma_H(k) = \sigma_0 - \sigma_2(ka)^2$. $C = \text{sgn}[\sigma_0] + \text{sgn}[\sigma_2]$ corresponds to the Chern number of the positive frequency band $\omega > 0$. The Chern number of the negative frequency band $\omega < 0$ is exactly opposite $-C$. When $\sigma_0\sigma_2 > 0$, the photon is in a nontrivial bosonic phase $C = \pm 2$, while $\sigma_0\sigma_2 < 0$ is a trivial phase $C = 0$. In the continuum theory, trivial and nontrivial phases can only be distinguished by incorporating nonlocality $\sigma_2 \neq 0$. (b) Continuum band diagram $\omega(k)$ of the even parity $C = 2$ topological bosonic phase. The negative frequency branch has a Chern number of -2; necessary for the total summation to vanish $2 - 2 = 0$. As an example, we have let $\sigma_0 = \sigma_2 a^2 = 1$ and $\varepsilon = 2$. The unidirectional edge state is spin-1 helically quantized and touches the bulk bands precisely where the nonlocal Hall conductivity passes through zero $\sigma_H(k) = 0$. At this point $ka = (\sigma_0/\sigma_2)^{1/2}$, the edge state joins the continuum of bulk bands. Notice that no edge solution exists for $k_y \to -k_y$ and the photon is immune to backscattering.

frequency band $\omega < 0$ has a Chern number of $-C$ which is exactly opposite of the positive band. This is necessary to ensure the summation over all bands vanishes $\sum_n C_n = 0$.

3.4.6 Edge (quantum gyroelectric effect)

Finally, we analyze the unique edge state of this bosonic phase, which has no counterpart in traditional surface photonics – such as plasmon polaritons, Tamm states, Dyakonov or Zenneck waves [105]. This is because topological boundary conditions are captured by

nonlocal (spatially and temporally dispersive) optical constants. In conventional problems, nonlocality introduces additional boundary conditions (ABCs) [95], [106] which need to be satisfied to uniquely determine the electromagnetic field. Our newly discovered photonic edge state is fundamentally different in this context. The behavior of the field outside the medium $x < 0$ becomes irrelevant due to topological open boundary conditions $f(x = 0^+) = 0$ [91]–[93], [107]. Open boundary conditions are commonly encountered in topological electronics [108], [109] but is surprising when dealing with photons. To be localized at the edge, all components of the field must decay into the bulk $f(x = \infty) = 0$ as $x \to \infty$ and simultaneously disappear on the edge. The exact bulk and edge dispersion is plotted in Fig. 3.4b and a diagram of the topological edge state is displayed in Fig. 3.5(a). We strongly emphasize that these special solutions point to the first unified topological theory of Maxwell-bosons and Dirac-fermions.

The specific phase $C = \pm 2$ will determine if the unidirectional photon is forward or backward propagating; forward for $C = 2$ and backward for $C = -2$. We stress again that for either $C = \pm 2$, there is only one bosonic solution at the boundary – not two. In either case, the solution in the $x > 0$ half-space has a similar form $f_{\pm}(x, y) = f_{\pm}(x)\mathrm{e}^{ik_y y}$. Inserting into the wave equation and applying open boundary conditions, the topological edge state emerges,

$$\omega_{\pm} = \pm \frac{k_y}{\sqrt{\varepsilon}}, \qquad -\sqrt{\frac{\sigma_0}{\sigma_2}} < k_y a < \sqrt{\frac{\sigma_0}{\sigma_2}}, \tag{3.51a}$$

$$f_{\pm}(x) = \begin{bmatrix} E_x \\ E_y \\ H_z \end{bmatrix}_{\pm} = f_0(\hat{x} \mp \sqrt{\varepsilon}\hat{z})\left(\mathrm{e}^{-\eta_1 x} - \mathrm{e}^{-\eta_2 x}\right). \tag{3.51b}$$

A solution only exists in the nontrivial phase $\sigma_0 \sigma_2 > 0$, confirming our theory. Notice the group velocity $v_{\pm} = \partial \omega_{\pm}/\partial k_y = \pm 1/\sqrt{\varepsilon}$ is constant and the edge state can propagate in opposite directions depending on the phase $C = \pm 2$. Moreover, since no solution exists for $k_y \to -k_y$, the photon is immune to backscattering. The decay lengths η_1 and η_2 are found from the two quadratic roots,

$$\eta_{1,2} = \frac{1}{2a^2 |\sigma_2|}\left\{\sqrt{\varepsilon} \pm \sqrt{\varepsilon + 4\sigma_2 a^2 [\sigma_2 (k_y a)^2 - \sigma_0]}\right\}, \tag{3.52}$$

101

which determine the degree of confinement at a particular wavevector k_y. A plot of the electromagnetic energy density is presented in Fig. 3.5(c). Intriguingly, the field is completely transverse polarized $\hat{k} \cdot \mathbf{E} = E_y = 0$ and helically quantized along the direction of momentum k_y,

$$\frac{f_{\pm}^{\dagger} \hat{S}_y f_{\pm}}{f_{\pm}^{\dagger} \bar{\mathcal{M}} f_{\pm}} = v_{\pm} = \pm \frac{1}{\sqrt{\varepsilon}}. \tag{3.53}$$

$\hat{k} \cdot \mathbf{S} = \hat{S}_y$ is the spin-1 helicity operator and quantization lies in the x-y plane. Consequently, the $C = 2$ phase corresponds to a massless (linearly dispersing) "spin-up" photon while the $C = -2$ phase is a counter-propagating "spin-down" photon. Note, the edge wave is $\hat{S}_y$ helically quantized for all momenta and is distinct from transverse $\hat{S}_z$ quantization of the bulk waves, which only occurs at HSPs.

3.4.7 Anomalous displacement currents

We also discover an anomalous edge current [110] propagating parallel to the interface,

$$J_y(x, y) = \mp \sqrt{\varepsilon} f_0 (\eta_1 e^{-\eta_1 x} - \eta_2 e^{-\eta_2 x}) e^{i k_y y}. \tag{3.54}$$

The displacement current is induced by the nonlocal Hall conductivity,

$$J_y = -\partial_x H_z = -\left(\sigma_0 + \sigma_2 a^2 \nabla^2\right) E_x, \tag{3.55}$$

and is highly conductive near the interface $J_y(x = 0^+) \neq 0$. However, a compensating current is generated in the bulk $x > 0$, such that the total induced charge is identically zero $\int_{0^+}^{\infty} J_y(x) dx = H_z(0^+) - H_z(\infty) = 0$. Notice that charge neutrality is only guaranteed by the open boundary condition $H_z(x = 0^+) = 0$, providing a profound physical basis for topological protection. The photonic edge state must exist if the medium is to remain neutral – there is no other option.
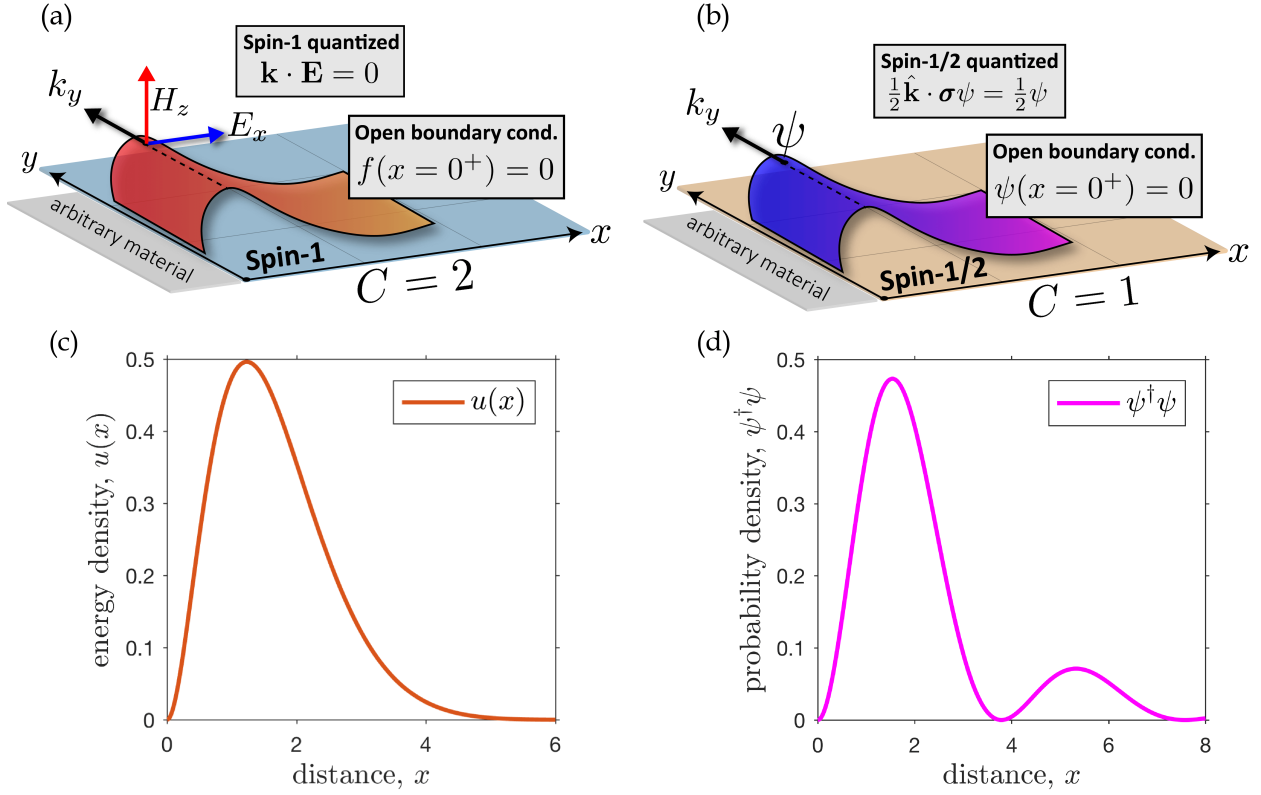
Figure 3.5. (a) Topological edge state of the even parity $C = 2$ bosonic phase. The photon is spin-1 helically quantized $\mathbf{k} \cdot \mathbf{E} = 0$ and satisfies open boundary conditions at the interface $f(x = 0^+) = 0$. This ensures the edge state is immune to boundary defects and can exist at any interface – even vacuum. (b) Topological edge state of the $C = 1$ fermionic phase. Like the photon, the electron is spin-½ helically quantized $\hat{k} \cdot \vec{\sigma}\psi = \psi$ and satisfies open boundary conditions $\psi(x = 0^+) = 0$. (c) Normalized energy density $u(x) = f^\dagger \bar{\mathcal{M}} f$ of the unidirectional photon as a function of distance x, at a momentum of $k_y = 0.5$. As an example we have let $\sigma_0 = \sigma_2 a^2 = 1$ and $\varepsilon = 2$. Notice the fields are identically zero at $x = 0$ and the edge state exists at the boundary of any interface. (d) Probability density $\psi^\dagger \psi$ of the electronic edge state, where we have let $\Lambda_0 = \Lambda_2 a^2 = 1$ and $v = 0.5$ as an example. The probability density is evaluated for a momentum of $k_y = 0.5$.

103
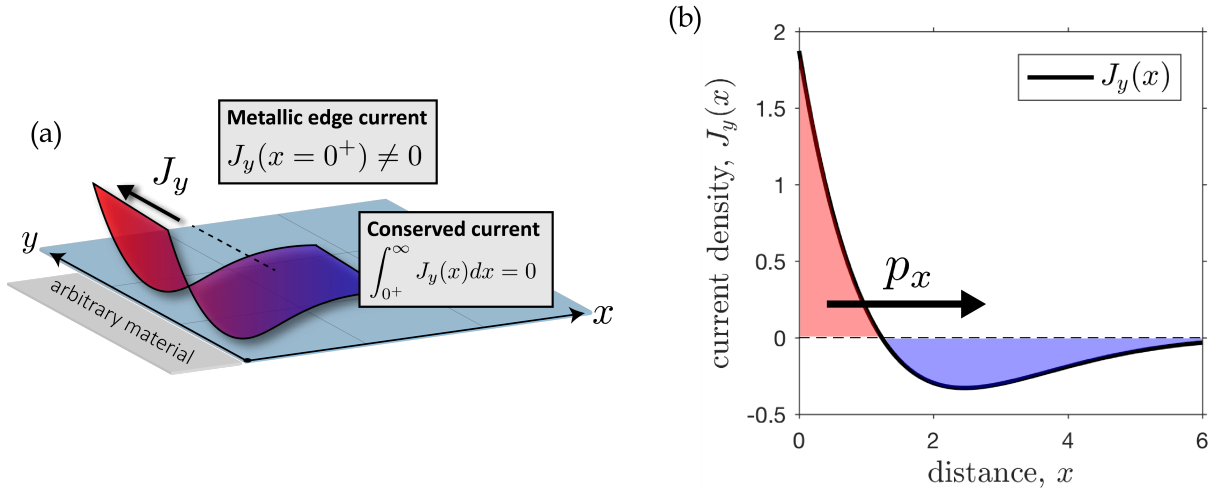
Figure 3.6. (a) Anomalous displacement current at the edge of the topological photonic medium. (b) Real current density $J_y(x)$ as a function of distance x, for a momentum of $k_y = 0.5$. We have let $\sigma_0 = \sigma_2 a^2 = 1$ and $\varepsilon = 2$ as an example. The displacement current is generated by the nonlocal Hall conductivity and is highly metallic near the interface $J_y(x = 0^+) \neq 0$. However, the total current is conserved $\int_{0^+}^{\infty} J_y(x)dx = 0$ which is clear from the positive (red) and negative (blue) charge density. Since the net charge is zero, this phenomenon can be interpreted as a propagating dipole bound to the edge of the material – with an intrinsic dipole moment $p_x = \int_{0^+}^{\infty} x\rho(x)dx$.

From the continuity equation $\omega\rho = k_y J_y$, this phenomenon can also be interpreted as a propagating dipole bound to the edge of the material,

$$p_x = \int_{0^+}^{\infty} x\rho(x)dx = -\varepsilon \int_{0^+}^{\infty} E_x(x)dx = \varepsilon f_0(\eta_1^{-1} - \eta_2^{-1}), \qquad (3.56)$$

with an intrinsic dipole moment p_x normal to the interface. The intriguing connection to the parity anomaly will be discussed in a future paper [11], [111]. The dipole is continuous $x\rho(x)$ and shields the electromagnetic field between regions of positive and negative charge density. This unusual effect allows highly confined photons to propagate at the boundary unimpeded, impervious to defects. A visualization of the anomalous current is displayed in Fig. 3.6.

3.5 Dirac-Maxwell supersymmetry: Direct correspondence between fermionic and bosonic phases

To validate our predictions of the Maxwell theory, we solve the equivalent continuum Dirac theory. These results present a unified topological field theory of Maxwell-bosons and Dirac-fermions. It also highlights the one-to-one correspondence between even parity bosonic phases $C = \pm 2$ and traditional fermionic phases $C = \pm 1$. Interestingly, the equivalent 2D Dirac theory is a supersymmetric partner of the 2D Maxwell theory [84]–[86]. The continuum Dirac Hamiltonian is given succinctly as,

$$H(\mathbf{k}) = v(k_x \sigma_x + k_y \sigma_y) + \Lambda(k)\sigma_z, \tag{3.57}$$

where σ_i are the SU(2) Pauli matrices. The dispersion relation of the positive energy state $E > 0$ is found as,

$$E^2(k) = v^2 k^2 + \Lambda^2(k), \tag{3.58}$$

and $\Lambda(k) = \Lambda_0 - \Lambda_2 (ka)^2$ is a spatially dispersive Dirac mass [91]–[93]. v being the Fermi velocity. Again, we include quadratic k dependence for proper regularization at $k \to \infty$. This direct correspondence makes our earlier claim, the necessity of nonlocality (momentum dependence), very clear.

The Hamiltonian possesses rotational symmetry, which is generated by the spin-½ operator $\hat{S}_z = \frac{1}{2}\sigma_z$. This is evidently a fermionic representation $\mathcal{R}(2\pi) = \exp[i2\pi\hat{S}_z] = -\mathbb{1}_2$. Furthermore, we can prove transverse spin-½ quantization at HSPs, $m(0) = \frac{1}{2}\mathrm{sgn}[\Lambda_0]$ and $m(\infty) = -\frac{1}{2}\mathrm{sgn}[\Lambda_2]$. This should be contrasted with our results for integer spin quantization of the 2D bosonic phase in Fig. (3.1). We obtain a Chern invariant of,

$$C = m(0) - m(\infty) = \frac{1}{2}\left(\mathrm{sgn}[\Lambda_0] + \mathrm{sgn}[\Lambda_2]\right). \tag{3.59}$$

The phase is only nontrivial $C = \pm 1$ when $\Lambda_0 \Lambda_2 > 0$, necessitating a zero in the effective mass $\Lambda(k) = 0$ – precisely at $ka = \sqrt{\Lambda_0/\Lambda_2}$. This is the simplest realization of a fermionic Chern insulator [94]. Notice that in two dimensions, the Hall conductivity σ_H for the photon plays an analogous role as the Dirac mass Λ for the electron.

The electronic edge state has a similar interpretation as the photon, but for spin-½ particles. Imposing open boundary conditions, a unidirectional edge state is revealed $\psi_\pm(x,y) = \psi_\pm(x)e^{ik_y y}$,

$$\psi_\pm(x) = \psi_0 \begin{bmatrix} 1 \\ \pm i \end{bmatrix} (e^{-\eta_1 x} - e^{-\eta_2 x}), \tag{3.60}$$

corresponding to a $C = \pm 1$ phase. The decay lengths have an identical form,

$$\eta_{1,2} = \frac{1}{2a^2|\Lambda_2|} \left\{ v \pm \sqrt{v^2 + 4\Lambda_2 a^2 [\Lambda_2(k_y a)^2 - \Lambda_0]} \right\}, \tag{3.61}$$

and the edge state is massless $E_\pm = \pm v k_y$, propagating in opposite directions depending on the phase. Furthermore, the edge state is spin-½ helically quantized $\frac{1}{2}\hat{k} \cdot \vec{\sigma}\psi_\pm = \frac{1}{2}\sigma_y\psi_\pm = \pm\frac{1}{2}\psi_\pm$, equating to a spin-up or spin-down electron for $C = 1$ or $C = -1$ respectively. The striking similarity of Maxwell-bosons and Dirac-fermions is shown in Fig. 3.5. A diagram of the electronic topological edge state is displayed in Fig. 3.5(b) and a plot of the probability density is given in Fig. 3.5(d).

3.6 Experimental search and conclusions

The standard approach of characterizing TRS broken fermionic phases is DC transport measurements (charge and spin Hall conductivity) or Faraday rotation angles at THz frequencies. It should be noted that the former measurement gives information at zero frequency and zero momentum $\sigma_H(0,0)$ whereas the latter experiment characterizes matter at finite frequency but close to zero momentum $\sigma_H(\omega,0)$. Our predictions of photon spin quantization and bosonic phases are fundamentally tied to $\sigma_H(\omega,k)$. This is a formidable challenge and therefore, for completeness, we suggest two new experimental approaches.

3.6.1 Momentum-resolved electron energy loss spectroscopy of gyrotropic plasmas

The high-frequency $\omega > 0$ and sub-wavelength $k > 0$ properties of matter can be probed by momentum-resolved electron energy loss spectroscopy (k-EELS) [112]. Here, highly energetic electrons pass through matter and their energy loss, as well as their momentum loss,

is measured to understand the bulk light-matter excitations. Fundamentally different from conventional STEM-EELS [113], this approach can also give insight into high momentum waves through scattering angle measurement of electrons passing through matter. We anticipate nonlocal gyrotropic plasmas to be ideal candidates for topological bosonic phases of matter and probing with k-EELS.

3.6.2 Cold atom near-field probes of nonlocal optical conductivity

Dynamical (high-frequency) conductivity is regularly studied by conventional tools such as ellipsometry and Faraday rotation using incident optical beams. However, the momentum carried by light waves is negligible compared to the Fermi momentum of electrons. Therefore, the large momentum $k > 0$ behavior of the conductivity requires fundamentally new probes. One approach is to use spontaneous emission from cold atoms in the near-field to investigate deep sub-wavelength response parameters of our predicted bosonic phases of matter. This is feasible since the GHz splitting in Rydberg atoms [114] and low-frequency gyrotropic response in systems such as quantum wells are comparable [76]. Recent work has shown trapping of cold atoms near photonic nanostructures [115] – a promising route for probing topological properties of matter.

3.6.3 Conclusions

In summary, we have developed the complete continuum field theory describing all 2+1D topological bosonic phases of the photon; incorporating both temporal and spatial dispersion as a necessary generalization. The topological phases are intimately connected to photon spin-1 quantization, with nonlocality being imperative to properly characterize the high-k global behavior. Two unique bosonic phases are predicted – an even parity phase $C = \pm 2$ which is understood in interacting bosonic systems, and an odd parity phase $C = \pm 1$ which has no immediate interpretation but presents possibly unexplored physics. We have studied the even parity phase $C = \pm 2$ utilizing a nonlocal Hall conductivity and reveal a single topologically protected unidirectional photon at the edge. This photon is helically quantized (spin-1), immune to backscattering, defects, and exists at the boundary of the $C = \pm 2$

bosonic phase and any interface – even vacuum. To validate our theory, we have compared all the low energy Maxwell phenomena to its supersymmetric Dirac counterpart, confirming that even parity bosonic phases $C = \pm 2$ are the exact analogue of traditional fermionic phases $C = \pm 1$.

Acknowledgements

4. PHOTONIC DIRAC MONOPOLES AND SKYRMIONS: SPIN-1 QUANTIZATION

We introduce the concept of a photonic Dirac monopole, appropriate for photonic crystals, metamaterials and 2D materials, by utilizing the Dirac-Maxwell correspondence. We start by exploring vacuum where the reciprocal momentum space of both Maxwell's equations and the massless Dirac equation (Weyl equation) possess a magnetic monopole. The critical distinction is the nature of magnetic monopole charges, which are integer valued for photons but half-integer for electrons. This inherent difference is directly tied to the spin and ultimately connects to the bosonic or fermionic behavior. We also show the presence of photonic Dirac strings, which are line singularities in the underlying Berry gauge potential. While the results in vacuum are intuitively expected, our central result is the application of this topological Dirac-Maxwell correspondence to 2D photonic (bosonic) materials, as opposed to conventional electronic (fermionic) materials. Intriguingly, within dispersive matter, the presence of photonic Dirac monopoles is captured by nonlocal quantum Hall conductivity – i.e. a spatiotemporally dispersive gyroelectric constant. For both 2D photonic and electronic media, the nontrivial topological phases emerge in the context of massive particles with broken time-reversal symmetry. However, the bulk dynamics of these bosonic and fermionic Chern insulators are characterized by spin-1 and spin-½ skyrmions in momentum space, which have fundamentally different interpretations. This is exemplified by their contrasting spin-1 and spin-½ helically quantized edge states. Our work sheds light on the recently proposed quantum gyroelectric phase of matter and the essential role of photon spin quantization in topological bosonic phases.

4.1 Introduction

Dirac's pioneering paper [8] showed that if magnetic monopoles are found in nature, their magnetic charges Q would be quantized in units of the elementary charge e of the electron,

$$2\frac{eQ}{h} \in \mathbb{Z}. \tag{4.1}$$

h being the Planck constant. This is the earliest example of topological quantization – fundamentally different from second quantization arising in quantum field theories. Although there exists no experimental proof of magnetic monopoles [117] to date, there is ample evidence of quantized topological charges in reciprocal (energy-momentum) space. Specifically, the appearance of such monopoles in the band structure of solids indicates the presence of quantized topological invariants, like the Chern number [7] and $\mathbb{Z}_2$ index [118]. Ultimately, experimental observables such as the quantum Hall conductivity can be traced back to the existence of this quantized topological charge [5], [119].

There have been significant efforts to construct synthetic gauge potentials that mimic these monopole physics in cold atoms [120] and spin ice [121]. One striking example is the realization of non-Abelian gauge theories with Yang-Lee monopoles [122]. The topological field theory of light has surfaced in knotted solutions of Maxwell's equations [79], [123], as well as the uncertainty relations for photons [124]. Along side this, there have been important recent developments to formulate topological properties for photons utilizing photonic crystals and metamaterials [18]–[20], [51], [52], [64], [74], [125]–[130]. The pioneering work in topological photonic crystals has shown the existence of edge states robust to disorder. In the previously explored scenarios, the photonic crystal unit cell is carefully structured to obtain an additional degree of freedom (artificial gauge field) – quite often realized on a graphene-like honeycomb lattice. This approach was first implemented by Haldane for spinless (scalar) electrons in his seminal paper on the parity anomaly [11]. However, it remains an open question whether robust topological photonic edge states can occur in atomic matter. The role of photon spin and its quantization is yet another unresolved problem since previous theories have focused exclusively on pseudo-spin-½ phenomena [131]–[134].

Our spin-1 theory [135] is fundamentally different in this respect since we do not ignore the polarization (spin) state of the photon, which cannot be neglected for a real gauge (vector) field. In our case, the topological theory is manifestly bosonic as it is connected to the winding of the gauge field itself – not pseudo-spin degrees of freedom. Another fundamental aspect of our theory is the inclusion of dispersion within matter, i.e. frequency and momentum dependence of conductivity, such that topological invariants emerge naturally from the global behavior of optical constants. For example, it has been shown that nonlocal gyrotropic [54] and magnetoelectric [63] media will host massless spin-1 quantized edge states with massive-like photons in the bulk. Thus, it is necessary to understand the concept of bosonic Dirac monopoles and the influence of integer spin in topological photonic phases of matter.

In this paper, we elucidate the fundamental difference between the magnetic monopoles appearing in Maxwell's equations and the Dirac equation. Our work shows that a magnetic monopole appears for both photons and massless fermions in the reciprocal energy-momentum space – even for vacuum. Using a Dirac-Maxwell correspondence, we identify the bosonic and fermionic nature of magnetic monopole charge, which is inherently present in the relativistic theories of both particles. While the results in vacuum are expected, we apply this topological theory to 2D photonic (bosonic) materials, in contrast to conventional electronic (fermionic) materials. The specific 2D photonic materials considered in this paper are gyroelectric which possess antisymmetric components of the conductivity tensor. We exploit the Dirac-Maxwell correspondence to show how dispersive gyroelectric media can support topologically massive particles, which are interpreted as photonic skyrmions. However, the differences in spin between bosons and fermions alter the behavior of these bulk skyrmions as well as their corresponding Chern numbers. We then analyze the unique topological edge states associated with nontrivial spin-1 and spin-½ skyrmions, which exhibit opposing helical quantization. This clearly shows how the integer and half-integer nature of monopoles is ultimately tied to the differing bosonic and fermionic spin symmetries. Our work sheds light on the recently proposed quantum gyroelectric phase of matter [54] which supports unidirectional transverse electro-magnetic (TEM) edge states with open boundary conditions (vanishing fields at the edge) – unlike any known phase of matter till date.

In the context of geometric phases, the concept of magnetic charges has a rich history starting from the pioneering works of Pancharatam, Berry, Chiao and Wu [136]. Unification of these geometric phases for bosons and fermions was shown for massive 3D particles using a relativistic quantum field theory [78]. In this paper, our focus is massless 3D particles and topologically massive 2D particles [137]–[139], as well as the direct demonstration of gauge discontinuities in Maxwell's and Weyl's equations. Our derivation does not utilize quantum field theoretic techniques and appeals only to the spin representation of the two particles. We note that spin quantization is fundamentally different from topological charges encountered in real space for OAM beams [81], [140], polarization singularities [141] and polarization vortices [142]. This is due to the central concept of gauge discontinuity in magnetic monopole quantization, which is related to the topological field theory of bosons and fermions. We function in momentum space of Maxwell's equations as opposed to real space so our work is specifically suited to develop topological invariants in the band structure of photonic crystals and wave dispersion within metamaterials [143], [144]. One important application of our current technique is in uncovering unique electromagnetic phases of matter displaying the quantum gyroelectric effect (QGEE) [54]. Our unified perspective also sheds light on recent developments of quantized bosonic Hall conductivity [58]–[60], [145] and topological bosonic phases of matter [57], [62], as opposed to fermionic phases [17].

Skyrmions have a storied past in condensed matter – appearing in both real and momentum space of topological systems. In real space, these localized topological defects were first discovered in chiral magnets and quantum Hall ferromagnets but have also been observed in Bose-Einstein condensates and superconductors [146]. The behavior of these magnetic skyrmions is intimately tied to the Dzyaloshinskii-Moriya (DM) interaction [147] which generates the nontrivial winding of the spin structure. In momentum space, skyrmions often characterize the monopoles arising in the band structure of solids and are emergent phenomena in topological insulators and superconductors [94]. By contrast, photonic skyrmions are a very recent field of interest. A classical optical analog of skyrmion-like behavior has been reported using surface plasmon polaritons [148]. This work focuses on photonic skyrmions in momentum space which ultimately govern the equations of motion of a topological elec-

tromagnetic field. The physics of these topological fields manifest in nontrivial windings of a spin-1 vector as opposed to a spin-½ vector.

Note: The manuscript theme is the Dirac-Maxwell correspondence which directly compares bosonic and fermionic topological field theories. Throughout, the subscript $s = 1$ stands for spin-1 photons and the subscript $s = 1/2$ denotes spin-½ electrons.

4.2 Three dimensions: massless particles

4.2.1 Dirac-Maxwell correspondence

The correspondence between Dirac's and Maxwell's equations is best expressed in the Riemann-Silberstein (R-S) basis [149], [150], which utilizes a vector wave function for light. Using this representation, we develop a topological field theory of the vacuum photon. In the R-S basis, we combine the electric $\vec{\mathcal{E}}$ and magnetic $\vec{\mathcal{H}}$ fields into a complex superposition,

$$\vec{\Psi} = \frac{1}{\sqrt{2}}(\vec{\mathcal{E}} + i\vec{\mathcal{H}}), \tag{4.2}$$

where $i = \sqrt{-1}$ is the imaginary unit and the electromagnetic fields are associated with plane waves. We strongly emphasize that relativity requires vectorial representations for spin-1 bosonic fields and spinor-½ representations for fermionic fields. Spin-0 particles constitute scalar fields while spin-2 particles, such as gravitons, are described by tensor fields. Therefore, to unravel the topological bosonic properties of light, we cannot work in a restricted subspace ignoring components of the electromagnetic field. Simultaneously, we do not describe polarizations separately. In the R-S basis, Maxwell's equations in vacuum can be combined into a first-order wave problem as follows,

$$i\vec{k} \times \vec{\Psi} = H_1\vec{\Psi} = \omega\vec{\Psi}, \tag{4.3}$$

which we label as spin $s = 1$. Here, ω is the frequency of light and we consider dynamical fields over all frequencies and wave vectors, not simple static fields. We can thus unambiguously identify a Hamiltonian for light,

$$H_1(\vec{k}) = \vec{k} \cdot \vec{S} = k_x S_x + k_y S_y + k_z S_z. \tag{4.4}$$

$\vec{k} = (k_x, k_y, k_z)$ is the momentum of the plane wave in vacuum and $\vec{S} = (S_x, S_y, S_z)$ are the set of SO(3) antisymmetric matrices,

$$S_x = \begin{bmatrix} 0 & 0 & 0 \\ 0 & 0 & -i \\ 0 & i & 0 \end{bmatrix}, \qquad S_y = \begin{bmatrix} 0 & 0 & i \\ 0 & 0 & 0 \\ -i & 0 & 0 \end{bmatrix}, \qquad S_z = \begin{bmatrix} 0 & -i & 0 \\ i & 0 & 0 \\ 0 & 0 & 0 \end{bmatrix}. \tag{4.5}$$

These operators obey the familiar Lie algebra $[S_i, S_j] = i\epsilon_{ijk} S_k$ which encode information about integer spin. Notice our photonic Hamiltonian $H_1 = \vec{k} \cdot \vec{S}$ represents optical helicity, i.e. the projection of spin $\vec{S}$ along the direction of momentum $\vec{k}$. This is further clarified on direct comparison with massless Dirac fermions (Weyl fermions), which are the supersymmetric partners of the massless photon [151]. The Weyl equation is expressed as,

$$H_{1/2} \psi = E \psi, \tag{4.6}$$

where the massless Dirac Hamiltonian $H_{1/2}$, corresponding to spin $s = 1/2$, is identified with electronic helicity,

$$H_{1/2}(\vec{k}) = \vec{k} \cdot \vec{\sigma} = k_x \sigma_x + k_y \sigma_y + k_z \sigma_z. \tag{4.7}$$

$\vec{\sigma} = (\sigma_x, \sigma_y, \sigma_z)$ are the Pauli matrices of SU(2) and obey the identical Lie algebra $[\sigma_i, \sigma_j] = 2i\epsilon_{ijk}\sigma_k$,

$$\sigma_x = \begin{bmatrix} 0 & 1 \\ 1 & 0 \end{bmatrix}, \qquad \sigma_y = \begin{bmatrix} 0 & -i \\ i & 0 \end{bmatrix}, \qquad \sigma_z = \begin{bmatrix} 1 & 0 \\ 0 & -1 \end{bmatrix}. \tag{4.8}$$

Both particles are massless and satisfy an analogous helicity equation. However, the critical difference is revealed in the group operations of the particular particle; encapsulated by the

114

SO(3) antisymmetric matrices for the spin-1 photon [Eq. (4.5)] and the SU(2) Pauli matrices for the spin-½ Weyl fermion [Eq. (4.8)].

4.2.2 Helical eigenstates

We now solve for the eigenstates of the above Hamiltonians. As expected, Maxwell and Weyls' equations possess two helical degrees of freedom. For the photon [Eq. (4.4)], these are conventional right- and left-handed circular polarization,

$$H_1 \vec{e}_\pm = \pm k \ \vec{e}_\pm, \qquad \vec{e}_\pm(\vec{k}) = \frac{1}{\sqrt{2}}(\hat{\theta} \pm \mathrm{i}\hat{\phi}), \tag{4.9}$$

where θ and ϕ are the spherical polar coordinates of $\vec{k}$ and $k = |\vec{k}|$ is the magnitude of the wave vector. The photon is massless and therefore linearly dispersing in vacuum $\omega_\pm = \pm k$. Similarly, the eigenstates of the Weyl equation [Eq. (4.7)] are comprised of two massless helical spinors, which are represented as,

$$H_{1/2} \psi_\pm = \pm k \ \psi_\pm, \qquad \psi_+(\vec{k}) = \begin{bmatrix} \cos(\theta/2) \\ \sin(\theta/2)\mathrm{e}^{\mathrm{i}\phi} \end{bmatrix}, \qquad \psi_-(\vec{k}) = \begin{bmatrix} \sin(\theta/2) \\ -\cos(\theta/2)\mathrm{e}^{\mathrm{i}\phi} \end{bmatrix}. \tag{4.10}$$

Indeed, these states are also linearly dispersing $E_\pm = \pm k$. An important observation can be made in $\vec{e}_\pm$ and $\psi_\pm$. The eigenstates are ill-defined at the origin of the momentum space $\vec{k} = 0$, since they are arbitrarily dependent on θ and ϕ at this point. In fact, by parameterizing θ as the inclination from k_z, the eigenstates are not well-behaved at the north $\theta = 0$ or south $\theta = \pi$ poles either – they are multivalued at both points. Such discontinuous behavior is impossible to remove and results from choosing a particular gauge for the eigenstates. This is the underlying source for Dirac monopoles and strings. The linear dispersion (light cone) of the massless helical states is displayed in Fig. 4.1(a).

4.2.3 Spin quantization in photonic Dirac monopoles and strings

In vacuum $\vec{k}$-space, we discover a magnetic Dirac monopole for both Maxwell's and Weyl's equations but with intrinsic differences. This is demonstrated by first defining the magnetic
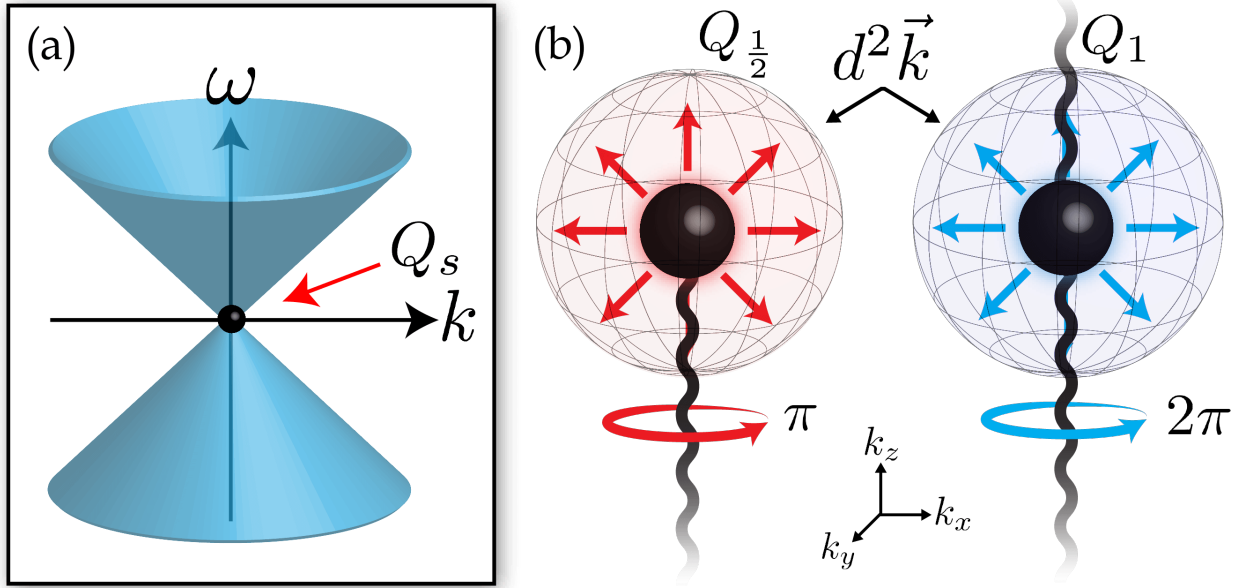
Figure 4.1. (a) Linear dispersion (light cone) of the 3D massless photon and electron $\omega_\pm = E_\pm = \pm k$. At the origin of the momentum space $\vec{k} = 0$ sits a magnetic monopole with quantized charge. This singularity is often called a Weyl point and is quantized to the spin of the particle $Q_s = s$. Integer and half-integer spin quantization is connected to bosonic and fermionic statistics respectively. (b) Dirac monopoles (Berry curvature) $\vec{F}_s = \vec{\nabla}_k \times \vec{A}_s$ of the massless electron $Q_{1/2} = {}^1/_2$ and photon $Q_1 = 1$ in momentum space. The monopole charge acts as a source for the magnetic field $\vec{\nabla}_k \cdot \vec{F}_s = 4\pi Q_s \delta^3(\vec{k})$ and arises due to the discontinuous behavior in the spin eigenstates. Notice that the flux through any surface enclosing the monopole is necessarily quantized $Q_s = (4\pi)^{-1} \oiint \vec{F}_s \cdot d^2\vec{k}$. This monopole is accompanied by a string of singularities in the underlying gauge potential $\vec{A}_s$. Any closed path around the equator of the string produces a quantized Berry phase $\gamma_s = \oint \vec{A}_s \cdot d\vec{k} = 2\pi Q_s$. The accumulated phase in $\vec{k}$-space is fundamentally tied to the spin of the particle $\mathcal{R}_s(2\pi) = \exp(i\gamma_s) = (-1)^{2s}$.

flux in momentum space – i.e. the Berry curvature. For the photon, the Berry curvature of either right- or left-handed helicity can be found from the circular eigenstates derived in Eq. (4.9),

$$\vec{F}_1^{\pm} = -i\vec{\nabla}_k \times [\vec{e}_{\pm}^* \cdot (\vec{\nabla}_k \, \vec{e}_{\pm})]. \tag{4.11}$$

For the massless electron, the analogous Berry curvature is found by evaluating the spinor eigenstates in Eq. (4.10),

$$\vec{F}_{1/2}^{\pm} = -i\vec{\nabla}_k \times [\psi_{\pm}^{\dagger} \vec{\nabla}_k \, \psi_{\pm}]. \tag{4.12}$$

Here, $\vec{\nabla}_k = \sum_i \hat{i}\partial_{k_i}$ is the gradient operator in 3D momentum space. Note that the Berry curvature is a vector in three dimensions but a scalar in two dimensions. On evaluating the Berry curvature for both particles with positive and negative helicities ($\pm$), we find that $\vec{F}_s^{\pm} = \pm\vec{F}_s$ possesses a Dirac monopole,

$$\vec{F}_s = Q_s \vec{F}. \tag{4.13}$$

$\vec{F}$ being the magnetic field of a Dirac monopole in $\vec{k}$-space,

$$\vec{F}(\vec{k}) = \frac{\vec{k}}{k^3}. \tag{4.14}$$

Note that Q_s in Eq. (4.13) is the topological magnetic charge which generates the magnetic field. This quantity is fundamentally different for the two particles,

$$Q_s = s. \tag{4.15}$$

s is precisely the spin of the particle, which takes integer $s = 1$ or half-integer $s = 1/2$ values for bosons or fermions respectively. We emphasize that the magnetic monopole charge is naturally quantized,

$$Q_s = \frac{1}{4\pi} \oiint \vec{F}_s \cdot d^2\vec{k}. \tag{4.16}$$

The charge is located at the origin $\vec{k} = 0$ of the momentum space, exactly where the eigenstates are ill-defined, and acts as a source for the magnetic field $\vec{\nabla}_k \cdot \vec{F}_s = 4\pi Q_s \delta^3(\vec{k})$. Notice that the magnetic monopole charge of the photon,

$$Q_1 = 2Q_{1/2} = 1, \tag{4.17}$$

is exactly twice the electron due to integer spin. The monopole charge for each helicity has opposite signs $Q_s^\pm = \pm Q_s$. This ensures the net charge vanishes $Q_s^+ + Q_s^- = 0$ at the origin $\vec{k} = 0$; as expected due to time-reversal symmetry in vacuum [152]. A visualization of the magnetic flux is shown in Fig. 4.1(b).

We note that the photonic Dirac monopole is accompanied by a string of singularities in the underlying gauge potential. This Dirac string is unobservable as it is a gauge dependent phenomenon but sheds light on the fundamental differences between electrons and photons. The Berry gauge potential for the massless photon and electron can be evaluated using the eigenstates in Eq. (4.9) and (4.10) respectively,

$$\vec{A}_1^\pm = -i\vec{e}_\pm^* \cdot (\vec{\nabla}_k \ \vec{e}_\pm), \qquad \vec{A}_{1/2}^\pm = -i\psi_\pm^\dagger \vec{\nabla}_k \ \psi_\pm. \tag{4.18}$$

Upon solving for $\vec{A}_s^\pm = \pm\vec{A}_s$, we again find a clear dependence on the magnetic monopole charge Q_s which is different for bosons and fermions,

$$\vec{A}_s(\vec{k}) = Q_s \frac{1 - \cos\theta}{k\sin\theta}\hat{\phi}, \tag{4.19}$$

and $\vec{F}_s = \vec{\nabla}_k \times \vec{A}_s$ reproduces the Berry curvature in Eq. (4.13). The gauge potential is singular along the k_z-axis, at $\theta = 0$ and π, where the eigenstates are multivalued. This line singularity that originates at the monopole and extends to infinity is known as a Dirac string. Fig. 4.1(b) displays a visualization of the Dirac monopole and strings for both massless particles. We note that the above equations are traditionally found in the theory of magnetic charges in real space [117] – not momentum space. Following this, quantization of magnetic charge naturally emerges from the requirement of a single-valued wave function in the presence of singular (multivalued) gauge potentials. Our rigorous derivation is unique as

118

it unifies the momentum space of Maxwell's equations and the Weyl equation. This makes it ideally suited for extension to topological theories of band structure in photonic crystals and wave dispersion in metamaterials.

4.2.4 Berry phase

We now provide a detailed comparison of $\vec{k}$-space Pancharatnam-Berry phase (hereon called geometric phase) for photons and electrons [9], [153], that arises from their corresponding spin properties. The geometric phase calculated for any closed path on the $\vec{k}$-sphere is gauge invariant,

$$\gamma_s = \oint \vec{A}_s \cdot d\vec{k} = \iint \vec{F}_s \cdot d^2\vec{k}. \qquad (4.20)$$

γ_s is the geometric phase and is equivalent to the flux of Berry curvature $\vec{F}_s$ through a surface bounded by the path. In this case, we see that $\iint \vec{F}_s \cdot d^2\vec{k} = Q_s \iint d\Omega$ is exactly the solid angle $\Omega(C)$ traced along the $\vec{k}$-sphere,

$$\gamma_s = Q_s \Omega(C), \qquad (4.21)$$

where C designates the bounded path. We now consider a closed path around a great circle of the $\vec{k}$-sphere (eg: the equatorial path $k_z = 0$), which encloses the monopole. For massless particles, this is equivalent to rotating the fields back into themselves. The accumulated phase must be quantized,

$$\gamma_s = 2\pi Q_s. \qquad (4.22)$$

This is the momentum space manifestation of Dirac's quantization condition $2Q_s \in \mathbb{Z}$ which ensures the massless particles acquire the same phase under a 2π or -2π rotation. We clearly see that geometric phases in $\vec{k}$-space are dependent on the spin of the particle,

$$\exp(i\gamma_s) = (-1)^{2Q_s}. \qquad (4.23)$$

Notice that $\exp\left(i\gamma_{1/2}\right) = -1$ and $\exp\left(i\gamma_1\right) = +1$ are antisymmetric or symmetric under a $\pm 2\pi$ rotation depending on the spin $Q_s = s$. Ultimately, the geometric phase of $\gamma_{1/2} = \pi$

or $\gamma_1 = 2\pi$ is tied to the fermionic or bosonic statistics of the particle. We note that this geometric phase $\gamma_{1/2} = \pi$ is routinely encountered for massless Dirac fermions in graphene [154], [155]. However, the direct correspondence with spin-1 massless photons $\gamma_1 = 2\pi$ has not been pointed out to date. Our results suggest that a thin wire supporting Dirac fermions would yield Chiao-Tomita phases [156] exactly half the value of photons. We also note that spin-momentum locking is a universal property in photonics [26], [83], [157] which arises entirely from the transversality $\vec{k} \cdot \vec{\Psi} = 0$ of electromagnetic waves in vacuum. This phenomenon can be explained with causal boundary conditions on evanescent fields and does not necessarily require topological considerations [158]. For example, conventional surface plasmon polaritons (SPPs) and waveguide modes show spin-momentum locking but these are not related to any topologically protected edge states or nontrivial phases.

4.2.5 Rotational symmetries

The nuance behind integer and half-integer geometric phases [Eq. (4.22)] is explained more rigorously by considering the operations of the rotational (spin) groups. Maxwell's equations [Eq. (4.3)] transform under the SO(3) group $\mathcal{R}_1(\alpha) = \exp\left(i\alpha\hat{n} \cdot \vec{S}\right)$, where α is the angle subtended about an axis $\hat{n}$. This is true for all vector fields. Conversely, the Weyl equation [Eq. (4.6)] transforms under the SU(2) group $\mathcal{R}_{1/2}(\alpha) = \exp\left(i\alpha\hat{n} \cdot \vec{\sigma}/2\right)$, characteristic of spinors. Although SO(3) and SU(2) obey the same Lie algebra, the group representations are inequivalent. The distinction is evident under a cyclic rotation,

$$\mathcal{R}_s(2\pi) = (-1)^{2s}. \tag{4.24}$$

Notice that the accumulated phase is different depending on the particle species. This is due to the fact that fermions are antisymmetric $\mathcal{R}_{1/2}(2\pi) = -1$ under rotations, while bosons are symmetric $\mathcal{R}_1(2\pi) = +1$ and this behavior is guaranteed by the spin-statistics theorem [159]. The difference fundamentally changes the interpretation of fermionic and bosonic topologies [160].

4.3 Two dimensions: topologically massive particles

4.3.1 Dirac-Maxwell correspondence

Up to this point, we have only considered the 3D dynamics of the vacuum photon and its analogies with the Weyl fermion. Now we shift to the 2D domain to harness these topological properties and elucidate the fundamental role of spin in nontrivial phases of matter. Nontrivial 2D materials are characterized by an integer topological invariant – the Chern number $C \in \mathbb{Z}$. In electronics, these materials are often called Chern insulators [13] because they are insulating in the bulk but host metallic one-way edge states that are robust to disorder. In the long wavelength limit $k \approx 0$, the simplest fermionic Chern insulator is described by the 2D Dirac equation [94],

$$\mathcal{H}_{1/2}\psi = E\psi, \qquad \mathcal{H}_{1/2}(\mathbf{k}) = v(k_x\sigma_x + k_y\sigma_y) + \Lambda(k)\sigma_z. \tag{4.25}$$

Equation (4.25) is essentially identical to the Weyl equation [Eq. (4.7)] except we have replaced the z-component of the momentum with a Dirac mass $k_z \to \Lambda(k)$. We have also introduced the Fermi velocity v to characterize the effective speed of electrons within the material. It is easy to check that $\Lambda(k)$ breaks time-reversal symmetry but preserves rotational symmetry about the z-axis, $\mathcal{R}_{1/2}(\alpha) = \exp(i\alpha\sigma_z/2)$. The meat of the topological physics lies in this spatially dispersive Dirac mass [93],

$$\Lambda(k) = \Lambda_0 - \Lambda_2 k^2. \tag{4.26}$$

$\Lambda_0 = \Lambda(0)$ opens a band gap and Λ_2 accounts for the curvature of the energy bands. Importantly, when $\Lambda_0\Lambda_2 > 0$ there is so-called band inversion [161] and the effective mass changes sign within the dispersion $\Lambda(k) = 0$, precisely at $k = \sqrt{\Lambda_0/\Lambda_2}$. The quadratic momentum dependence $k^2 = \mathbf{k}\cdot\mathbf{k}$ is also crucial to regularize the long wavelength theory [15], [54]. This means we can project the planar momentum space onto the surface of the Riemann sphere $\mathbb{R}^2 \simeq S^2$, a necessary constraint for continuum topological field theories.

121

We now study the equivalent 2D dynamics of the photon – the bosonic Chern insulator. As anticipated, the 2D Maxwell theory is the supersymmetric partner of the 2D Dirac theory [54], [84] and takes an analogous form,

$$\mathcal{H}_1 \vec{\Psi} = \omega \vec{\Psi}, \qquad \mathcal{H}_1(\mathbf{k}) = v(k_x S_x + k_y S_y) + \Lambda(k) S_z. \tag{4.27}$$

Equation (4.27) is formally equivalent to the 3D Maxwell equation [Eq. (4.4)] with the substitution of a mass term $k_z \to \Lambda(k)$. Here, $v = 1/\sqrt{\varepsilon}$ is the effective speed of light which is governed by the dielectric permittivity $\varepsilon > 1$. Like the Dirac equation [Eq. (4.25)], time-reversal symmetry is broken but rotational symmetry is preserved about the z-axis, $\mathcal{R}_1(\alpha) = \exp(i\alpha S_z)$. There is one caveat however; the photonic wave function $\vec{\Psi}$ is slightly altered since we only retain transverse-magnetic (TM) waves in two dimensions,

$$\vec{\Psi} = \frac{1}{\sqrt{2}} \left(\sqrt{\varepsilon} E_x, \sqrt{\varepsilon} E_y, i H_z \right) = \frac{1}{\sqrt{2}} \left(\sqrt{\varepsilon} \mathbf{E}, i H_z \right). \tag{4.28}$$

The transverse-electric (TE) component cannot couple to a 2D material as all electrical currents lie in the x-y plane. Nevertheless, the underlying topological physics remain unchanged.

4.3.2 Dispersive transverse conductivity

Our central result is that the above mentioned Maxwell Hamiltonian can possess a mass term arising from dispersion of optical constants. Still, one might question the seemingly ad hoc insertion of a photonic mass $\Lambda(k)$ for two reasons: 1. *Are Maxwell's equations still gauge invariant?* 2. *Does this mass have any physical origin?* The answer is *yes* to both [84], [85]. In fact, it is nothing but the Hall conductivity [2],

$$\varepsilon \Lambda(k) = \sigma_H(k) = \sigma_0 - \sigma_2 k^2. \tag{4.29}$$

Remarkably, our result shows that the Hall conductivity for 2D photons plays the exact same role as the Dirac mass for 2D electrons. We note that the Hall conductivity is related to the anti-symmetric components of the conductivity tensor. $\sigma_0 = \sigma_H(0)$ is the conventional
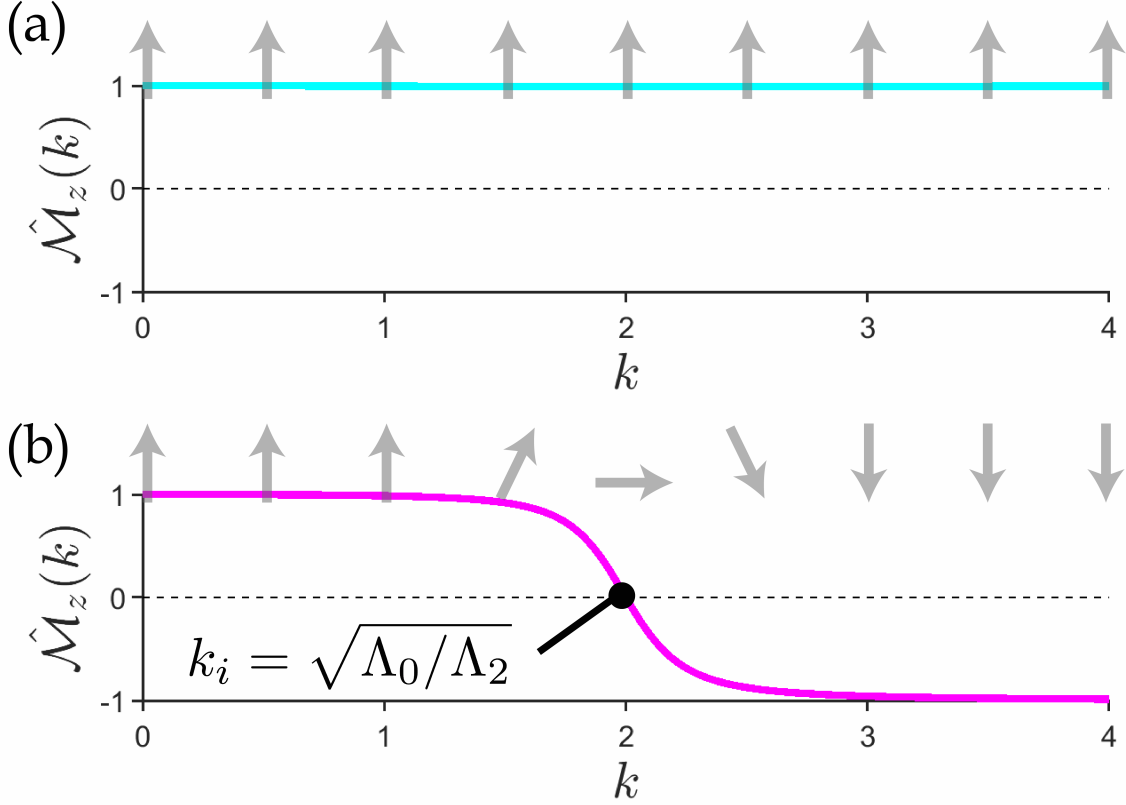
Figure 4.2. Spin expectation value $\hat{\mathcal{M}}_z(k)$ as a function of k. (a) $N = 0$ skyrmion with no band inversion $\Lambda_0\Lambda_2 < 0$. The spin returns to initial state $\hat{\mathcal{M}}_z(0) = \hat{\mathcal{M}}_z(\infty)$ and the total winding is trivial. (b) $N = 1$ skyrmion with band inversion $\Lambda_0\Lambda_2 > 0$. In this case, the spin flips direction $\hat{\mathcal{M}}_z(0) \neq \hat{\mathcal{M}}_z(\infty)$ and the total winding is nontrivial.

static (DC) component which opens a band gap in the vacuum dispersion. This property of low energy bandgap is fundamentally similar to the role of the Dirac mass for fermions. σ_2 is the nonlocal (momentum dependent) correction to σ_H which dictates the curvature of the photonic bands. Until very recently, the momentum dependence of σ_H had never been considered for topological purposes [54]. This type of behavior can also be generalized to its high-frequency (AC) equivalent in the context of nonlocal gyrotropy, but we restrict ourselves to the low-energy limit $\omega \approx 0$ for simplicity. In this limit, nonlocal Hall conductivity defines the quantum gyroelectric phase of matter.

4.3.3 Spin-1 photonic skyrmions

The electronic [Eq. (4.25)] and photonic [Eq. (4.27)] Hamiltonians can be written in a more suggestive form by introducing the skyrmion spin vector $\vec{\mathcal{M}} = (\mathcal{M}_x, \mathcal{M}_y, \mathcal{M}_z)$,

$$\mathcal{H}_1 = \vec{\mathcal{M}} \cdot \vec{S}, \qquad \mathcal{H}_{1/2} = \vec{\mathcal{M}} \cdot \vec{\sigma}. \tag{4.30}$$

As we can see, this new vector $\vec{\mathcal{M}}$ has replaced the original 3D wave vector $\vec{k}$ in the massless equations and closely resembles the Zeeman interaction [146]. Indeed, the spin precesses about an axis formed by $\vec{\mathcal{M}}$,

$$\dot{\vec{S}} = -\mathrm{i}[\vec{S}, \mathcal{H}_1] = g_1 \vec{\mathcal{M}} \times \vec{S}. \tag{4.31}$$

It is important to reiterate that $\vec{S}$ represents spin-1 operators while $\vec{\sigma}$ is spin-½. This is exemplified by the fact that bosonic (vector) particles possess gyromagnetic g-factors of $g_1 = (Q_1)^{-1} = 1$, while fermionic (spinor) particles have g-factors of $g_{1/2} = (Q_{1/2})^{-1} = 2$,

$$\dot{\vec{\sigma}} = -\mathrm{i}[\vec{\sigma}, \mathcal{H}_{1/2}] = g_{1/2} \vec{\mathcal{M}} \times \vec{\sigma}. \tag{4.32}$$

The Larmor frequency Ω_s is fundamentally different between the two. The skyrmions precess at different rates depending on the spin representation,

$$\Omega_s = g_s \mathcal{M}, \qquad g_s = (Q_s)^{-1}, \tag{4.33}$$

where $\mathcal{M} = |\vec{\mathcal{M}}|$ is the magnitude of the skyrmion vector.

Note though, the skyrmion vector $\vec{\mathcal{M}}(\mathbf{k})$ is a function of a 2D momentum $\mathbf{k}$ and actually describes a parametric surface $\vec{\mathcal{M}}(\mathbf{k}) = (vk_x, vk_y, \Lambda(k)) = (v\mathbf{k}, \Lambda(k))$. The eigenstates assume an identical form with the substitution of $\vec{k} \to \vec{\mathcal{M}}$,

$$\mathcal{H}_1 \vec{e}_\pm = \pm \mathcal{M} \, \vec{e}_\pm, \qquad \mathcal{H}_{1/2} \psi_\pm = \pm \mathcal{M} \, \psi_\pm. \tag{4.34}$$

$\vec{e}_\pm$ are the right- and left-handed helical eigenstates derived in Eq. (4.9) and $\psi_\pm$ are the equivalent spinors in Eq. (4.10). The dispersion relation for each of the eigenstates reads,

$$\omega_\pm(k) = E_\pm(k) = \pm\mathcal{M}(k) = \pm\sqrt{v^2 k^2 + \Lambda^2(k)}, \qquad (4.35)$$

which are clearly gapped since $\mathcal{M}(0) = |\Lambda_0|$. These states have acquired mass in 2D. The critical difference of these new eigenstates is that the polar coordinate θ no longer parametrizes the inclination from k_z. Instead, it is governed by the spatially dispersive mass $\tan\theta(k) = vk/\Lambda(k)$, which is a function of the in-plane momentum $\mathbf{k}$. We can understand this phenomenon more clearly by evaluating the spin expectation value along the $\hat{z}$ direction,

$$\langle S_z \rangle_\pm = \vec{e}_\pm^* \cdot S_z \vec{e}_\pm = \pm Q_1 \hat{\mathcal{M}}_z, \qquad (4.36)$$

where $\hat{\mathcal{M}}_z(k) = \Lambda(k)/\mathcal{M}(k) = \cos\theta(k)$ is a normalized vector. Notice the spin comes in units of bosonic charge $Q_1 = 1$, as we would expect for an integer particle $s = 1$. Analogously, the half-integer skyrmion $s = 1/2$ arises in units of fermionic charge $Q_{1/2} = 1/2$,

$$\langle \sigma_z/2 \rangle_\pm = \psi_\pm^\dagger (\sigma_z/2)\psi_\pm = \pm Q_{1/2}\hat{\mathcal{M}}_z. \qquad (4.37)$$

At $k = 0$, the spin points directly along $\hat{\mathcal{M}}_z(0) = \text{sgn}[\Lambda_0]$. However, as the momentum increases, $\vec{\mathcal{M}}$ tilts away from the z-axis and in some cases can flip directions entirely $\hat{\mathcal{M}}_z(\infty) = -\text{sgn}[\Lambda_2]$. This is a nontrivial topology. A depiction of trivial and nontrivial $\hat{\mathcal{M}}_z(k)$ as a function of k is presented in Fig. 4.2.

An aside: the zero helicity (longitudinal) state

For completeness, there is technically one additional eigenstate associated with the photonic Hamiltonian [Eq. (4.27)] – the zero helicity (longitudinal) state,

$$\mathcal{H}_1 \vec{e}_0 = 0, \qquad \vec{e}_0 = \hat{\mathcal{M}} = \vec{\mathcal{M}}/\mathcal{M}. \qquad (4.38)$$
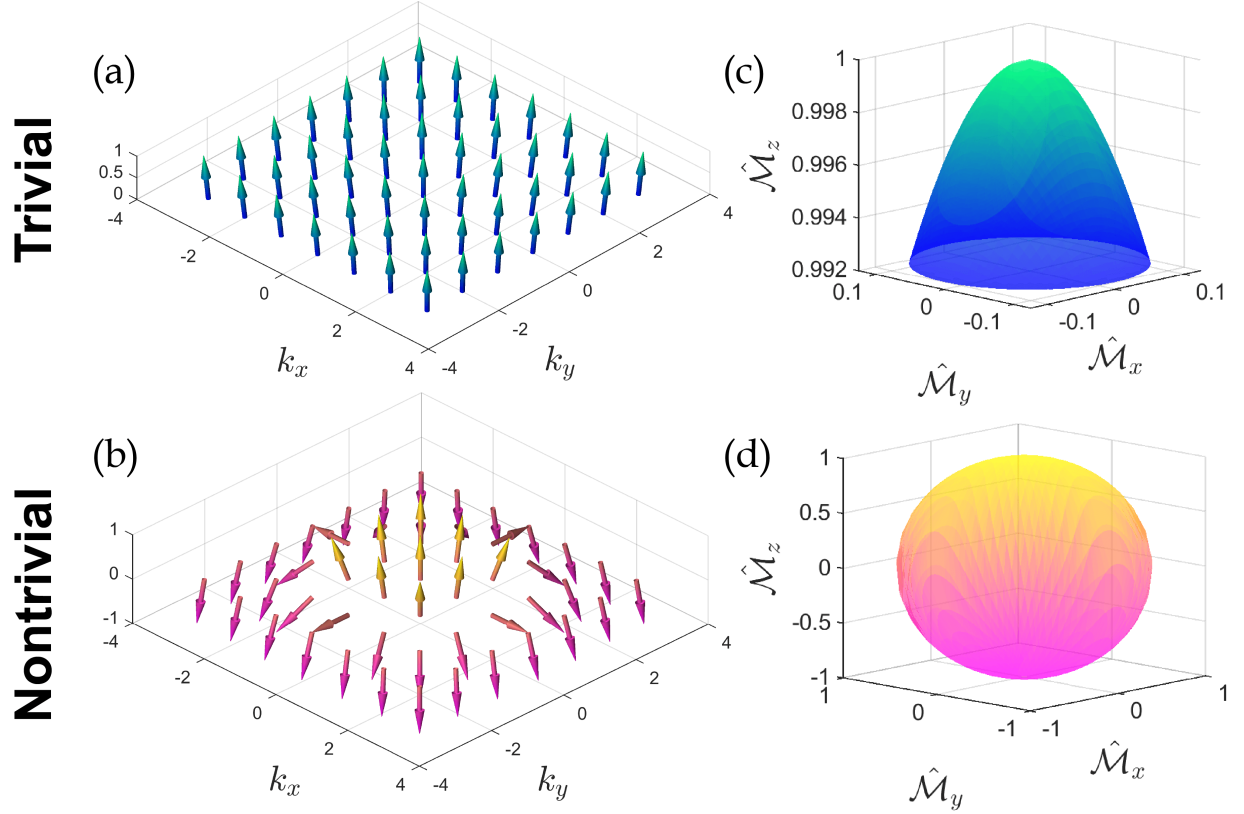
Figure 4.3. Left: spin texture $\hat{\mathcal{M}}(\mathbf{k})$ as a function of $\mathbf{k}$ for trivial and nontrivial skyrmions. (a) $N = 0$ skyrmion with no band inversion $\Lambda_0\Lambda_2 < 0$. As an example, we have let $v = 0.5$, $\Lambda_0 = 4$ and $\Lambda_2 = -2$. Since the spin returns to initial state within the dispersion $\hat{\mathcal{M}}_z(0) = \hat{\mathcal{M}}_z(\infty)$, the total winding is trivial. (b) $N = 1$ skyrmion with band inversion $\Lambda_0\Lambda_2 > 0$. To demonstrate, we have let $v = 0.5$, $\Lambda_0 = 4$ and $\Lambda_2 = 2$. In this case, the spin flips direction within the dispersion $\hat{\mathcal{M}}_z(0) \neq \hat{\mathcal{M}}_z(\infty)$ and the total winding is nontrivial. Right: spin texture $\hat{\mathcal{M}}$ of the skyrmion projected on the unit sphere. As the momentum varies over all possible values, $\hat{\mathcal{M}}(\mathbf{k})$ can perform either a (c) retracted or (d) full evolution over the unit sphere. This corresponds to a total solid angle of $\Omega = 0$ or 4π respectively.

$\vec{e}_0$ is a completely flat band $\omega_0 = 0$ and represents the electrostatic limit (irrotational fields). This band belongs to the Hilbert space but can be removed from the spectrum by enforcing $\mathbf{k} \cdot \mathbf{D} = 0$ at zero frequency, which implies there is no static charge present. Moreover, since $\vec{e}_0 = \vec{e}_0^*$ can always be chosen real, the Chern number of this band necessarily vanishes $C_0 = 0$.

4.3.4 Skyrmion magnetic field

We are now ready to assess the Berry curvature. In two dimensions, the Berry curvature is a scalar and characterizes the "magnetic" flux through the planar momentum space $\mathbb{R}^2$. Since our long wavelength theory is regularized, this is equivalent to the flux through the Riemann sphere S^2. For the 2D photon, the Berry curvature $\mathcal{F}_1^{\pm}$ is found by varying the in-plane momentum $\mathbf{k}$ of the right- and left-handed eigenstates $\vec{e}_{\pm}$,

$$\mathcal{F}_1^{\pm} = -\mathrm{i}(\partial_{k_x}\vec{e}_{\pm}^{\,*} \cdot \partial_{k_y}\vec{e}_{\pm} - \partial_{k_y}\vec{e}_{\pm}^{\,*} \cdot \partial_{k_x}\vec{e}_{\pm}). \tag{4.39}$$

The Berry curvature $\mathcal{F}_{1/2}^{\pm}$ of the 2D electron $\psi_{\pm}$ is derived in a similar fashion,

$$\mathcal{F}_{1/2}^{\pm} = -\mathrm{i}(\partial_{k_x}\psi_{\pm}^{\dagger}\partial_{k_y}\psi_{\pm} - \partial_{k_y}\psi_{\pm}^{\dagger}\partial_{k_x}\psi_{\pm}). \tag{4.40}$$

Just like the 3D massless particles [Eq. (4.13)], the Berry curvature $\mathcal{F}_s^{\pm} = \pm\mathcal{F}_s$ comes in units of quantized magnetic charge $Q_s = s$,

$$\mathcal{F}_s = Q_s\mathcal{F}. \tag{4.41}$$

This emergent magnetic field $\mathcal{F}$ is generated by the momentum dependent variations in the spin texture $\hat{\mathcal{M}} = \vec{\mathcal{M}}/\mathcal{M}$,

$$\mathcal{F} = \hat{\mathcal{M}} \cdot (\partial_{k_x}\hat{\mathcal{M}} \times \partial_{k_y}\hat{\mathcal{M}}) = \vec{F} \cdot d^2\vec{\mathcal{M}}. \tag{4.42}$$

$\mathcal{F}$ is precisely the magnetic field of a skyrmion [147] and has several profound interpretations. Mathematically, its the Jacobian and dictates the degree of continuous mapping from the

127

momentum space (the Riemann sphere) onto the unit sphere $\hat{\mathcal{M}}$, i.e. $S^2 \to S^2$. In another context, it tells us the differential flux of the Dirac monopole $\vec{F}$ onto the parametric surface $\vec{\mathcal{M}}(\mathbf{k})$,

$$\vec{F} = \frac{\vec{\mathcal{M}}}{\mathcal{M}^3}, \qquad d^2\vec{\mathcal{M}} = \partial_{k_x}\vec{\mathcal{M}} \times \partial_{k_y}\vec{\mathcal{M}}, \qquad (4.43)$$

where $d^2\vec{\mathcal{M}}$ is the surface normal. As the momentum varies over all possible values, the spin vector $\vec{\mathcal{M}}(\mathbf{k})$ can enclose the monopole any number of times. Hence, the total magnetic flux counts the number of Q_s monopoles enclosed by the skyrmion spin vector $\vec{\mathcal{M}}$,

$$N = \frac{1}{4\pi} \iint_{\mathbb{R}^2} \mathcal{F}dk_x dk_y = \frac{1}{4\pi} \iint_{\mathbb{R}^2} \hat{\mathcal{M}} \cdot (\partial_{k_x}\hat{\mathcal{M}} \times \partial_{k_y}\hat{\mathcal{M}})dk_x dk_y, \qquad N \in \mathbb{Z}. \qquad (4.44)$$

This is known as the skyrmion (or winding) number. Since the momentum space is bounded on the Riemann sphere $\mathbb{R}^2 \simeq S^2$, the skyrmion number N is guaranteed to be an integer. A visualization of the $\hat{\mathcal{M}}$ unit sphere for trivial and nontrivial skyrmions is displayed in Fig. 4.3.

4.3.5 Chern insulators

The Chern number C_s is directly proportional to the skyrmion number N but has a very different meaning depending on the particle species. It counts twice the total magnetic charge of the skyrmion,

$$C_s = \frac{1}{2\pi} \iint_{\mathbb{R}^2} \mathcal{F}_s dk_x dk_y = \frac{Q_s}{2\pi} \iint_{\mathbb{R}^2} \mathcal{F}dk_x dk_y = 2Q_s N. \qquad (4.45)$$

For spin-½ skyrmions, the Chern number is an integer $C_{1/2} = N \in \mathbb{Z}$ and is indistinguishable from the skyrmion number itself. Spin-1 skyrmions are quite different by comparison; the Chern number is an even integer $C_1 = 2N \in 2\mathbb{Z}$. From fermionic Chern arguments, one would expect to always find an even number of photonic edge states – but this is not the case [58]–[60], [145]. Although a widely held belief, the conventional bulk-boundary correspondence fails for spin-1 bosons [162]. We will demonstrate this fact explicitly.

Utilizing our spin vector $\vec{\mathcal{M}}$ defined in Eq. (4.30), the skyrmion magnetic field $\mathcal{F}$ in circular polar coordinates $\mathbf{k} = k(\cos\phi, \ \sin\phi)$ reads,

$$\mathcal{F}(k) = \frac{vk[\Lambda(k) - vk\Lambda(k)]}{[v^2 k^2 + \Lambda^2(k)]^{3/2}} = \sin\theta(k)\partial_k\theta(k) = -\partial_k\hat{\mathcal{M}}_z(k). \qquad (4.46)$$

Due to rotational symmetry, $\mathcal{F}(k)$ depends only on the magnitude of k. The geometric interpretation is clear – it describes variations in the solid angle $\mathcal{F}(k)dkd\phi = d\Omega(\mathbf{k})$ traced by $\hat{\mathcal{M}}(\mathbf{k})$. Integrating the magnetic flux over all momenta, we acquire the skyrmion number,

$$N = \frac{1}{2}[\cos\theta(0) - \cos\theta(\infty)] = \frac{1}{2}[\hat{\mathcal{M}}_z(0) - \hat{\mathcal{M}}_z(\infty)] = \frac{1}{2}\left(\text{sgn}[\Lambda_0] + \text{sgn}[\Lambda_2]\right). \qquad (4.47)$$

When band inversion is present $\Lambda_0\Lambda_2 > 0$, the z-component of the spin vector $\hat{\mathcal{M}}_z(0) \neq \hat{\mathcal{M}}_z(\infty)$ flips directions within the dispersion. This represents north $\theta = 0$ and south $\theta = \pi$ poles on the unit sphere, which means $\hat{\mathcal{M}}(\mathbf{k})$ traces out a full solid angle, regardless of the relative magnitudes of Λ_0 and Λ_2. This is equivalent to saying the parametric surface $\vec{\mathcal{M}}(\mathbf{k})$ always encloses a monopole $N = \pm 1$. In the trivial regime $\Lambda_0\Lambda_2 < 0$, the z-component $\hat{\mathcal{M}}_z(0) = \hat{\mathcal{M}}_z(\infty)$ returns to its initial state at either the north or south poles and $\vec{\mathcal{M}}(\mathbf{k})$ never encloses a monopole $N = 0$. Consequently, the Chern number in the nontrivial phase equates to $C_s = \pm 2Q_s$, which is an integer for the electron $C_{1/2} = \pm 1$, but an even integer for the photon $C_1 = \pm 2$. In conventional spin-½ and pseudo-spin-½ problems, a large Chern number $|C_{1/2}| > 1$ corresponds to multiple gapless edge states within the bulk topological band gap. This is not true for spin-1 bosonic particles. For $|C_1| = 2$ there is a single spin-1 quantized edge state within the topological band gap which is illustrated in Fig. (4.4).

4.3.6 Topological edge states

We now solve for the topology protected edge states of both particles. We stress that for both spin-1 and spin-½ phases, there is exactly one unidirectional solution at the edge. This makes intuitive sense because a single monopole $N = \pm 1$ exists in the band structure. A nontrivial skyrmion $N = \pm 1$ corresponds to either a forward or backward propagating edge state – forward for $N = +1$ and backward for $N = -1$. We take the boundary in the
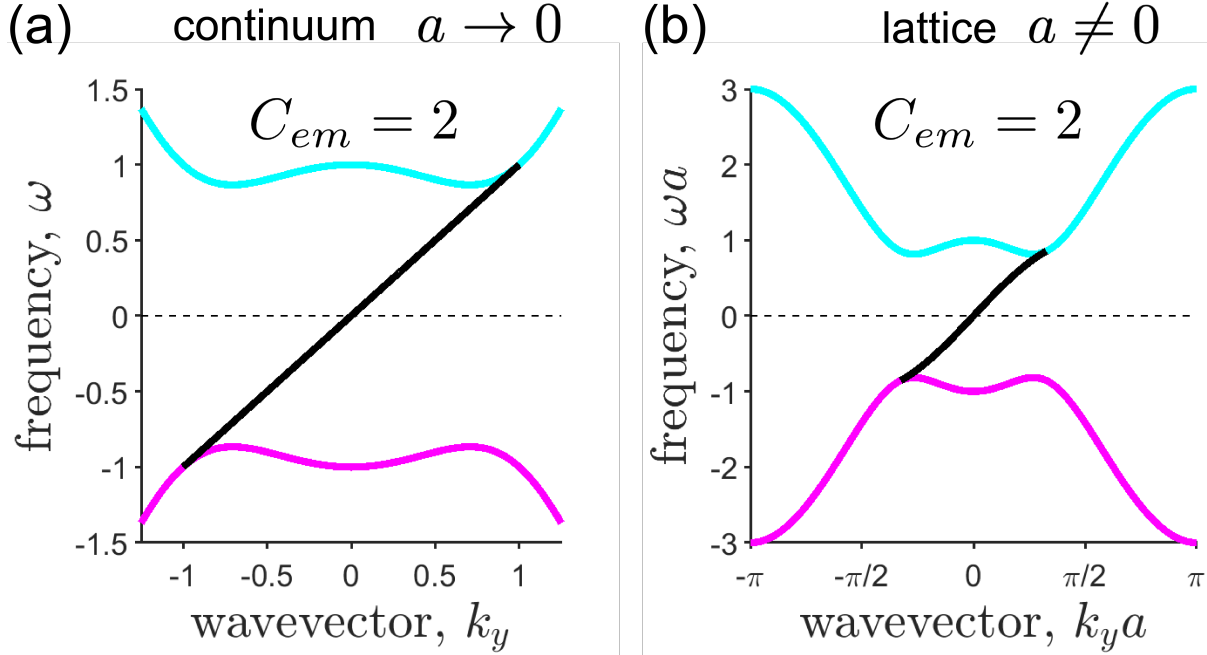
Figure 4.4. Dispersion relation of the bulk and gapless edge bands (black lines) of the topologically massive 2D particles. (a) The conventional fermionic Chern insulator is characterized by a spin-½ skyrmion (Dirac equation). (b) The bosonic Chern insulator is described by a spin-1 skyrmion (Maxwell's equations). The bulk Chern number $C_s = 2Q_s N$ depends on both the magnetic charge (spin) $Q_s = s$ and the skyrmion number $N \in \mathbb{Z}$. This corresponds to integer phases for electrons $C_{1/2} \in \mathbb{Z}$ but even integer phases for photons $C_1 \in 2\mathbb{Z}$. At low energy, a band gap is formed at $E = \omega = 0$ by a spatially dispersive effective mass $\Lambda(k) = \Lambda_0 - \Lambda_2 k^2$. (a) For the 2D electron, this is simply the Dirac mass. (b) For the 2D photon, this mass is equivalent to a nonlocal Hall conductivity $\varepsilon \Lambda(k) = \sigma_H(k)$. In the presence of band inversion $\Lambda_0 \Lambda_2 > 0$, there is a point where the effective mass changes sign $\Lambda(k) = 0$, precisely at $k = (\Lambda_0/\Lambda_2)^{1/2}$. The massless helically quantized edge states touch the bulk bands at this point. This is known as the quantum anomalous Hall effect (QAHE) for electrons and the quantum gyroelectric effect (QGEE) for photons. The flat longitudinal band $\omega_0 = 0$ is shown for completeness and represents the electrostatic limit (irrotational fields). However, this band can be removed from the spectrum by requiring that all static charges vanish.

x dimension such that k_y is still a good quantum number. We then look for solutions of the form $\vec{\Psi}^e_\pm(x,y) = \vec{\Psi}^e_\pm(x)e^{ik_y y}$ and $\psi^e_\pm(x,y) = \psi^e_\pm(x)e^{ik_y y}$ that satisfy the boundary condition at infinity $\vec{\Psi}^e_\pm(x=+\infty) = \psi^e_\pm(x=+\infty) = 0$. We also impose topological open boundary conditions [108], [109] at the interface,

$$\vec{\Psi}^e_\pm(x=0^+) = \psi^e_\pm(x=0^+) = 0. \tag{4.48}$$

If this constraint is satisfied simultaneously, a solution will exist at any interface (even vacuum) because the edge state is insensitive to fields in the $x < 0$ region.

Substituting into the Hamiltonians [Eq. (4.25) and (4.27)] and applying boundary conditions, the topological edge states emerge. For photonic spin-1 states we have,

$$\vec{\Psi}^e_\pm(x) = \begin{bmatrix} \sqrt{\varepsilon}E_x \\ \sqrt{\varepsilon}E_y \\ iH_z \end{bmatrix}^e_\pm = \Psi_0 \begin{bmatrix} 1 \\ 0 \\ \mp i \end{bmatrix} \left(e^{-\eta_1 x} - e^{-\eta_2 x} \right). \tag{4.49}$$

Carrying out the same procedure, the electronic spin-½ states are expressed as,

$$\psi^e_\pm(x) = \psi_0 \begin{bmatrix} 1 \\ \pm i \end{bmatrix} \left(e^{-\eta_1 x} - e^{-\eta_2 x} \right). \tag{4.50}$$

The wave functions of the spin-1 and spin-½ particles appear quite similar. The fundamental difference lies in the fact that $\vec{\Psi}$ is a vector (bosonic) field and its polarization state is defined in real space. ψ is a spinor (fermionic) field – its polarization state is more abstract as it lives in a complex space. Notice there are two characteristic decay scales for the edge states $\eta_{1,2}$, like a damped harmonic oscillator, but in spatial frequency. These are the quadratic roots of the secular equation,

$$\Lambda_0 + \Lambda_2(\eta^2 - k_y^2) \mp v\eta = 0. \tag{4.51}$$

If $\mathrm{sgn}[\Lambda_0] = \mathrm{sgn}[\Lambda_2] = +1$ the skyrmion number is $N = +1$ and only a forward propagating solution (+) exists. On the other hand, if $\mathrm{sgn}[\Lambda_0] = \mathrm{sgn}[\Lambda_2] = -1$ the skyrmion is $N = -1$

and only the backward propagating solution $(-)$ is permitted. $\eta_{1,2}$ characterize the degree of confinement at a particular momentum k_y and are solved straightforwardly,

$$\eta_{1,2}(k_y) = \frac{1}{2|\Lambda_2|}\left[v \pm \sqrt{v^2 + 4\Lambda_2(\Lambda_2 k_y^2 - \Lambda_0)}\right].\tag{4.52}$$

The spatial width of the wave packet depends on the size of the band gap formed by Λ_0 and Λ_2. However, regardless of their relative magnitudes, as long as $\Lambda_0\Lambda_2 > 0$ a solution always exists within the band gap – they are topologically protected.

Intriguingly, the edge waves are also helically quantized along the direction of propagation $\hat{k} = \hat{y}$,

$$S_y\vec{\Psi}^{\mathrm{e}}_\pm = \pm Q_1\vec{\Psi}^{\mathrm{e}}_\pm.\tag{4.53}$$

Note that $\hat{k}\cdot\vec{S} = S_y$ is the spin-1 helicity operator and the edge photon carries a discrete unit of bosonic charge $Q_1 = 1$. Likewise, the electronic edge wave carries a discrete unit of fermionic charge $Q_{1/2} = 1/2$,

$$(\sigma_y/2)\psi^{\mathrm{e}}_\pm = \pm Q_{1/2}\psi^{\mathrm{e}}_\pm,\tag{4.54}$$

where $\hat{k}\cdot\vec{\sigma}/2 = \sigma_y/2$ is the spin-½ helicity operator. For spin-1, helical quantization means the field is completely transverse to the momentum $\hat{k}\cdot\vec{\Psi}^{\mathrm{e}}_\pm = 0$ and the edge state behaves identically to a massless photon. This is known as the quantum gyroelectric effect (QGEE) [54]. Similarly, the edge electron behaves just like a helical Weyl fermion. Their dispersion relations read,

$$\omega_\pm(k_y) = E_\pm(k_y) = \pm v k_y, \qquad -\sqrt{\frac{\Lambda_0}{\Lambda_2}} < k_y < \sqrt{\frac{\Lambda_0}{\Lambda_2}}.\tag{4.55}$$

No solution exists for $k_y \to -k_y$ and the edge states are back-scatter immune. Notice they are linearly dispersing (massless) such that the group velocity is constant $\partial_{k_y}\omega_\pm = \partial_{k_y}E_\pm = \pm v$. Moreover, the edge states are gapless and touch the bulk bands precisely at the band inversion point $k_y = \sqrt{\Lambda_0/\Lambda_2}$, where $\Lambda(k_y) = 0$. At this particular momentum, one of the decay lengths becomes infinite $1/\eta(k_y) \to \infty$ and the edge states join the continuum of bulk bands. A diagram of the bulk and edge dispersion is shown in Fig. 4.4.

Note: It should be pointed out that the photonic edge states $\vec{\Psi}^{\mathrm{e}}_\pm$ are ill-defined in the zero energy limit $\omega = k_y = 0$, which is characteristic of all transverse waves. This is where

the edge dispersion intersects the longitudinal band $\omega_0 = 0$. Since this state is removed from the spectrum (no static charges present), the electromagnetic field vanishes at this point. No zero modes exist for the photon. On the other hand, the electronic edge states $\psi_{\pm}^{\mathrm{e}}$ have a smooth limit at $E = k_y = 0$ and zero modes are permitted. This is yet another significant difference between bosons and fermions which is related to the fact that the Dirac equation can host Majorana bound modes [163]. Since photons are their own antiparticles, no such Majorana states are possible.

4.4 Conclusion

In conclusion, we have introduced the concept of a photonic Dirac monopole appropriate for the field of spin photonics, topological photonic crystals and metamaterials. It shows magnetic monopole charge quantization in momentum space arising solely from spin-1 properties of the photon. We elucidated this phenomenon using a Dirac-Maxwell correspondence in the Riemann-Silberstein basis and applied this topological theory to 2D photonic materials. These topologically massive photons are interpreted as spin-1 skyrmions and arise from nonlocal Hall conductivity. Our work illuminates the role of photon spin in the recently proposed quantum gyroelectric phase of matter and topological bosonic phases [54], [63]. The edge states of such a topological phase exhibit spin-1 quantization as opposed to spin-½ quantization in fermionic phases of matter. This is ultimately connected to the presence of quantized monopole charges (bosonic- or fermionic-like [58], [59]) in the dispersion of bulk matter. Experimentally probing monopole charge in momentum space can shed light on fundamental symmetries in topological electrodynamics of photons and electrons.

Acknowledgements

5. NONLOCAL TOPOLOGICAL ELECTROMAGNETIC PHASES OF MATTER

From [T. Van Mechelen and Z. Jacob, "Nonlocal topological electromagnetic phases of matter," *Phys. Rev. B*, vol. 99, p. 205146, 20 May 2019]. © 2020 American Physical Society. [164]

In 2+1D, nonlocal topological electromagnetic phases are defined as atomic-scale media which host photonic monopoles in the bulk band structure and respect bosonic symmetries (e.g. time-reversal $\mathcal{T}^2 = +1$). Additionally, they support topologically protected spin-1 edge states, which are fundamentally different than spin-½ and pseudo-spin-½ edge states arising in fermionic and pseudo-fermionic systems. The striking feature of the edge state is that all electric and magnetic field components vanish at the boundary – in stark contrast to analogs of Jackiw-Rebbi domain wall states. This surprising open boundary solution of Maxwell's equations, dubbed the quantum gyroelectric effect [Phys. Rev. A **98**, 023842 (2018)], is the supersymmetric partner of the topological Dirac edge state where the spinor wave function completely vanishes at the boundary. The defining feature of such phases is the presence of temporal and spatial dispersion in conductivity (the linear response function). In this paper, we generalize these topological electromagnetic phases beyond the continuum approximation to the exact lattice field theory of a periodic atomic crystal. To accomplish this, we put forth the concept of microscopic photonic band structure of solids – analogous to the traditional theory of electronic band structure. Our definition of topological invariants utilizes optical Bloch modes and can be applied to naturally occurring crystalline materials. For the photon propagating within a periodic atomic crystal, our theory shows that besides the Chern invariant $\mathfrak{C} \in \mathbb{Z}$, there are also symmetry-protected topological (SPT) invariants $\nu \in \mathbb{Z}_N$ which are related to the cyclic point group C_N of the crystal $\nu = \mathfrak{C} \mod N$. Due to the rotational symmetries of light $\mathcal{R}(2\pi) = +1$, these SPT phases are manifestly bosonic and behave very differently from their fermionic counterparts $\mathcal{R}(2\pi) = -1$ encountered in conventional condensed matter systems. Remarkably, the nontrivial bosonic phases $\nu \neq 0$ are determined entirely from rotational (spin-1) eigenvalues of the photon at high-symmetry

points in the Brillouin zone. Our work accelerates progress towards the discovery of bosonic phases of matter where the electromagnetic field within an atomic crystal exhibits topological properties.

5.1 Introduction

From a material science standpoint, all known topological phases of matter to date have been characterized by electronic phenomena [15], [17]. This is true for both time-reversal broken phases – often called Chern insulators [11], [13], [72], [73], [94] and time-reversal unbroken phases – known as topological insulators [27]–[29]. The signature of time-reversal broken phases is the quantum Hall conductivity $\sigma_{xy} = ne^2/h$, which is quantized in terms of the electronic Chern invariant $n \in \mathbb{Z}$ [3], [5], [7]. e being the elementary charge of the electron and h the Planck constant. Only recently has the idea of bosonic Hall conductivity and topological bosonic phases been put forth [56]–[62], [165], [166].

However, it should be emphasized that the traditional Hall conductivity [55], [104] only has topological significance, with respect to the electron, in the static $\omega = 0$ and long wavelength $k = 0$ limits of the electromagnetic field $\sigma_{xy}(0,0) = ne^2/h$. At high frequency $\omega \neq 0$ and short wavelength $k \neq 0$, the Hall conductivity $\sigma_{xy}(\omega, \mathbf{k})$ acquires new physical meaning. We have shown that the electromagnetic field itself becomes topological [54], [116], [167]. These topological electromagnetic phases of matter depend on the *global* behavior of $\sigma_{xy}(\omega, \mathbf{k})$, over all frequencies and wave vectors.

Like electrons, the signature of electromagnetic Chern phases $\mathfrak{C} \neq 0$ is topologically-protected unidirectional (chiral) edge states. Unlike electrons however, no physical observable (response/correlation function) is topologically quantized as their is no known equivalent for photons. Nevertheless, the origin of topological quantization $\mathfrak{C} \in \mathbb{Z}$ is always a discontinuity in the underlying Berry connection (gauge field [117]) of the eigenmodes. This phenomenon of gauge discontinuity in the *photonic* eigenmodes fundamentally requires non-local gyrotropy (Hall conductivity). Nonlocality, or spatial dispersion, is the momentum dependence of optical parameters. If the Hall conductivity changes sign with momentum $\sigma_{xy}(\omega, \mathbf{k}_{\text{crit}}) = 0$, ie. the handedness changes, the electromagnetic field is topologically non-trivial $\mathfrak{C} \neq 0$. In two dimensions, σ_{xy} behaves as an effective mass [84], [85], [139] and this

change in sign is the photonic counterpart of the Chern insulator [11], [13], [72], [73], [94], where the exact same situation occurs. This intriguing nonlocal behavior leads to a new topological bosonic phase of matter – a quantum gyroelectric phase [54], [116], [167] – which is unlike any known fermionic phase as it is intrinsically tied to the electromagnetic field.

As of yet, only the continuum topological theory of the aforementioned quantum gyro-electric effect (QGEE) has been solved [54], [116], [167]. Our goal is to extend this concept beyond the long wavelength approximation to the exact lattice field theory of optical Bloch waves. In this regime, we must consider not only the first spatial component $\sigma_{xy}(\omega, \mathbf{k}) = \sigma_{xy}(\omega, \mathbf{k}, \mathbf{0})$ but all spatial harmonics of the crystal $\mathbf{g} \neq \mathbf{0}$, to infinite order,

$$J_x^{\mathrm{Hall}}(\omega, \mathbf{k}) = \sum_{\mathbf{g}} \sigma_{xy}(\omega, \mathbf{k}, \mathbf{g}) E_y(\omega, \mathbf{k} + \mathbf{g}). \tag{5.1}$$

$\mathbf{g} \cdot \mathbf{R} \in 2\pi\mathbb{Z}$ are the reciprocal lattice vectors and $\mathbf{R}$ is the primitive vector of the crystal. In this case, E_i is the microscopic electric field. The electromagnetic field must be described to the same scale as the electronic wave functions, i.e. for photon momenta on the order of the lattice constant $ka = \pi$. Since topological invariants are fundamentally global properties, these astronomically deep subwavelength fields actually play a role in the topological physics.

The idea of lattice topologies in electromagnetism was first proposed by Haldane [19], [20] in the context of photonic crystals [23], [64]–[69]. These are artificial materials composed of two or more different constituents which form a macroscopic crystalline structure. A few important examples are gyrotropic photonic crystals [23], [68], [69], Floquet topological insulators [52], [168], [169] and bianisotropic metamaterials [53], [70], [71], [74], [76], [77], [125], [127], [129], [130], [143], [144], [170]–[172]. Instead, we focus on the microscopic domain and utilize the periodicity of the atomic lattice itself. Thus, the topological invariants in our theory are connected to the microscopic atomic lattice and not artificially engineered macroscopic structures. We stress that in the microscopic case, the electromagnetic theory is manifestly bosonic [78], [79], [140], [173] (e.g. time-reversal $\mathcal{T}^2 = +1$) and characterizes topological phases of matter fundamentally distinct from known fermionic and pseudo-fermionic phases.

With that in mind, this paper is dedicated to solving two longstanding problems, which is of interest to both photonics and condensed matter physics. The first, is developing the rigorous theory of optical Bloch modes in natural crystal solids. This problem gained significant interest in the 60's and 70's in the context of spatial dispersion (nonlocality) as it lead to qualitatively new phenomena – such as natural optical activity (gyrotropy) [87], [174]–[176]. The current paper builds on our recent discovery of the quantum gyroelectric effect [54], [116], [167] where we have shown that nonlocality is also essential for topological phenomena and is a necessary ingredient in any long wavelength theory. However, since topological field theories are global constructs, a complete picture can only be achieved in the microscopic domain of Bloch waves. Most of the foundations have been summarized by Agronovich and Ginzburg in their seminal monograph on crystal optics [95]. Nevertheless, topological properties have never been tackled to date and a few fundamental quantities, such as the Bloch energy density, have not been defined.

This leads to the second problem – deriving the electromagnetic topological invariants of these systems given only the atomic lattice. We solve this problem and also provide a systematic bosonic classification of all 2+1D topological photonic matter. Utilizing the optical Bloch modes, we show that a Chern invariant $\mathfrak{C} \in \mathbb{Z}$ can be found for any two-dimensional crystal and characterizes distinct topological phases. We then go one step further and classify these topological phases with respect to the symmetry group of the crystal – the cyclic point groups C_N. These are known as symmetry-protected topological (SPT) phases [16], [100], [177]–[186] and the spin of the photon is critical to their definition. The rotational symmetries of light $\mathcal{R}(2\pi) = +1$ impart an intrinsically bosonic nature to these phases, which are fundamentally different than their fermionic counterparts $\mathcal{R}(2\pi) = -1$ encountered in conventional condensed matter systems. We illustrate this fact by directly comparing SPT bosonic and fermionic phases side-by-side. Our rigorous formalism of microscopic photonic band structure provides an immediate parallel with the traditional theory of electronic band structure in crystal solids.

This article is organized as follows. In Sec. 5.2 we develop the general formalism of 2+1D lattice electromagnetism. First we derive the generalized linear response function – accounting for spatiotemporal dispersion to infinite order in the crystal's spatial harmonics **g**.

Thereafter, we find the equivalent Hamiltonian that governs all light-matter Bloch excitations of the material. In Sec. 5.3 we study the discrete rotational symmetries (point groups) of the crystal and the implications on spin-1 quantization [135], [187]–[191] of the photon. The following Sec. 5.4 discusses the electromagnetic Chern number and its relationship to symmetry-protected topological (SPT) bosonic phases. The bosonic classification of each phase is related directly to integer quantization of the photon [Tab. 5.1] and this is compared alongside their fermionic counterparts [Tab. 5.2]. Sec. 5.5 presents our conclusions.

The focus of this paper is 2+1D topological electromagnetic (bosonic) phases of matter $\mathfrak{C} \neq 0$ which requires breaking time-reversal symmetry. These bosonic Chern insulators are ultimately related to nonlocal gyrotropic response (Hall conductivity) and show unidirectional, completely transverse electro-magnetic (TEM) edge states [54], [116], [167]. However, time-reversal symmetric topological phenomena can arise in higher dimensional systems in the context of nonlocal magnetoelectricity [63]. These time-reversal symmetric phases possess counter-propagating TEM edge states and are interpreted as two copies of a bosonic Chern insulator. Features of topological phenomena, such as spin-momentum locking [26], [83], [157], [158], [192], have also been reported in conventional surface state problems – surface plasmon-polaritons (SPPs), Dyakonov waves, etc. However, these traditional surface properties are not connected to any topologically protected edge states or nontrivial phases.

5.2 Lattice electromagnetism

5.2.1 2+1D electrodynamics

In this paper we focus on two-dimensional materials and the topological electromagnetic phases associated with them. The preliminaries for 2+1D electromagnetism can be found in App. A of Ref. [54]. Conveniently, the restriction to 2D limits the degrees of freedom of both the electromagnetic field and the induced response of the material, such that strictly transverse-magnetic (TM) waves propagate. The corresponding wave equation reads,

$$\mathcal{H}_0 f = \mathrm{i}\partial_t g, \qquad f = \begin{bmatrix} E_x \\ E_y \\ H_z \end{bmatrix}, \qquad g = \begin{bmatrix} D_x \\ D_y \\ B_z \end{bmatrix}. \tag{5.2}$$

138

Table 5.1. Summary of 2+1D topological electromagnetic (bosonic) phases. Symmetry-protected topological (SPT) bosonic phases exist in all cyclic point groups C_N. The continuous group C_∞ describes the long wavelength theory $k \approx 0$. The topological phases are characterized by their Chern invariant $\mathfrak{C} \in \mathbb{Z}$ and SPT invariant $\nu \in \mathbb{Z}_N$. These numbers are not independent – but intimately related by the symmetries of the crystal: $\nu = \mathfrak{C} \mod N$. ν is protected by N-fold rotational symmetry and determines the Chern number up to a factor of N. The bosonic classification of ν represents the direct product of rotational eigenvalues $(\eta_N)^N = +1$ (roots of unity) of the electromagnetic field at high-symmetry points (HSPs) in the Brillouin zone.

Point group, C_N	Symmetry, $\mathbb{Z}_N$	Bosonic classification, $(\eta_N)^N = +1$
C_1	-	-
C_2	$\mathbb{Z}_2$	$\exp\left(\mathrm{i}2\pi\mathfrak{C}/2\right) = \eta_2(\Gamma)\eta_2(\mathrm{X})\eta_2(\mathrm{Y})\eta_2(\mathrm{M})$
C_3	$\mathbb{Z}_3$	$\exp\left(\mathrm{i}2\pi\mathfrak{C}/3\right) = \eta_3(\Gamma)\eta_3(\mathrm{K})\eta_3(\mathrm{K})$
C_4	$\mathbb{Z}_4$	$\exp\left(\mathrm{i}2\pi\mathfrak{C}/4\right) = \eta_4(\Gamma)\eta_4(\mathrm{M})\eta_2(\mathrm{Y})$
C_6	$\mathbb{Z}_6$	$\exp\left(\mathrm{i}2\pi\mathfrak{C}/6\right) = \eta_6(\Gamma)\eta_3(\mathrm{K})\eta_2(\mathrm{M})$
C_∞	$\mathbb{Z}$	$\exp\left(\mathrm{i}\theta\mathfrak{C}\right) = \eta_\theta(0)\eta_\theta^*(\infty), \quad \eta_\theta = \exp(\mathrm{i}\theta m)$

Table 5.2. Summary of 2+1D SPT fermionic phases for comparison. The fermionic classification of ν represents the direct product of rotational eigenvalues $(\zeta_N)^N = -1$ (roots of negative unity) of the spinor field at HSPs in the Brillouin zone.

Point group, C_N	Symmetry, $\mathbb{Z}_N$	Fermionic classification, $(\zeta_N)^N = -1$
C_1	-	-
C_2	$\mathbb{Z}_2$	$\exp\left(\mathrm{i}2\pi\mathfrak{C}/2\right) = \zeta_2(\Gamma)\zeta_2(\mathrm{X})\zeta_2(\mathrm{Y})\zeta_2(\mathrm{M})$
C_3	$\mathbb{Z}_3$	$\exp\left(\mathrm{i}2\pi\mathfrak{C}/3\right) = -\zeta_3(\Gamma)\zeta_3(\mathrm{K})\zeta_3(\mathrm{K})$
C_4	$\mathbb{Z}_4$	$\exp\left(\mathrm{i}2\pi\mathfrak{C}/4\right) = -\zeta_4(\Gamma)\zeta_4(\mathrm{M})\zeta_2(\mathrm{Y})$
C_6	$\mathbb{Z}_6$	$\exp\left(\mathrm{i}2\pi\mathfrak{C}/6\right) = -\zeta_6(\Gamma)\zeta_3(\mathrm{K})\zeta_2(\mathrm{M})$
C_∞	$\mathbb{Z}$	$\exp\left(\mathrm{i}\theta\mathfrak{C}\right) = \zeta_\theta(0)\zeta_\theta^*(\infty), \quad \zeta_\theta = \exp(\mathrm{i}\theta m)$

f is the TM polarization state of the electromagnetic field and the material response is captured by the displacement field g. $\mathcal{H}_0(\mathbf{p}) = \mathbf{p} \cdot \mathbf{S}$ are the vacuum Maxwell equations in real space and describe the dynamics of the free photon,

$$\mathcal{H}_0(\mathbf{p}) = p_x \hat{S}_x + p_y \hat{S}_y = \begin{bmatrix} 0 & 0 & -p_y \\ 0 & 0 & p_x \\ -p_y & p_x & 0 \end{bmatrix}. \tag{5.3}$$

$\mathbf{p} = -i\nabla$ is the two-dimensional momentum operator. $\hat{S}_x$ and $\hat{S}_y$ are spin-1 operators that satisfy the angular momentum algebra $[\hat{S}_i, \hat{S}_j] = i\epsilon_{ijk}\hat{S}_k$,

$$\hat{S}_z = \begin{bmatrix} 0 & -i & 0 \\ i & 0 & 0 \\ 0 & 0 & 0 \end{bmatrix}. \tag{5.4}$$

Here, $(\hat{S}_z)_{ij} = -i\epsilon_{ijz}$ is the generator of rotations in the x-y plane and is represented by the antisymmetric matrix. In two dimensions, $\hat{S}_z$ governs all rotational symmetries of the electromagnetic field.

5.2.2 2+1D linear response theory

The effective electromagnetic properties of a material are very accurately described by a linear response theory – assuming nonlinear interactions are negligible. This is true for low intensity light $|f| \lesssim 10^8$ V/m that is sufficiently weak compared to the atomic fields governing the binding of the crystal itself. Our goal is to characterize the topological field theory in this regime. With this in mind, the most general linear response of a 2D material is nonlocal in both space and time coordinates,

$$g(t, \mathbf{r}) = \int d^2\mathbf{r}' \int_{-\infty}^t dt' \mathcal{M}(t, t', \mathbf{r}, \mathbf{r}') f(t', \mathbf{r}'). \tag{5.5}$$

140

$\mathcal{M}$ is the response function and compactly represents the constitutive relations in space-time,

$$\mathcal{M}(t, t', \mathbf{r}, \mathbf{r}') = \begin{bmatrix} \varepsilon_{xx} & \varepsilon_{xy} & \chi_x \\ \varepsilon_{yx} & \varepsilon_{yy} & \chi_y \\ \zeta_x & \zeta_y & \mu \end{bmatrix}. \tag{5.6}$$

Note that $\mathcal{M}$ is a 3×3 dimensional matrix and we include all possible material responses as a generalization, for instance magnetism μ and magnetoelectricity χ_i, ζ_i.

If the properties of the crystal are not changing temporally (no external modulation), the response function is translationally invariant in time,

$$\mathcal{M}(t, t', \mathbf{r}, \mathbf{r}') = \mathcal{M}(t - t', \mathbf{r}, \mathbf{r}') = \int d\omega \mathcal{M}(\omega, \mathbf{r}, \mathbf{r}') e^{-i\omega(t-t')}. \tag{5.7}$$

Equation (5.7) implies energy conservation in Hermitian systems $\omega = \omega$. However, a crystal is not translationally invariant in space – momentum is not conserved $\mathbf{k}' \neq \mathbf{k}$. Instead, the crystal is periodic and possesses discrete translational symmetry [95], [193],

$$\mathcal{M}(\omega, \mathbf{r}, \mathbf{r}') = \mathcal{M}(\omega, \mathbf{r} + \mathbf{R}, \mathbf{r}' + \mathbf{R}), \tag{5.8}$$

where $\mathbf{R}$ is the primitive lattice vector of the crystal. Due to nonlocality, it is necessary to convert to the reciprocal space,

$$\mathcal{M}(\omega, \mathbf{k}, \mathbf{k}') = \frac{1}{(2\pi)^2} \iint d^2\mathbf{r} d^2\mathbf{r}' \mathcal{M}(\omega, \mathbf{r}, \mathbf{r}') e^{-i\mathbf{k}\cdot\mathbf{r}} e^{i\mathbf{k}'\cdot\mathbf{r}'}. \tag{5.9}$$

$\mathcal{M}(\omega, \mathbf{k}, \mathbf{k}')$ determines the linear transformation properties of an input wave with momentum $\mathbf{k}'$ to an output wave with momentum $\mathbf{k}$. In a periodic crystal, the momentum is conserved up to a reciprocal vector $\mathbf{k}' = \mathbf{k} + \mathbf{g}$ and represents a discrete spectrum,

$$\mathcal{M}(\omega, \mathbf{k}, \mathbf{k}') = \sum_{\mathbf{g}} \mathcal{M}_{\mathbf{g}}(\omega, \mathbf{k}) \delta^2(\mathbf{k} + \mathbf{g} - \mathbf{k}'), \tag{5.10}$$

where $\mathcal{M}_{\mathbf{g}}(\omega, \mathbf{k})$ is the Fourier transformed function with respect to $\bar{\mathbf{r}} = \mathbf{r} - \mathbf{r}'$,

$$\mathcal{M}_{\mathbf{g}}(\omega, \mathbf{k}) = \int d^2\bar{\mathbf{r}} \, \mathcal{M}_{\mathbf{g}}(\omega, \bar{\mathbf{r}}) e^{-i\mathbf{k}\cdot\bar{\mathbf{r}}}. \tag{5.11}$$

$\delta^2(\mathbf{k} + \mathbf{g} - \mathbf{k}')$ is the momentum conserving delta function. Each Fourier element of the response function $\mathcal{M}_{\mathbf{g}}(\omega, \mathbf{k})$ determines the polarization dependent scattering amplitude from $\mathbf{k} + \mathbf{g} \to \mathbf{k}$. These are essentially the photonic structure factors of the two-dimensional crystal.

In this case, $\mathbf{k}$ is the crystal momentum and is only uniquely defined within the first Brillouin zone (BZ). Hence, the electromagnetic eigenstates of the medium are Bloch waves,

$$\mathcal{H}_0(\mathbf{k}) f_{\mathbf{k}} = \omega \int d^2\mathbf{k}' \mathcal{M}(\omega, \mathbf{k}, \mathbf{k}') f_{\mathbf{k}'} = \omega \sum_{\mathbf{g}} \mathcal{M}_{\mathbf{g}}(\omega, \mathbf{k}) f_{\mathbf{k}+\mathbf{g}}. \tag{5.12}$$

$\mathcal{H}_0(\mathbf{k}) = \mathbf{k} \cdot \mathbf{S}$ are the vacuum Maxwell equations in momentum space. The Bloch photonic wave function $\tilde{f}_{\mathbf{k}}(\mathbf{r})$ corresponds to the net propagation of all $\mathbf{k} + \mathbf{g}$ scattered waves in the medium,

$$\tilde{f}_{\mathbf{k}}(\mathbf{r}) = \frac{1}{\sqrt{V}} \sum_{\mathbf{g}} f_{\mathbf{k}+\mathbf{g}} e^{i\mathbf{g}\cdot\mathbf{r}}, \tag{5.13}$$

where $\tilde{f}_{\mathbf{k}}(\mathbf{r} + \mathbf{R}) = \tilde{f}_{\mathbf{k}}(\mathbf{r})$ is periodic in the atomic crystal lattice and we have normalized by the unit cell area V. For clarity, we use tildes to identify cell-periodic Bloch functions. $f_{\mathbf{k}+\mathbf{g}}$ are the collection of Fourier coefficients associated with each Bloch wave. Note that Eq. (5.12) and (5.13) reduce to the continuum theory [54], [116], [167] when considering only the 0th order harmonic $\mathbf{g} = \mathbf{0}$.

5.2.3 Generalized response function

Nevertheless, Eq. (5.12) poses a few serious problems; it does not represent a proper first-order in time Hamiltonian since all harmonics of the response function $\mathcal{M}_{\mathbf{g}}(\omega, \mathbf{k})$ depend on the eigenvalue ω. Moreover, it is not evident that the Bloch waves in Eq. (5.13) are normalizable, as the system contains complex spatial and temporal dispersion. Due to these issues, it is advantageous to return to the more general form of $\mathcal{M}(\omega, \mathbf{k}, \mathbf{k}')$ without assuming

discrete translational symmetry. This will allow us to derive very robust properties of the response function that can also be applied to amorphous materials or quasicrystals.

First, we demand Hermiticity,

$$\mathcal{M}(\omega, \mathbf{k}, \mathbf{k}') = \mathcal{M}^\dagger(\omega, \mathbf{k}', \mathbf{k}), \tag{5.14}$$

such that the response is lossless. To account for normalizable electromagnetic waves, the energy density must be positive definite for all ω,

$$U(\omega) = \iint d^2\mathbf{k} d^2\mathbf{k}' f_{\mathbf{k}}^\dagger \bar{\mathcal{M}}(\omega, \mathbf{k}, \mathbf{k}') f_{\mathbf{k}'} > 0, \tag{5.15}$$

where $\bar{\mathcal{M}}$ describes the inner product space in a dispersive medium,

$$\bar{\mathcal{M}}(\omega, \mathbf{k}, \mathbf{k}') = \frac{\partial}{\partial\omega} \left[\omega \mathcal{M}(\omega, \mathbf{k}, \mathbf{k}')\right]. \tag{5.16}$$

Notice that $U(\omega) = U^*(\omega)$ is only real-valued when $\mathcal{M}$ is Hermitian. For realistic materials, the energy density is also stable at static equilibrium $\omega = 0$,

$$U(0) = \iint d^2\mathbf{k} d^2\mathbf{k}' f_{\mathbf{k}}^\dagger \mathcal{M}(0, \mathbf{k}, \mathbf{k}') f_{\mathbf{k}'} > 0, \tag{5.17}$$

with $\mathcal{M}(0, \mathbf{k}, \mathbf{k}') = \bar{\mathcal{M}}(0, \mathbf{k}, \mathbf{k}')$ at zero frequency. Stability implies the response function is nonsingular at $\omega = 0$, such that there is a smooth transition to the electrostatic limit $\lim_{\omega \to 0} \omega \mathcal{M}(\omega, \mathbf{k}, \mathbf{k}') \to 0$. All dielectric (insulating) materials satisfy this constraint since the induced current arises strictly from time-varying polarizations $J_i = \dot{P}_i + \epsilon_{ij}\partial^j M_z$. By relaxing the stability condition [Eq. (5.17)], metallic (plasmonic) models can be easily included with slight modifications to $\mathcal{M}$. Metallic materials are singular (unstable) at $\omega = 0$ as they possess dc (static) currents. However, the main focus of this paper is the ground state of dielectric (insulating) materials so we assume the response function is well-behaved around $\omega = 0$.

To ensure the electromagnetic field is real-valued, i.e. represents a neutral particle, we always require the reality condition,

$$\mathcal{M}(\omega, \mathbf{k}, \mathbf{k}') = \mathcal{M}^*(-\omega, -\mathbf{k}, -\mathbf{k}').$$

(5.18)

Furthermore, the response is transparent at high frequency $\omega \to \infty$, as the material cannot respond to sufficiently fast temporal oscillations,

$$\lim_{\omega \to \infty} \mathcal{M}(\omega, \mathbf{k}, \mathbf{k}') = \mathbb{1}_3 \delta_{\mathbf{k}-\mathbf{k}'}^2.$$

(5.19)

$\mathbb{1}_3$ is the 3×3 identity matrix and $\delta_{\mathbf{k}-\mathbf{k}'}^2 = \delta^2(\mathbf{k} - \mathbf{k}')$ is the momentum conserving delta function. Lastly, the response must be causal and satisfy the Kramers-Kronig relations,

$$\oint_{\mathrm{Im}\,[\omega'] \geq 0} \frac{\mathcal{M}(\omega', \mathbf{k}, \mathbf{k}') - \mathbb{1}_3 \delta_{\mathbf{k}-\mathbf{k}'}^2}{\omega' - \omega} d\omega' = 0.$$

(5.20)

This ensures the response function is analytic in the upper complex plane and decays at least as fast as $|\omega|^{-1}$.

Combining all the above criteria, we find that $\mathcal{M}$ can always be expanded via a partial fraction decomposition,

$$\mathcal{M}(\omega, \mathbf{k}, \mathbf{k}') = \mathbb{1}_3 \delta_{\mathbf{k}-\mathbf{k}'}^2 - \sum_\alpha \int d^2\mathbf{k}' \frac{\mathcal{C}_{\alpha\mathbf{k}'\mathbf{k}}^\dagger \mathcal{C}_{\alpha\mathbf{k}'\mathbf{k}'}}{\omega_{\alpha\mathbf{k}'}(\omega - \omega_{\alpha\mathbf{k}'})}.$$

(5.21)

Any Hermitian (lossless) response function can be expressed in this form. Equation (5.21) is easily extended to 3D materials but our focus is 2D topological field theories. $\omega_{\alpha\mathbf{k}}$ is the resonant energy of the oscillator and corresponds to a first-order (real-valued) pole of the response function. Note, to satisfy the reality condition [Eq. (5.18)], each oscillator $\omega_{\alpha\mathbf{k}}$ must always come in pairs with a negative energy resonance $-\omega_{\alpha-\mathbf{k}}$, which we assume is captured by the summation over α.

144

In this case, α labels an arbitrary bosonic excitation in the material, such as an exciton or phonon, which couples linearly to the electromagnetic fields via the tensor,

$$\mathcal{C}_\alpha(\mathbf{k}, \mathbf{k}') = \frac{1}{(2\pi)^2} \iint d^2\mathbf{r} d^2\mathbf{r}' \mathcal{C}_\alpha(\mathbf{r}, \mathbf{r}') \mathrm{e}^{-\mathrm{i}\mathbf{k}\cdot\mathbf{r}} \mathrm{e}^{\mathrm{i}\mathbf{k}'\cdot\mathbf{r}'}. \tag{5.22}$$

In the general case, $\mathrm{rank}[\mathcal{C}_\alpha] = 3$ couples to both the electric E_i and magnetic field H_z. Pure electric excitations only contribute to the permittivity tensor $\mathrm{rank}[\mathcal{C}_\alpha] = 2$ and couple strictly to the electric field E_i. Likewise, pure magnetic excitations only contribute to the scalar permeability $\mathrm{rank}[\mathcal{C}_\alpha] = 1$ and couple strictly to the magnetic field H_z. All such excitations are accounted for simply by specifying the rank of $\mathcal{C}_\alpha$. The rank of $\mathcal{C}_\alpha$ also determines the number of additional eigenmodes arising from each oscillator α. The total number of modes is therefore $N = 3 + \sum_\alpha \mathrm{rank}[\mathcal{C}_\alpha]$, where 3 arise from Maxwell's equations $\mathrm{rank}[\mathcal{H}_0] = 3$.

Substituting Eq. (5.21) into Eq. (5.15), we can exchange the order of integration $U(\omega) = \int d^2\mathbf{k} U(\omega, \mathbf{k})$ and define,

$$U(\omega, \mathbf{k}) = |f_\mathbf{k}|^2 + \sum_\alpha \left| \int d^2\mathbf{k}' \frac{\mathcal{C}_{\alpha\mathbf{k}\mathbf{k}'} f_{\mathbf{k}'}}{(\omega - \omega_{\alpha\mathbf{k}})} \right|^2 > 0, \tag{5.23}$$

which is positive definite for all ω and $\mathbf{k}$. Equation (5.23) is the generalized inner product for the electromagnetic field and represents the energy density at an arbitrary frequency and wave vector. We will now show that Eq. (5.21) is derived from a first-order in time Hamiltonian.

5.2.4 Generalized Hamiltonian

To find the corresponding Hamiltonian, we expand the response function $\mathcal{M}$ in terms of three-component matter oscillators ψ_α. Similar to a Lorentz oscillator [194], these describe the internal polarization and magnetization modes of the material,

$$\omega\psi_{\alpha\mathbf{k}} = \omega_{\alpha\mathbf{k}}\psi_{\alpha\mathbf{k}} + \int d^2\mathbf{k}' \mathcal{C}_{\alpha\mathbf{k}\mathbf{k}'} f_{\mathbf{k}'}. \tag{5.24}$$

Substituting Eq. (5.24) and (5.21) into Eq. (5.12) we obtain,

$$\omega f_{\mathbf{k}} = \mathcal{H}_0(\mathbf{k}) f_{\mathbf{k}} + \sum_\alpha \iint \frac{d^2\mathbf{k}' d^2\mathbf{k}'}{\omega_{\alpha\mathbf{k}'}} \mathcal{C}^\dagger_{\alpha\mathbf{k}'\mathbf{k}} \mathcal{C}_{\alpha\mathbf{k}'\mathbf{k}'} f_{\mathbf{k}'} + \sum_\alpha \int d^2\mathbf{k}' \mathcal{C}^\dagger_{\alpha\mathbf{k}'\mathbf{k}} \psi_{\alpha\mathbf{k}'}. \tag{5.25}$$

The first two terms on the right hand side of Eq. (5.25) represent the vacuum equations and self-energy of the electromagnetic field. The third term is the linear coupling to the oscillators. Combining Eq. (5.24) and (5.25) into a single algebraic matrix, we write the generalized Hamiltonian $H(\mathbf{k}, \mathbf{k}')$ as,

$$H(\mathbf{k}, \mathbf{k}') = \begin{bmatrix} \mathcal{H}_0(\mathbf{k})\delta^2_{\mathbf{k}-\mathbf{k}'} + \sum_\alpha \int \frac{d^2\mathbf{k}'}{\omega_{\alpha\mathbf{k}'}} \mathcal{C}^\dagger_{\alpha\mathbf{k}'\mathbf{k}} \mathcal{C}_{\alpha\mathbf{k}'\mathbf{k}'} & \mathcal{C}^\dagger_{1\mathbf{k}'\mathbf{k}} & \mathcal{C}^\dagger_{2\mathbf{k}'\mathbf{k}} & \cdots \\ \mathcal{C}_{1\mathbf{k}\mathbf{k}'} & \omega_{1\mathbf{k}}\delta^2_{\mathbf{k}-\mathbf{k}'} & 0 & \cdots \\ \mathcal{C}_{2\mathbf{k}\mathbf{k}'} & 0 & \omega_{2\mathbf{k}}\delta^2_{\mathbf{k}-\mathbf{k}'} & \cdots \\ \vdots & \vdots & \vdots & \ddots \end{bmatrix}, \tag{5.26}$$

which is manifestly Hermitian $H(\mathbf{k}, \mathbf{k}') = H^\dagger(\mathbf{k}', \mathbf{k})$. The dimension of the Hamiltonian is determined by the rank of all the coupling matrices $\text{rank}[H] = N = 3 + \sum_\alpha \text{rank}[\mathcal{C}_\alpha]$.

We now define $u_{\mathbf{k}}$ as the generalized state vector of the electromagnetic problem; accounting for the photon $f_{\mathbf{k}}$ and all possible internal excitations $\psi_{\alpha\mathbf{k}}$,

$$\int d^2\mathbf{k}' H_{\mathbf{k}\mathbf{k}'} u_{\mathbf{k}'} = \omega u_{\mathbf{k}}, \qquad u_{\mathbf{k}} = \begin{bmatrix} f_{\mathbf{k}} \\ \psi_{1\mathbf{k}} \\ \psi_{2\mathbf{k}} \\ \vdots \end{bmatrix}, \tag{5.27}$$

which is a first-order wave equation. Notice that contraction of $u_{\mathbf{k}}$ naturally reproduces the energy density [Eq. (5.23)] upon summation over all degrees of freedom,

$$u^\dagger_{\mathbf{k}} u_{\mathbf{k}} = |f_{\mathbf{k}}|^2 + \sum_\alpha |\psi_{\alpha\mathbf{k}}|^2 = |f_{\mathbf{k}}|^2 + \sum_\alpha \left| \int d^2\mathbf{k}' \frac{\mathcal{C}_{\alpha\mathbf{k}\mathbf{k}'} f_{\mathbf{k}'}}{(\omega - \omega_{\alpha\mathbf{k}})} \right|^2 = U(\omega, \mathbf{k}). \tag{5.28}$$

The complete set of eigenvectors and eigenvalues is represented by $u_{\mathbf{k}}$. We must define all relevant electromagnetic quantities in terms of this generalized state vector.

146

5.2.5 Crystal Hamiltonian

We are now ready to enforce crystal periodicity. Instead of expanding $\mathcal{M}$ directly, we utilize the periodicity of the coupling tensors $\mathcal{C}_\alpha(\mathbf{r}, \mathbf{r}') = \mathcal{C}_\alpha(\mathbf{r}+\mathbf{R}, \mathbf{r}'+\mathbf{R})$, which is a discrete spectrum in $\mathbf{g}$,

$$\mathcal{C}_\alpha(\mathbf{r}, \mathbf{r}') = \sum_\mathbf{g} \mathcal{C}_{\alpha\mathbf{g}}(\mathbf{r} - \mathbf{r}')e^{-i\mathbf{r}'\cdot\mathbf{g}}. \tag{5.29}$$

After Fourier transforming, we obtain the components in the momentum space,

$$\mathcal{C}_\alpha(\mathbf{k}, \mathbf{k}') = \sum_\mathbf{g} \mathcal{C}_{\alpha\mathbf{g}}(\mathbf{k})\delta^2(\mathbf{k} + \mathbf{g} - \mathbf{k}'), \tag{5.30}$$

with respect to $\bar{\mathbf{r}} = \mathbf{r} - \mathbf{r}'$,

$$\mathcal{C}_{\alpha\mathbf{g}}(\mathbf{k}) = \int d^2\bar{\mathbf{r}}\, \mathcal{C}_{\alpha\mathbf{g}}(\bar{\mathbf{r}})e^{-i\mathbf{k}\cdot\bar{\mathbf{r}}}. \tag{5.31}$$

$\mathcal{C}_{\alpha\mathbf{g}}(\mathbf{k})$ tells us the scattering amplitude of a photon $f_{\mathbf{k}+\mathbf{g}}$ with momentum $\mathbf{k} + \mathbf{g}$ into an internal mode of the material $\psi_{\alpha\mathbf{k}}$ at momentum $\mathbf{k}$, and vice versa. The crystal Hamiltonian accounts for all such scattering events,

$$H(\mathbf{k}, \mathbf{k}') = \sum_\mathbf{g} H_\mathbf{g}(\mathbf{k})\delta^2(\mathbf{k} + \mathbf{g} - \mathbf{k}'), \tag{5.32}$$

with Hermiticity $H_\mathbf{g}(\mathbf{k}) = H_{-\mathbf{g}}^\dagger(\mathbf{k} + \mathbf{g})$ satisfied by definition.

The quasiparticle eigenstates of the Hamiltonian describe the complete spectrum of Bloch waves,

$$\sum_\mathbf{g} H_\mathbf{g}(\mathbf{k})u_{n\mathbf{k}+\mathbf{g}} = \omega_{n\mathbf{k}}u_{n\mathbf{k}}, \tag{5.33}$$

and the eigenenergies $\omega_{n\mathbf{k}+\mathbf{g}} = \omega_{n\mathbf{k}}$ are periodic Bloch bands. Note, it is important not to confuse the polaritonic eigenenergies $\omega_{n\mathbf{k}}$ with the oscillator energies $\omega_{\alpha\mathbf{k}}$. The eigenenergies $\omega_{n\mathbf{k}}$ constitute modes of the coupled light-matter system while $\omega_{\alpha\mathbf{k}}$ describe the natural matter oscillations in the absence of the electromagnetic field. n labels a particular polaritonic energy band of the material with its associated Bloch eigenstate $\tilde{u}_{n\mathbf{k}}(\mathbf{r})$. The total wave

function $\tilde{u}_{n\mathbf{k}}(\mathbf{r})$ contains the photon $\tilde{f}_{n\mathbf{k}}(\mathbf{r})$ and all internal degrees of freedom describing the linear response $\tilde{\psi}_{n\alpha\mathbf{k}}(\mathbf{r})$. This is expressed compactly in the Fourier basis,

$$\tilde{u}_{n\mathbf{k}}(\mathbf{r}) = \frac{1}{\sqrt{V}} \sum_{\mathbf{g}} u_{n\mathbf{k}+\mathbf{g}} e^{i\mathbf{g}\cdot\mathbf{r}}, \qquad u_{n\mathbf{k}+\mathbf{g}} = \begin{bmatrix} f_{n\mathbf{k}+\mathbf{g}} \\ \psi_{n1\mathbf{k}+\mathbf{g}} \\ \psi_{n2\mathbf{k}+\mathbf{g}} \\ \vdots \end{bmatrix}, \tag{5.34}$$

where $\tilde{u}_{n\mathbf{k}}(\mathbf{r} + \mathbf{R}) = \tilde{u}_{n\mathbf{k}}(\mathbf{r})$ is periodic in the atomic crystal lattice and we have normalized by the unit cell area V. In this basis, $\tilde{u}_{n\mathbf{k}}(\mathbf{r})$ is normalized to unit energy as,

$$
\begin{aligned}
1 &= \int_{\text{cell}} d^2\mathbf{r} \; \tilde{u}_{n\mathbf{k}}^\dagger(\mathbf{r})\tilde{u}_{n\mathbf{k}}(\mathbf{r}) = \sum_{\mathbf{g}} u_{n\mathbf{k}+\mathbf{g}}^\dagger u_{n\mathbf{k}+\mathbf{g}} \\
&= \sum_{\mathbf{g}} \left(f_{n\mathbf{k}+\mathbf{g}}^\dagger f_{n\mathbf{k}+\mathbf{g}} + \sum_{\alpha} \psi_{n\alpha\mathbf{k}+\mathbf{g}}^\dagger \psi_{n\alpha\mathbf{k}+\mathbf{g}} \right) \\
&= \sum_{\mathbf{g}\mathbf{g}'} f_{n\mathbf{k}+\mathbf{g}}^\dagger \bar{\mathcal{M}}_{\mathbf{g}'-\mathbf{g}}(\omega_{n\mathbf{k}}, \mathbf{k}+\mathbf{g}) f_{n\mathbf{k}+\mathbf{g}'}.
\end{aligned} \tag{5.35}
$$

The integration is taken over the 2D unit cell. To simplify Eq. (5.35), we have utilized the linear response theory to express ψ_α in terms of the driving field f,

$$\psi_{n\alpha\mathbf{k}+\mathbf{g}} = \frac{\sum_{\mathbf{g}'} \mathcal{C}_{\alpha\mathbf{g}'}(\mathbf{k}+\mathbf{g}) f_{n\mathbf{k}+\mathbf{g}'+\mathbf{g}}}{\omega_{n\mathbf{k}} - \omega_{\alpha\mathbf{k}+\mathbf{g}}}. \tag{5.36}$$

$\bar{\mathcal{M}}_{\mathbf{g}}(\omega, \mathbf{k}) = \partial_\omega[\omega\mathcal{M}_{\mathbf{g}}(\omega, \mathbf{k})]$ is the contribution to the energy density arising from each spatial harmonic of the crystal.

Finally, the eigenenergies $\omega_{n\mathbf{k}}$ are the n nontrivial roots of the characteristic wave equation,

$$\mathcal{H}_0(\mathbf{k}) f_{n\mathbf{k}} = \omega_{n\mathbf{k}} \sum_{\mathbf{g}} \mathcal{M}_{\mathbf{g}}(\omega_{n\mathbf{k}}, \mathbf{k}) f_{n\mathbf{k}+\mathbf{g}}, \tag{5.37}$$

which generates all possible photonic bands of the crystal. Note, the response function $\mathcal{M}_{\mathbf{g}}(\omega, \mathbf{k})$ is now expressed in terms of $\mathcal{C}_{\alpha\mathbf{g}}(\mathbf{k})$ and describes the net summation of all scattering and back-scattering events in the material,

$$\mathcal{M}_{\mathbf{g}}(\omega, \mathbf{k}) = \mathbb{1}_3 \delta_{\mathbf{g}} - \sum_{\alpha\mathbf{g}'} \frac{\mathcal{C}^{\dagger}_{\alpha-\mathbf{g}'}(\mathbf{k}+\mathbf{g}')\mathcal{C}_{\alpha\mathbf{g}-\mathbf{g}'}(\mathbf{k}+\mathbf{g}')}{\omega_{\alpha\mathbf{k}+\mathbf{g}'}(\omega - \omega_{\alpha\mathbf{k}+\mathbf{g}'})}. \tag{5.38}$$

This proves that the wave equation is derived from a first-order Hamiltonian, has real eigenvalues $\omega = \omega_{n\mathbf{k}}$ for all momenta, and is normalizable with respect to the total state vector $\tilde{u}_{n\mathbf{k}}(\mathbf{r})$.

5.3   Discrete rotational symmetry

5.3.1   Point groups in 2D

Point groups are the discrete analogs of continuous rotations and reflections. They represent the number of ways the atomic lattice can be transformed into itself [97], [98]. Due to the crystallographic restriction theorem (CRT), there are ten such point groups in 2D. The first five are the cyclic groups C_N,

$$C_1, \ C_2, \ C_3, \ C_4, \ C_6. \tag{5.39}$$

For instance, C_3 implies threefold cyclic symmetry while C_1 is no symmetry. The last five are the dihedral groups D_N,

$$D_1, \ D_2, \ D_3, \ D_4, \ D_6. \tag{5.40}$$

The dihedral group D_N contains C_N plus reflections. However, it can be proven that the Chern number for all D_N point groups vanish [100]. In fact, any space group containing mirror symmetry has a vanishing Chern number [16]. Therefore, we concern ourselves with only the (abelian) cyclic groups C_N. The Brillouin zone of each point group is displayed in Fig. 5.1.
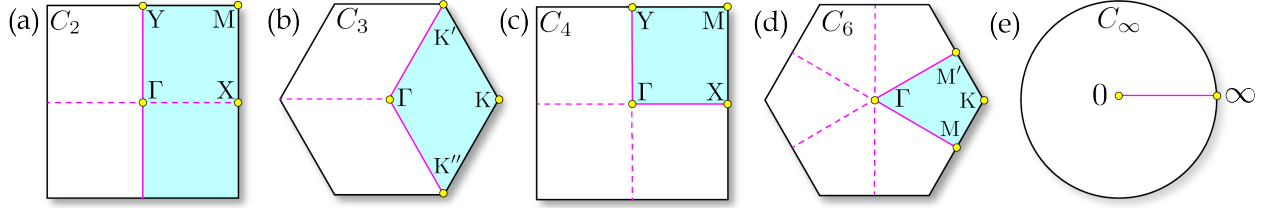
Figure 5.1. Brillouin zone of each cyclic point group C_N. (a), (b), (c), (d), and (e) correspond to $N = 2, 3, 4, 6$, and ∞ respectively. Due to rotational symmetry, the total BZ is equivalent to N copies of the IBZ, which is represented by the blue quadrant. For continuous symmetry $N = \infty$, this is simply a line. The yellow circles label HSPs $\mathcal{R}\mathbf{k}_p = \mathbf{k}_p$ where the crystal Hamiltonian is invariant under a certain rotation $\hat{\mathcal{R}}$. At these specific momenta, a Bloch photonic wave function $\mathcal{R}\tilde{f}_{\mathbf{k}_p}(R^{-1}\mathbf{r}) = \eta(\mathbf{k}_p)\tilde{f}_{\mathbf{k}_p}(\mathbf{r})$ is an eigenstate of an N-fold rotation $\eta(\mathbf{k}_p) = \eta_N(\mathbf{k}_p) = [\mathrm{i}2\pi m_N(\mathbf{k}_p)/N]$ such that the photon possesses quantized integer eigenvalues $m_N(\mathbf{k}_p) \in \mathbb{Z}_N$. Since m_N are discrete quantum numbers, their values cannot vary continuously if the crystal symmetry is preserved – they can only be changed at a topological phase transition.

The defining characteristic of each cyclic group is the fermionic or bosonic representation. When we rotate the fields by 2π, we take the particle into itself and acquire a phase,

$$\mathcal{R}(2\pi) = (-1)^F. \tag{5.41}$$

F is twice the total spin of particle, or equivalently, the fermion number. Fermions with half-integer spin are antisymmetric under rotations $\mathcal{R}(2\pi) = -1$, while bosons with integer spin are symmetric $\mathcal{R}(2\pi) = +1$. Depending on the symmetries of the lattice, the topology fundamentally changes for fermions and bosons. We will understand the implications this has for spin-1 photons.

5.3.2 Spin-1 discrete symmetries

If the two-dimensional crystal belongs to a cyclic point group C_N, the Hamiltonian possesses discrete rotational symmetry about the z-axis,

$$\mathcal{R}^{-1}H_{R\mathbf{g}}(R\mathbf{k})\mathcal{R} = H_{\mathbf{g}}(\mathbf{k}), \qquad \omega_{nR\mathbf{k}} = \omega_{n\mathbf{k}}, \tag{5.42}$$

150

where $\mathcal{R}$ is any rotation in C_N. The eigenenergies $\omega_{n\mathbf{k}}$ respect the symmetry of the crystal – the energy at $R\mathbf{k}$ and $\mathbf{k}$ are identical. It is important to note that $\mathcal{R}$ is diagonal in u, meaning the photon and each oscillator is rotated individually, $f \to \mathcal{R}f$ and $\psi_\alpha \to \mathcal{R}\psi_\alpha$. This implies there is no mixing of fields. The symmetries of the Hamiltonian are endowed by the coupling tensors, which dictates the degrees of freedom of the material response,

$$\mathcal{R}^{-1}\mathcal{C}_{\alpha R\mathbf{g}}(R\mathbf{k})\mathcal{R} = \mathcal{C}_{\alpha\mathbf{g}}(\mathbf{k}), \qquad \omega_{\alpha R\mathbf{k}} = \omega_{\alpha\mathbf{k}}. \tag{5.43}$$

After summation over all $\mathcal{C}_{\alpha\mathbf{g}}(\mathbf{k})$, we can prove that the response function transforms identically under such a rotation,

$$\mathcal{R}^{-1}\mathcal{M}_{R\mathbf{g}}(\omega, R\mathbf{k})\mathcal{R} = \mathcal{M}_{\mathbf{g}}(\omega, \mathbf{k}). \tag{5.44}$$

Therefore, the photon inherits all symmetries of the crystal.

In this case, the $\mathcal{R}$ matrix represents a discrete rotation and can be expressed as the exponential of the spin-1 generator $(\hat{S}_z)_{ij} = -\mathrm{i}\epsilon_{ijz}$,

$$\mathcal{R}_N = \exp\left(-\mathrm{i}\frac{2\pi}{N}\hat{S}_z\right) = \begin{bmatrix} R_N & 0 \\ 0 & 1 \end{bmatrix}, \tag{5.45}$$

where $\frac{2\pi}{N}$ is an N-fold rotation,

$$R_N = \begin{bmatrix} \cos(\frac{2\pi}{N}) & -\sin(\frac{2\pi}{N}) \\ \sin(\frac{2\pi}{N}) & \cos(\frac{2\pi}{N}) \end{bmatrix}. \tag{5.46}$$

Electric components transform as 2D vectors and rotate into one another under $\mathcal{R}$. Magnetic components transform as scalars and are left invariant under $\mathcal{R}$. We stress that every cyclic group for the photon is a vector representation, which is bosonic,

$$(\mathcal{R}_N)^N = \mathcal{R}(2\pi) = +\mathbb{1}_3. \tag{5.47}$$

The electromagnetic field returns in phase under cyclic revolution.

5.3.3 High-symmetry points

The Bloch eigenstates $\tilde{u}_{n\mathbf{k}}(\mathbf{r})$ are essentially a collection of periodic vector fields. To rotate the fields, we must perform an operation on both the coordinates $\mathbf{r}$ and the polarization states f and ψ_α. In real space, the operation of a rotation $\hat{\mathcal{R}}$ is preformed as,

$$\mathcal{R}\tilde{u}_{n\mathbf{k}}(R^{-1}\mathbf{r}) = \eta_n(\mathbf{k})\tilde{u}_{nR\mathbf{k}}(\mathbf{r}), \tag{5.48}$$

where $\mathcal{R}$ is a discrete rotation defined in Eq. (5.45). This implies the Fourier coefficients obey,

$$\mathcal{R}u_{n\mathbf{k}+R^{-1}\mathbf{g}} = \eta_n(\mathbf{k})u_{nR\mathbf{k}+\mathbf{g}}. \tag{5.49}$$

It follows from symmetry that the operation of $\hat{\mathcal{R}}$ takes a wave function at $\mathbf{k}$ to $R\mathbf{k}$ with the same energy $\omega_{n\mathbf{k}} = \omega_{nR\mathbf{k}}$ – but with a possibly different phase $|\eta_n(\mathbf{k})|^2 = 1$. Utilizing the linear response theory, we notice that the phase factor $\eta_n(\mathbf{k})$ is governed entirely by the photon,

$$
\begin{aligned}
\mathcal{R}\psi_{n\alpha\mathbf{k}+R^{-1}\mathbf{g}} &= \frac{\sum_{\mathbf{g}'} \mathcal{R}\mathcal{C}_{\alpha\mathbf{g}'}(\mathbf{k}+R^{-1}\mathbf{g})f_{n\mathbf{k}+\mathbf{g}'+R^{-1}\mathbf{g}}}{\omega_{n\mathbf{k}} - \omega_{\alpha\mathbf{k}+R^{-1}\mathbf{g}}} \\
&= \frac{\sum_{\mathbf{g}'} \mathcal{C}_{\alpha R\mathbf{g}'}(R\mathbf{k}+\mathbf{g})\mathcal{R}f_{n\mathbf{k}+\mathbf{g}'+R^{-1}\mathbf{g}}}{\omega_{n\mathbf{k}} - \omega_{\alpha\mathbf{k}+R^{-1}\mathbf{g}}} \\
&= \frac{\sum_{\mathbf{g}'} \mathcal{C}_{\alpha\mathbf{g}'}(R\mathbf{k}+\mathbf{g})\eta_n(\mathbf{k})f_{nR\mathbf{k}+\mathbf{g}'+\mathbf{g}}}{\omega_{n\mathbf{k}} - \omega_{\alpha R\mathbf{k}+\mathbf{g}}} \\
&= \eta_n(\mathbf{k})\psi_{n\alpha R\mathbf{k}+\mathbf{g}}.
\end{aligned}
\tag{5.50}
$$

This is an incredibly convenient simplification and implies the precise coordinates of the matter oscillations ψ_α are superfluous when discussing symmetries. The electromagnetic field f tells us everything.

Importantly, there are specific points in the Brillouin zone where $\mathbf{k}$ is invariant under a discrete rotation,

$$R\mathbf{k}_p = \mathbf{k}_p. \tag{5.51}$$

152

This is because the crystal momentum only differs by a lattice translation at these points $R\mathbf{k}_p = \mathbf{k}_p + \mathbf{g}$, which leaves a Bloch wave function unchanged,

$$e^{iR\mathbf{k}_p\cdot\mathbf{r}}\tilde{u}_{nR\mathbf{k}_p}(\mathbf{r}) = e^{i(\mathbf{k}_p+\mathbf{g})\cdot\mathbf{r}}\tilde{u}_{n\mathbf{k}_p+\mathbf{g}}(\mathbf{r}) = e^{i\mathbf{k}_p\cdot\mathbf{r}}\tilde{u}_{n\mathbf{k}_p}(\mathbf{r}). \qquad (5.52)$$

These are called high-symmetry points (HSPs); they occur at the center and certain vertices of the Brillouin zone. The crystal Hamiltonian is rotationally invariant at these momenta – i.e. it commutes with $\hat{\mathcal{R}}$. Therefore, the wave functions are simultaneous eigenstates of $\hat{\mathcal{R}}$ at HSPs,

$$\mathcal{R}\tilde{u}_{n\mathbf{k}_p}(R^{-1}\mathbf{r}) = \eta_n(\mathbf{k}_p)\tilde{u}_{n\mathbf{k}_p}(\mathbf{r}), \qquad (5.53)$$

which immediately implies,

$$\mathcal{R}\tilde{f}_{n\mathbf{k}_p}(R^{-1}\mathbf{r}) = \eta_n(\mathbf{k}_p)\tilde{f}_{n\mathbf{k}_p}(\mathbf{r}). \qquad (5.54)$$

Here, $\eta_n(\mathbf{k}_p)$ is the eigenvalue of $\hat{\mathcal{R}}$ at $\mathbf{k}_p$ for the nth band.

5.3.4 Spin-1 eigenvalues

Depending on the point group and the precise HSP, $\eta_n(\mathbf{k}_p) = \eta_{N,n}(\mathbf{k}_p)$ can represent any Nth root of unity corresponding to the N-fold rotation operator $\hat{\mathcal{R}}_N$,

$$\eta_{N,n}(\mathbf{k}_p) = \exp\left[i\frac{2\pi}{N}m_{N,n}(\mathbf{k}_p)\right], \qquad (\eta_{N,n})^N = +1. \qquad (5.55)$$

$m_{N,n}(\mathbf{k}_p) \in \mathbb{Z}_N$ is a modulo integer – it labels the N possible spin-1 eigenvalues at $\mathbf{k}_p$. In C_4 for example, the Γ and M points are invariant under $\hat{\mathcal{R}}_4$ rotations, while the X and Y points are invariant under $\hat{\mathcal{R}}_2$ rotations (inversion). This means there are 4 possible spin-1 charges located at $m_{4,n}(\Gamma)$ & $m_{4,n}(M) \in \mathbb{Z}_4$ respectively and 2 possible charges located at $m_{2,n}(X) = m_{2,n}(Y) \in \mathbb{Z}_2$. A visualization of these topological charges is presented in Fig. 5.2 and this is contrasted with their fermionic counterparts in Fig. 5.3. In Sec. 5.4 we will connect these rotational eigenvalues directly to the topological invariants.
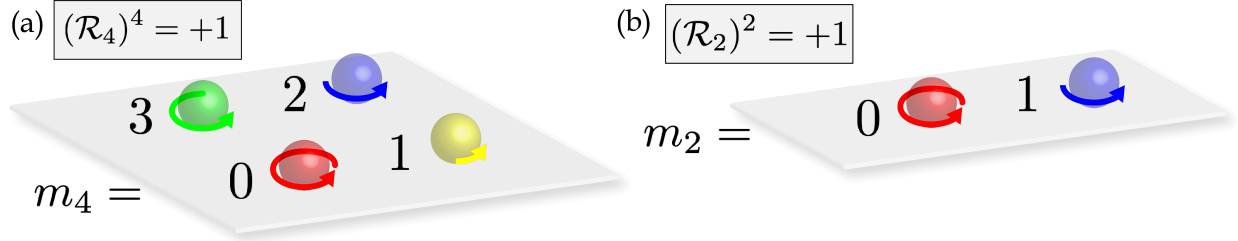
Figure 5.2. The collection of spin-1 (bosonic) charges for the C_4 point group. (a) Fourfold rotations $(\mathcal{R}_4)^4 = +1$; there are four unique eigenvalues $\eta_4 = \exp[i2\pi m_4/4]$ corresponding to the roots of unity $(\eta_4)^4 = +1$. These represent the modulo 4 integers $m_4 \in \mathbb{Z}_4$. Note that $m_4 = 3 = -1$ can also be interpreted as a left-handed eigenstate. (b) Bosonic inversion $(\mathcal{R}_2)^2 = +1$; there are two unique eigenvalues $\eta_2 = \exp[i2\pi m_2/2]$ corresponding to the roots of unity $(\eta_2)^2 = +1$. These represent the modulo 2 integers $m_2 \in \mathbb{Z}_2$.
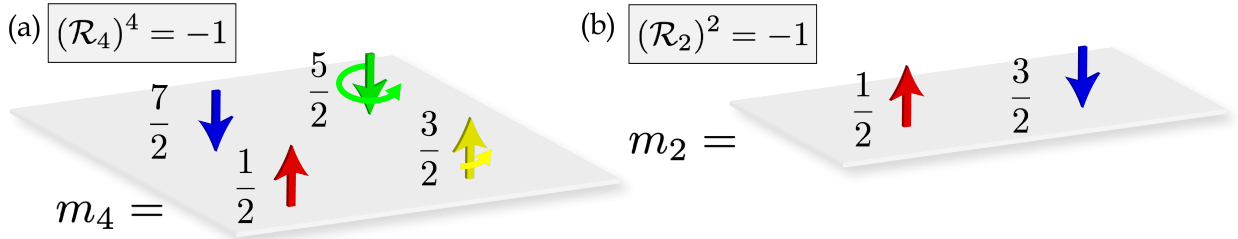
Figure 5.3. The collection of spin-½ (fermionic) charges for the C_4 point group. (a) Fourfold rotations $(\mathcal{R}_4)^4 = -1$; there are four unique eigenvalues $\zeta_4 = \exp[i2\pi m_4/4]$ corresponding to the roots of negative unity $(\zeta_4)^4 = -1$. These represent the modulo 4 half-integers $m_4 \in \mathbb{Z}_4 + 1/2$. Note that $m_4 = 7/2 = -1/2$ can be interpreted as a spin-down fermion while $m_4 = 3/2 = 1/2 + 1$ and $m_4 = 5/2 = -1/2 + 3$ constitute a fermion plus a boson. (b) Fermionic inversion $(\mathcal{R}_2)^2 = -1$; there are two unique eigenvalues $\zeta_2 = \exp[i2\pi m_2/2]$ corresponding to the roots of negative unity $(\zeta_2)^2 = -1$. These represent the modulo 2 half-integers $m_2 \in \mathbb{Z}_2 + 1/2$. Note that $m_2 = 3/2 = -1/2$ can also be interpreted as a spin-down fermion under modulo 2.

5.4 Topological electromagnetic (bosonic) phases of matter

5.4.1 Electromagnetic Chern number

The Berry connection for a band n is found by varying the total Bloch wave function $\tilde{u}_{n\mathbf{k}}(\mathbf{r})$ with respect to the momentum,

$$\mathbf{A}_n(\mathbf{k}) = -\mathrm{i} \int_{\text{cell}} d^2\mathbf{r} \; \tilde{u}_{n\mathbf{k}}^\dagger(\mathbf{r}) \partial_\mathbf{k} \tilde{u}_{n\mathbf{k}}(\mathbf{r}) = -\mathrm{i} \sum_\mathbf{g} u_{n\mathbf{k}+\mathbf{g}}^\dagger \partial_\mathbf{k} u_{n\mathbf{k}+\mathbf{g}}. \tag{5.56}$$

This can be simplified slightly to obtain,

$$\mathbf{A}_n(\mathbf{k}) = -\mathrm{i} \sum_{\mathbf{g}\mathbf{g}'} f_{n\mathbf{k}+\mathbf{g}}^\dagger \bar{\mathcal{M}}_{\mathbf{g}'-\mathbf{g}}(\omega_{n\mathbf{k}}, \mathbf{k}+\mathbf{g}) \partial_\mathbf{k} f_{n\mathbf{k}+\mathbf{g}'} + \sum_{\mathbf{g}\mathbf{g}'} f_{n\mathbf{k}+\mathbf{g}}^\dagger \boldsymbol{\mathcal{A}}_{\mathbf{g}'-\mathbf{g}}(\omega_{n\mathbf{k}}, \mathbf{k}+\mathbf{g}) f_{n\mathbf{k}+\mathbf{g}'}. \tag{5.57}$$

The first term gives the Berry connection of the photon, while the second term $\boldsymbol{\mathcal{A}}_\mathbf{g}(\omega, \mathbf{k})$ arises solely from the matter oscillations,

$$\boldsymbol{\mathcal{A}}_\mathbf{g}(\omega, \mathbf{k}) = -\mathrm{i} \sum_{\alpha\mathbf{g}'} \frac{\mathcal{C}_{\alpha-\mathbf{g}'}^\dagger(\mathbf{k}+\mathbf{g}') \partial_\mathbf{k} \mathcal{C}_{\alpha\mathbf{g}-\mathbf{g}'}(\mathbf{k}+\mathbf{g}')}{(\omega - \omega_{\alpha\mathbf{k}+\mathbf{g}'})^2}. \tag{5.58}$$

Due to nonlocality, Eq. (5.58) does not generally vanish. This additional contribution to the Berry phase corresponds to vortices in the response function itself – independent of the Berry gauge of the photon. This means the Chern number can be nonzero $\mathfrak{C}_n \neq 0$ even if the winding of electromagnetic field is trivial. However, we will show in the proceeding sections that all symmetry constraints on the Chern number can be established entirely in terms of the photon.

As can be seen from Eq. (5.57), the Berry connection is only defined within the Brillouin zone $\mathbf{A}_{n\mathbf{k}+\mathbf{g}} = \mathbf{A}_{n\mathbf{k}} + \partial_\mathbf{k} \chi_{n\mathbf{k}}$, up to a possible U(1) gauge. Hence, the gauge invariant Berry curvature is periodic $F_{n\mathbf{k}+\mathbf{g}} = F_{n\mathbf{k}}$,

$$F_n(\mathbf{k}) = \hat{\mathbf{z}} \cdot [\partial_\mathbf{k} \times \mathbf{A}_n(\mathbf{k})]. \tag{5.59}$$
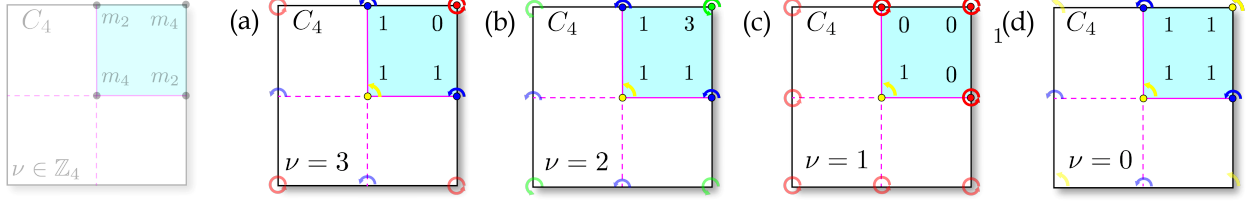
Figure 5.4. Examples of SPT bosonic phases in a crystal with C_4 symmetry. These phases are characterized by their SPT invariant $\nu = m_4(\Gamma) + m_4(M) + 2m_2(Y) \mod 4$ which determines the electromagnetic Chern number up to a multiple of 4. Here, $m_4 \in \mathbb{Z}_4$ and $m_2 \in \mathbb{Z}_2$ are modulo integers. (a), (b), (c) and (d) correspond to SPT bosonic phases of $\nu = 3, 2, 1$ and 0 respectively. For bosons, we simply add up all the integer charges within the irreducible Brillouin zone. For instance, the $\nu = 2$ phase has eigenvalues of $m_4(\Gamma) = 1$ at the center and $m_4(M) = 3 = -1$ at the vertices, with inversion eigenvalues of $m_2(Y) = m_2(X) = 1$ at the edge centers: $\nu = 1 + 3 + 2 \times 1 = 2$.
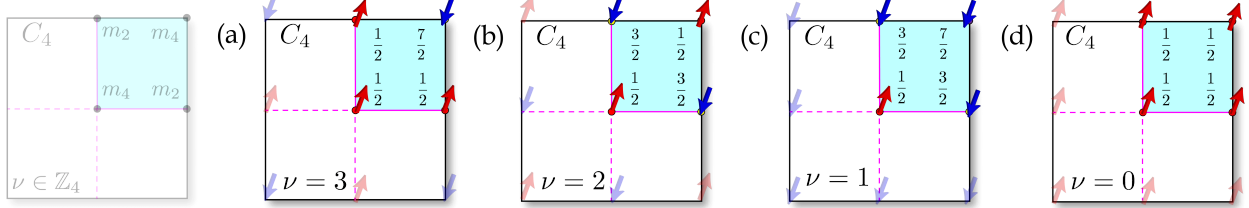
Figure 5.5. Examples of SPT fermionic phases in a crystal with C_4 symmetry. These phases are characterized by their SPT invariant $\nu = m_4(\Gamma) + m_4(M) + 2m_2(Y) + 2 \mod 4$ which determines the electronic Chern number up to a multiple of 4. In this case, $m_4 \in \mathbb{Z}_4 + {}^1\!/_2$ and $m_2 \in \mathbb{Z}_2 + {}^1\!/_2$ are modulo *half-integers*. (a), (b), (c) and (d) correspond to SPT fermionic phases of $\nu = 3, 2, 1$ and 0 respectively. The problem is more complicated for fermions because the charges are fractional and we must also account for the antisymmetric phases of a spinor wave function. As an example, the $\nu = 2$ phase has eigenvalues of $m_4(\Gamma) = m_4(M) = {}^1\!/_2$ at the center and vertices, with inversion eigenvalues of $m_2(Y) = m_2(X) = {}^3\!/_2 = -{}^1\!/_2$ at the edge centers: $\nu = {}^1\!/_2 + {}^1\!/_2 + 2 \times {}^3\!/_2 + 2 = 2$.

The Chern number is found by integrating the Berry curvature over the two-dimensional Brillouin zone,

$$\mathfrak{C}_n = \frac{1}{2\pi} \int_{\mathrm{BZ}} F_n(\mathbf{k}) d^2\mathbf{k}, \qquad \mathfrak{C}_n \in \mathbb{Z}, \tag{5.60}$$

which determines the winding number of the collective light-matter excitations over the torus $\mathbb{T}^2 = S^1 \times S^1$. Equation (5.60) is one of the central results of this paper. An electromagnetic Chern invariant can be found for any 2D crystal and characterizes distinct topological phases of matter $\mathfrak{C}_n \neq 0$.

5.4.2 Symmetry-protected topological bosonic phases

Evaluating the Chern number by brute force requires knowledge of the wave function at every point in the Brillouin zone. However, by invoking symmetry constraints of the cyclic groups, we can determine important properties of the topological phase from only a few isolated points in the Brillouin zone. This constitutes a type of symmetry-protected topological (SPT) phase [16], [100], [177]–[186] and is intimately tied to the spin-1 nature of electromagnetic field. SPT phases are protected by the N-fold rotational symmetry of C_N and this gives rise to an additional topological invariant $\nu_n \in \mathbb{Z}_N$. Remarkably, ν_n is classified entirely from $\eta_n(\mathbf{k}_p)$ eigenvalues at HSPs and requires no complicated integration to compute. This invariant is related to the Chern number up to a multiple of N,

$$\nu_n = \mathfrak{C}_n \mod N, \qquad \mathfrak{C}_n \in N\mathbb{Z} + \nu_n. \tag{5.61}$$

The interpretation of ν_n is quite simple – it tells us the geometric phase around the irreducible Brillouin zone (IBZ) of the crystal,

$$\exp\left(\mathrm{i}\frac{2\pi}{N}\mathfrak{C}_n\right) = \exp\left(\mathrm{i}\int_{\mathrm{IBZ}} F_n(\mathbf{k})d^2\mathbf{k}\right) = \exp\left(\mathrm{i}\oint_{\partial\mathrm{IBZ}} \mathbf{A}_n(\mathbf{k}) \cdot d\mathbf{k}\right), \tag{5.62}$$

where $\partial\mathrm{IBZ}$ is the path around IBZ. This follows from rotational symmetry of the Berry curvature $F_n(\mathbf{k}) = F_n(R\mathbf{k})$. For instance, the path in C_4 is $\partial(\mathrm{IBZ})_4 = \Gamma\mathrm{XMY}\Gamma$. Applying the logarithm, ν_n is equivalent to,

$$\nu_n = \frac{N}{2\pi}\oint_{\partial\mathrm{IBZ}} \mathbf{A}_n(\mathbf{k}) \cdot d\mathbf{k} \mod N. \tag{5.63}$$

As we will see more explicitly, ν_n is tied entirely to η_n. The reason is subtle – any vortex within the interior of the IBZ contributes a Berry phase of 2π, and by symmetry, there are N such vortices within the total Brillouin zone $\mathfrak{C}_n \to \mathfrak{C}_n + N$. However, this has no effect on $\nu_n \to \nu_n$. Only the vortices lying at HSPs contribute to ν_n because these come in fractions of 2π.

In the following sections we will discuss the bosonic classification of ν_n for each cyclic point group and the SPT phases associated with them. We do not present the full derivations here since the rigorous proofs have been carried out by others (see Ref. [100]) – we simply state the salient results. For completeness, in App. C.1 we also discuss the SPT *fermionic* phases associated with each point group. We do this to emphasize that fermionic and bosonic systems represent distinct topological field theories, with fundamentally different interpretations. These differences are highlighted with a few examples [Fig. 5.4 and 5.5].

5.4.3 Twofold (inversion) symmetry: C_2

For the C_2 point group, or simply inversion symmetry, the SPT phase is related to the Chern number by $\nu_n = \mathfrak{C}_n \mod 2$ which is a $\mathbb{Z}_2$ invariant. There is only one nontrivial SPT phase and it can be found modulo 2 from,

$$\exp\left(i\frac{2\pi}{2}\mathfrak{C}_n\right) = \eta_{2,n}(\Gamma)\eta_{2,n}(X)\eta_{2,n}(Y)\eta_{2,n}(M). \tag{5.64}$$

Applying the logarithm, this classification can be expressed equivalently in terms of $m_{2,n} \in \mathbb{Z}_2$ inversion eigenvalues,

$$\nu_n = m_{2,n}(\Gamma) + m_{2,n}(X) + m_{2,n}(Y) + m_{2,n}(M) \mod 2. \tag{5.65}$$

If the summation of $m_{2,n}$ eigenvalues is odd, the SPT phase is nontrivial $\nu_n = 1$ and corresponds to an odd-valued Chern number. Likewise, $\nu_n = 0$ is an even-valued Chern number.

5.4.4 Threefold symmetry: C_3

C_3 is unique because it is the only point group with an odd rotational symmetry – i.e. it lacks inversion symmetry. This means the parity of Chern number (odd or even) is not restricted by the symmetries of the crystal. For C_3, the SPT phase is $\nu_n = \mathfrak{C}_n \mod 3$ which is a $\mathbb{Z}_3$ invariant. There are two nontrivial SPT phases and they can be found modulo 3 from,

$$\exp\left(i\frac{2\pi}{3}\mathfrak{C}_n\right) = \eta_{3,n}(\Gamma)\,\eta_{3,n}(K)\,\eta_{3,n}(K). \tag{5.66}$$

This classification is expressed equivalently in terms of quantized modulo 3 integers $m_{3,n} \in \mathbb{Z}_3$ at HSPs,

$$\nu_n = m_{3,n}(\Gamma) + m_{3,n}(\mathrm{K}) + m_{3,n}(\mathrm{K}) \quad \mathrm{mod}\ 3. \tag{5.67}$$

Note though, odd and even phases are not distinct $\nu = -2 = 1 = 4$ under modulo 3.

5.4.5 Fourfold symmetry: C_4

For the C_4 point group, the SPT phase is related to the Chern number by $\nu_n = \mathfrak{C}_n$ mod 4 which is a $\mathbb{Z}_4$ invariant. There are three nontrivial SPT phases and they can be found modulo 4 from,

$$\exp\left(i\frac{2\pi}{4}\mathfrak{C}_n\right) = \eta_{4,n}\left(\Gamma\right)\eta_{4,n}\left(\mathrm{M}\right)\eta_{2,n}\left(\mathrm{Y}\right). \tag{5.68}$$

The classification is expressed equivalently in terms of spin-1 eigenvalues,

$$\nu_n = m_{4,n}(\Gamma) + m_{4,n}(\mathrm{M}) + 2m_{2,n}(\mathrm{Y}) \quad \mathrm{mod}\ 4, \tag{5.69}$$

where $m_{4,n}(\Gamma)$ & $m_{4,n}(\mathrm{M}) \in \mathbb{Z}_4$ are modulo 4 integers and $m_{2,n}(\mathrm{Y}) \in \mathbb{Z}_2$ is a modulo 2 integer. Examples of all SPT phases of the C_4 point group are displayed in Fig. 5.4 and these are compared with their fermionic counterparts in Fig. 5.5.

5.4.6 Sixfold symmetry: C_6

For the C_6 point group, the SPT phase is $\nu_n = \mathfrak{C}_n \quad \mathrm{mod}\ 6$ which is a $\mathbb{Z}_6$ invariant. There are five nontrivial SPT phases and they can be found modulo 6 from,

$$\exp\left(i\frac{2\pi}{6}\mathfrak{C}_n\right) = \eta_{6,n}\left(\Gamma\right)\eta_{3,n}\left(\mathrm{K}\right)\eta_{2,n}\left(\mathrm{M}\right). \tag{5.70}$$

This is equivalent to the summation of spin-1 eigenvalues at the HSPs,

$$\nu_n = m_{6,n}(\Gamma) + 2m_{3,n}(\mathrm{K}) + 3m_{2,n}(\mathrm{M}) \quad \mathrm{mod}\ 6, \tag{5.71}$$

where $m_{6,n}(\Gamma) \in \mathbb{Z}_6$ is a modulo 4 integer, $m_{6,n}(\mathrm{K}) \in \mathbb{Z}_3$ is a modulo 3 integer and $m_{2,n}(\mathrm{M}) \in \mathbb{Z}_2$ is a modulo 2 integer. This completes the classification of all 2+1D topological electromagnetic (bosonic) phases of matter which is summarized in Tbl. 5.1. These are compared alongside their fermionic counterparts in Tbl. 5.2.

5.4.7 Continuous symmetry: C_∞

To finish, we briefly discuss the continuum limit $\mathbf{g} = \mathbf{0}$ and the topological phases that can be described by a long wavelength theory $k \approx 0$. The physics is significantly more tractable here and exactly solvable models are possible [54], [116], [167]. In this limit, the rotational symmetry of the crystal is approximately continuous C_∞. The SPT invariant ν_n and Chern number $\mathfrak{C}_n$ are thus equivalent,

$$\nu_n = \mathfrak{C}_n = m_n(0) - m_n(\infty). \tag{5.72}$$

Note that $\nu_n \in \mathbb{Z}$ and $m_n \in \mathbb{Z}$ are not modulo integers in this limit and do not have the same interpretation as the lattice theory. This is because we have gained the full rotational symmetry in the continuum approximation. Clearly though, the spin eigenvalues must change at HSPs $m_n(0) \neq m_n(\infty)$ for a nontrivial phase to exist $\mathfrak{C}_n \neq 0$. In the continuum regularization, $k_p = 0$ represents the Γ point and $k_p = \infty$ is interpreted as mapping the vertices of the Brillouin zone into one another. We have provided a simple example of a continuum topological electromagnetic phase in App. C.2.

5.5 Conclusions

In summary, we have developed the complete 2+1D lattice field theory describing symmetry-protected topological bosonic phases of the photon. To accomplish this, we analyzed the electromagnetic Bloch waves in microscopic crystals and derived the Chern invariant of these light-matter excitations. Thereafter, the rotational symmetries of the crystal were examined extensively and the implications these have on photonic spin. We have studied all two dimensional point groups C_N with nonvanishing Chern number $\mathfrak{C} \neq 0$ and linked the topological

invariants directly to spin-1 quantized eigenvalues of the electromagnetic field – establishing the bosonic classification for each topological phase.

Acknowledgements

6. UNIDIRECTIONAL MAXWELLIAN SPIN WAVES

We develop a unified perspective of unidirectional topological edge waves in non-reciprocal media. We focus on the inherent role of photonic spin in non-reciprocal gyroelectric media, ie. magnetized metals or magnetized insulators. Due to the large body of contradicting literature, we point out at the outset that these Maxwellian spin waves are fundamentally different from well-known topologically trivial surface plasmon polaritons (SPPs). We first review the concept of a Maxwell Hamiltonian in non-reciprocal media, which immediately reveals that the gyrotropic coefficient behaves as a photon mass in two dimensions. Similar to the Dirac mass, this photonic mass opens bandgaps in the energy dispersion of bulk propagating waves. Within these bulk photonic bandgaps, three distinct classes of Maxwellian edge waves exist – each arising from subtle differences in boundary conditions. On one hand, the edge wave solutions are rigorous photonic analogs of Jackiw-Rebbi electronic edge states. On the other hand, for the exact same system, they can be high frequency photonic counterparts of the integer quantum Hall effect, familiar at zero frequency. Our Hamiltonian approach also predicts the existence of a third distinct class of Maxwellian edge wave exhibiting topological protection. This occurs in an intriguing topological bosonic phase of matter, fundamentally different from any known electronic or photonic medium. The Maxwellian edge state in this unique quantum gyroelectric phase of matter necessarily requires a sign change in gyrotropy arising from non-locality (spatial dispersion). In a Drude system, this behavior emerges from a spatially dispersive cyclotron frequency that switches sign with momentum. A signature property of these topological electromagnetic edge states is that they are oblivious to the contacting medium, ie. they occur at the interface of the quantum gyroelectric phase and any medium (even vacuum). This is because the edge state satisfies open boundary conditions – all components of the electromagnetic field vanish at the interface. Furthermore, the Maxwellian spin waves exhibit photonic spin-1 quantization in exact analogy with their supersymmetric spin-½ counterparts. The goal of this paper is to

discuss these three foundational classes of edge waves in a unified perspective while providing in-depth derivations, taking into account non-locality and various boundary conditions. Our work sheds light on the important role of photonic spin in condensed matter systems, where this definition of spin is also translatable to topological photonic crystals and metamaterials.

6.1 Introduction

Gyroelectric media, or magnetized plasmas, form the canonical system to study non-reciprocity [195]–[200]. There has been recent interest in such media for their potential to break the time-bandwidth limit inside cavities [201], [202], sub-diffraction imaging [203], unique absorption [204] and thermal properties [205], and for one-way topological transitions [206]. It should be emphasized that the gyroelectric coefficient (g), which embodies antisymmetric components of the permittivity tensor (ε_{ij}), is intimately related to its low frequency counterpart in condensed matter physics – the transverse Hall conductivity $(\sigma_H = \sigma_{xy} = -\mathrm{i}\omega g)$ [207], [208]. The goal of this paper is to bridge the gap between modern concepts in nanophotonics, magnetized plasma physics, and condensed matter physics.

Historically, gyroelectric media was popularized in plasma physics [87], [209] where the "gyration vector" or "rotation axis" sets a preferred handedness to the medium. This causes non-reciprocal (direction dependent) wave propagation along the axis of the medium. The non-reciprocal properties are now well understood but only recently has the connection with the Dirac equation been revealed [54], [63], [116], [139], [149], [150]. This immediately leads to multiple new insights related to energy density, photon spin and photon mass for wave propagation within two-dimensional gyrotropic media [54], [84], [116], [139]. In particular, a unique phenomenon related to gyrotropic media is the presence of unidirectional edge waves, fundamentally different from surface plasmon polaritons (SPPs) or Dyakonov waves [210]–[212]. We note that photonic crystals [213]–[215] or metamaterials [170], [216], [217] are not necessary for this phenomenon and even a continuous medium (eg: magnetized plasma or doped semiconductor) can host unidirectional edge waves.

The role of spin has not been revealed till date but chiral (unidirectional) photonic waves in gyrotropic media have a rich history. Early work introduced the concept of optical isomers [218] which is the interface of two gyrotropic media with opposite signs of non-

reciprocal coefficients (half-space of $g > 0$ interfaced with another half-space of $g < 0$). It was shown that unique chiral edge states emerge, addressed as the "quantum Cotton-Mouton effect", which are similar in nature to the electronic quantum Hall effect. These chiral edge states were also predicted on the interface of Weyl semimetals [219]. Raghu and Haldane's original model to realize a one-way waveguide dealt with the gyroelectric photonic crystals [19], [20]. More recently, gyroelectric magneto-plasmons have been demonstrated in quantum well structures under biasing magnetic fields [76], [220]. Another important example of unidirectional edge waves occurs when a gyrotropic medium is terminated with a perfect electric conductor (PEC), as shown by Silveirinha [74], [221]. Horsley [139] recently proved that this PEC boundary is equivalent to antisymmetric solutions of optical isomers (two gyrotropic media with opposite signs $\pm g$) and leads to unidirectional Jackiw-Rebbi type photonic waves [222].

However, in all the above examples, the electromagnetic boundary conditions are drastically different from the *open* boundary conditions utilized for topologically-protected solutions of the Dirac equation [92]–[94], [223]–[225]. This challenge was recently overcome when a Dirac-Maxwell correspondence was applied to gyrotropic media [54], [116], which derived the supersymmetric (spin-1) partner of the topological Dirac equation. This framework gave rise to a new unidirectional edge wave with open boundary conditions, such that the electromagnetic field completely vanishes at the material interface [54], [116]. The necessary conditions for the existence of such a wave is non-reciprocity g, temporal dispersion $g(\omega)$, and spatial dispersion $g(\omega, k)$. A momentum dependent sign change in the gyrotropic coefficient $g(\omega, k_{\mathrm{crit}}) = 0$ leads to a topologically nontrivial electromagnetic field – a quantum gyroelectric phase of matter. In Drude systems, this corresponds to a momentum dependent sign change of the cyclotron frequency. It should be emphasized that this topological phase of matter is Maxwellian (spin-1 bosonic) and is unlike any known spin-½ fermionic phases of matter (eg: graphene, Chern insulator, etc.). The unidirectional photonic edge wave is a fundamental mode of this nonlocal, non-reciprocal medium and cannot be separated from the bulk. The contacting medium has no influence on the edge wave, unlike the previously mentioned examples which are sensitive to boundary conditions. We address this

phenomenon as the quantum gyroelectric effect (QGEE) and it remains an open question whether such a Maxwellian phase of matter can be found in nature [164].

The purpose of this paper is to present the first unified view of all the aforementioned unidirectional edge waves in non-reciprocal media. The essence of our results is captured in Fig. 6.1 and Tab. 6.1 which contrasts unidirectional edge waves of the quantum gyroelectric effect (QGEE), photonic quantum Hall (PQH) states and photonic Jackiw-Rebbi (PJR) states. All such waves appear in gyroelectric media but boast surprisingly different behavior. The QGEE displays bulk-boundary correspondence [224] since it is defined independent of the contacting medium [Sec. 6.4]. The PQH states host a high frequency quantum Hall edge current which arises from a discontinuity in the electromagnetic field [Sec. 6.6]. Lastly, the PJR edge waves are domain wall states [Sec. 6.7]. Another important result of our paper is illustrated in Fig. 6.2 which shows that the two classes of unidirectional waves, PQH and PJR, can be realized at perfect magnetic conductor (PMC) and perfect electric conductor (PEC) boundary conditions respectively.

This article is organized as follows. Sec. 6.2 presents an overview of spin waves. In Sec. 6.3 and 6.4 we show that a nonlocal, non-reciprocal medium is foundational to the concept of 2+1D topological phases of matter. We review the concept of Dirac-Maxwell correspondence which can be exploited to introduce a Hamiltonian for light within complex photonic media. This framework allows us to rigorously define helicity and spin while also identifying a photonic mass, which is directly proportional to the gyrotropic coefficient. We then discuss the necessity of temporally and spatially dispersive optical response parameters to define electromagnetic topological invariants for bulk continuous media. Although commonly ignored, nonlocality is absolutely essential for the electromagnetic theory to be consistent with the tenfold way [15], which describes all possible continuum topological phases, in every dimension. In the topologically nontrivial regime $C \neq 0$, the unidirectional Maxwellian spin wave is derived and satisfies open boundary conditions – this is the QGEE. Following these results, we analyze the interface of optical isomers [Sec. 6.5], deriving the photonic quantum Hall [Sec. 6.6] and photonic Jackiw-Rebbi edge states [Sec. 6.7]. The final Sec. 6.8 presents our conclusions. As a resource, we have also provided a general review of topological phases in continuum photonic media which can be found in the Appendix.

6.2 Overview of spin waves

We outline the key properties of chiral Maxwellian spin waves which, surprisingly, emerge in two distinct physical systems. First, it is identified in the low momentum dispersion $k \approx 0$ of the QGEE. Second, it also represents the photonic counterpart of the Jackiw-Rebbi domain wall state known in the continuum Dirac equation [93], [225]–[227]. The Dirac Jackiw-Rebbi wave exists at the interface of inverted masses, $\Lambda > 0$ and $\Lambda < 0$, and is an eigenstate of the spin-½ helicity (Pauli) operator. The exact parallel in photonics can now be established as it has been proven that gyrotropy plays the role of photonic mass. Thus, a unique Maxwellian spin wave exists at the interface of optical isomers, $g > 0$ and $g < 0$. Furthermore, this electromagnetic wave is an eigenstate of the SO(3) operator (spin-1 helicity operator) and exhibits helical quantization. This is intuitively clear since the edge wave is purely transverse electro-magnetic (TEM); the polarization is orthogonal to the momentum $\hat{k} \cdot \mathbf{E} = 0$.

To avoid confusion, we contrast between conventional surface plasmon polaritons (SPPs) and Maxwellian spin waves which both display spin-momentum locking phenomena but in fundamentally different forms. Even SPPs on magnetized plasmas do not show the same characteristics as chiral Maxwellian spin waves as they are not eigenstates of the SO(3) vector operators. We strongly emphasize that SPPs on conventional (electric) metals, magnetic metals, as well as negative index media [228] do not possess any topological characteristics. There exists no bulk-boundary correspondence as the bulk media are trivial. Spin-momentum locking in these surface waves is transverse and not quantized [26], [36], [83], [157], [158], [229]–[232]. This means the spin is perpendicular to the momentum and is a continuous (classical) number. On the contrary, spin-momentum locking arising in Maxwellian spin waves is longitudinal and quantized. This means the spin is parallel to the momentum and is a discrete (quantum) number, assuming values of ± 1 only. Despite recent observations of spin-momentum locking phenomena in waveguides [33], [233], resonators [234], [235] and surface plasmon polaritons [38], no wave has been discovered to be a pure spin state with quantized eigenvalues of the helicity operator. Our work is an answer to this endeavor.

As an aside, we must also point out that orbital angular momentum (OAM) quantization for photons is unrelated to topological quantization, such as Chern number quantization.

OAM quantization is routinely encountered for classical optical waves in free-space beams [140], microdisk resonators, optical fibers, whispering gallery mode resonators [236], etc. The origin of topological quantization is always a singularity/discontinuity in the underlying gauge potential [237]–[239]. This phenomenon of gauge singularity/discontinuity has been proven to occur in the Berry connection of the quantum gyroelectric phase [54], [116]. Nevertheless, it remains an open question whether such topological quantization is connected to physical observables (response/correlation functions) of the photon, like they are for the electron. For example, quantization of the Hall conductivity σ_H was the first striking experimental observable connected to topology [108], [240]. No photonic equivalent is known to date.

6.3 Maxwell Hamiltonian

6.3.1 Vacuum

Before defining Maxwellian spin waves [Fig. 6.1], that emerge at the boundaries of matter, we illustrate the direct correspondence of spin operators arising in Maxwell's equations and the massless Dirac equation in 2+1D. We will then show that this correspondence extends to *massive* particles in Sec. 6.3.3. In two spatial dimensions we can focus strictly on transverse-magnetic (TM) waves, where the magnetic field H_z is perpendicular to the plane of propagation $\mathbf{k} = k_x \hat{x} + k_y \hat{y}$. Maxwell's equations in the reciprocal momentum space $\mathcal{H}_0(\mathbf{k})$ are expressed compactly as [54], [116], [139],

$$\mathcal{H}_0(\mathbf{k})f = \omega f, \qquad f = \begin{bmatrix} E_x \\ E_y \\ H_z \end{bmatrix}. \tag{6.1}$$
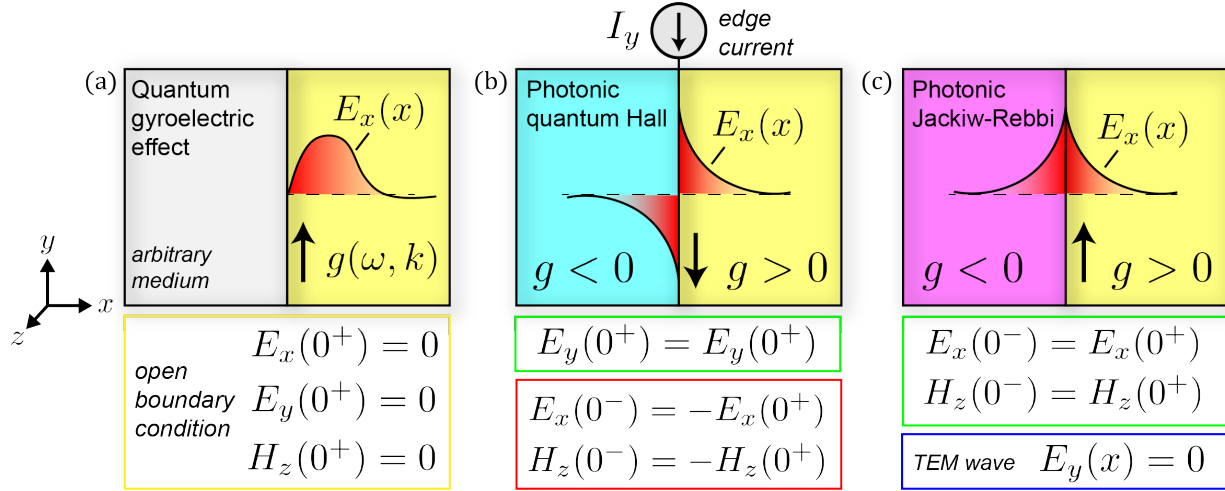
Figure 6.1. (a), (b) and (c) are schematics of the quantum gyroelectric effect (QGEE), photonic quantum Hall (PQH) and photonic Jackiw-Rebbi (PJR) edge states respectively. The characteristic spatial profile of $E_x(x)$ is displayed for each edge state along with the corresponding boundary conditions. (a) The QGEE is a topologically-protected unidrectional (chiral) edge state and exists at the boundary of any medium – even vacuum. The QGEE is fundamentally tied to nonlocal (spatially dispersive) gyrotropy $g(\omega, k)$ and can never be realized in a purely local model. (b) The PQH edge state is the photonic analogue of the quantum Hall effect and hosts a high-frequency edge current I_y. The presence of the edge current $I_y \neq 0$ creates a discontinuity in the fields across the boundary, $E_x(0^-) \neq E_x(0^+)$ and $H_z(0^-) \neq H_z(0^+)$. (c) The PJR edge state is the photonic equivalent of the inverted mass problem arising in the Dirac equation. This state possesses no edge current $I_y = 0$ and is completely transverse electro-magnetic (TEM) as the longitudinal field vanishes entirely $E_y(x) = 0$.

f is the TM polarization of the electromagnetic field and is operated on by the free-space "Maxwell Hamiltonian",

$$\mathcal{H}_0(\mathbf{k}) = \begin{bmatrix} 0 & 0 & -k_y \\ 0 & 0 & k_x \\ -k_y & k_x & 0 \end{bmatrix} = k_x \hat{S}_x + k_y \hat{S}_y. \tag{6.2}$$

Maxwell's equations describe optical helicity, ie. the projection of the momentum $\mathbf{k}$ onto the spin $\vec{S}$. In this case, $\hat{S}_x$ and $\hat{S}_y$ are spin-1 operators that satisfy the angular momentum algebra $[\hat{S}_i, \hat{S}_j] = i\epsilon_{ijk}\hat{S}_k$. These operators are expressed in matrix form as,

$$\hat{S}_x = \begin{bmatrix} 0 & 0 & 0 \\ 0 & 0 & 1 \\ 0 & 1 & 0 \end{bmatrix}, \qquad \hat{S}_y = \begin{bmatrix} 0 & 0 & -1 \\ 0 & 0 & 0 \\ -1 & 0 & 0 \end{bmatrix}, \qquad \hat{S}_z = \begin{bmatrix} 0 & -i & 0 \\ i & 0 & 0 \\ 0 & 0 & 0 \end{bmatrix}. \tag{6.3}$$

$\hat{S}_z$ is the spin-1 operator along $\hat{z}$ and generates rotations in the x-y plane. As we will see, $\hat{S}_z$ is fundamentally tied to photonic mass in two dimensions. To prove this, we will first review the definition of mass for two-dimensional Dirac particles and show there is a one-to-one correspondence with photons.

6.3.2 Dirac equation

For comparison, consider the two-dimensional massless Dirac equation, which often describes the quasiparticle dynamics of graphene [241], [242]. This is also known as the Weyl equation,

$$H_0(\mathbf{k})\Psi = E\Psi. \tag{6.4}$$

Ψ is a two-component spinor function and is acted on by the massless Dirac Hamiltonian,

$$H_0(\mathbf{k}) = k_x\sigma_x + k_y\sigma_y. \tag{6.5}$$

Like Maxwell's equations, the Weyl equation represents electronic helicity – the projection of momentum $\mathbf{k}$ onto the spin $\vec{\sigma}$. In this case, $[\sigma_i, \sigma_j] = 2i\epsilon_{ijk}\sigma_k$ are the Pauli matrices and describe the dynamics of a spin-½ or pseudospin-½ particle,

$$\sigma_x = \begin{bmatrix} 0 & 1 \\ 1 & 0 \end{bmatrix}, \qquad \sigma_y = \begin{bmatrix} 0 & -i \\ i & 0 \end{bmatrix}, \qquad \sigma_z = \begin{bmatrix} 1 & 0 \\ 0 & -1 \end{bmatrix}. \tag{6.6}$$

As we can see, the σ_z Pauli matrix is clearly missing from the Weyl equation [Eq. (6.5)]. We cannot add a term proportional to σ_z due to time-reversal symmetry,

$$\mathcal{T}^{-1} H_0(-\mathbf{k})\mathcal{T} = H_0(\mathbf{k}), \qquad \mathcal{T} = i\sigma_y \mathcal{K}. \tag{6.7}$$

$\mathcal{K}$ represents the complex conjugation operator in this context and $\mathcal{T}^2 = -\mathbb{1}_2$ is a fermionic operator.

However, if we break time-reversal symmetry $\mathcal{T}^{-1} H(-\mathbf{k})\mathcal{T} \neq H(\mathbf{k})$ then σ_z is permitted. This transforms the massless Weyl equation to the massive Dirac equation $H_0(\mathbf{k}) \to H(\mathbf{k})$,

$$H(\mathbf{k}) = v(k_x \sigma_x + k_y \sigma_y) + \Lambda \sigma_z. \tag{6.8}$$

We have also introduced the Fermi velocity v which describes the effective electron speed. Equation (6.8) models a multitude of problems in condensed matter physics, such as Dirac particles and the p-wave superconductor [243]. The Dirac mass Λ has many important properties. It respects rotational symmetry in the x-y plane and opens a band gap at $E = 0$,

$$E^2 - \Lambda^2 = v^2 k^2, \tag{6.9}$$

with $k^2 = k_x^2 + k_y^2$. It is clear that when $E^2 < \Lambda^2$, waves decay exponentially into the medium. The rest energy $E^2 = \Lambda^2$ defines the stationary point $k = 0$. Furthermore, the Dirac mass also breaks parity (mirror) symmetry in both x and y dimensions. For Dirac particles, the mirror operators are simply,

$$\mathcal{P}_x = \sigma_y, \qquad \mathcal{P}_y = \sigma_x. \tag{6.10}$$

One can easily check that $\mathcal{P}_x^{-1} H(-k_x) \mathcal{P}_x \neq H(k_x)$ and $\mathcal{P}_y^{-1} H(-k_y) \mathcal{P}_y \neq H(k_y)$ do not commute when $\Lambda \neq 0$. A review of Jackiw-Rebbi Dirac states arising at the interface of inverted masses $\pm \Lambda$ is presented in App. D.1.

6.3.3 Definition of photon mass in gyrotropic media

The question now: what is the equivalent of mass for the photon? In analogy with the Dirac equation, the photon mass must respect rotational symmetry but break parity and time-reversal. The answer is a bit subtle. There are two components of the permittivity tensor ε_{ij} that are permitted by rotational symmetry in the plane,

$$\varepsilon_{ij} = \varepsilon \delta_{ij} + ig\epsilon_{ij}. \tag{6.11}$$

ε is the diagonal part (scalar permittivity) and g is the off-diagonal part (gyrotropy). $\epsilon_{ij} = -\epsilon_{ji}$ is the 2D antisymmetric tensor and should not be confused with the permittivity tensor ε_{ij} itself. To put Maxwell's equations into a more enlightening form, we normalize f by,

$$f \rightarrow \mathfrak{F} = \begin{bmatrix} \sqrt{\varepsilon} E_x \\ \sqrt{\varepsilon} E_y \\ H_z \end{bmatrix}. \tag{6.12}$$

Inserting the permittivity tensor, the vacuum wave equation [Eq. (6.1)] is transformed to $\mathcal{H}_0(\mathbf{k}) \rightarrow \mathcal{H}(\mathbf{k})$,

$$\mathcal{H}(\mathbf{k})\mathfrak{F} = \omega \mathfrak{F}, \tag{6.13}$$

where the effective Maxwell Hamiltonian is expressed as,

$$\mathcal{H}(\mathbf{k}) = v_p(k_x \hat{S}_x + k_y \hat{S}_y) + \Lambda_p \hat{S}_z. \tag{6.14}$$

171

By direct comparison with the massive Dirac equation [Eq. (6.8)], we see that v_p is the effective speed of light and Λ_p is the effective photon mass,

$$v_p = \frac{1}{\sqrt{\varepsilon}}, \qquad \Lambda_p = \omega \frac{g}{\varepsilon}. \tag{6.15}$$

The one significant difference between the two equations is that $\vec{S}$ are spin-1 operators while $\vec{\sigma}$ are spin-½ operators. This is intuitive because the photon is a bosonic particle. In fact, massive Dirac particles [Eq. (6.8)] and massive photons [Eq. (6.14)] are supersymmetric partners in two dimensions [151]. It should be emphasized however, that ε and g are always dispersive which means the effective speed $v_p = v_p(\omega)$ and effective mass $\Lambda_p = \Lambda_p(\omega)$ depend on the energy ω.

Like the Dirac equation, the photon mass $\Lambda_p \neq 0$ is proportional to the $\hat{S}_z$ operator and breaks time-reversal symmetry,

$$\mathcal{T}^{-1}\mathcal{H}(-\mathbf{k})\mathcal{T} \neq \mathcal{H}(\mathbf{k}), \qquad \mathcal{T} = \begin{bmatrix} 1 & 0 & 0 \\ 0 & 1 & 0 \\ 0 & 0 & -1 \end{bmatrix} \mathcal{K}, \tag{6.16}$$

where $\mathcal{T}^2 = +\mathbb{1}_3$ is a bosonic operator. For photons, the mirror operators in the x and y dimensions are defined as,

$$\mathcal{P}_x = \begin{bmatrix} -1 & 0 & 0 \\ 0 & 1 & 0 \\ 0 & 0 & -1 \end{bmatrix}, \qquad \mathcal{P}_y = \begin{bmatrix} 1 & 0 & 0 \\ 0 & -1 & 0 \\ 0 & 0 & -1 \end{bmatrix}. \tag{6.17}$$

Note, $H_z \to -H_z$ is odd under mirror symmetry since it transforms as a pseudoscalar. One can easily check that parity (mirror) symmetry is broken in both dimensions, $\mathcal{P}_x^{-1}\mathcal{H}(-k_x)\mathcal{P}_x \neq \mathcal{H}(k_x)$ and $\mathcal{P}_y^{-1}\mathcal{H}(-k_y)\mathcal{P}_y \neq \mathcal{H}(k_y)$, when $\Lambda_p \neq 0$. Hence, Λ_p transforms exactly as a mass but for spin-1 particles.

Utilizing Maxwell's equations [Eq. (6.14)], it is straightforward to derive the dispersion relation of the bulk TM waves,

$$\omega^2 - \Lambda_p^2 = v_p^2 k^2, \tag{6.18}$$

which is identical to the massive Dirac dispersion [Eq. (6.9)]. Rearranging, we obtain the dispersion relation in terms of ε and g explicitly,

$$\omega^2 \left(\frac{\varepsilon^2 - g^2}{\varepsilon} \right) = \omega^2 \varepsilon_{\text{eff}} = k^2. \tag{6.19}$$

ε_{eff} is the effective permittivity seen by the electromagnetic field,

$$\varepsilon_{\text{eff}} = \frac{\varepsilon^2 - g^2}{\varepsilon}. \tag{6.20}$$

It is clear that whenever $\varepsilon_{\text{eff}} < 0$, electromagnetic waves decay exponentially into the medium. The "rest energies" are the frequencies at which $\varepsilon_{\text{eff}} = 0$ and define the stationary points $k = 0$. This occurs precisely when $\varepsilon^2 = g^2$, or equivalently $\omega^2 = \Lambda_p^2$.

6.3.4 Drude model under an applied magnetic field

The conventional Drude model, under a biasing magnetic field B_0, treats the electron density as an incompressible gas. The Drude model is characterized by two parameters: the plasma frequency ω_p and the cyclotron frequency $\omega_c = eB_0/M^*$, where e is elementary charge and M^* is the effective mass of the electron. Assuming an applied field in the $-\hat{z}$ direction, the scalar permittivity ε and gyrotropic coefficient g are expressed as,

$$\varepsilon = 1 + \frac{\omega_p^2}{\omega_c^2 - \omega^2}, \qquad g = \frac{\omega_c \omega_p^2}{\omega(\omega_c^2 - \omega^2)}. \tag{6.21}$$

The effective photonic mass Λ_p is therefore,

$$\Lambda_p = \omega \frac{g}{\varepsilon} = \frac{\omega_c \omega_p^2}{\omega_p^2 + \omega_c^2 - \omega^2}. \tag{6.22}$$

Due to dispersion, the photon sees a different mass at varying frequencies ω and vanishes at sufficiently high energy $\lim_{\omega \to \infty} \Lambda_p \to 0$. However, the mass is infinite $\lim_{\omega \to \omega_0} \Lambda_p \to \infty$ when the frequency is on resonance $\omega_0 = \sqrt{\omega_p^2 + \omega_c^2}$, which corresponds to the epsilon-near-zero (ENZ) [244] condition $\varepsilon(\omega_0) = 0$.

The natural eigenmodes of the system $\omega = \omega(k)$, ie. the bulk propagating modes, represent self-consistent solutions to the wave equation, when k and ω are both real-valued. Plugging our Drude parameters into Eq. (6.19), we uncover two bulk eigenmode branches $\omega = \omega_\pm$,

$$\omega_\pm^2 = \frac{1}{2} \left[2\omega_p^2 + \omega_c^2 + k^2 \pm \sqrt{4\omega_p^2 \omega_c^2 + (\omega_c^2 - k^2)^2} \right]. \tag{6.23}$$

ω_+ and ω_- are the high and low energy eigenmodes respectively. Besides breaking parity and time-reversal, gyrotropy also hybridizes transverse and longitudinal waves. When $\omega_c = 0$, the high frequency mode reduces to the transverse $(\mathbf{k} \cdot \mathbf{E} = 0)$ bulk plasmon $\omega_+ = \sqrt{\omega_p^2 + k^2}$ while the low frequency mode $\omega_- = \omega_p$ reduces to the longitudinal $(\mathbf{k} \cdot \mathbf{E} \neq 0)$ plasmon. These modes are degenerate at the stationary point $k = 0$. However, when $\omega_c \neq 0$, the $\omega_\pm$ bands are fully gapped and the degeneracy at $k = 0$ is removed,

$$\omega_\pm(0) = \frac{1}{2} \left| \sqrt{4\omega_p^2 + \omega_c^2} \pm \omega_c \right|. \tag{6.24}$$

These represent the rest energies $\varepsilon^2 = g^2$ (or $\omega^2 = \Lambda_p^2$). Likewise, the asymptotic dependence in the local Drude model is,

$$\lim_{k \to \infty} \omega_+ \to k, \qquad \lim_{k \to \infty} \omega_- \to \omega_0 = \sqrt{\omega_p^2 + \omega_c^2}. \tag{6.25}$$

The high energy branch ω_+ approaches the free-photon dispersion where the effective photon mass $\Lambda_p \to 0$ vanishes. The low energy branch ω_- approaches a completely flat dispersion due to an infinite effective mass $\Lambda_p \to \infty$.

Table 6.1. Summary of the three unidirectional (chiral) photonic edge states arising in two-dimensional gyroelectric media, with their important properties listed. The quantum gyroelectric effect (QGEE) is a topologically-protected edge state and exists at any boundary – even vacuum. The photonic quantum Hall (PQH) edge state emerges at a perfect magnetic conductor (PMC) boundary condition. These edge states are unique because they carry a high frequency quantum Hall edge current I_y. The photonic Jackiw-Rebbi (PJR) edge states are the electromagnetic analogue of the inverted Dirac mass problem and arise at a perfect electric conductor (PEC) boundary condition.

Edge state	QGEE	PQH	PJR
Boun. cond.	Open: $f(0) = 0$	PMC: $\mathcal{P}_x f(-x) = +f(x)$	PEC: $\mathcal{P}_x f(-x) = -f(x)$
Nonlocality?	yes	no	no
Chiral?	yes	yes	yes
$\mathcal{T}$ broken?	yes	yes	yes
$\mathcal{P}_x$ broken?	yes	no	no
$\mathcal{P}_y$ broken?	yes	yes	yes
TEM wave?	yes ($k \approx 0$)	no	yes
Top.-protected?	yes	no	no

6.4 Quantum gyroelectric effect (QGEE)

6.4.1 Topological Drude model

To make the Drude model topological and uncover topologically-protected edge states, we need to incorporate spatial dispersion (nonlocality). This purely nonlocal phenomenon has been dubbed the quantum gyroelectric effect (QGEE) and has only been proposed very recently [54], [116]. A more thorough discussion of temporal and spatial dispersion is provided in App. D.3 and D.4. In the hydrodynamic Drude model, nonlocality emerges when we treat the electron density as a compressible gas. The electron pressure behaves like a restoring force and introduces a first order momentum correction to the longitudinal plasma frequency,

$$(\omega_p^2)_L \to \omega_p^2 + \beta^2 k^2 = (\omega_p + \beta k)^2 - 2\omega_p \beta k. \tag{6.26}$$

However, topological phases require second order momentum corrections at minimum – we must go beyond the hydrodynamic Drude model. Both the plasma frequency,

$$\omega_p \to \Omega_p = \omega_p + \beta_p k^2, \tag{6.27}$$

and the cyclotron frequency,

$$\omega_c \to \Omega_c = \omega_c + \beta_c k^2, \tag{6.28}$$

must be expanded to second order in k. This will alter the behavior of deep subwavelength fields $k \to \infty$ [Eq. (6.25)] which has very important topological implications. We stress this point as it is imperative to all topological field theories. Spatial dispersion is fundamentally necessary if the electromagnetic theory is to be consistent with the tenfold way [15], which describes all possible continuum topological phases. A rigorous proof is provided in App. D.5.

Physically, this nonlocal behaviour arises from high momentum corrections to the effective electron mass M^*, since the electronic bands are not perfectly parabolic,

$$\frac{1}{M^*} = \frac{1}{\hbar^2} \frac{\partial^2 E}{\partial k^2} = \frac{1}{M_0} + \frac{1}{M_2}(ka)^2 + \dots \tag{6.29}$$

a is the lattice constant in this case. The cyclotron frequency corrected to second order $\Omega_c = \omega_c + \beta_c k^2$ is thus,

$$\omega_c = \frac{eB_0}{M_0}, \qquad \beta_c = \frac{eB_0 a^2}{M_2}. \tag{6.30}$$

In App. D.6, we show that the electromagnetic Chern number $C_\pm$ for each band $\omega = \omega_\pm$, is determined by the relative sign of the cyclotron parameters,

$$C_\pm = \mp \left[\text{sgn}(\omega_c) - \text{sgn}(\beta_c) \right]. \tag{6.31}$$

Alternately, Eq. (6.31) is expressed in terms of the relative signs of the effective electron masses, M_0 and M_2, and the applied magnetic field B_0,

$$C_\pm = \mp[\text{sgn}(M_0) - \text{sgn}(M_2)]\text{sgn}(B_0). \tag{6.32}$$

If $M_0 M_2 < 0$, the electromagnetic phase is topologically nontrivial $|C_\pm| = 2$ which requires a change in sign of $1/M^*$ with momentum k. In other words, the cyclotron frequency must change sign $\omega_c \beta_c < 0$. This implies the electronic band has an inflection point at some finite momentum $1/M^* = \partial^2 E / \partial k^2 = 0$ such that the curvature of the band changes. More precisely, if there are an odd number of inflection points, $1/M^*$ changes sign an odd number of times, which always produces $|C_\pm| = 2$. It is important to note; in the continuum theory, a Chern number of $|C| = 1$ is only possible when magnetism (μ) is present. All gyrotropic phases possess Chern numbers of $|C| = 2$ which is guaranteed by continuous SO(2) rotational symmetry [54]. A proof is provided in App. D.6. However, in a lattice theory [100], [164], the restrictions on C are relaxed because we only have discrete rotational symmetries – any Chern number is generally permitted $C \in \mathbb{Z}$.

6.4.2 Weak magnetic field approximation

A complete analysis of the topological Drude model warrants its own dedicated paper. Here, we examine only the topological edge states arising in a weak magnetic field $\Omega_c \approx 0$ approximation, at energies far above the cyclotron frequency $\omega \gg \omega_c$. We also ignore any hydrodynamic corrections since they do not affect the topology of the electromagnetic field.

The main goal of this section is to demonstrate how nonlocal gyrotropy $g(\omega, k)$ leads to topological phenomena [54], [116] that can never be realized in a purely local theory.

Assuming $\Omega_c \approx 0$ is sufficiently small and $\omega \gg \omega_c$, we obtain at first approximation ($k \approx 0$),

$$\varepsilon(\omega) \approx 1 - \frac{\omega_p^2}{\omega^2}, \qquad g(\omega, k) \approx -\frac{\omega_p^2}{\omega^3}(\omega_c + \beta_c k^2). \tag{6.33}$$

Only the gyrotropic coefficient g adds nonlocal corrections since it is linearly proportional in Ω_c, but is considerably weak. Nevertheless, a unidirectional edge state always exists if $\omega_c \beta_c < 0$, which corresponds to the topologically nontrivial regime [Eq. (6.31)]. We now define,

$$g(\omega, k) = g_0(\omega) - g_2(\omega)k^2, \tag{6.34}$$

with,

$$g_0 = -\frac{\omega_c \omega_p^2}{\omega^3}, \qquad g_2 = \frac{\beta_c \omega_p^2}{\omega^3}. \tag{6.35}$$

Due to nonlocality in g, there are now two characteristic wavelengths $k_{1,2}^2$, which implies two decay channels are active $\eta_{1,2} = \sqrt{k_y^2 - k_{1,2}^2}$. The edge state dispersion $\omega = \omega(k_y)$ is determined by the boundary condition which must be insensitive to perturbations at $x = 0$. Therefore, we must search for open boundary solutions, such that every component of the electromagnetic field vanishes at $x = 0$,

$$f(0) = 0. \tag{6.36}$$

The open boundary condition [92]–[94], [223]–[225] is fundamental to topologically-protected edge states. No conventional surface wave, such as SPPs, Dyakonov, Tamm waves, etc. [245] satisfies this constraint since their very existence hinges on the boundary condition. For instance, SPPs intrinsically require a metal-dielectric boundary condition. Conversely, topologically-protected edge states of the QGEE exist at any boundary, since they are defined independent of the contacting medium. This is a statement of bulk-boundary correspondence [224].

6.4.3 Topologically-protected chiral edge states

We now impose open boundary conditions on the electromagnetic $f(0) = 0$ and look for nontrivial solutions $f(x > 0) \neq 0$ that simultaneously decay into the bulk $f(x \to \infty) \to 0$. Since f contains three components, E_x, E_y and H_z, the system of equations is overdetermined unless one of the equations can be made linearly dependent on the other two. Based on insight derived from the Dirac equation, we find that the only nontrivial solution requires $E_y(x) = 0$. This represents a completely transverse electro-magnetic (TEM) wave as there is no component of the field parallel to the momentum k_y. The two decay lengths $\eta_{1,2}$ are roots of the secular equation,

$$\frac{k_y}{\varepsilon} \left(g_0 - g_2 k_y^2 + g_2 \eta^2 \right) = \eta, \qquad k_y^2 = \omega^2 \varepsilon, \tag{6.37}$$

which produces,

$$\eta_{1,2} = \frac{1}{2g_2} \left[\frac{\varepsilon}{k_y} \pm \sqrt{\left(\frac{\varepsilon}{k_y} \right)^2 + 4g_2(g_2 k_y^2 - g_0)} \right]. \tag{6.38}$$

Notice that an edge state only exists when $\varepsilon > 0$ is positive. This is very different from SPPs which require a negative permittivity. For our weak field approximation, the edge dispersion is simply,

$$\omega^2 = \omega_p^2 + k_y^2. \tag{6.39}$$

A solution always exists whenever $k_y^2 < g_0 g_1 > 0$ such that both $\mathrm{Re}\,[\eta_{1,2}] > 0$ are decaying modes. This criterion is only satisfied in the topologically nontrivial regime $\omega_c \beta_c < 0$, confirming our theory. $\mathrm{sgn}(\omega_c) = \mathrm{sgn}(-\beta_c) = +1$ is a backward propagating wave while $\mathrm{sgn}(\omega_c) = \mathrm{sgn}(-\beta_c) = -1$ is forward propagating. The edge state is completely unidirectional (chiral) since $k_y \to -k_y$ cannot be a simultaneous solution. Back-scattering is forbidden.

After a bit of work, we obtain the final expression for the (low momentum) topologically-protected edge state,

$$f(x \geq 0) = \begin{bmatrix} E_x \\ E_y \\ H_z \end{bmatrix} = f_0\left(\hat{x} - s_{k_y}\sqrt{\varepsilon}\hat{z} \right)\left(\mathrm{e}^{-\eta_1 x} - \mathrm{e}^{-\eta_2 x} \right). \tag{6.40}$$

$s_{k_y} = \mathrm{sgn}(k_y)$ is the sign of the momentum which dictates the direction of propagation. f_0 is a proportionality constant. Remarkably, the edge wave behaves identically to a vacuum photon (completely transverse polarized) but with a modified dispersion. Indeed, they are helically quantized along the direction of propagation $\hat{k} = \hat{y}$. This is the definition of longitudinal spin-momentum locking as f is an eigenstate of $\hat{S}_y$,

$$\hat{S}_y\mathfrak{F} = s_{k_y}\mathfrak{F}, \qquad \mathfrak{F} = \begin{bmatrix} \sqrt{\varepsilon}E_x \\ \sqrt{\varepsilon}E_y \\ H_z \end{bmatrix}. \tag{6.41}$$

$\hat{k} \cdot \vec{S} = \hat{S}_y$ is the helicity operator along $\hat{y}$, which was defined in Eq. (6.3). Notice that the spin is quantized $s_{k_y} = \mathrm{sgn}(k_y) = \pm 1$ and completely locked to the momentum as it depends on the direction of propagation. A summary of the QGEE and its intriguing properties is listed in Tab. 6.1. Its important to note; from the conventional bulk-boundary correspondence (BBC), a Chern number of $|C| = 2$ usually suggests two unidirectional edge states. However, spin-1 bosons (like the photon) have shown single edge states [56], [58]–[61] even though the Chern number is $|C| > 1$. A rigorous proof of BBC for gauge theories is still an open problem. Nevertheless, that does not leave out the possibility of another edge state, at perhaps higher momentum, as we only solved the long wavelength limit $k \approx 0$. This will be considered in a future paper that analyzes the topological Drude model more thoroughly.

6.5   Interface of optical isomers

In Sec. 6.4, we showed that nonlocal gyrotropy $g(\omega, k)$ can lead to topologically-protected chiral edge states that satisfy open boundary conditions. In the Drude model, this arises
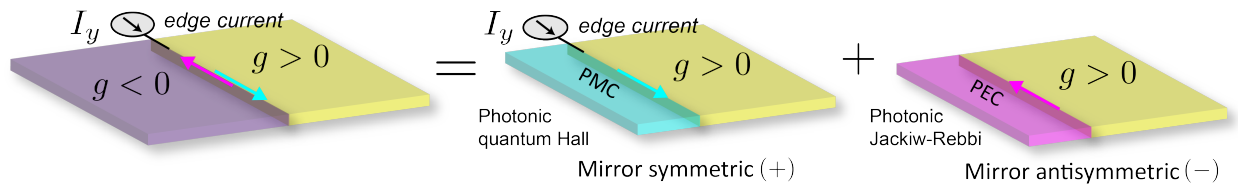
Figure 6.2. The interface of two optical isomers with positive $+g$ and negative $-g$ gyrotropy. In the Drude model, this corresponds to reversed magnetic biasing $\pm B_0$. The interface hosts two edge states that can be decomposed into two chiral (unidirectional) subsystems with perfect magnetic conductor (PMC) and perfect electric conductor (PEC) boundary conditions. PMC and PEC are mirror symmetric $(+)$ and mirror antiysmmetric $(-)$ respectively, designating photonic quantum Hall (PQH) and photonic Jackiw-Rebbi (PJR) states. The particular mirror symmetry $(\pm)$ dictates how the electromagnetic field transforms into the virtual photon $\mathcal{P}_x f(-x) = \pm f(x)$.

from a momentum dependent cyclotron frequency $\Omega_c(k) = \omega_c + \beta_c k^2$ that changes sign within the dispersion $\omega_c \beta_c < 0$. Discovering such a material and observing these topological edge waves remains an open problem and could be a considerable challenge. Here, we consider a more practical scenario that does not involve nonlocality $\beta_c = 0$, but hosts intriguing physics nonetheless.

Instead of having g change sign with momentum, we let g vary with position $g \rightarrow g(x)$ such that it defines the boundary between two distinct materials. The simplest case represents the boundary of two "optical isomers" [218], [219], with g in the $x > 0$ space and $-g$ in the $x < 0$ space but ε identical in both media. The permittivity tensors are therefore complex conjugates of one another $\varepsilon_{ij}(x) = \varepsilon_{ij}^*(-x)$ and there is perfect mirror symmetry about $x = 0$. In the Drude model, this represents the interface between two biased plasmas, but with reversed applied fields $\pm B_0$. The cyclotron frequencies in each half-space are exactly opposite $\pm \omega_c = \pm eB_0 / M_0$. Note though, this implies the biasing field is discontinuous across the boundary $B_0(0^+) \neq B_0(0^-)$ which is an idealization. In reality, there must be a field gradient $B_0 \rightarrow B_0(x)$ that interpolates between the two regions. However, we get this desired behavior for free if we assume a perfect mirror in the $x < 0$ half-space, such that the virtual photon is the exact mirror image [139]. This is because the permittivity is even under mirror symmetry $\varepsilon \rightarrow \varepsilon$ while gyrotropy is odd $g \rightarrow -g$.

There are two types of mirrors we can introduce: a perfect magnetic conductor (PMC) or a perfect electric conductor (PEC). The difference between the two lies in the type of symmetry of the boundary condition. PMC represents symmetric $(+)$ boundary conditions and PEC is antisymmetric $(-)$. Under each symmetry $(\pm)$ the electromagnetic field f must transform into its mirror image as $\mathcal{P}_x f(-x) = \pm f(x)$. As we will see, each mirror has a chiral (unidirectional) edge state associated with it, but with very different properties. A visualization of the two mirror boundary conditions is displayed in Fig. 6.2. It must be stressed that a *real* interface of optical isomers hosts both edge states. A symmetric (PMC) state propagates in one direction while the antisymmetric (PEC) state propagates in the opposite direction. Only when we enforce a specific boundary condition can we isolate for either edge state.

6.6 Photonic quantum Hall (PQH) edge states

The photonic quantum Hall (PQH) edge states are symmetric (PMC) solutions of the optical isomer problem. These states are unique in that they support a high frequency quantum Hall edge current at the interface. The first step is to derive the δ-potential characterizing the potential energy at the discontinuity $x = 0$. This arises from a sudden change in the gyrotropic coefficient $g \rightarrow g\,\text{sgn}(x)$. Assuming the longitudinal field is nonzero $E_y \neq 0$, it can be shown that E_y satisfies a Schrödinger-like wave equation,

$$-\partial_x^2 E_y + V(x)E_y = \mathcal{E}E_y. \tag{6.42}$$

$V(x)$ is the "potential energy" and after differentiating reduces to a δ-function,

$$V(x) = k_y\frac{g}{\varepsilon}\partial_x\text{sgn}(x) = 2k_y\frac{g}{\varepsilon}\delta(x). \tag{6.43}$$

$\mathcal{E}$ is the corresponding "energy eigenvalue",

$$\mathcal{E} = \omega^2\left(\varepsilon - \frac{g^2}{\varepsilon}\right) - k_y^2. \tag{6.44}$$

It is well known that δ-potentials always possess a bound state when the potential energy is attractive $V(x) < 0$. Therefore, $k_y g/\varepsilon < 0$ must always be satisfied for any given frequency and wave vector. The chirality of the bound state is immediately apparent. If a solution exists for a particular k_y, then $k_y \rightarrow -k_y$ is never a simultaneous solution. Back-scattering is forbidden.

To solve Eq. (6.42), we integrate both sides of the equation from $\int_{0-}^{0+} dx$ while assuming $E_y(x) = E_y(0)\exp(-\eta|x|)$. In this case, the longitudinal electric field is continuous across the domain wall $E_y(0^+) = E_y(0^-)$. We obtain a surprisingly simple characteristic equation,

$$\eta = -k_y\frac{g}{\varepsilon}, \qquad k_y^2 = \omega^2\varepsilon. \tag{6.45}$$

Notice that an edge state only exists when $\varepsilon > 0$ is positive. This is very different from SPPs which require a negative permittivity. After some algebra, the E_x and H_z fields can be expressed as,

$$E_x(x) = -\mathrm{i}s_x \frac{\varepsilon^2 + g^2}{2\varepsilon g} E_y(0) \mathrm{e}^{-\eta|x|}, \tag{6.46a}$$

$$H_z(x) = \mathrm{i}s_x s_{k_y} \frac{\varepsilon^2 - g^2}{2\sqrt{\varepsilon} g} E_y(0) \mathrm{e}^{-\eta|x|}, \tag{6.46b}$$

where $s_x = \mathrm{sgn}(x)$ and $s_{k_y} = \mathrm{sgn}(k_y)$ denotes the sign of x and k_y respectively. It is easy to check that the PQH state is mirror symmetric $\mathcal{P}_x f(-x) = +f(x)$ about $x = 0$.

However, one might expect the normal electric field E_x and tangential magnetic field H_z to vanish at $x = 0$ due to PMC boundary conditions. This is not the case. A free edge current is running parallel to the interface, such that the fields are discontinuous,

$$I_y = \frac{1}{2} \left[H_z(0^-) - H_z(0^+) \right] = -\mathrm{i}s_{k_y} \frac{\varepsilon^2 - g^2}{2\sqrt{\varepsilon} g} E_y(0). \tag{6.47}$$

Note, we divide by a factor of 2 to remove the contribution from the virtual photon. I_y is the high frequency analogue of the quantum Hall edge current. Interestingly, these photonic edge waves can be excited by passing a time-varying current along the boundary – similar to a transmission line. However, current can only flow in one direction and the system behaves like a simultaneous photonic and electronic diode.

Now we look for self-consistent solutions to the dispersion relation [Eq. (6.45)] which correspond to propagating edge modes, with both k_y and ω real-valued. There are in fact two edge bands which span the gaps between the bulk bands,

$$\omega_{\uparrow\downarrow}^2 = \frac{1}{2} \left[\omega_p^2 + \omega_c^2 + k_y^2 \pm \sqrt{(\omega_p^2 + \omega_c^2 + k_y^2)^2 - 4k_y^2 \omega_c^2} \right]. \tag{6.48}$$

$\omega_\uparrow$ spans the region between the upper ω_+ and lower ω_- bulk TM bands while $\omega_\downarrow$ spans between ω_c and 0. Now we need to check when $\eta > 0$ represents a decaying wave for the two edge modes,

$$\eta_{\uparrow\downarrow} = -k_y \frac{g(\omega_{\uparrow\downarrow})}{\varepsilon(\omega_{\uparrow\downarrow})} = \frac{k_y \omega_c \omega_p^2}{\omega_{\uparrow\downarrow}(\omega_{\uparrow\downarrow}^2 - \omega_p^2 - \omega_c^2)}. \tag{6.49}$$
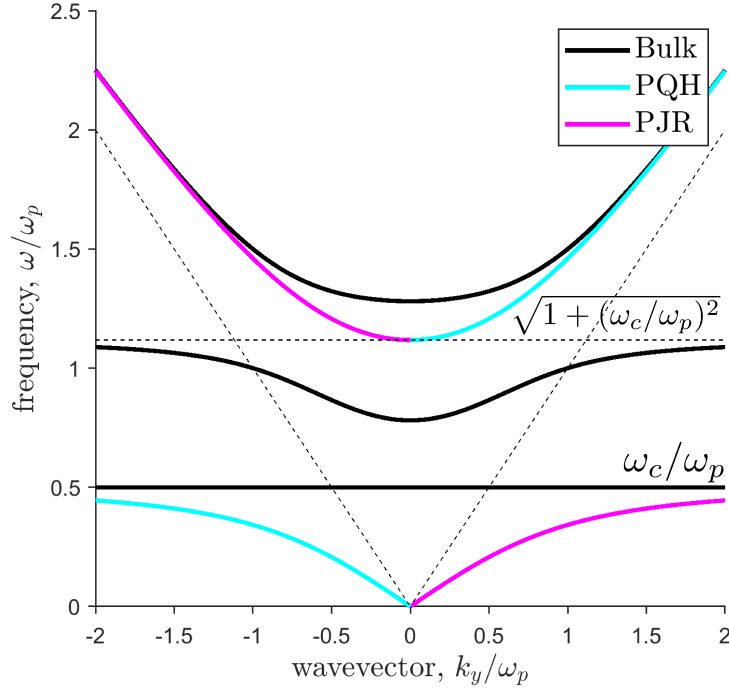
Figure 6.3. Dispersion relation of the local Drude model under an applied magnetic field with $\omega_c/\omega_p = 1/2$ as an example. Black lines indicate bulk bands while cyan and magnetic lines represent unidirectional photonic quantum Hall (PQH) and photonic Jackiw-Rebbi (PJR) edge states respectively. There are a total of 3 positive energy bulk bands. Two correspond to high and low frequency TM modes $\omega = \omega_\pm$ while the third represents pure cyclotron orbits $\omega = \omega_c$. The PQH states emerge at a PMC boundary while the PJR states require a PEC boundary. Unlike conventional SPPs, the PQH and PJR states asymptotically approach the bulk bands in the $k_y \to \infty$ limit. The upper branch approaches the free photon dispersion $\omega_\uparrow \to k_y$ while the lower branch approaches pure cyclotron orbits $\omega_\downarrow \to \omega_c$. The frequency range where no edge state exists $\omega_c < \omega < \omega_0$, corresponds to the plasmonic region $\varepsilon < 0$.

Since $\omega_\uparrow^2 \geq \omega_p^2 + \omega_c^2$ for all k_y, then $\omega_c k_y > 0$ must always be satisfied in the $\omega_\uparrow$ frequency region. Choosing $\omega_c > 0$, the upper edge branch propagates strictly in the $k_y > 0$ direction. Similarly, since $\omega_\downarrow^2 < \omega_p^2 + \omega_c^2$ for all k_y, then $\omega_c k_y < 0$ must always be satisfied in the $\omega_\downarrow$ frequency region. The lower edge branch propagates strictly in the $k_y < 0$ direction. The dispersion relation of the PQH edge states are displayed in Fig. 6.3.

6.7 Photonic Jackiw-Rebbi (PJR) edge states

The photonic Jackiw-Rebbi (PJR) edge states are antisymmetric (PEC) solutions of the optical isomer problem. Like the QGEE, these edge states are completely transverse electro-magnetic (TEM) waves. PJR states share many important properties with the QGEE [Sec. 6.4] even though they arise by a very different means. The only significant difference is that they do not satisfy open boundary conditions and necessarily require a PEC boundary. This means they are not topologically-protected as they are sensitive to boundary conditions. However, this particular system is the most practical experimentally.

To solve, we first assume the magnetic field is continuous across the domain wall $H_z(0^+) = H_z(0^-)$ such that zero edge current $I_y = 0$ is excited. We obtain an identical dispersion relation as the PQH states [Eq. (6.45)], except the wave propagates in the reverse direction,

$$\eta = k_y \frac{g}{\varepsilon}, \qquad k_y^2 = \omega^2 \varepsilon. \tag{6.50}$$

There is an immediate connection with the Dirac Jackiw-Rebbi dispersion with respect to the effective speed of light v_p and effective photon mass Λ_p,

$$\eta = \frac{\omega g}{\sqrt{\varepsilon}} = \frac{|\Lambda_p|}{v_p}, \qquad \omega^2 = \frac{k_y^2}{\varepsilon} = v_p^2 k_y^2. \tag{6.51}$$

Surprisingly, the electromagnetic field profile of the PJR state is drastically different than the PQH state. The longitudinal field vanishes $E_y(x) = 0$ entirely because $E_y(0^+) = E_y(0^-) = 0$ is required by symmetry. Hence, the PEC states correspond to completely transverse electro-magnetic (TEM) edge waves,

$$f(x) = E_x(0)\left(\hat{x} - s_{k_y}\sqrt{\varepsilon}\hat{z}\right)e^{-\eta|x|}. \tag{6.52}$$

It is easy to check that the PJR state is mirror antisymmetric $\mathcal{P}_x f(-x) = -f(x)$ about $x = 0$. The edge wave behaves identically to a vacuum photon (transverse polarized) but with a modified dispersion. Indeed, they are elically quantized along the direction of propagation

$\hat{k} \cdot \mathbf{E} = \hat{y} \cdot \mathbf{E} = E_y = 0$. This is the definition of longitudinal spin-momentum locking as f is an eigenstate of $\hat{S}_y$,

$$\hat{S}_y \mathfrak{F} = s_{k_y} \mathfrak{F}, \qquad \mathfrak{F} = \begin{bmatrix} \sqrt{\varepsilon} E_x \\ \sqrt{\varepsilon} E_y \\ H_z \end{bmatrix}. \tag{6.53}$$

$\hat{k} \cdot \vec{S} = \hat{S}_y$ is the helicity operator along $\hat{y}$, which was defined in Eq. (6.3). Notice that the spin is quantized $s_{k_y} = \text{sgn}(k_y) = \pm 1$ and completely locked to the momentum as it depends on the direction of propagation. This should be contrasted with their electron (spin-½) equivalent. The dispersion relation of the PJR edge states are displayed in Fig. 6.3. A short discussion on the robustness of PQH and PJR states is presented in App. D.2.

6.8 Conclusion

In summary, we have identified the three fundamental classes of unidirectional photonic edge waves arising in gyroelectric media. The quantum gyroelectric effect (QGEE) is a topologically-protected edge state that requires nonlocal gyrotropy. This wave satisfies open boundary conditions and displays bulk-boundary correspondence as it is defined independent of the contacting medium. The photonic quantum Hall (PQH) and photonic Jackiw-Rebbi (PJR) states are local phenomena and emerge at the interface of optical isomers – two media with inverted gyrotropy.

Acknowledgements

7. VISCOUS MAXWELL-CHERN-SIMONS THEORY FOR TOPOLOGICAL ELECTROMAGNETIC PHASES OF MATTER

From [T. Van Mechelen and Z. Jacob, "Viscous Maxwell-Chern-Simons theory for topological electromagnetic phases of matter," *Phys. Rev. B*, vol. 102, p. 155425, 15 Oct. 2020]. © 2020 American Physical Society. [246]

Chern-Simons theories have been very successful in explaining integer and fractional quantum Hall phases of matter, topological insulators and Weyl semi-metals. However, it remains an open question whether Chern-Simons theories can be adapted to topological photonics. We develop viscous Maxwell-Chern-Simons theory to capture the fundamental physics of a topological electromagnetic phase of matter. We show the existence of a unique spin-1 skyrmion in the viscous Hall fluid arising from a photonic Zeeman interaction in momentum space. Our work bridges the gap between electromagnetic and condensed matter topological physics while also demonstrating the central role of photon spin-1 quantization in identifying new phases of matter.

7.1 Introduction

Chern-Simons theory has been studied in condensed matter and high-energy physics for over three decades [84], [247]. In a two-dimensional (2D) quantum Hall fluid, it describes the transverse current generated by an applied electric field, which manifests in the Hall conductivity σ_{xy}. Interestingly, 2D Chern-Simons theory also provides an elegant explanation of Hall quantization as well as the chiral edge currents, with no need to invoke electronic band structure. In addition, it has successfully described the fractional quantum Hall effect in many-body systems and even captures the physics of anyons [248]. On the other hand, three-dimensional (3D) Chern-Simons theory, also known as axion electrodynamics, emerges as a residual magnetoelectric response in topological insulators [249]. Lattice gauge theories are also of significant interest in quantum simulation [250].

However, in both 2D and 3D, Chern-Simons theory only elucidates the topological properties of the electron. The topology of the electromagnetic field in these quantum materials

has remained largely unexplored. Here, we mean quantities such as the *photonic* Chern number and the topological invariants associated with the electromagnetic field coupled to condensed matter. To characterize these topological properties, it is fundamentally necessary to define the photon wavefunction and understand the dynamical $\omega \neq 0$ and subwavelength $k \neq 0$ behavior of the material response [54], [116]. In solids, the topology of the photon wavefunction is encapsulated in the spatiotemporal dispersion of optical coefficients like the conductivity tensor $\sigma_{ij}(\omega, \mathbf{k})$. This unique insight has led to a new electromagnetic classification of topological matter [164] and intriguing phenomena such as unidirectional electromagnetic spin waves [167] that are fundamentally different than magneto-plasmons. These so-called topological electromagnetic phases of matter are intrinsically bosonic (spin-1) and are fundamentally different from fermionic (spin-½) phases as they obey differing symmetries. E.g. time-reversal: $\mathcal{T}^2 = +1$ for bosons vs. $\mathcal{T}^2 = -1$ for fermions. The prototypical model of a gapped topological electromagnetic phase, with nontrivial photonic Chern number $C_{em} \neq 0$, was first connected to nonlocality (momentum dependence) of the Hall conductivity $\sigma_{xy}(k) = \lambda(\kappa - \xi k^2)$ [54], [116]. These observations necessarily require a formalism beyond conventional Chern-Simons theory.

In this paper, we lay the foundations for a field theory approach to topological photonic phases. The specific class of systems we focus on are quantum fluids with Hall viscosity. Hall viscosity η_H [251], [252], also known as odd viscosity [253] in fluid dynamics, is a fundamental property of quantum Hall fluids and can exhibit topological quantization analogous to the Hall conductivity [254]–[256]. Like conventional viscosity, it is related to the stress response of the system under deformations and governs the diffusive flow of the electron fluid. However, Hall viscosity is unique because it is dissipationless, inducing diffusive flow in a direction perpendicular to a pressure (force) gradient and therefore does no work. We show that Hall viscosity, intriguingly, defines a topological electromagnetic phase of matter with spin-1 photonic skyrmions. We further describe the central idea of a viscous photon mass arising in viscous Chern-Simons theories – fundamentally different from the Proca mass which breaks gauge invariance [257]. Our viscous Maxwell-Chern-Simons Lagrangian also reveals topologically-protected chiral (unidirectional) edge states that minimize the surface variation and correspond to massless excitations costing an infinitesimal amount of energy.
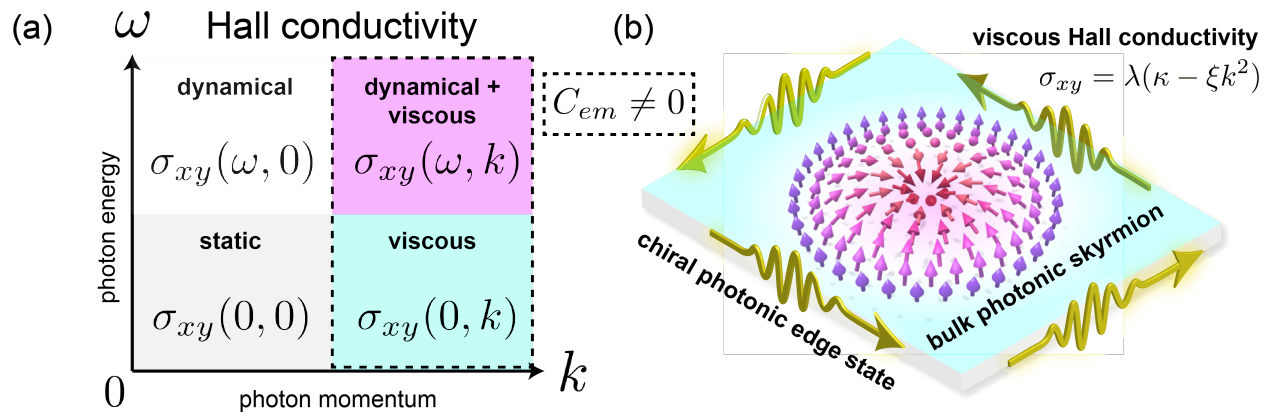
Figure 7.1. (a) Summary of the four quantum Hall regimes. Hall quantization and plateauing behavior has been demonstrated in both static and dynamical regimes. However, topological electromagnetic phases $C_{em} \neq 0$ are only realized in the dynamical + viscous (nonlocal) regimes. (b) Overview of viscous Maxwell-Chern-Simons theory. The bulk topology is governed by a spin-1 photonic skyrmion in momentum space which arises from viscous Hall conductivity $\sigma_{xy}(k) = \lambda(\kappa - \xi k^2)$. The arrows represent the direction of the effective spin $\hat{d}$ of the photon. The boundary of the nontrivial phase $\kappa\xi > 0$ hosts topologically-protected chiral photons which are linearly dispersing (massless).

An overview of the problem is depicted in Fig. 7.1. The low energy $\omega \approx 0$ and long wavelength $k \approx 0$ quantized Hall conductivity is well understood as a topological phase of electrons. At THz frequencies $\omega \neq 0$ but low momentum $k \approx 0$, plateaus and quantized Faraday rotation have been observed in the integer quantum Hall regime [258]. However, at finite $\omega \neq 0$ and $k \neq 0$, the Hall conductivity becomes dynamical and viscous, paving the route for the first known topological phase for photons in condensed matter. We argue that our low energy theory applies to graphene's electron fluid [259] where appreciable Hall viscosity [25] was experimentally demonstrated, even under weak magnetic fields. The viscous MCS theory possesses a few limitations as it neglects Coulomb interactions and the high frequency screening of the magnetic field, which require more sophisticated hydrodynamic models [260]. The main goal here is to formulate a field-theoretic approach to topological photonic phases, make the connection with Chern-Simons theories, and illustrate the importance of Hall viscosity in realizing nontrivial phases. To guide experimentalists in the search for such new topological electromagnetic phases of matter, we have included a summary of a few physical systems exhibiting Hall viscosity along with their characteristic parameters in Tbl. 7.1.

We note that our work is closely related to ideas in topological photonics but the physical platforms are fundamentally different. We are concerned with condensed matter systems such as viscous Hall fluids. Topological wave phenomena [18], [139], [173] have transcended all of photonics: from plasmonics [137], [261], metamaterials [217], [262], [263] and photonic crystals [215], [264]. Nevertheless, it remains an open question whether topological photonic phases can be expressed in terms of an effective gauge theory – i.e. a field-theoretic approach. The advantage of our viscous MCS theory is the proof that the topological edge wave minimizes the action on the boundary. Furthermore, the boundary conditions we derive are fundamentally different from those used for conventional nanoscale systems such as photonic crystals and plasmonics. This difference arises from the presence of Hall viscosity which is a necessary physical property for defining topological electromagnetic phases of matter.

7.2 Lagrangian formulation for topological electromagnetic phases

7.2.1 Maxwell-Chern-Simons theory

In 2+1 dimensions, the MCS Lagrangian is defined as,

$$\mathcal{L}_A = -\frac{1}{4}F^{\mu\nu}F_{\mu\nu} - \frac{\kappa}{4}\epsilon^{\mu\nu\rho}A_\mu F_{\nu\rho}. \tag{7.1}$$

$A_\mu = (\phi, A_x, A_y)$ are the two-dimensional (2D) gauge fields and $F_{\mu\nu} = \partial_\mu A_\nu - \partial_\nu A_\mu$ is the field strength tensor [84], [247]. We have set the dielectric constant to unity $\varepsilon = 1$ but the case with $\varepsilon > 1$ is easily handled and does not alter the topological physics – it simply scales the electric field and the effective speed of light. The first term in $\mathcal{L}_A$ is the familiar Maxwell Lagrangian. The second term is the Chern-Simons Lagrangian and κ is the coupling constant. Alternately, the MCS theory can be formulated in the more aesthetically pleasing "self-dual" picture [265],

$$\mathcal{L}_F = \frac{\kappa}{2}\tilde{F}^\mu \tilde{F}_\mu + \frac{1}{2}\epsilon^{\mu\nu\rho}\tilde{F}_\mu \partial_\nu \tilde{F}_\rho, \tag{7.2}$$

which is equivalent to Eq. (7.1) up to a Legendre transformation [266]. In this case, the field theory is described in terms of the electromagnetic dual $\tilde{F}^\mu = \frac{1}{2}\epsilon^{\mu\nu\rho}F_{\nu\rho}$, which satisfies the Bianchi identity (Faraday equation) $\partial_\mu \tilde{F}^\mu = 0$ upon variation of the action. In 2D, the dual field $\tilde{F}_\mu$ is a covariant vector

$$\tilde{F}_\mu = (B_z, E_y, -E_x), \tag{7.3}$$

with the same number of components as the gauge fields $A_\mu = (\phi, A_x, A_y)$ and therefore is an equally valid description of the field theory.

7.2.2 Viscous Maxwell-Chern-Simons theory

Although traditional MCS theory has been studied extensively, we analyze the role of viscosity (non-dissipative nonlocality) [267] that leads to topological implications on the electromagnetic field [54], [116], [164], [167]. Originally, Hall viscosity was conceived from a geometric perspective, associated with deformations of the underlying metric of the quantum fluid [254]. An equivalent but alternative point of view is to include nonlocal terms that

Table 7.1. Summary of two physical systems exhibiting significant Hall viscosity and topologically nontrivial electromagnetic phases $C_{em} \neq 0$. In general, Hall viscosity is always present if the system breaks both parity and time-reversal symmetry. When viscosity repels the magnetic field $\mathcal{C}_2 > 0$, the electromagnetic phase is nontrivial [Eq. (7.9)], which occurs in both quantum Hall $\nu \in \mathbb{Z}$ [255] and graphene Hall fluids [259]. Hall viscosity is also appreciable in the semiclassical graphene fluid [25] around room temperature $100 - 300$ K and for weak magnetic fields $B \approx 10$ mT.

	Hall fluid	**Graphene fluid**
Biasing magnetic field, B	Quantizing	10 T
D.C. Hall conductivity, $\sigma_{xy}(0)$	$\nu e^2/(2\pi\hbar)$	6.97×10^5 m/s
MCS mass, $\kappa/2\pi$	$\sigma_{xy}(0)/(2\pi\lambda)$	4.43 THz
Magnetic length, l	$\sqrt{\hbar c/(eB)}$	81 A
Cyclotron frequency, $\omega_c/2\pi$	$eB/(2\pi cm)$	22.6 THz
Hall viscosity, $\eta_H/(\hbar n)$	$\nu/4$	$\nu/4 = 1/4$
Energy density, $\epsilon(B)$	$\nu^2\hbar\omega_c/(4\pi l^2)$	403 μJ/m^2
Topological phase? $\mathcal{C}_2 = \xi/(\kappa l^2)$	yes: $\mathcal{C}_2 = 3\nu/4 > 0$	yes: $\mathcal{C}_2 \approx 1/2 > 0$

account for the stress-strain response of the quantum Hall fluid. To this end, we introduce the viscous MCS Lagrangian,

$$\mathcal{L}_A = -\frac{1}{4}F^{\mu\nu}F_{\mu\nu} - \frac{\kappa}{4}\epsilon^{\mu\nu\rho}A_\mu F_{\nu\rho} - \frac{\xi}{4}\epsilon^{\mu\nu\rho}A_\mu\nabla^2 F_{\nu\rho}, \qquad (7.4)$$

which will elucidate these topological electromagnetic phases of matter. An effective action to describe a medium with Hall viscosity was first proposed by Hoyos and Son [255] which was motivated by Galilean invariance, as opposed to relativistic invariance. Similarly, our viscous Lagrangian Eq. (7.4) is Galilean invariant. The one significant difference is that the Hoysos and Son Lagrangian was limited to longitudinal fields $\mathbf{E} = -\boldsymbol{\nabla}\phi$. Our theory is a slight generalization in flat space time that includes the response of the transverse field $\boldsymbol{\nabla} \times \mathbf{E} \neq 0$. A proof is provided in the supplementary information. ξ is the nonlocal Chern-Simons coupling and accounts for viscosity in the MCS Lagrangian.

As before, we can transform to the self-dual picture to obtain an intuitive interpretation,

$$\mathcal{L}_F = \frac{\kappa}{2}\tilde{F}^\mu\tilde{F}_\mu - \frac{\xi}{2}\nabla\tilde{F}^\mu \cdot \nabla\tilde{F}_\mu + \frac{1}{2}\epsilon^{\mu\nu\rho}\tilde{F}_\mu\partial_\nu\tilde{F}_\rho. \qquad (7.5)$$

We note there is a striking one-to-one correspondence between Eq. (7.5) which we derived and the minimal topological Dirac model [93],

$$\mathcal{L}_\psi = m\bar{\psi}\psi - b\nabla\bar{\psi} \cdot \nabla\psi - \mathrm{i}\bar{\psi}\gamma^\mu\partial_\mu\psi, \qquad (7.6)$$

where γ^μ are the 2+1D gamma matrices and ψ is a two-component spinor. Equations (7.5) and (7.6) are in fact supersymmetric partners [247], describing spin-1 bosons and spin-½ fermions respectively. By direct comparison, we see that κ plays the role of photonic mass, in the same way as m for the electron. Likewise, ξ and b dictate the kinetic (viscous) terms, which are essential to realize nontrivial phases. In the long wavelength (continuum) limit $k \approx 0$, the viscous term regularizes the field at $k \to \infty$, such that the momentum space is effectively a sphere $\mathbb{R}^2 \simeq S^2$. This means topological invariants of the electromagnetic field, like the Chern number C_{em}, can be defined [15]. We also show in the lattice regularized

theory [Sec. 7.4], that nontrivial photonic phases $C_{em} \neq 0$ are only possible when viscosity is non-zero $\xi \neq 0$.

7.2.3 Viscous Hall conductivity

Physically, the Chern-Simons coupling is interpreted as a dissipationless Hall conductivity, as the induced current density is,

$$J_{\text{ind}}^{\mu} = -\lambda \frac{\partial \mathcal{L}_A}{\partial A_{\mu}} = \lambda(\kappa + \xi \nabla^2)\tilde{F}^{\mu}. \tag{7.7}$$

Since the induced current J_{ind}^{μ} is proportional to the dual field $\tilde{F}^{\mu}$, the nonlocal conductivity tensor $\sigma_{\text{ij}}(k)$ is purely antisymmetric,

$$\sigma_{xy}(k) = -\sigma_{yx}(k) = \lambda(\kappa - \xi k^2), \tag{7.8}$$

with vanishing symmetric components $\sigma_{xx} = \sigma_{yy} = 0$. The prefactor λ is a characteristic length scale of the problem and ensures correct units of the conductivity. For simplicity, we assume λ is the Thomas-Fermi screening length which is approximately $\lambda \approx 25$ nm in graphene [14]. The viscous Chern-Simons coupling ξ therefore describes the quadratic correction to the Hall response [255],

$$\frac{\sigma_{xy}(k)}{\sigma_{xy}(0)} = 1 - \frac{\xi}{\kappa}k^2 = 1 - \mathcal{C}_2(kl)^2, \tag{7.9}$$

$\sigma_{xy}(0) = \lambda\kappa = \nu \mathrm{e}^2/(2\pi\hbar)$ is the intrinsic D.C. Hall response, ν is the filling factor and $l = \sqrt{\hbar c/(eB)}$ is the magnetic length. $\hbar$ is the reduced Planck constant, c is the speed of light, e is the elementary charge and B is the biasing magnetic field. The coefficient $\mathcal{C}_2 = \xi/(\kappa l^2)$ depends on the Hall viscosity η_H and the energy density $\epsilon(B)$ of the Hall fluid,

$$\mathcal{C}_2 = \frac{2\pi}{\nu} \frac{l^2}{\hbar\omega_c} B_0^2 \epsilon(B) - \frac{\eta_H}{\hbar n}, \tag{7.10}$$

where $\omega_c = \mathrm{e}B/(cm)$ is the cyclotron frequency and n is the density of electrons. The first term involving $B_0^2\epsilon(B)$ is a thermodynamic property related to the internal compressibility

[268], while the second term involving η_H is universal. Depending on the material platform, $\mathcal{C}_2$ can be either positive $\mathcal{C}_2 > 0$ or negative $\mathcal{C}_2 < 0$, which either inhibits or enhances the total Hall response. We argue that the *inhibiting* regime $\mathcal{C}_2 > 0$, i.e. when $\kappa\xi > 0$, corresponds to a topologically nontrivial electromagnetic phase [54], [116], [164], [167].

7.2.4 Equations of motion

$\mathcal{L}_A$ and $\mathcal{L}_F$ generate the same equations of motion when one varies the action with respect to the gauge fields (A_μ) or the dual fields $(\tilde{F}_\mu)$. However, to ensure the action does not break gauge invariance on a boundary, it is more convenient to work with the self-dual theory $\mathcal{L}_F$. Varying the dual field $\tilde{F}_\mu \to \tilde{F}_\mu + \delta\tilde{F}_\mu$, we naturally obtain a bulk and surface term $\delta\mathcal{S} = \delta\mathcal{S}_b + \delta\mathcal{S}_s$,

$$\delta\mathcal{S}_b = \int dV \left[\partial_\mu F^{\mu\nu} + \left(\kappa + \xi\nabla^2 \right) \tilde{F}^\nu \right] \delta\tilde{F}_\nu, \tag{7.11}$$

and,

$$\delta\mathcal{S}_s = \int_{\partial V} dtdy \left[\left(\frac{1}{2} F^{x\mu} - \xi\partial_x\tilde{F}^\mu \right) \delta\tilde{F}_\mu \right]_{x=0}. \tag{7.12}$$

$dV = dtdxdy$ is the differential space-time volume and we have taken the boundary at $x = 0$. The minimization principle states that a physical system tends to its lowest energy state, which requires that the fields satisfy the equations of motion within V and the boundary conditions on ∂V. Here we consider an isolated system with no external fields or sources. By requiring a vanishing bulk term $\delta\mathcal{S}_b = 0$, we arrive at the viscous wave equation in the quantum fluid,

$$\partial_\mu F^{\mu\nu} + \left(\kappa + \xi\nabla^2 \right) \tilde{F}^\nu = 0, \tag{7.13}$$

where $F^{\mu\nu} = \epsilon^{\mu\nu\rho}\tilde{F}_\rho$ is the field strength. Equation (7.13) represents the equations of motion of the viscous MCS theory. On the other hand, the surface term $\delta\mathcal{S}_s = 0$ vanishes for two distinct boundary conditions. The first is a Dirichlet condition,

$$\delta\tilde{F}^\mu|_{x=0} = 0, \tag{7.14}$$

196

where the value of the field is fixed on $x = 0$, usually to zero $\tilde{F}^\mu|_{x=0} = 0$, corresponding to an open boundary. The second possibility is slightly more interesting and represents the natural (mixed) boundary condition,

$$j_s^\mu = \frac{\delta \mathcal{S}_s}{\delta \tilde{F}_\mu|_{x=0}} = \left[F^{x\mu} - 2\xi \partial_x \tilde{F}^\mu \right]_{x=0} = 0. \tag{7.15}$$

Equation (7.15) has a particularly nice explanation – it implies the induced surface current j_s^μ vanishes on the boundary. We emphasize that this boundary condition is formally identical to its fermionic counterpart derived from the Dirac equation [Eq. (7.6)]. Together, the above equations define the bulk and edge physics of photons propagating in the viscous Hall fluid.

7.3 Viscous photon mass

7.3.1 Photonic Zeeman interaction

Our first goal is to study the bulk photonic physics of the viscous Hall fluid by exploiting the equations of motions derived above [Eq. (7.13)]. For that, we introduce a Hamiltonian formalism of the electromagnetic field coupled to a medium described by its macroscopic response (complete conductivity tensor). To construct the electromagnetic "Dirac equation" it is convenient to utilize the Riemann-Silberstein (RS) vector $\vec{F}$ [149], which is often called the photon wavefunction. In 2+1D, the RS vector is defined as,

$$\vec{F} = \begin{bmatrix} E_x & E_y & iB_z \end{bmatrix}. \tag{7.16}$$

In this Maxwell Hamiltonian picture, $\vec{F}$ is a 3D vector propagating in the 2D plane, while the dual field ($\tilde{F}^\mu$) is a covariant vector, but the two are equivalent up to a unitary transformation. We now combine Eq. (7.13) with the Bianchi identity (Faraday equation) to obtain a first-order (in time) wave equation,

$$i\partial_t \vec{F} = i\vec{d} \times \vec{F} = H\vec{F}. \tag{7.17}$$

We call $\vec{d}$ the effective magnetic field of the photon which is a 3D vector operator,

$$\vec{d} = \begin{bmatrix} p_x & p_y & \kappa - \xi p^2 \end{bmatrix}, \tag{7.18}$$

and $p_j = -i\nabla_j$ are the corresponding momentum operators. H is the "Maxwell Hamiltonian" and is the projection of the effective magnetic field $\vec{d}$ onto the vector spin operators $\vec{S} = \begin{bmatrix} S_x & S_y & S_z \end{bmatrix}$,

$$H = \vec{d} \cdot \vec{S} = p_x S_x + p_y S_y + (\kappa - \xi p^2) S_z. \tag{7.19}$$

The Maxwell Hamiltonian $H = \vec{d} \cdot \vec{S}$ resembles the Zeeman interaction but for photons [146]. The essential difference is that $\vec{S}$ are spin-1 operators for the photon, as opposed to the Pauli matrices $\vec{\sigma}$ which are spin-½ operators for the electron. In the RS basis, $[S_j, S_k] = i\epsilon_{jkl}S^l$ are antisymmetric SO(3) matrices that generate the spin-1 algebra [188], [190]. Note that the photon propagating within the viscous Hall fluid experiences a net magnetic field that depends on its momentum, Hall conductivity, as well as the Hall viscosity. The dielectric constant ε simply scales the momentum operators and does not effect the behavior of the net magnetic field $\vec{d}$. This "photonic Zeeman interaction" in a viscous quantum Hall fluid leads to a remarkable spin-1 skyrmion in momentum space [Sec. 7.4].

7.3.2 Difference from Proca mass

The topological physics of the electron is tied to the quantization of Hall conductivity. Our intriguing result is that topological properties for the photon arise from the *viscous* nature of the Hall conductivity. The Chern-Simons coupling (Hall conductivity) $\kappa \neq 0$ behaves as a gauge invariant photonic mass Λ that opens a low energy band gap for electromagnetic waves at $\omega = 0$ in the quantum fluid. We note that the MCS mass is fundamentally different from the Proca mass that is often encountered in superconductivity [257]. By choosing a Lorenz gauge $\partial_\mu A^\mu = 0$, the London penetration depth λ_L of a superconductor is identified with the Proca mass $\lambda_L^{-1} = m$. Conversely, the MCS mass does not require the specification of a gauge. The Stueckelberg [269] mechanism is an alternative way of generating mass for the photon but in the quantum Hall effect, parity and time-reversal symmetry breaking is

(a) continuum $a \to 0$

$C_{em} = 2$

frequency, ω

wavevector, k_y

(b) lattice $a \neq 0$

$C_{em} = 2$

frequency, ωa

wavevector, $k_y a$
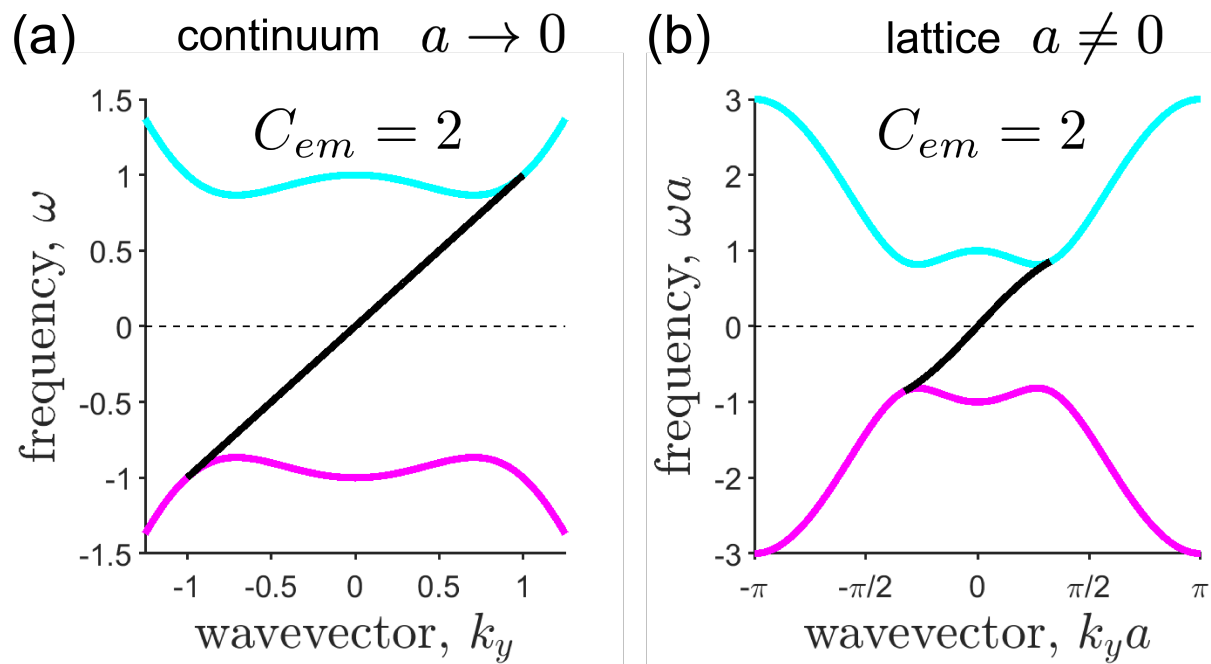
Figure 7.2. Bulk and edge dispersion of (a) continuum and (b) lattice models of viscous Maxwell-Chern-Simons theory. Cyan and magnetic lines are positive and negative energy topological bands while the black line is the chiral edge state. (a) Parameters are $\kappa = \xi = 1$ in the continuum theory $a \to 0$. (b) Parameters are $\kappa a = \xi/a = 1$ in the lattice theory $a \neq 0$.

captured specifically by the Chern-Simons coupling term. Since the MCS mass does not pre-serve parity or time-reversal symmetry, it admits the possibility of nontrivial Chern phases $C_{em} \neq 0$. The Hall viscosity is crucial to realize these nontrivial topological electromagnetic phase $\xi \neq 0$ and makes this photonic mass spatially dispersive,

$$\Lambda(p) = \lambda^{-1}\sigma_{xy}(p) = \kappa - \xi p^2. \tag{7.20}$$

To appreciate its significance, we translate the system to the energy-momentum space and place the MCS theory on a square lattice $x = n_x a$ and $y = n_y a$. Here, $n_{x,y} \in \mathbb{Z}$ is an integer and a is the lattice constant. The lattice regularizes the field theory at high-k and ensures quantization of topological invariants like the photonic Chern number. Due to discretization of space [270], the momentum is only unique up to $|k_{x,y}| \leq \pi/a$, which defines a torus $\mathbb{T}^2$ in two dimensions. That is, $\mathbf{k}$ is defined within the first Brillouin zone (BZ). The dispersion relation of the dynamical $\omega \neq 0$ modes is found straightforwardly,

$$\omega^2(\mathbf{k}) = \vec{d}^2(\mathbf{k}). \tag{7.21}$$

where $\vec{d}(\mathbf{k}+\mathbf{g}) = \vec{d}(\mathbf{k})$ is periodic in the reciprocal lattice and $g_{x,y} = N_{x,y}2\pi/a$ is an arbitrary reciprocal vector $N_{x,y} \in \mathbb{Z}$,

$$\vec{d}(\mathbf{k}) = \left[a^{-1}\sin(k_x a) \quad a^{-1}\sin(k_y a) \quad \Lambda(\mathbf{k}) \right]. \tag{7.22}$$

$\Lambda(\mathbf{k})$ is the viscous photon mass in the lattice theory and is quadratic in the momentum,

$$\Lambda(\mathbf{k}) = \kappa - \xi\left(\frac{2}{a}\right)^2 \left[\sin^2\left(\frac{k_x a}{2}\right) + \sin^2\left(\frac{k_y a}{2}\right) \right]. \tag{7.23}$$

It is easy to check that the continuum limit is recovered when $a \to 0$. The dispersion relation is depicted in Fig. 7.2 which shows the bulk bands and the gapless edge states within the band gap. The positive energy $\omega = d > 0$ bulk eigenstate is then derived as,

$$\vec{F}_{\mathbf{k}} = \frac{1}{\sqrt{2}}\left[\frac{\vec{d} \times \hat{z}}{|\vec{d} \times \hat{z}|} + i\frac{\vec{d} \times (\vec{d} \times \hat{z})}{d|\vec{d} \times \hat{z}|} \right], \tag{7.24}$$
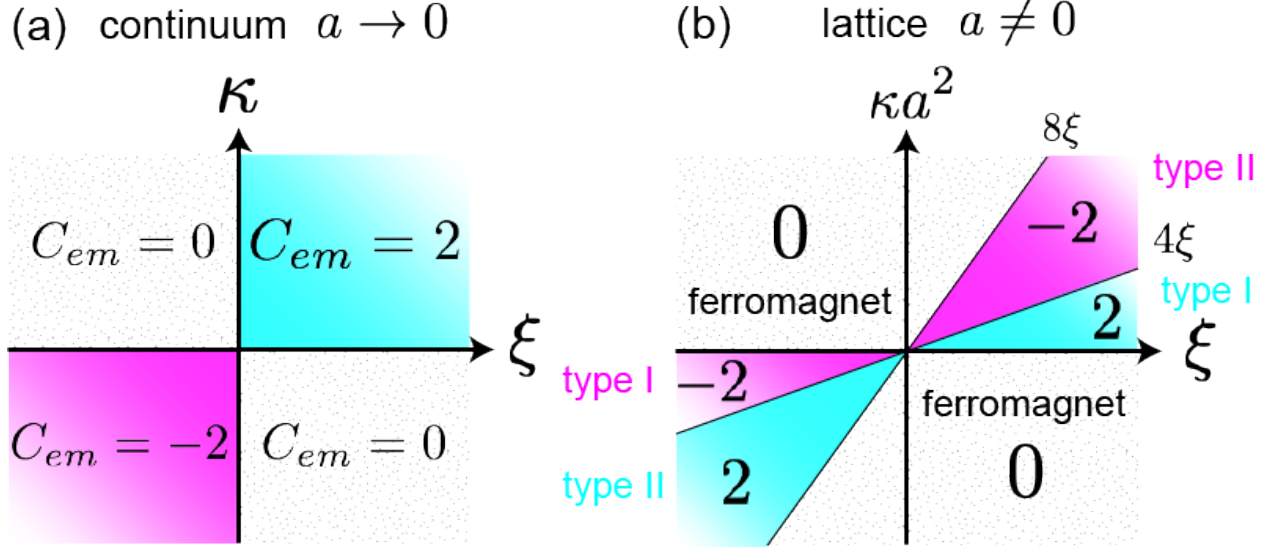
Figure 7.3. Topological phase diagrams for (a) continuum and (b) lattice models of viscous Maxwell-Chern-Simons theory. $C_{em} = \pm 2, 0$ is the photonic Chern number of the positive energy band $\omega > 0$ for different parameters. κ and ξ are the Chern-Simons and viscous Chern-Simons coupling respectively. a is the lattice constant of a square grid. $\kappa a^2 = 0, 4\xi, 8\xi$ denote the phase transition lines in the lattice model. These correspond to points of accidental degeneracy, where the band gap closes at $\mathbf{k} = \Gamma, X/Y, M$ respectively. Importantly, conventional MCS theory $\xi = 0$ always corresponds to a topologically trivial phase $C_{em} = 0$ in the lattice regularization.

which has been normalized to unit energy $|\vec{F}_{\mathbf{k}}|^2 = |\mathbf{E}|^2 + |B_z|^2 = 1$.

7.4 Spin-1 photonic skyrmions

We now show that a spin-1 photonic skyrmion emerges within the viscous Hall fluid. Our momentum space skyrmion is analogous to those predicted in p-wave superconductors [94]. The reason the skyrmion is spin-1 is because the MCS mass $\Lambda(\mathbf{k})$ also defines the representation theory of the 2+1D Poincaré algebra [84],

$$j_m = \frac{\Lambda(\mathbf{k})}{|\Lambda(\mathbf{k})|} = \text{sgn}[\Lambda(\mathbf{k})], \tag{7.25}$$

which is a massive spin-1 excitation $j_m = \pm 1$. The representation j_m indicates whether the wave is right $(+1)$ or left (-1) circularly polarized in the x-y plane. The topology is
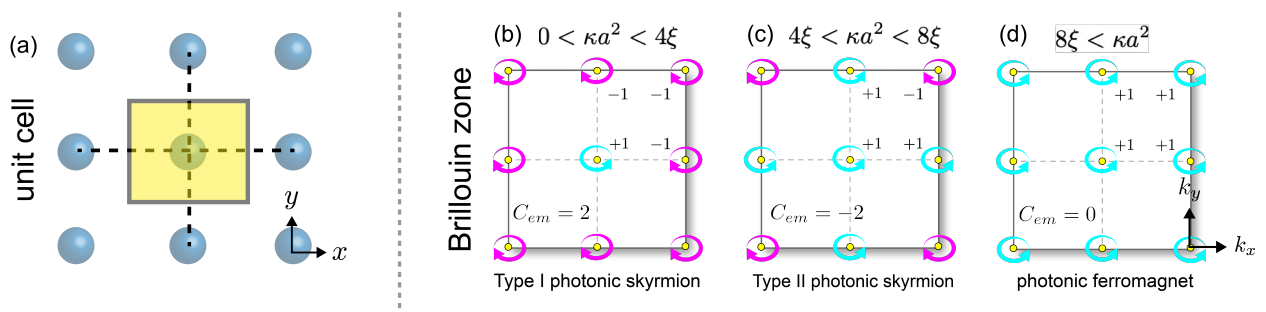
Figure 7.4. (a) Unit cell of a square lattice with the primitive Wigner-Seitz cell shown in yellow. (b), (c) and (d) show the Brillouin zone of the three phases $C_{em} = \pm 2, 0$ in the lattice regularized theory. $\kappa > 0$ and $\xi > 0$ are chosen positive such that (b) and (c) label type I and type II photonic skyrmions respectively. (d) is the photonic ferromagnet. The eigenvalue at high-symmetry points denotes the sign of the Maxwell-Chern-Simons mass $j_m = \text{sgn}(\Lambda) = \pm 1$, which determines the spin-1 representation – if the field is right ($+1$) or left (-1) circularly polarized. The two nontrivial phases possess skyrmion numbers of $N = \pm 1$ corresponding to a spin-1 Chern number of $C_{em} = 2N = \pm 2$.

intimately tied to the spin-1 representation of the electromagnetic field. The Berry curvature Ω is precisely [116],

$$\Omega = -\mathrm{i}\left(\partial_x \vec{F}_\mathbf{k}^* \cdot \partial_y \vec{F}_\mathbf{k} - \partial_y \vec{F}_\mathbf{k}^* \cdot \partial_x \vec{F}_\mathbf{k}\right) = \hat{d} \cdot (\partial_x \hat{d} \times \partial_y \hat{d}), \qquad (7.26)$$

where $\hat{d} = \vec{d}/d$ is a unit vector. Note, the photonic Chern number for the viscous Hall fluid is always an even integer $C_{\mathrm{em}} \in 2\mathbb{Z}$,

$$C_{\mathrm{em}} = \frac{1}{2\pi} \int_{\mathrm{BZ}} d\mathbf{k} \; \hat{d} \cdot (\partial_x \hat{d} \times \partial_y \hat{d}) = 2N. \qquad (7.27)$$

$N \in \mathbb{Z}$ is the skyrmion winding number [147], [148] that counts the number of times $\hat{d}(\mathbf{k})$ wraps around the unit sphere $\mathbb{T}^2 \to S^2$. We define the skyrmion number N and Chern number C_{em} through the photon wavefunction $\vec{F}$. The topological invariant is a property of the U(1) gauge field coupled to the viscous quantum Hall fluid. This is in stark contrast to electronic topological materials where the electron wavefunction ψ plays the central role.

Importantly, at high-symmetry points $\mathbf{k} = \Gamma, X/Y, M$, the spin-1 representation [16], [183] can only change if $\kappa\xi > 0$ which requires the Hall coefficient $\mathcal{C}_2 > 0$. After a bit of work, it can be shown that the Chern number is [271],

$$\begin{aligned}
C_{\mathrm{em}} &= \mathrm{sgn}[\Lambda(\Gamma)] + \mathrm{sgn}[\Lambda(M)] - 2\mathrm{sgn}[\Lambda(X)] \\
&= \mathrm{sgn}(\kappa) + \mathrm{sgn}\left(\kappa - \frac{8\xi}{a^2}\right) - 2\mathrm{sgn}\left(\kappa - \frac{4\xi}{a^2}\right).
\end{aligned} \qquad (7.28)$$

The eigenvalues at $\Lambda(X) = \Lambda(Y)$ are identical and thus appears twice in Eq. (7.28). The topological phase diagram is shown in Fig. 7.3. For standard MCS theory, the Hall viscosity is zero $\xi = 0$ and the photonic Chern number is identically zero $C_{\mathrm{em}} = 0$ in the lattice regularization. This is due to the inherent field doubling that occurs in a periodic system [272] which cancels any parity anomalies that may arise in the continuum limit. Hence, the Hall conductivity κ alone cannot describe a photonic skyrmion or a topological electromagnetic phase. A nontrivial phase with spin-1 photonic skyrmions $|C_{\mathrm{em}}| = 2$ is only possible when Hall viscosity is non-zero $\xi \neq 0$. Note that the continuum limit is recovered when the Hall viscosity is sufficiently large $\sqrt{\xi/\kappa} \gg a$, such that the Chern number reduces to $C_{\mathrm{em}} =$
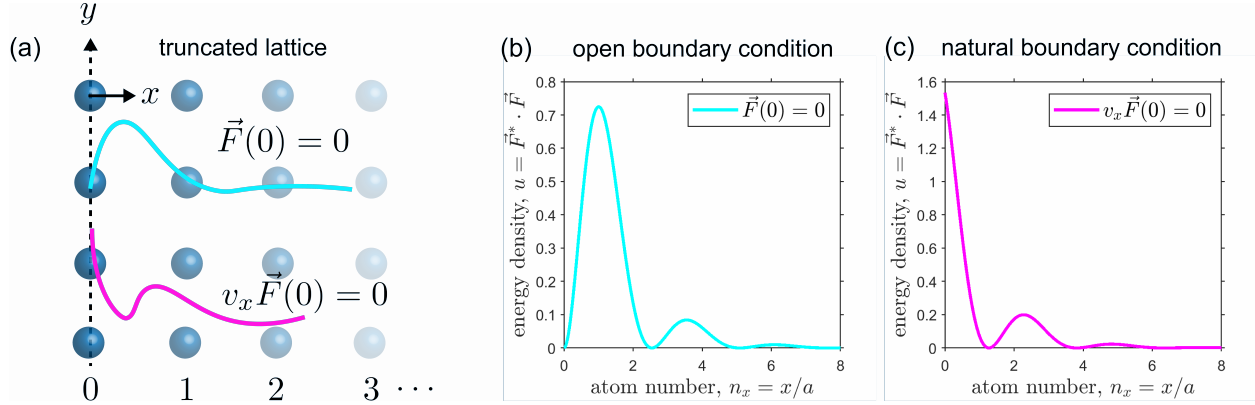
Figure 7.5. The two boundary conditions for the viscous Hall fluid that minimize the surface variation $\delta \mathcal{S}_s = 0$ at $x = 0$. (a) Schematic of the truncated atomic lattice at $x = 0$. (b) and (c) plot the normalized energy density $u = |\vec{F}|^2 = |\mathbf{E}|^2 + |B_z|^2$ of the chiral photonic edge state. The parameters are $\kappa a = 0.1$, $\xi/a = 0.2$ and $k_y a = 0.1$ as a demonstration. (b) The Dirichlet (open) boundary condition $\vec{F}(0) = 0$ has zero measure at $x = 0$. (c) The natural boundary condition $v_x \vec{F}(0) = 0$ is more localized at the surface and resembles an evanescent wave.

$\text{sgn}(\kappa) + \text{sgn}(\xi)$. The continuum theory predicts the existence of a spin-1 photonic skyrmion. Our work builds on the continuum theory to include lattice symmetries which delineates these skyrmions into type I and type II. As a visualization, examples of type I and type II photonic skyrmions are displayed in Fig. 7.4.

7.5   Topological boundary conditions

We now analyze the edge physics for the viscous Hall fluid using the MCS theory. We emphasize that the topological boundary conditions are derived through a minimization principle [Eq. (7.12)]. This is in stark contrast to the conventional approach to solving for topological photonic waves. Thus, the edge wave solutions of the viscous Hall fluid satisfy fundamentally different boundary conditions than photonic crystal edge waves or edge magneto-plasmons [261]. These Maxwellian waves are not only unidirectional but are also eigenstates of the photon spin operator [167]. The most striking property is that the contacting medium has no influence and cannot introduce a gap in the edge wave dispersion – the edge wave always exists. This is also a fundamentally unique property of the viscous

Hall fluid as conventional edge magneto-plasmons simply disappear if the contacting medium is a metal (eg: gold-InSb interface).

The topological boundary conditions have an intuitive interpretation in the RS basis. The open (Dirichlet) boundary condition [Eq. (7.14)] implies all components of the field vanish at the boundary $\vec{F}|_{x=0} = 0$. This is similar to the no-slip boundary condition in fluid mechanics. On the other hand, the natural boundary condition [Eq. (7.15)] guarantees that the induced surface current vanishes $v_x \vec{F}|_{x=0} = 0$. Fig. 7.5 shows the truncated lattice corresponding to a viscous Hall fluid and the unidirectional Maxwellian spin waves for two different boundary conditions. The detailed derivation of the bulk-boundary correspondence is appended to the supplementary information.

7.6 Conclusions

We have presented viscous Maxwell-Chern-Simons theory – the fundamental (exactly solvable) model of a topological electromagnetic phase. The topological physics of which is ultimately governed by viscous (nonlocal) Hall conductivity. To rigorously analyze the problem, we introduced the viscous Maxwell-Chern-Simons Lagrangian and derived the equations of motion, as well as the boundary conditions, from the principle of least action. Our work puts forth a fundamentally new field theoretic approach to merge the fields of topological photonics and quantum Hall fluids.

8. SUMMARY

At the outset of this thesis, the study of topological electromagnetism was solely the realm of photonic crystals and metamaterials. The main achievement of this work is translating these profound ideas in topological photonics to condensed matter physics. Due to a massive effort realizing strongly-correlated electron fluids, we now have convincing evidence that topological electromagnetic states can exist as distinct phases of matter. Magnetohydrodynamics is the first platform to study topological electrodynamics in the solid-state and there are potentially many more nontrivial electromagnetic materials waiting to be discovered. The theoretical framework developed in this thesis will help predict and characterize this fundamentally Maxwellian class of matter.

Advanced experimental techniques will need to be devised to probe the topological signatures of these exotic materials. In this thesis, we have proposed a few approaches such as momentum-resolved electron energy loss spectroscopy (k-EELS) and cold atom near-field probes to access the large momentum behavior of gyrotropic plasmas. We also expect evanescent magneto-optic-Kerr-effect (e-MOKE) spectroscopy to provide useful insight into the unusual polarization effects of nontrivial gyrotropic media at optical frequencies and large momentum. We are confident our work will create considerable impact in the condensed matter community and stimulate growth in this area of topological electromagnetic phases of matter. The unique topological photonic phenomena in these materials could revolutionize nanophotonic devices and provide robust electromagnetic pathways that are currently unreachable.

In summary, we have derived both the lattice and continuum topological electromagnetic field theories in condensed matter. Interactions between photons and dipole-carrying excitations, like plasmons and excitons, is the fundamental origin of temporal and spatial dispersion in the optical response. We have shown that spatiotemporal dispersion and non-reciprocity is a requirement for nontrivial topology in the solid-state. Specifically, nonlocal Hall conductivity is identified as the dispersive effective mass of the spin-1 photon which originates from Hall viscosity in strongly-correlated materials. A viscous Maxwell-Chern-Simons theory was proposed to study the electrodynamics of these highly nontrivial systems. We

have shown that Hall viscosity leads to many intriguing bulk effects in electromagnetism such as photonic skyrmions, Dirac monopoles and strings, singular Berry gauges and magnetic field repulsion. We also rigorously analyzed the boundary physics which revealed gapless chiral edge states that are immune to perturbations. Our work promises a new generation of effects at the interface of topological photonics and condensed matter physics.

REFERENCES

[1] J. Munkres, *Topology*, ser. Featured Titles for Topology Series. Prentice Hall, Incorporated, 2000, ISBN: 9780131816299.

[2] E. H. Hall, "On a New Action of the Magnet on Electric Currents," *American Journal of Mathematics*, vol. 2, no. 3, pp. 287–292, 1879, ISSN: 00029327, 10806377.

[3] K. v. Klitzing, G. Dorda, and M. Pepper, "New Method for High-Accuracy Determination of the Fine-Structure Constant Based on Quantized Hall Resistance," *Phys. Rev. Lett.*, vol. 45, pp. 494–497, 6 Aug. 1980. DOI: 10.1103/PhysRevLett.45.494.

[4] B. Jeckelmann and B. Jeanneret, "The quantum Hall effect as an electrical resistance standard," *Reports on Progress in Physics*, vol. 64, no. 12, pp. 1603–1655, Nov. 2001. DOI: 10.1088/0034-4885/64/12/201.

[5] R. B. Laughlin, "Quantized Hall conductivity in two dimensions," *Phys. Rev. B*, vol. 23, pp. 5632–5633, 10 May 1981. DOI: 10.1103/PhysRevB.23.5632.

[6] J. G. Analytis, S. J. Blundell, and A. Ardavan, "Landau levels, molecular orbitals, and the Hofstadter butterfly in finite systems," *American Journal of Physics*, vol. 72, no. 5, pp. 613–618, 2004. DOI: 10.1119/1.1615568.

[7] D. J. Thouless, M. Kohmoto, M. P. Nightingale, and M. den Nijs, "Quantized Hall Conductance in a Two-dimensional Periodic Potential," *Phys. Rev. Lett.*, vol. 49, pp. 405–408, 6 Aug. 1982. DOI: 10.1103/PhysRevLett.49.405.

[8] P. Dirac, "Quantised singularities in the electromagnetic field," *Proceedings of the Royal Society of London A: Mathematical, Physical and Engineering Sciences*, vol. 133, no. 821, pp. 60–72, 1931, ISSN: 0950-1207. DOI: 10.1098/rspa.1931.0130.

[9] M. V. Berry, "Quantal phase factors accompanying adiabatic changes," *Proceedings of the Royal Society of London. A. Mathematical and Physical Sciences*, vol. 392, no. 1802, pp. 45–57, Mar. 1984. DOI: 10.1098/rspa.1984.0023.

[10] M. R. Hirsbrunner, T. M. Philip, and M. J. Gilbert, "Topology and observables of the non-hermitian Chern insulator," *Phys. Rev. B*, vol. 100, p. 081 104, 8 Aug. 2019. DOI: 10.1103/PhysRevB.100.081104.

[11] F. D. M. Haldane, "Model for a Quantum Hall Effect without Landau Levels: Condensed Matter Realization of the "Parity Anomaly"," *Phys. Rev. Lett.*, vol. 61, pp. 2015–2018, 18 Oct. 1988. DOI: 10.1103/PhysRevLett.61.2015.

[12] C.-Z. Chang, J. Zhang, X. Feng, J. Shen, Z. Zhang, M. Guo, K. Li, Y. Ou, P. Wei, L.-L. Wang, Z.-Q. Ji, Y. Feng, S. Ji, X. Chen, J. Jia, X. Dai, Z. Fang, S.-C. Zhang, K. He, Y. Wang, L. Lu, X.-C. Ma, and Q.-K. Xue, "Experimental Observation of the Quantum Anomalous Hall Effect in a Magnetic Topological Insulator," *Science*, vol. 340, no. 6129, pp. 167–170, 2013, ISSN: 0036-8075. DOI: 10.1126/science.1234414.

[13] G. Jotzu, M. Messer, R. Desbuquois, M. Lebrat, T. Uehlinger, D. Greif, and T. Esslinger, "Experimental realization of the topological Haldane model with ultracold fermions," *Nature*, vol. 515, p. 237, Nov. 2014. DOI: https://doi.org/10.1038/nature13915.

[14] A. H. Castro Neto, F. Guinea, N. M. R. Peres, K. S. Novoselov, and A. K. Geim, "The electronic properties of graphene," *Rev. Mod. Phys.*, vol. 81, pp. 109–162, 1 Jan. 2009. DOI: 10.1103/RevModPhys.81.109.

[15] S. Ryu, A. P. Schnyder, A. Furusaki, and A. W. W. Ludwig, "Topological insulators and superconductors: Tenfold way and dimensional hierarchy," *New Journal of Physics*, vol. 12, no. 6, p. 065 010, Jun. 2010. DOI: 10.1088/1367-2630/12/6/065010.

[16] J. Kruthoff, J. de Boer, J. van Wezel, C. L. Kane, and R.-J. Slager, "Topological Classification of Crystalline Insulators through Band Structure Combinatorics," *Phys. Rev. X*, vol. 7, p. 041 069, 4 Dec. 2017. DOI: 10.1103/PhysRevX.7.041069.

[17] M. Z. Hasan and C. L. Kane, "Colloquium: Topological insulators," *Rev. Mod. Phys.*, vol. 82, pp. 3045–3067, 4 Nov. 2010. DOI: 10.1103/RevModPhys.82.3045.

[18] L. Lu, J. D. Joannopoulos, and M. Soljacic, "Topological photonics," *Nat Photon*, vol. 8, no. 11, pp. 821–829, Nov. 2014, ISSN: 1749-4885. DOI: https://doi.org/10.1038/nphoton.2014.248.

[19] S. Raghu and F. D. M. Haldane, "Analogs of quantum-Hall-effect edge states in photonic crystals," *Phys. Rev. A*, vol. 78, p. 033 834, 3 Sep. 2008. DOI: 10.1103/PhysRevA.78.033834.

[20] F. D. M. Haldane and S. Raghu, "Possible Realization of Directional Optical Waveguides in Photonic Crystals with Broken Time-Reversal Symmetry," *Phys. Rev. Lett.*, vol. 100, p. 013 904, 1 Jan. 2008. DOI: 10.1103/PhysRevLett.100.013904.

[21] J. D. Joannopoulos, P. R. Villeneuve, and S. Fan, "Photonic crystals: Putting a new twist on light," *Nature*, vol. 386, no. 6621, pp. 143–149, Mar. 1997, ISSN: 1476-4687. DOI: 10.1038/386143a0.

[22] N. Schine, A. Ryou, A. Gromov, A. Sommer, and J. Simon, "Synthetic Landau levels for photons," *Nature*, vol. 534, no. 7609, pp. 671–675, Jun. 2016, ISSN: 1476-4687. DOI: 10.1038/nature17943.

[23] Z. Wang, Y. Chong, J. D. Joannopoulos, and M. Soljacic, "Observation of unidirectional backscattering-immune topological electromagnetic states," *Nature*, vol. 461, no. 7265, pp. 772–775, Oct. 2009, ISSN: 0028-0836. DOI: 10.1038/nature08293.

[24] T. Ozawa, H. M. Price, A. Amo, N. Goldman, M. Hafezi, L. Lu, M. C. Rechtsman, D. Schuster, J. Simon, O. Zilberberg, and I. Carusotto, "Topological photonics," *Rev. Mod. Phys.*, vol. 91, p. 015 006, 1 Mar. 2019. DOI: 10.1103/RevModPhys.91.015006.

[25] A. I. Berdyugin, S. G. Xu, F. M. D. Pellegrino, R. Krishna Kumar, A. Principi, I. Torre, M. Ben Shalom, T. Taniguchi, K. Watanabe, I. V. Grigorieva, M. Polini, A. K. Geim, and D. A. Bandurin, "Measuring Hall viscosity of graphene's electron fluid," *Science*, vol. 364, no. 6436, pp. 162–165, 2019, ISSN: 0036-8075. DOI: 10.1126/science.aau0685.

[26] T. V. Mechelen and Z. Jacob, "Universal spin-momentum locking of evanescent waves," *Optica*, vol. 3, no. 2, pp. 118–126, Feb. 2016. DOI: 10.1364/OPTICA.3.000118.

[27] C. L. Kane and E. J. Mele, "Quantum Spin Hall Effect in Graphene," *Phys. Rev. Lett.*, vol. 95, p. 226 801, 22 Nov. 2005. DOI: 10.1103/PhysRevLett.95.226801.

[28] B. A. Bernevig, T. L. Hughes, and S.-C. Zhang, "Quantum Spin Hall Effect and Topological Phase Transition in HgTe Quantum Wells," *Science*, vol. 314, no. 5806, pp. 1757–1761, 2006, ISSN: 0036-8075. DOI: 10.1126/science.1133734.

[29] J. Maciejko, T. L. Hughes, and S.-C. Zhang, "The Quantum Spin Hall Effect," *Annual Review of Condensed Matter Physics*, vol. 2, no. 1, pp. 31–53, Dec. 2011. DOI: 10.1146/annurev-conmatphys-062910-140538.

[30] M. Neugebauer, T. Bauer, P. Banzer, and G. Leuchs, "Polarization tailored light driven directional optical nanobeacon," *Nano Letters*, vol. 14, no. 5, pp. 2546–2551, May 2014, ISSN: 1530-6984. DOI: 10.1021/nl5003526.

[31] J. Petersen, J. Volz, and A. Rauschenbeutel, "Chiral nanophotonic waveguide interface based on spin-orbit interaction of light," *Science*, vol. 346, no. 6205, pp. 67–71, 2014, ISSN: 0036-8075. DOI: 10.1126/science.1257671.

[32] D. O'Connor, P. Ginzburg, F. Rodríguez-Fortuño, G. Wurtz, and A. Zayats, "Spin-orbit coupling in surface plasmon scattering by nanostructures," *Nature Communications*, vol. 5, 2014. DOI: https://doi.org/10.1038/ncomms6327.

[33] P. V. Kapitanova, P. Ginzburg, F. J. Rodríguez-Fortuño, D. S. Filonov, P. M. Voroshilov, P. A. Belov, A. N. Poddubny, Y. S. Kivshar, G. A. Wurtz, and A. V. Zayats, "Photonic spin Hall effect in hyperbolic metamaterials for polarization-controlled routing of subwavelength modes," *Nature Communications*, vol. 5, p. 3226, Feb. 2014. DOI: https://doi.org/10.1038/ncomms4226.

[34] I. Söllner, S. Mahmoodian, S. L. Hansen, L. Midolo, A. Javadi, G. Kiršanske, T. Pregnolato, H. El-Ella, E. H. Lee, J. D. Song, *et al.*, "Deterministic photon-emitter coupling in chiral photonic circuits," *Nat. Nano.*, vol. 10, no. 9, pp. 775–778, 2015. DOI: https://doi.org/10.1038/nnano.2015.159.

[35] B. le Feber, N. Rotenberg, and L. Kuipers, "Nanophotonic control of circular dipole emission," *Nature Communications*, vol. 6, no. 1, p. 6695, Apr. 2015, ISSN: 2041-1723. DOI: 10.1038/ncomms7695.

[36] R. Mitsch, C. Sayrin, B. Albrecht, P. Schneeweiss, and A. Rauschenbeutel, "Quantum state-controlled directional spontaneous emission of photons into a nanophotonic waveguide," *Nature Communications*, vol. 5, p. 5713, Dec. 2014. DOI: https://doi.org/10.1038/ncomms6713.

[37] F. J. Rodríguez-Fortuño, G. Marino, P. Ginzburg, D. O'Connor, A. Martínez, G. A. Wurtz, and A. V. Zayats, "Near-field interference for the unidirectional excitation of electromagnetic guided modes," *Science*, vol. 340, no. 6130, pp. 328–330, 2013.

[38] J. Lin, J. P. B. Mueller, Q. Wang, G. Yuan, N. Antoniou, X.-C. Yuan, and F. Capasso, "Polarization-Controlled Tunable Directional Coupling of Surface Plasmon Polaritons," *Science*, vol. 340, no. 6130, pp. 331–334, 2013, ISSN: 0036-8075. DOI: 10.1126/science.1233746.

[39] K. Y. Bliokh, A. Y. Bekshaev, and F. Nori, "Extraordinary momentum and spin in evanescent waves," *Nature Communications*, vol. 5, Mar. 2014. DOI: https://doi.org/10.1038/ncomms4300.

[40] K. Y. Bliokh and F. Nori, "Transverse spin of a surface polariton," *Physical Review A*, vol. 85, no. 6, p. 061 801, Jun. 2012. DOI: https://doi.org/10.1103/PhysRevA.85.061801.

[41] W. H. McMaster, "Matrix Representation of Polarization," *Rev. Mod. Phys.*, vol. 33, pp. 8–28, 1 Jan. 1961. DOI: 10.1103/RevModPhys.33.8.

[42] F. Fedorov, "Covariant description of the properties of light beams," *Journal of Applied Spectroscopy*, vol. 2, no. 6, pp. 344–351, Jun. 1965. DOI: https://doi.org/10.1007/BF00655106.

[43] R. P. Cameron, S. M. Barnett, and A. M. Yao, "Optical helicity, optical spin and related quantities in electromagnetic theory," *New Journal of Physics*, vol. 14, no. 5, p. 053 050, May 2012. DOI: 10.1088/1367-2630/14/5/053050.

[44] K. Y. Bliokh, A. Y. Bekshaev, and F. Nori, "Dual electromagnetism: Helicity, spin, momentum and angular momentum," *New Journal of Physics*, vol. 15, no. 3, p. 033 026, Mar. 2013. DOI: 10.1088/1367-2630/15/3/033026.

[45] M. Livio, *The golden ratio: The story of phi, the world's most astonishing number.* Broadway Books, 2008.

[46] G. Ford and W. Weber, "Electromagnetic interactions of molecules with metal surfaces," *Physics Reports*, vol. 113, no. 4, pp. 195–287, 1984, ISSN: 0370-1573. DOI: https://doi.org/10.1016/0370-1573(84)90098-X.

[47] V. V. Klimov, D. V. Guzatov, and M. Ducloy, "Engineering of radiation of optically active molecules with chiral nano-meta-particles," *EPL (Europhysics Letters)*, vol. 97, no. 4, p. 47 004, Feb. 2012. DOI: 10.1209/0295-5075/97/47004.

[48] S.-Y. Lee, I.-M. Lee, J. Park, S. Oh, W. Lee, K.-Y. Kim, and B. Lee, "Role of Magnetic Induction Currents in Nanoslit Excitation of Surface Plasmon Polaritons," *Phys. Rev. Lett.*, vol. 108, p. 213 907, 21 May 2012. DOI: 10.1103/PhysRevLett.108.213907.

[49] T.-I. Jeon and D. Grischkowsky, "THz Zenneck surface wave (Thz surface plasmon) propagation on a metal sheet," *Applied Physics Letters*, vol. 88, no. 6, p. 061 113, 2006. DOI: 10.1063/1.2171488.

[50] M. D'yakonov, "New type of electromagnetic wave propagating at the interface," *Zh. Eksp. Teor. Fiz*, vol. 94, no. 4, pp. 119–123, 1988.

[51] A. B. Khanikaev, S. Hossein Mousavi, W.-K. Tse, M. Kargarian, A. H. MacDonald, and G. Shvets, "Photonic topological insulators," *Nat Mater*, vol. 12, no. 3, pp. 233–239, Mar. 2013, ISSN: 1476-1122. DOI: 10.1038/nmat3520.

[52] M. C. Rechtsman, J. M. Zeuner, Y. Plotnik, Y. Lumer, D. Podolsky, F. Dreisow, S. Nolte, M. Segev, and A. Szameit, "Photonic Floquet topological insulators," *Nature*, vol. 496, no. 7444, pp. 196–200, Apr. 2013, ISSN: 0028-0836. DOI: https://doi.org/10.1038/nature12066.

[53] W. Gao, M. Lawrence, B. Yang, F. Liu, F. Fang, B. Béri, J. Li, and S. Zhang, "Topological Photonic Phase in Chiral Hyperbolic Metamaterials," *Phys. Rev. Lett.*, vol. 114, p. 037 402, 3 Jan. 2015. DOI: 10.1103/PhysRevLett.114.037402.

[54] T. Van Mechelen and Z. Jacob, "Quantum gyroelectric effect: Photon spin-1 quantization in continuum topological bosonic phases," *Phys. Rev. A*, vol. 98, p. 023 842, 2 Aug. 2018. DOI: 10.1103/PhysRevA.98.023842.

[55] Y. Ikebe, T. Morimoto, R. Masutomi, T. Okamoto, H. Aoki, and R. Shimano, "Optical Hall Effect in the Integer Quantum Hall Regime," *Phys. Rev. Lett.*, vol. 104, p. 256 802, 25 Jun. 2010. DOI: 10.1103/PhysRevLett.104.256802.

[56] T. Lan, L. Kong, and X.-G. Wen, "Theory of (2+1)-dimensional fermionic topological orders and fermionic/bosonic topological orders with symmetries," *Phys. Rev. B*, vol. 94, p. 155 113, 15 Oct. 2016. DOI: 10.1103/PhysRevB.94.155113.

[57] X. Chen, Z.-C. Gu, Z.-X. Liu, and X.-G. Wen, "Symmetry-Protected Topological Orders in Interacting Bosonic Systems," *Science*, vol. 338, no. 6114, pp. 1604–1606, 2012. DOI: 10.1126/science.1227224.

[58] A. Vishwanath and T. Senthil, "Physics of Three-dimensional Bosonic Topological Insulators: Surface-Deconfined Criticality and Quantized Magnetoelectric Effect," *Phys. Rev. X*, vol. 3, p. 011 016, 1 Feb. 2013. DOI: 10.1103/PhysRevX.3.011016.

[59] M. A. Metlitski, C. L. Kane, and M. P. A. Fisher, "Bosonic topological insulator in three dimensions and the statistical Witten effect," *Phys. Rev. B*, vol. 88, p. 035 131, 3 Jul. 2013. DOI: 10.1103/PhysRevB.88.035131.

[60] T. Senthil and M. Levin, "Integer Quantum Hall Effect for Bosons," *Phys. Rev. Lett.*, vol. 110, p. 046 801, 4 Jan. 2013. DOI: 10.1103/PhysRevLett.110.046801.

[61] Y.-M. Lu and A. Vishwanath, "Theory and classification of interacting integer topological phases in two dimensions: A Chern-Simons approach," *Phys. Rev. B*, vol. 86, p. 125 119, 12 Sep. 2012. DOI: 10.1103/PhysRevB.86.125119.

[62] X. Chen, Z.-X. Liu, and X.-G. Wen, "Two-dimensional symmetry-protected topological orders and their protected gapless edge excitations," *Phys. Rev. B*, vol. 84, p. 235 141, 23 Dec. 2011. DOI: 10.1103/PhysRevB.84.235141.

[63] T. V. Mechelen and Z. Jacob, "Dirac-Maxwell correspondence: Spin-1 bosonic topological insulator," in *Conference on Lasers and Electro-Optics*, Optical Society of America, May 2018, FTu3E.4. DOI: 10.1364/CLEO_QELS.2018.FTu3E.4.

[64] M. Hafezi, S. Mittal, J. Fan, A. Migdall, and J. M. Taylor, "Imaging topological edge states in silicon photonics," *Nat Photon*, vol. 7, no. 12, pp. 1001–1005, Dec. 2013, ISSN: 1749-4885. DOI: https://doi.org/10.1038/nphoton.2013.274.

[65] T. Karzig, C.-E. Bardyn, N. H. Lindner, and G. Refael, "Topological Polaritons," *Phys. Rev. X*, vol. 5, p. 031 001, 3 Jul. 2015. DOI: 10.1103/PhysRevX.5.031001.

[66] Y. Hadad, V. Vitelli, and A. Alu, "Solitons and Propagating Domain Walls in Topological Resonator Arrays," *ACS Photonics*, vol. 4, no. 8, pp. 1974–1979, 2017. DOI: 10.1021/acsphotonics.7b00303.

[67] Z.-C. Gu, Z. Wang, and X.-G. Wen, "Classification of two-dimensional fermionic and bosonic topological orders," *Phys. Rev. B*, vol. 91, p. 125149, 12 Mar. 2015. DOI: 10.1103/PhysRevB.91.125149.

[68] L. Lu, L. Fu, J. D. Joannopoulos, and M. Soljacic, "Weyl points and line nodes in gyroid photonic crystals," *Nat Photon*, vol. 7, no. 4, pp. 294–299, Apr. 2013, ISSN: 1749-4885. DOI: 10.1038/nphoton.2013.42.

[69] Z. Wang and S. Fan, "Optical circulators in two-dimensional magneto-optical photonic crystals," *Opt. Lett.*, vol. 30, no. 15, pp. 1989–1991, Aug. 2005. DOI: 10.1364/OL.30.001989.

[70] A. Slobozhanyuk, S. H. Mousavi, X. Ni, D. Smirnova, Y. S. Kivshar, and A. B. Khanikaev, "Three-dimensional all-dielectric photonic topological insulator," *Nat Photon*, vol. 11, no. 2, pp. 130–136, Feb. 2017, ISSN: 1749-4885. DOI: https://doi.org/10.1038/nphoton.2016.253.

[71] C. He, X.-C. Sun, X.-P. Liu, M.-H. Lu, Y. Chen, L. Feng, and Y.-F. Chen, "Photonic topological insulator with broken time-reversal symmetry," *Proceedings of the National Academy of Sciences*, vol. 113, no. 18, pp. 4924–4928, 2016, ISSN: 0027-8424. DOI: 10.1073/pnas.1525502113.

[72] J. Koch, A. A. Houck, K. L. Hur, and S. M. Girvin, "Time-reversal-symmetry breaking in circuit-QED-based photon lattices," *Phys. Rev. A*, vol. 82, p. 043811, 4 Oct. 2010. DOI: 10.1103/PhysRevA.82.043811.

[73] D. Jaksch and P. Zoller, "Creation of effective magnetic fields in optical lattices: The Hofstadter butterfly for cold neutral atoms," *New Journal of Physics*, vol. 5, no. 1, p. 56, 2003. DOI: 10.1088/1367-2630/5/1/356.

[74] M. G. Silveirinha, "Chern invariants for continuous media," *Phys. Rev. B*, vol. 92, p. 125153, 12 Sep. 2015. DOI: 10.1103/PhysRevB.92.125153.

[75] M. G. Silveirinha, "$\mathcal{P}\cdot\mathcal{T}\cdot\mathcal{D}$ symmetry-protected scattering anomaly in optics," *Phys. Rev. B*, vol. 95, p. 035153, 3 Jan. 2017. DOI: 10.1103/PhysRevB.95.035153.

[76] D. Jin, L. Lu, Z. Wang, C. Fang, J. D. Joannopoulos, M. Soljacic, L. Fu, and N. X. Fang, "Topological magnetoplasmon," *Nature Communications*, vol. 7, p. 13486, Nov. 2016. DOI: https://doi.org/10.1038/ncomms13486.

[77] L.-k. Shi and J. C. W. Song, "Plasmon Geometric Phase and Plasmon Hall Shift," *Phys. Rev. X*, vol. 8, p. 021 020, 2 Apr. 2018. DOI: 10.1103/PhysRevX.8.021020.

[78] I. Bialynicki-Birula and Z. Bialynicka-Birula, "Berry's phase in the relativistic theory of spinning particles," *Phys. Rev. D*, vol. 35, pp. 2383–2387, 8 Apr. 1987. DOI: 10.1103/PhysRevD.35.2383.

[79] M. Stone, "Berry phase and anomalous velocity of Weyl fermions and Maxwell photons," *International Journal of Modern Physics B*, vol. 30, no. 02, p. 1 550 249, 2016. DOI: 10.1142/S0217979215502495.

[80] M. Z. Hasan and C. L. Kane, "Colloquium: Topological insulators," *Rev. Mod. Phys.*, vol. 82, pp. 3045–3067, 4 Nov. 2010. DOI: 10.1103/RevModPhys.82.3045.

[81] S. M. Barnett, L. Allen, R. P. Cameron, C. R. Gilson, M. J. Padgett, F. C. Speirits, and A. M. Yao, "On the natures of the spin and orbital parts of optical angular momentum," *Journal of Optics*, vol. 18, no. 6, p. 064 004, 2016, ISSN: 2040-8986. DOI: 10.1088/2040-8978/18/6/064004.

[82] K. Y. Bliokh and F. Nori, "Transverse and longitudinal angular momenta of light," *Physics Reports*, vol. 592, pp. 1–38, 2015, ISSN: 0370-1573. DOI: https://doi.org/10.1016/j.physrep.2015.06.003.

[83] F. Kalhor, T. Thundat, and Z. Jacob, "Universal spin-momentum locked optical forces," *Applied Physics Letters*, vol. 108, no. 6, p. 061 102, Feb. 2016, ISSN: 0003-6951. DOI: 10.1063/1.4941539.

[84] G. V. Dunne, "Aspects of Chern-Simons Theory," in *Aspects topologiques de la physique en basse dimension. Topological aspects of low dimensional systems*, A. Comtet, T. Jolicœur, S. Ouvry, and F. David, Eds., Berlin, Heidelberg: Springer Berlin Heidelberg, 1999, pp. 177–263, ISBN: 978-3-540-46637-6. DOI: https://doi.org/10.1007/3-540-46637-1_3.

[85] D. Boyanovsky, R. Blankenbecler, and R. Yahalom, "Physical origin of topological mass in 2 + 1 dimensions," *Nuclear Physics B*, vol. 270, pp. 483–505, 1986, ISSN: 0550-3213. DOI: https://doi.org/10.1016/0550-3213(86)90564-X.

[86] K. Ziegler, "Delocalization of 2D Dirac Fermions: The Role of a Broken Supersymmetry," *Phys. Rev. Lett.*, vol. 80, pp. 3113–3116, 14 Apr. 1998. DOI: 10.1103/PhysRevLett.80.3113.

[87] L. D. Landau, J. Bell, M. Kearsley, L. Pitaevskii, E. Lifshitz, and J. Sykes, *Electrodynamics of continuous media*. Elsevier, 2013, vol. 8.

[88] S. A. R. Horsley and T. G. Philbin, "Canonical quantization of electromagnetism in spatially dispersive media," *New Journal of Physics*, vol. 16, no. 1, p. 013 030, 2014. DOI: 10.1088/1367-2630/16/1/013030.

[89] S. T. Ivanov and N. I. Nikolaev, "Singular waves along the boundary of gyrotropic plasma," *Journal of Physics D: Applied Physics*, vol. 29, no. 4, p. 1107, 1996. DOI: 10.1088/0022-3727/29/4/027.

[90] A. Eroglu, *Wave propagation and radiation in gyrotropic and anisotropic media.* Springer Science & Business Media, 2010. DOI: 10.1007/978-1-4419-6024-5.

[91] W.-Y. Shan, H.-Z. Lu, and S.-Q. Shen, "Effective continuous model for surface states and thin films of three-dimensional topological insulators," *New Journal of Physics*, vol. 12, no. 4, p. 043 048, 2010. DOI: 10.1088/1367-2630/12/4/043048.

[92] A. Medhi and V. B. Shenoy, "Continuum theory of edge states of topological insulators: Variational principle and boundary conditions," *Journal of Physics: Condensed Matter*, vol. 24, no. 35, p. 355 001, Jul. 2012. DOI: 10.1088/0953-8984/24/35/355001.

[93] S.-Q. Shen, W.-Y. Shan, and H.-Z. Lu, "Topological insulator and the Dirac equation," *SPIN*, vol. 01, no. 01, pp. 33–44, 2011. DOI: 10.1142/S2010324711000057.

[94] B. A. Bernevig and T. L. Hughes, *Topological insulators and topological superconductors.* Princeton University Press, 2013.

[95] V. M. Agranovich and V. Ginzburg, *Crystal optics with spatial dispersion, and excitons.* Springer Science & Business Media, 2013, vol. 42. DOI: 10.1007/978-3-662-02406-5.

[96] A. A. Rukhadze and V. P. Silin, "Electrodynamics of media with spatial dispersion," *Soviet Physics Uspekhi*, vol. 4, no. 3, p. 459, 1961.

[97] D. Hestenes, "Point Groups and Space Groups in Geometric Algebra," in *Applications of Geometric Algebra in Computer Science and Engineering*, L. Dorst, C. Doran, and J. Lasenby, Eds. Boston, MA: Birkhäuser Boston, 2002, pp. 3–34, ISBN: 978-1-4612-0089-5. DOI: 10.1007/978-1-4612-0089-5_1.

[98] J. F. Nye, *Physical properties of crystals: their representation by tensors and matrices.* Oxford University Press, 1985.

[99] B. C. Hall, *Lie Groups, Lie Algebras, and Representations*, ser. Graduate Texts in Mathematics. Cham: Springer International Publishing, 2015, vol. 222, ISBN: 978-3-319-13467-3. DOI: 10.1007/978-3-319-13467-3.

[100] C. Fang, M. J. Gilbert, and B. A. Bernevig, "Bulk topological invariants in noninteracting point group symmetric insulators," *Phys. Rev. B*, vol. 86, p. 115 112, 11 Sep. 2012. DOI: 10.1103/PhysRevB.86.115112.

[101] N. R. Heckenberg, R. McDuff, C. P. Smith, H. Rubinsztein-Dunlop, and M. J. Wegener, "Laser beams with phase singularities," *Optical and Quantum Electronics*, vol. 24, no. 9, S951–S962, Sep. 1992, ISSN: 1572-817X. DOI: 10.1007/BF01588597.

[102] T.-S. Zeng, W. Zhu, and D. N. Sheng, "Bosonic integer quantum Hall states in topological bands with Chern number two," *Phys. Rev. B*, vol. 93, p. 195 121, 19 May 2016. DOI: 10.1103/PhysRevB.93.195121.

[103] N. Read, "Lowest-Landau-level theory of the quantum Hall effect: The Fermi-liquid-like state of bosons at filling factor one," *Phys. Rev. B*, vol. 58, pp. 16 262–16 290, 24 Dec. 1998. DOI: 10.1103/PhysRevB.58.16262.

[104] Y. Zheng and T. Ando, "Hall conductivity of a two-dimensional graphite system," *Phys. Rev. B*, vol. 65, p. 245 420, 24 Jun. 2002. DOI: 10.1103/PhysRevB.65.245420.

[105] O. Takayama, L.-C. Crasovan, S. K. Johansen, D. Mihalache, D. Artigas, and L. Torner, "Dyakonov Surface Waves: A Review," *Electromagnetics*, vol. 28, no. 3, pp. 126–145, 2008. DOI: 10.1080/02726340801921403.

[106] P. Halevi and R. Fuchs, "Generalised additional boundary condition for non-local dielectrics. i. reflectivity," *Journal of Physics C: Solid State Physics*, vol. 17, no. 21, p. 3869, 1984. DOI: 10.1088/0022-3719/17/21/017.

[107] I. Gelfand, S. Fomin, and R. Silverman, *Calculus of Variations*, ser. Dover Books on Mathematics. Dover Publications, 2000, ISBN: 9780486414485.

[108] Y. Hatsugai, "Chern number and edge states in the integer quantum Hall effect," *Phys. Rev. Lett.*, vol. 71, pp. 3697–3700, 22 Nov. 1993. DOI: 10.1103/PhysRevLett.71.3697.

[109] J. C. Avila, H. Schulz-Baldes, and C. Villegas-Blas, "Topological Invariants of Edge States for Periodic Two-Dimensional Models," *Mathematical Physics, Analysis and Geometry*, vol. 16, no. 2, pp. 137–170, Jun. 2013, ISSN: 1572-9656. DOI: 10.1007/s11040-012-9123-9.

[110] N. Nagaosa, J. Sinova, S. Onoda, A. H. MacDonald, and N. P. Ong, "Anomalous Hall effect," *Rev. Mod. Phys.*, vol. 82, pp. 1539–1592, 2 May 2010. DOI: 10.1103/RevModPhys.82.1539.

[111] E. Fradkin, E. Dagotto, and D. Boyanovsky, "Physical Realization of the Parity Anomaly in Condensed Matter physics," *Phys. Rev. Lett.*, vol. 57, pp. 2967–2970, 23 Dec. 1986. DOI: 10.1103/PhysRevLett.57.2967.

[112] P. Shekhar, M. Malac, V. Gaind, N. Dalili, A. Meldrum, and Z. Jacob, "Momentum-Resolved Electron Energy loss Spectroscopy for Mapping the Photonic Density of States," *ACS Photonics*, vol. 4, no. 4, pp. 1009–1014, 2017. DOI: 10.1021/acsphotonics.7b00103.

[113] J. A. Scholl, A. L. Koh, and J. A. Dionne, "Quantum plasmon resonances of individual metallic nanoparticles," *Nature*, vol. 483, p. 421, Mar. 2012. DOI: https://doi.org/10.1038/nature10904.

[114] M. Saffman, T. G. Walker, and K. Mølmer, "Quantum information with Rydberg atoms," *Rev. Mod. Phys.*, vol. 82, pp. 2313–2363, 3 Aug. 2010. DOI: 10.1103/RevModPhys.82.2313.

[115] A. Goban, C.-L. Hung, J. D. Hood, S.-P. Yu, J. A. Muniz, O. Painter, and H. J. Kimble, "Superradiance for Atoms Trapped along a Photonic Crystal Waveguide," *Phys. Rev. Lett.*, vol. 115, p. 063 601, 6 Aug. 2015. DOI: 10.1103/PhysRevLett.115.063601.

[116] T. V. Mechelen and Z. Jacob, "Photonic Dirac monopoles and skyrmions: Spin-1 quantization [invited]," *Opt. Mater. Express*, vol. 9, no. 1, pp. 95–111, Jan. 2019. DOI: 10.1364/OME.9.000095.

[117] J. Preskill, "Magnetic Monopoles," *Annual Review of Nuclear and Particle Science*, vol. 34, no. 1, pp. 461–530, 1984. DOI: 10.1146/annurev.ns.34.120184.002333.

[118] C. L. Kane and E. J. Mele, "$\mathbb{Z}_2$ Topological Order and the Quantum Spin Hall Effect," *Phys. Rev. Lett.*, vol. 95, p. 146 802, 14 Sep. 2005. DOI: 10.1103/PhysRevLett.95.146802.

[119] S.-Y. Xu, I. Belopolski, N. Alidoust, M. Neupane, G. Bian, C. Zhang, R. Sankar, G. Chang, Z. Yuan, C.-C. Lee, S.-M. Huang, H. Zheng, J. Ma, D. S. Sanchez, B. Wang, A. Bansil, F. Chou, P. P. Shibayev, H. Lin, S. Jia, and M. Z. Hasan, "Discovery of a Weyl fermion semimetal and topological Fermi arcs," *Science*, vol. 349, no. 6248, pp. 613–617, 2015, ISSN: 0036-8075. DOI: 10.1126/science.aaa9297.

[120] K. Osterloh, M. Baig, L. Santos, P. Zoller, and M. Lewenstein, "Cold atoms in Non-Abelian Gauge Potentials: From the hofstadter "Moth" to Lattice Gauge Theory," *Phys. Rev. Lett.*, vol. 95, p. 010 403, 1 Jun. 2005. DOI: 10.1103/PhysRevLett.95.010403.

[121] D. J. P. Morris, D. A. Tennant, S. A. Grigera, B. Klemke, C. Castelnovo, R. Moessner, C. Czternasty, M. Meissner, K. C. Rule, J.-U. Hoffmann, K. Kiefer, S. Gerischer, D. Slobinsky, and R. S. Perry, "Dirac strings and Magnetic Monopoles in the Spin Ice Dy2Ti2O7," *Science*, vol. 326, no. 5951, pp. 411–414, 2009, ISSN: 0036-8075. DOI: 10.1126/science.1178868.

[122] S. Sugawa, F. Salces-Carcoba, A. R. Perry, Y. Yue, and I. B. Spielman, "Second Chern number of a quantum-simulated non-Abelian Yang monopole," *Science*, vol. 360, no. 6396, pp. 1429–1434, 2018, ISSN: 0036-8075. DOI: 10.1126/science.aam9031.

[123] H. Kedia, I. Bialynicki-Birula, D. Peralta-Salas, and W. T. M. Irvine, "Tying Knots in Light Fields," *Phys. Rev. Lett.*, vol. 111, p. 150 404, 15 Oct. 2013. DOI: 10.1103/PhysRevLett.111.150404.

[124] I. Bialynicki-Birula and Z. Bialynicka-Birula, "Uncertainty Relation for Photons," *Phys. Rev. Lett.*, vol. 108, p. 140 401, 14 Apr. 2012. DOI: 10.1103/PhysRevLett.108.140401.

[125] K. Ding, G. Ma, M. Xiao, Z. Q. Zhang, and C. T. Chan, "Emergence, Coalescence, and Topological Properties of Multiple Exceptional Points and Their Experimental Realization," *Phys. Rev. X*, vol. 6, p. 021 007, 2 Apr. 2016. DOI: 10.1103/PhysRevX.6.021007.

[126] H. Wang, L. Xu, H. Chen, and J.-H. Jiang, "Three-dimensional photonic Dirac points stabilized by point group symmetry," *Phys. Rev. B*, vol. 93, p. 235 155, 23 Jun. 2016. DOI: 10.1103/PhysRevB.93.235155.

[127] Y. Guo, M. Xiao, and S. Fan, "Topologically protected complete polarization conversion," *Phys. Rev. Lett.*, vol. 119, p. 167 401, 16 Oct. 2017. DOI: 10.1103/PhysRevLett.119.167401.

[128] W. Gao, M. Lawrence, B. Yang, F. Liu, F. Fang, B. Béri, J. Li, and S. Zhang, "Topological Photonic Phase in Chiral Hyperbolic Metamaterials," *Phys. Rev. Lett.*, vol. 114, p. 037 402, 3 Jan. 2015. DOI: 10.1103/PhysRevLett.114.037402. [Online]. Available: https://link.aps.org/doi/10.1103/PhysRevLett.114.037402.

[129] S. B. Glybovski, S. A. Tretyakov, P. A. Belov, Y. S. Kivshar, and C. R. Simovski, "Metasurfaces: From microwaves to visible," *Physics Reports*, vol. 634, pp. 1–72, 2016, ISSN: 0370-1573. DOI: https://doi.org/10.1016/j.physrep.2016.04.004.

[130] N. Papasimakis, Z. Luo, Z. X. Shen, F. D. Angelis, E. D. Fabrizio, A. E. Nikolaenko, and N. I. Zheludev, "Graphene in a photonic metamaterial," *Opt. Express*, vol. 18, no. 8, pp. 8353–8359, Apr. 2010. DOI: 10.1364/OE.18.008353.

[131] L. Lu, Z. Wang, D. Ye, L. Ran, L. Fu, J. D. Joannopoulos, and M. Soljačić, "Experimental observation of Weyl points," *Science*, vol. 349, no. 6248, pp. 622–624, 2015, ISSN: 0036-8075. DOI: 10.1126/science.aaa9273.

[132] W.-J. Chen, M. Xiao, and C. T. Chan, "Photonic crystals possessing multiple Weyl points and the experimental observation of robust surface states," *Nature Communications*, vol. 7, p. 13 038, Oct. 2016. DOI: https://doi.org/10.1038/ncomms13038.

[133] B. Yang, Q. Guo, B. Tremain, R. Liu, L. E. Barr, Q. Yan, W. Gao, H. Liu, Y. Xiang, J. Chen, C. Fang, A. Hibbins, L. Lu, and S. Zhang, "Ideal Weyl points and helicoid surface states in artificial photonic crystal structures," *Science*, 2018, ISSN: 0036-8075. DOI: 10.1126/science.aaq1221.

[134] L. Wang, S.-K. Jian, and H. Yao, "Topological photonic crystal with equifrequency Weyl points," *Phys. Rev. A*, vol. 93, p. 061 801, 6 Jun. 2016. DOI: 10.1103/PhysRevA.93.061801.

[135] H. Hu and C. Zhang, "Spin-1 topological monopoles in the parameter space of ultracold atoms," *Phys. Rev. A*, vol. 98, p. 013 627, 1 Jul. 2018. DOI: 10.1103/PhysRevA.98.013627.

[136] D. Chruscinski and A. Jamiolkowski, *Geometric Phases in Classical and Quantum Mechanics*, ser. Progress in Mathematical Physics. Birkhäuser Basel, 2004, ISBN: 978-0-8176-4282-2. DOI: 10.1007/978-0-8176-8176-0.

[137] L.-k. Shi and J. C. W. Song, "Plasmon Geometric Phase and Plasmon Hall Shift," *Phys. Rev. X*, vol. 8, p. 021 020, 2 Apr. 2018. DOI: 10.1103/PhysRevX.8.021020.

[138] P. A. D. Gon çalves, L. P. Bertelsen, S. Xiao, and N. A. Mortensen, "Plasmon-exciton polaritons in two-dimensional semiconductor/metal interfaces," *Phys. Rev. B*, vol. 97, p. 041 402, 4 Jan. 2018. DOI: 10.1103/PhysRevB.97.041402.

[139] S. A. R. Horsley, "Topology and the optical Dirac equation," *Phys. Rev. A*, vol. 98, p. 043 837, 4 Oct. 2018. DOI: 10.1103/PhysRevA.98.043837.

[140] O. E. Gawhary, T. Van Mechelen, and H. P. Urbach, "Role of Radial Charges on the Angular Momentum of Electromagnetic Fields: Spin-3/2 Light," *Phys. Rev. Lett.*, vol. 121, p. 123 202, 12 Sep. 2018. DOI: 10.1103/PhysRevLett.121.123202.

[141] B. Zhen, C. W. Hsu, L. Lu, A. D. Stone, and M. Solja či ć, "Topological Nature of Optical Bound States in the Continuum," *Phys. Rev. Lett.*, vol. 113, p. 257 401, 25 Dec. 2014. DOI: 10.1103/PhysRevLett.113.257401.

[142] D. C. Marinica, A. G. Borisov, and S. V. Shabanov, "Bound States in the Continuum in Photonics," *Phys. Rev. Lett.*, vol. 100, p. 183 902, 18 May 2008. DOI: `10.1103/PhysRevLett.100.183902`.

[143] I. V. Lindell and A. H. Sihvola, "Realization of the PEMC boundary," *IEEE Transactions on Antennas and Propagation*, vol. 53, no. 9, pp. 3012–3018, Sep. 2005, ISSN: 0018-926X. DOI: `10.1109/TAP.2005.854524`.

[144] J. Li, C. Shen, A. Díaz-Rubio, S. A. Tretyakov, and S. A. Cummer, "Systematic design and experimental demonstration of bianisotropic metasurfaces for scattering-free manipulation of acoustic wavefronts," *Nature Communications*, vol. 9, no. 1, p. 1342, 2018, ISSN: 2041-1723. DOI: `10.1038/s41467-018-03778-9`.

[145] Y.-M. Lu and A. Vishwanath, "Theory and classification of interacting integer topological phases in two dimensions: A Chern-Simons approach," *Phys. Rev. B*, vol. 86, p. 125 119, 12 Sep. 2012. DOI: `10.1103/PhysRevB.86.125119`.

[146] J. H. Han, *Skyrmions in Condensed Matter*, en, ser. Springer Tracts in Modern Physics. Springer International Publishing, 2017, ISBN: 978-3-319-69244-9. DOI: `10.1007/978-3-319-69246-3`.

[147] N. Nagaosa and Y. Tokura, "Topological properties and dynamics of magnetic skyrmions," *Nat Nano*, vol. 8, no. 12, pp. 899–911, Dec. 2013, ISSN: 1748-3387. DOI: `https://doi.org/10.1038/nnano.2013.243`.

[148] S. Tsesses, E. Ostrovsky, K. Cohen, B. Gjonaj, N. Lindner, and G. Bartal, "Optical skyrmion lattice in evanescent electromagnetic fields," 2018, ISSN: 0036-8075. DOI: `10.1126/science.aau0227`.

[149] I. Bialynicki-Birula and Z. Bialynicka-Birula, "The role of the Riemann-Silberstein vector in classical and quantum theories of electromagnetism," *Journal of Physics A: Mathematical and Theoretical*, vol. 46, no. 5, p. 053 001, 2013. DOI: `10.1088/1751-8113/46/5/053001`.

[150] S. M. Barnett, "Optical Dirac equation," *New Journal of Physics*, vol. 16, no. 9, p. 093 008, Sep. 2014. DOI: `10.1088/1367-2630/16/9/093008`.

[151] S. P. Martin, "A supersymmetry primer," *Perspectives on Supersymmetry*, pp. 1–98, 2011. DOI: `10.1142/9789812839657_0001`.

[152] S. M. Young, S. Zaheer, J. C. Y. Teo, C. L. Kane, E. J. Mele, and A. M. Rappe, "Dirac Semimetal in Three Dimensions," *Phys. Rev. Lett.*, vol. 108, p. 140 405, 14 Apr. 2012. DOI: `10.1103/PhysRevLett.108.140405`.

[153] S. Pancharatnam, "Generalized theory of interference, and its applications," *Proceedings of the Indian Academy of Sciences - Section A*, vol. 44, no. 5, pp. 247–262, Nov. 1956, ISSN: 0370-0089. DOI: 10.1007/BF03046050.

[154] C.-H. Park and N. Marzari, "Berry phase and pseudospin winding number in bilayer graphene," *Phys. Rev. B*, vol. 84, p. 205 440, 20 Nov. 2011. DOI: 10.1103/PhysRevB.84.205440.

[155] K. S. Novoselov, E. McCann, S. V. Morozov, V. I. Fal'ko, M. I. Katsnelson, U. Zeitler, D. Jiang, F. Schedin, and A. K. Geim, "Unconventional quantum Hall effect and Berry's phase of 2π in bilayer graphene," *Nature Physics*, vol. 2, p. 177, Feb. 2006. DOI: https://doi.org/10.1038/nphys245.

[156] R. Y. Chiao and Y.-S. Wu, "Manifestations of Berry's Topological Phase for the Photon," *Phys. Rev. Lett.*, vol. 57, pp. 933–936, 8 Aug. 1986. DOI: 10.1103/PhysRevLett.57.933.

[157] S. Pendharker, F. Kalhor, T. V. Mechelen, S. Jahani, N. Nazemifard, T. Thundat, and Z. Jacob, "Spin photonic forces in non-reciprocal waveguides," *Opt. Express*, vol. 26, no. 18, pp. 23 898–23 910, Sep. 2018. DOI: 10.1364/OE.26.023898.

[158] K. Y. Bliokh, D. Smirnova, and F. Nori, "Quantum spin Hall effect of light," *Science*, vol. 348, no. 6242, pp. 1448–1451, 2015. DOI: 10.1126/science.aaa9519.

[159] W. Pauli, "The Connection Between Spin and Statistics," *Phys. Rev.*, vol. 58, pp. 716–722, 8 Oct. 1940. DOI: 10.1103/PhysRev.58.716.

[160] N. Regnault and T. Senthil, "Microscopic model for the boson integer quantum Hall effect," *Phys. Rev. B*, vol. 88, p. 161 106, 16 Oct. 2013. DOI: 10.1103/PhysRevB.88.161106.

[161] Z. Zhu, Y. Cheng, and U. Schwingenschlögl, "Band inversion mechanism in topological insulators: A guideline for materials design," *Phys. Rev. B*, vol. 85, p. 235 401, 23 Jun. 2012. DOI: 10.1103/PhysRevB.85.235401.

[162] A. Tiwari, X. Chen, K. Shiozaki, and S. Ryu, "Bosonic topological phases of matter: Bulk-boundary correspondence, symmetry protected topological invariants, and gauging," *Phys. Rev. B*, vol. 97, p. 245 133, 24 Jun. 2018. DOI: 10.1103/PhysRevB.97.245133.

[163] Y. Oreg, G. Refael, and F. von Oppen, "Helical Liquids and Majorana Bound States in Quantum Wires," *Phys. Rev. Lett.*, vol. 105, p. 177 002, 17 Oct. 2010. DOI: 10.1103/PhysRevLett.105.177002.

[164] T. Van Mechelen and Z. Jacob, "Nonlocal topological electromagnetic phases of matter," *Phys. Rev. B*, vol. 99, p. 205 146, 20 May 2019. DOI: `10.1103/PhysRevB.99.205146`.

[165] Z. Lin and Z. Liu, "Spin-1 Dirac-Weyl fermions protected by bipartite symmetry," *The Journal of Chemical Physics*, vol. 143, no. 21, p. 214 109, 2015. DOI: `10.1063/1.4936774`.

[166] T. Zhang, Z. Song, A. Alexandradinata, H. Weng, C. Fang, L. Lu, and Z. Fang, "Double-Weyl Phonons in Transition-Metal Monosilicides," *Phys. Rev. Lett.*, vol. 120, p. 016 401, 1 Jan. 2018. DOI: `10.1103/PhysRevLett.120.016401`.

[167] T. V. Mechelen and Z. Jacob, "Unidirectional maxwellian spin waves," *Nanophotonics*, vol. 8, no. 8, pp. 1399–1416, Aug. 2019. DOI: `https://doi.org/10.1515/nanoph-2019-0092`.

[168] N. H. Lindner, G. Refael, and V. Galitski, "Floquet topological insulator in semiconductor quantum wells," *Nature Physics*, vol. 7, p. 490, Mar. 2011. DOI: `https://doi.org/10.1038/nphys1926`.

[169] J. Cayssol, B. Dora, F. Simon, and R. Moessner, "Floquet topological insulators," *physica status solidi (RRL) – Rapid Research Letters*, vol. 7, no. 1-2, pp. 101–108, 2013. DOI: `10.1002/pssr.201206451`.

[170] A. B. Khanikaev and G. Shvets, "Two-dimensional topological photonics," *Nature Photonics*, vol. 11, no. 12, pp. 763–773, 2017, ISSN: 1749-4893. DOI: `10.1038/s41566-017-0048-5`.

[171] R. Alaee, M. Farhat, C. Rockstuhl, and F. Lederer, "A perfect absorber made of a graphene micro-ribbon metamaterial," *Opt. Express*, vol. 20, no. 27, pp. 28 017–28 024, Dec. 2012. DOI: `10.1364/OE.20.028017`.

[172] S. A. H. Gangaraj, M. G. Silveirinha, and G. W. Hanson, "Berry Phase, Berry Connection, and Chern Number for a Continuum Bianisotropic Material From a Classical Electromagnetics Perspective," *IEEE Journal on Multiscale and Multiphysics Computational Techniques*, vol. 2, pp. 3–17, Jan. 2017, ISSN: 2379-8815. DOI: `10.1109/JMMCT.2017.2654962`.

[173] M. Stone, "Topology, spin, and light," *Science*, vol. 348, no. 6242, pp. 1432–1433, 2015, ISSN: 0036-8075. DOI: `10.1126/science.aac4368`.

[174] J. Hubbard, "The Dielectric Theory of Electronic Interactions in Solids," *Proceedings of the Physical Society. Section A*, vol. 68, no. 11, pp. 976–986, Nov. 1955. DOI: `10.1088/0370-1298/68/11/304`.

[175] D. S. Falk, "Effect of the Lattice on Dielectric Properties of an Electron Gas," *Phys. Rev.*, vol. 118, pp. 105–109, 1 Apr. 1960. DOI: 10.1103/PhysRev.118.105.

[176] D. R. Penn, "Wave-Number-Dependent Dielectric Function of Semiconductors," *Phys. Rev.*, vol. 128, pp. 2093–2097, 5 Dec. 1962. DOI: 10.1103/PhysRev.128.2093.

[177] L. Fu, "Topological Crystalline Insulators," *Phys. Rev. Lett.*, vol. 106, p. 106 802, 10 Mar. 2011. DOI: 10.1103/PhysRevLett.106.106802.

[178] T. L. Hughes, E. Prodan, and B. A. Bernevig, "Inversion-symmetric topological insulators," *Phys. Rev. B*, vol. 83, p. 245 132, 24 Jun. 2011. DOI: 10.1103/PhysRevB.83.245132.

[179] R.-J. Slager, A. Mesaros, V. Juricic, and J. Zaanen, "The space group classification of topological band-insulators," *Nature Physics*, vol. 9, p. 98, Dec. 2012. DOI: https://doi.org/10.1038/nphys2513.

[180] B. Bradlyn, L. Elcoro, J. Cano, M. G. Vergniory, Z. Wang, C. Felser, M. I. Aroyo, and B. A. Bernevig, "Topological quantum chemistry," *Nature*, vol. 547, p. 298, Jul. 2017. DOI: https://doi.org/10.1038/nature23268.

[181] H. Song, S.-J. Huang, L. Fu, and M. Hermele, "Topological Phases Protected by Point Group Symmetry," *Phys. Rev. X*, vol. 7, p. 011 020, 1 Feb. 2017. DOI: 10.1103/PhysRevX.7.011020.

[182] T. A. Sedrakyan, V. M. Galitski, and A. Kamenev, "Topological spin ordering via Chern-Simons superconductivity," *Phys. Rev. B*, vol. 95, p. 094 511, 9 Mar. 2017. DOI: 10.1103/PhysRevB.95.094511.

[183] H. C. Po, A. Vishwanath, and H. Watanabe, "Symmetry-based indicators of band topology in the 230 space groups," *Nature Communications*, vol. 8, no. 1, p. 50, Oct. 2017, ISSN: 2041-1723. DOI: 10.1038/s41467-017-00133-2.

[184] R. Thorngren and D. V. Else, "Gauging Spatial Symmetries and the Classification of Topological Crystalline Phases," *Phys. Rev. X*, vol. 8, p. 011 040, 1 Mar. 2018. DOI: 10.1103/PhysRevX.8.011040.

[185] A. Matsugatani, Y. Ishiguro, K. Shiozaki, and H. Watanabe, "Universal Relation among the Many-body Chern Number, Rotation Symmetry, and Filling," *Phys. Rev. Lett.*, vol. 120, p. 096 601, 9 Feb. 2018. DOI: 10.1103/PhysRevLett.120.096601.

[186] H. Watanabe, H. C. Po, and A. Vishwanath, "Structure and topology of band structures in the 1651 magnetic space groups," *Science Advances*, vol. 4, no. 8, Aug. 2018. DOI: 10.1126/sciadv.aat8685.

[187] B. Bradlyn, J. Cano, Z. Wang, M. G. Vergniory, C. Felser, R. J. Cava, and B. A. Bernevig, "Beyond Dirac and Weyl fermions: Unconventional quasiparticles in conventional crystals," *Science*, vol. 353, no. 6299, Aug. 2016, ISSN: 0036-8075. DOI: 10.1126/science.aaf5037.

[188] Y.-Q. Zhu, D.-W. Zhang, H. Yan, D.-Y. Xing, and S.-L. Zhu, "Emergent pseudospin-1 Maxwell fermions with a threefold degeneracy in optical lattices," *Phys. Rev. A*, vol. 96, p. 033 634, 3 Sep. 2017. DOI: 10.1103/PhysRevA.96.033634.

[189] H. Hu, J. Hou, F. Zhang, and C. Zhang, "Topological Triply Degenerate Points Induced by Spin-Tensor-Momentum Couplings," *Phys. Rev. Lett.*, vol. 120, p. 240 401, 24 Jun. 2018. DOI: 10.1103/PhysRevLett.120.240401.

[190] I. C. Fulga, L. Fallani, and M. Burrello, "Geometrically protected triple-point crossings in an optical lattice," *Phys. Rev. B*, vol. 97, p. 121 402, 12 Mar. 2018. DOI: 10.1103/PhysRevB.97.121402.

[191] X. Tan, D.-W. Zhang, Q. Liu, G. Xue, H.-F. Yu, Y.-Q. Zhu, H. Yan, S.-L. Zhu, and Y. Yu, "Topological Maxwell Metal Bands in a Superconducting Qutrit," *Phys. Rev. Lett.*, vol. 120, p. 130 503, 13 Mar. 2018. DOI: 10.1103/PhysRevLett.120.130503.

[192] X. Yin, Z. Ye, J. Rho, Y. Wang, and X. Zhang, "Photonic Spin Hall Effect at Metasurfaces," *Science*, vol. 339, no. 6126, pp. 1405–1407, Mar. 2013, ISSN: 0036-8075. DOI: 10.1126/science.1231758.

[193] M. Born and K. Huang, "Dynamical Theory of Crystal Lattices," *American Journal of Physics*, vol. 23, no. 7, pp. 474–474, 1955. DOI: 10.1119/1.1934059.

[194] A. F. J. Levi, "The Lorentz oscillator model," in *Essential Classical Mechanics for Device Physics*, ser. 2053-2571, Morgan & Claypool Publishers, 2016, 1 to 21, ISBN: 978-1-6817-4413-1. DOI: 10.1088/978-1-6817-4413-1ch5.

[195] T. G. Mackay and A. Lakhtakia, "Nonreciprocal Dyakonov-wave propagation supported by topological insulators," *J. Opt. Soc. Am. B*, vol. 33, no. 6, pp. 1266–1270, Jun. 2016. DOI: 10.1364/JOSAB.33.001266.

[196] C. Caloz, A. Alù, S. Tretyakov, D. Sounas, K. Achouri, and Z.-L. Deck-Léger, "Electromagnetic Nonreciprocity," *Phys. Rev. Applied*, vol. 10, p. 047 001, 4 Oct. 2018. DOI: 10.1103/PhysRevApplied.10.047001.

[197] M. S. Mirmoosa, Y. Ra'di, V. S. Asadchy, C. R. Simovski, and S. A. Tretyakov, "Polarizabilities of Nonreciprocal Bianisotropic Particles," *Phys. Rev. Applied*, vol. 1, p. 034 005, 3 Apr. 2014. DOI: 10.1103/PhysRevApplied.1.034005.

[198] J. Valente, J.-Y. Ou, E. Plum, I. J. Youngs, and N. I. Zheludev, "A magneto-electro-optical effect in a plasmonic nanowire material," *Nature Communications*, vol. 6, p. 7021, Apr. 2015. DOI: https://doi.org/10.1038/ncomms8021.

[199] D. Floess and H. Giessen, "Nonreciprocal hybrid magnetoplasmonics," *Reports on Progress in Physics*, vol. 81, no. 11, p. 116 401, Oct. 2018. DOI: 10.1088/1361-6633/aad6a8.

[200] V. A. Zyuzin, "Landau levels for an electromagnetic wave," *Phys. Rev. A*, vol. 96, p. 043 830, 4 Oct. 2017. DOI: 10.1103/PhysRevA.96.043830.

[201] S. A. Mann, D. L. Sounas, and A. Alù, "Nonreciprocal cavities and the time–bandwidth limit," *Optica*, vol. 6, no. 1, pp. 104–110, Jan. 2019. DOI: 10.1364/OPTICA.6.000104.

[202] K. L. Tsakmakidis, L. Shen, S. A. Schulz, X. Zheng, J. Upham, X. Deng, H. Altug, A. F. Vakakis, and R. W. Boyd, "Breaking Lorentz reciprocity to overcome the time-bandwidth limit in physics and engineering," *Science*, vol. 356, no. 6344, pp. 1260–1264, 2017, ISSN: 0036-8075. DOI: 10.1126/science.aam6662.

[203] S. Zhang, Y. Xiong, G. Bartal, X. Yin, and X. Zhang, "Magnetized Plasma for Reconfigurable Subdiffraction Imaging," *Phys. Rev. Lett.*, vol. 106, p. 243 901, 24 Jun. 2011. DOI: 10.1103/PhysRevLett.106.243901.

[204] M. A. Green, "Time-Asymmetric Photovoltaics," *Nano Letters*, vol. 12, no. 11, pp. 5985–5988, Oct. 2012. DOI: 10.1021/nl3034784.

[205] L. Zhu and S. Fan, "Persistent Directional Current at Equilibrium in Nonreciprocal Many-Body Near Field Electromagnetic Heat Transfer," *Phys. Rev. Lett.*, vol. 117, p. 134 303, 13 Sep. 2016. DOI: 10.1103/PhysRevLett.117.134303.

[206] A. Leviyev, B. Stein, A. Christofi, T. Galfsky, H. Krishnamoorthy, I. L. Kuskovsky, V. Menon, and A. B. Khanikaev, "Nonreciprocity and one-way topological transitions in hyperbolic metamaterials," *APL Photonics*, vol. 2, no. 7, p. 076 103, Jun. 2017. DOI: 10.1063/1.4985064.

[207] A. Stern, "Anyons and the quantum hall effect—a pedagogical review," *Annals of Physics*, vol. 323, no. 1, pp. 204–249, Jan. 2008, ISSN: 0003-4916. DOI: https://doi.org/10.1016/j.aop.2007.10.008.

[208] S. Vandendriessche, V. K. Valev, and T. Verbiest, "Faraday rotation and its dispersion in the visible region for saturated organic liquids," *Phys. Chem. Chem. Phys.*, vol. 14, pp. 1860–1864, 6 Dec. 2012. DOI: 10.1039/C2CP23311H.

[209] L. Landau and E. Lifshitz, *The Classical Theory of Fields*, ser. Course of theoretical physics. Elsevier Science, 1975, ISBN: 9780750627689. DOI: https://doi.org/10.1016/C2009-0-14608-1.

[210] F. R. Prudêncio and M. G. Silveirinha, "Asymmetric Cherenkov emission in a topological plasmonic waveguide," *Phys. Rev. B*, vol. 98, p. 115 136, 11 Sep. 2018. DOI: 10.1103/PhysRevB.98.115136.

[211] A. R. Davoyan and N. Engheta, "Theory of Wave Propagation in Magnetized Near-Zero-Epsilon Metamaterials: Evidence for One-Way Photonic States and Magnetically Switched Transparency and Opacity," *Phys. Rev. Lett.*, vol. 111, p. 257 401, 25 Dec. 2013. DOI: 10.1103/PhysRevLett.111.257401.

[212] J. C. W. Song and M. S. Rudner, "Chiral plasmons without magnetic field," *Proceedings of the National Academy of Sciences*, vol. 113, no. 17, pp. 4658–4663, Apr. 2016, ISSN: 0027-8424. DOI: 10.1073/pnas.1519086113.

[213] L. Lu, J. D. Joannopoulos, and M. Soljacic, "Topological states in photonic systems," *Nature Physics*, vol. 12, p. 626, Jun. 2016. DOI: https://doi.org/10.1038/nphys3796.

[214] M. I. Shalaev, S. Desnavi, W. Walasik, and N. M. Litchinitser, "Reconfigurable topological photonic crystal," *New Journal of Physics*, vol. 20, no. 2, p. 023 040, Feb. 2018. DOI: 10.1088/1367-2630/aaac04.

[215] J. Noh, W. A. Benalcazar, S. Huang, M. J. Collins, K. P. Chen, T. L. Hughes, and M. C. Rechtsman, "Topological protection of photonic mid-gap defect modes," *Nature Photonics*, vol. 12, no. 7, pp. 408–415, Jun. 2018, ISSN: 1749-4893. DOI: 10.1038/s41566-018-0179-3.

[216] M.-L. Chang, M. Xiao, W.-J. Chen, and C. T. Chan, "Multiple Weyl points and the sign change of their topological charges in woodpile photonic crystals," *Phys. Rev. B*, vol. 95, p. 125 136, 12 Mar. 2017. DOI: 10.1103/PhysRevB.95.125136.

[217] Q. Lin, X.-Q. Sun, M. Xiao, S.-C. Zhang, and S. Fan, "A three-dimensional photonic topological insulator using a two-dimensional ring resonator lattice with a synthetic frequency dimension," *Science Advances*, vol. 4, no. 10, Oct. 2018. DOI: 10.1126/sciadv.aat2774.

[218] L. E. Zhukov and M. E. Raikh, "Chiral electromagnetic waves at the boundary of optical isomers: Quantum Cotton-Mouton effect," *Phys. Rev. B*, vol. 61, pp. 12 842–12 847, 19 May 2000. DOI: 10.1103/PhysRevB.61.12842.

[219] A. A. Zyuzin and V. A. Zyuzin, "Chiral electromagnetic waves in Weyl semimetals," *Phys. Rev. B*, vol. 92, p. 115 310, 11 Sep. 2015. DOI: 10.1103/PhysRevB.92.115310.

[220] A. C. Mahoney, J. I. Colless, S. J. Pauka, J. M. Hornibrook, J. D. Watson, G. C. Gardner, M. J. Manfra, A. C. Doherty, and D. J. Reilly, "On-Chip Microwave Quantum Hall Circulator," *Phys. Rev. X*, vol. 7, p. 011 007, 1 Jan. 2017. DOI: 10.1103/PhysRevX.7.011007.

[221] S. Lannebère and M. G. Silveirinha, "Link between the photonic and electronic topological phases in artificial graphene," *Phys. Rev. B*, vol. 97, p. 165 128, 16 Apr. 2018. DOI: 10.1103/PhysRevB.97.165128.

[222] S. A. H. Gangaraj and F. Monticone, "Do truly unidirectional surface plasmon-polaritons exist?" *Optica*, vol. 6, no. 9, pp. 1158–1165, Sep. 2019. DOI: 10.1364/OPTICA.6.001158.

[223] P. Delplace, D. Ullmo, and G. Montambaux, "Zak phase and the existence of edge states in graphene," *Phys. Rev. B*, vol. 84, p. 195 452, 19 Nov. 2011. DOI: 10.1103/PhysRevB.84.195452.

[224] R. S. K. Mong and V. Shivamoggi, "Edge states and the bulk-boundary correspondence in Dirac Hamiltonians," *Phys. Rev. B*, vol. 83, p. 125 109, 12 Mar. 2011. DOI: 10.1103/PhysRevB.83.125109.

[225] S. Shen, *Topological Insulators: Dirac Equation in Condensed Matter*, ser. Springer Series in Solid-State Sciences. Springer Singapore, 2017, ISBN: 9789811046056. DOI: 10.1007/978-3-642-32858-9.

[226] R. Jackiw and C. Rebbi, "Solitons with fermion number ½," *Phys. Rev. D*, vol. 13, pp. 3398–3409, 12 Jun. 1976. DOI: 10.1103/PhysRevD.13.3398.

[227] T. Schuster, T. Iadecola, C. Chamon, R. Jackiw, and S.-Y. Pi, "Dissipationless conductance in a topological coaxial cable," *Phys. Rev. B*, vol. 94, p. 115 110, 11 Sep. 2016. DOI: 10.1103/PhysRevB.94.115110.

[228] D. R. Smith, J. B. Pendry, and M. C. K. Wiltshire, "Metamaterials and Negative Refractive Index," *Science*, vol. 305, no. 5685, pp. 788–792, Aug. 2004, ISSN: 0036-8075. DOI: 10.1126/science.1096796.

[229] A. B. Young, A. C. T. Thijssen, D. M. Beggs, P. Androvitsaneas, L. Kuipers, J. G. Rarity, S. Hughes, and R. Oulton, "Polarization Engineering in Photonic Crystal Waveguides for Spin-Photon Entanglers," *Phys. Rev. Lett.*, vol. 115, p. 153 901, 15 Oct. 2015. DOI: 10.1103/PhysRevLett.115.153901.

[230] K. Y. Bliokh, F. J. Rodríguez-Fortuño, F. Nori, and A. V. Zayats, "Spin-orbit interactions of light," *Nature Photonics*, vol. 9, p. 796, Nov. 2015. DOI: https://doi.org/10.1038/nphoton.2015.201.

[231] P. Lodahl, S. Mahmoodian, S. Stobbe, A. Rauschenbeutel, P. Schneeweiss, J. Volz, H. Pichler, and P. Zoller, "Chiral quantum optics," *Nature*, vol. 541, p. 473, Jan. 2017. DOI: https://doi.org/10.1038/nature21037.

[232] M. F. Picardi, A. V. Zayats, and F. J. Rodríguez-Fortuño, "Janus and Huygens Dipoles: Near-Field Directionality Beyond Spin-Momentum Locking," *Phys. Rev. Lett.*, vol. 120, p. 117 402, 11 Mar. 2018. DOI: 10.1103/PhysRevLett.120.117402.

[233] S. Luo, L. He, and M. Li, "Spin-momentum locked interaction between guided photons and surface electrons in topological insulators," *Nature Communications*, vol. 8, no. 1, p. 2141, Dec. 2017, ISSN: 2041-1723. DOI: 10.1038/s41467-017-02264-y.

[234] B. Bahari, A. Ndao, F. Vallini, A. El Amili, Y. Fainman, and B. Kanté, "Nonreciprocal lasing in topological cavities of arbitrary geometries," *Science*, vol. 358, no. 6363, pp. 636–640, 2017, ISSN: 0036-8075. DOI: 10.1126/science.aao4551.

[235] S. Wang, B. Hou, W. Lu, Y. Chen, Z. Q. Zhang, and C. T. Chan, "Arbitrary order exceptional point induced by photonic spin-orbit interaction in coupled resonators," *Nature Communications*, vol. 10, no. 1, p. 832, Feb. 2019, ISSN: 2041-1723. DOI: 10.1038/s41467-019-08826-6.

[236] A. M. Yao and M. J. Padgett, "Orbital angular momentum: Origins, behavior and applications," *Adv. Opt. Photon.*, vol. 3, no. 2, pp. 161–204, Jun. 2011. DOI: 10.1364/AOP.3.000161.

[237] T. T. Wu and C. N. Yang, "Dirac monopole without strings: Monopole harmonics," *Nuclear Physics B*, vol. 107, no. 3, pp. 365–380, 1976, ISSN: 0550-3213. DOI: https://doi.org/10.1016/0550-3213(76)90143-7.

[238] A. Rajantie, "Introduction to magnetic monopoles," *Contemporary Physics*, vol. 53, no. 3, pp. 195–211, 2012. DOI: 10.1080/00107514.2012.685693.

[239] Z. Fang, N. Nagaosa, K. S. Takahashi, A. Asamitsu, R. Mathieu, T. Ogasawara, H. Yamada, M. Kawasaki, Y. Tokura, and K. Terakura, "The Anomalous Hall Effect and Magnetic Monopoles in Momentum Space," *Science*, vol. 302, no. 5642, pp. 92–95, 2003, ISSN: 0036-8075. DOI: 10.1126/science.1089408.

[240] Y. Hatsugai, "Topological aspects of the quantum Hall effect," *Journal of Physics: Condensed Matter*, vol. 9, no. 12, pp. 2507–2549, Mar. 1997. DOI: 10.1088/0953-8984/9/12/003.

[241] P. B. Pal, "Dirac, Majorana, and Weyl fermions," *American Journal of Physics*, vol. 79, no. 5, pp. 485–498, Dec. 2011. DOI: 10.1119/1.3549729.

[242] V. B. Mohan, K.-t. Lau, D. Hui, and D. Bhattacharyya, "Graphene-based materials and their composites: A review on production, applications and product limitations," *Composites Part B: Engineering*, vol. 142, pp. 200–220, Jun. 2018, ISSN: 1359-8368. DOI: https://doi.org/10.1016/j.compositesb.2018.01.013.

[243] N. Read and D. Green, "Paired states of fermions in two dimensions with breaking of parity and time-reversal symmetries and the fractional quantum Hall effect," *Phys. Rev. B*, vol. 61, pp. 10 267–10 297, 15 Apr. 2000. DOI: 10.1103/PhysRevB.61.10267.

[244] A. Alù, M. G. Silveirinha, A. Salandrino, and N. Engheta, "Epsilon-near-zero metamaterials and electromagnetic sources: Tailoring the radiation phase pattern," *Phys. Rev. B*, vol. 75, p. 155 410, 15 Apr. 2007. DOI: 10.1103/PhysRevB.75.155410.

[245] J. Polo, T. Mackay, and A. Lakhtakia, *Electromagnetic Surface Waves: A Modern Perspective*. United States: Elsevier Inc., May 2013, ISBN: 9780123970244. DOI: 10.1016/C2011-0-07510-5.

[246] T. Van Mechelen and Z. Jacob, "Viscous Maxwell-Chern-Simons theory for topological electromagnetic phases of matter," *Phys. Rev. B*, vol. 102, p. 155 425, 15 Oct. 2020. DOI: 10.1103/PhysRevB.102.155425.

[247] S. Deser, R. Jackiw, and S. Templeton, "Topologically massive gauge theories," *Annals of Physics*, vol. 140, no. 2, pp. 372–411, 1982, ISSN: 0003-4916. DOI: https://doi.org/10.1016/0003-4916(82)90164-6.

[248] F. Wilczek, "Quantum Mechanics of Fractional-Spin Particles," *Phys. Rev. Lett.*, vol. 49, pp. 957–959, 14 Oct. 1982. DOI: 10.1103/PhysRevLett.49.957.

[249] L. Wu, M. Salehi, N. Koirala, J. Moon, S. Oh, and N. P. Armitage, "Quantized Faraday and Kerr rotation and axion electrodynamics of a 3D topological insulator," *Science*, vol. 354, no. 6316, pp. 1124–1127, 2016, ISSN: 0036-8075. DOI: 10.1126/science.aaf5541.

[250] E. A. Martinez, C. A. Muschik, P. Schindler, D. Nigg, A. Erhard, M. Heyl, P. Hauke, M. Dalmonte, T. Monz, P. Zoller, and R. Blatt, "Real-time dynamics of lattice gauge theories with a few-qubit quantum computer," *Nature*, vol. 534, no. 7608, pp. 516–519, Jun. 2016, ISSN: 1476-4687. DOI: 10.1038/nature18318.

[251] T. I. Tuegel and T. L. Hughes, "Hall viscosity and momentum transport in lattice and continuum models of the integer quantum Hall effect in strong magnetic fields," *Phys. Rev. B*, vol. 92, p. 165 127, 16 Oct. 2015. DOI: 10.1103/PhysRevB.92.165127.

[252] T. Scaffidi, N. Nandi, B. Schmidt, A. P. Mackenzie, and J. E. Moore, "Hydrodynamic Electron Flow and Hall Viscosity," *Phys. Rev. Lett.*, vol. 118, p. 226 601, 22 Jun. 2017. DOI: 10.1103/PhysRevLett.118.226601.

[253] A. Souslov, K. Dasbiswas, M. Fruchart, S. Vaikuntanathan, and V. Vitelli, "Topological Waves in Fluids with Odd Viscosity," *Phys. Rev. Lett.*, vol. 122, p. 128 001, 12 Mar. 2019. DOI: 10.1103/PhysRevLett.122.128001.

[254] J. E. Avron, R. Seiler, and P. G. Zograf, "Viscosity of Quantum Hall Fluids," *Phys. Rev. Lett.*, vol. 75, pp. 697–700, 4 Jul. 1995. DOI: 10.1103/PhysRevLett.75.697.

[255] C. Hoyos and D. T. Son, "Hall Viscosity and Electromagnetic Response," *Phys. Rev. Lett.*, vol. 108, p. 066 805, 6 Feb. 2012. DOI: 10.1103/PhysRevLett.108.066805. [Online]. Available: https://link.aps.org/doi/10.1103/PhysRevLett.108.066805.

[256] N. Read and E. H. Rezayi, "Hall viscosity, orbital spin, and geometry: Paired superfluids and quantum Hall systems," *Phys. Rev. B*, vol. 84, p. 085 316, 8 Aug. 2011. DOI: 10.1103/PhysRevB.84.085316.

[257] M. Tajmar, "Electrodynamics in superconductors explained by Proca equations," *Physics Letters A*, vol. 372, no. 18, pp. 3289–3291, 2008, ISSN: 0375-9601. DOI: https://doi.org/10.1016/j.physleta.2007.10.070.

[258] Y. Ikebe, T. Morimoto, R. Masutomi, T. Okamoto, H. Aoki, and R. Shimano, "Optical Hall Effect in the Integer Quantum Hall Regime," *Phys. Rev. Lett.*, vol. 104, p. 256 802, 25 Jun. 2010. DOI: 10.1103/PhysRevLett.104.256802.

[259] M. Sherafati, A. Principi, and G. Vignale, "Hall viscosity and electromagnetic response of electrons in graphene," *Phys. Rev. B*, vol. 94, p. 125 427, 12 Sep. 2016. DOI: 10.1103/PhysRevB.94.125427.

[260] R. Cohen and M. Goldstein, "Hall and dissipative viscosity effects on edge magnetoplasmons," *Phys. Rev. B*, vol. 98, p. 235 103, 23 Dec. 2018. DOI: 10.1103/PhysRevB.98.235103.

[261] S. A. Hassani Gangaraj, G. W. Hanson, M. G. Silveirinha, K. Shastri, M. Antezza, and F. Monticone, "Unidirectional and diffractionless surface plasmon polaritons on three-dimensional nonreciprocal plasmonic platforms," *Phys. Rev. B*, vol. 99, p. 245 414, 24 Jun. 2019. DOI: 10.1103/PhysRevB.99.245414.

[262] Q. Guo, O. You, B. Yang, J. B. Sellman, E. Blythe, H. Liu, Y. Xiang, J. Li, D. Fan, J. Chen, C. T. Chan, and S. Zhang, "Observation of Three-Dimensional Photonic Dirac Points and Spin-Polarized Surface Arcs," *Phys. Rev. Lett.*, vol. 122, p. 203 903, 20 May 2019. DOI: 10.1103/PhysRevLett.122.203903.

[263] E. Lustig, S. Weimann, Y. Plotnik, Y. Lumer, M. A. Bandres, A. Szameit, and M. Segev, "Photonic topological insulator in synthetic dimensions," *Nature*, vol. 567, no. 7748, pp. 356–360, 2019, ISSN: 1476-4687. DOI: 10.1038/s41586-019-0943-7.

[264] Y. Yang, Z. Gao, H. Xue, L. Zhang, M. He, Z. Yang, R. Singh, Y. Chong, B. Zhang, and H. Chen, "Realization of a three-dimensional photonic topological insulator," *Nature*, vol. 565, no. 7741, pp. 622–626, 2019, ISSN: 1476-4687. DOI: 10.1038/s41586-018-0829-0.

[265] P. Townsend, K. Pilch, and P. V. Nieuwenhuizen, "Self-duality in odd dimensions," *Physics Letters B*, vol. 136, no. 1, pp. 38–42, 1984, ISSN: 0370-2693. DOI: https://doi.org/10.1016/0370-2693(84)92051-3.

[266] E. Fradkin and A. Tseytlin, "Quantum equivalence of dual field theories," *Annals of Physics*, vol. 162, no. 1, pp. 31–48, 1985, ISSN: 0003-4916. DOI: https://doi.org/10.1016/0003-4916(85)90225-8.

[267] S. Zhong, J. Orenstein, and J. E. Moore, "Optical Gyrotropy from Axion Electrodynamics in Momentum Space," *Phys. Rev. Lett.*, vol. 115, p. 117403, 11 Sep. 2015. DOI: 10.1103/PhysRevLett.115.117403.

[268] B. Bradlyn, M. Goldstein, and N. Read, "Kubo formulas for viscosity: Hall viscosity, Ward identities, and the relation with conductivity," *Phys. Rev. B*, vol. 86, p. 245309, 24 Dec. 2012. DOI: 10.1103/PhysRevB.86.245309.

[269] B. Körs and P. Nath, "Aspects of the Stueckelberg extension," *Journal of High Energy Physics*, vol. 2005, no. 07, pp. 069–069, Jul. 2005. DOI: 10.1088/1126-6708/2005/07/069.

[270] F. L. Teixeira and W. C. Chew, "Lattice electromagnetic theory from a topological viewpoint," *Journal of Mathematical Physics*, vol. 40, no. 1, pp. 169–187, 1999. DOI: 10.1063/1.532767.

[271] L. O. Nascimento, "Introduction to Topological Phases and Electronic Interactions in (2+1) Dimensions," *Brazilian Journal of Physics*, vol. 47, no. 2, pp. 215–230, Apr. 2017, ISSN: 1678-4448. DOI: 10.1007/s13538-017-0485-0.

[272] T. Olesen, N. Vlasii, and U.-J. Wiese, "From doubled Chern-Simons-Maxwell lattice gauge theory to extensions of the toric code," *Annals of Physics*, vol. 361, pp. 303–329, 2015, ISSN: 0003-4916. DOI: https://doi.org/10.1016/j.aop.2015.06.020.

[273] A. Blasi, N. Maggiore, N. Magnoli, and S. Storace, "Maxwell-Chern-Simons theory with a boundary," *Classical and Quantum Gravity*, vol. 27, no. 16, p. 165018, Jul. 2010. DOI: 10.1088/0264-9381/27/16/165018.

A. UNIVERSAL SPIN-MOMENTUM LOCKING OF EVANESCENT WAVES [SUPPLEMENTAL MATERIAL]

From [T. V. Mechelen and Z. Jacob, "Universal spin-momentum locking of evanescent waves," *Optica*, vol. 3, no. 2, pp. 118–126, Feb. 2016]. © 2020 Optical Society of America. [26]

This document provides supplementary information to: "Universal spin-momentum locking of evanescent waves". This includes the full derivations of the complex dispersion relation and polarization basis, Stokes parameters in terms of complex angles, and boundary conditions at the interface of an evanescent wave. We also show the derivation of the directionally dependent emission of a chiral quantum emitter placed inside a single mode optical fiber.

A.0.1 Complex dispersion relation

When we express the wavenumber in the most general complex form as $\vec{k} = \vec{\kappa} + \mathrm{i}\vec{\eta}$, the dispersion relation in free space, $\vec{k}^2 = \vec{k} \cdot \vec{k} = k_0{}^2$ implies that,

$$\kappa^2 - \eta^2 = k_0{}^2 \tag{A.1a}$$

$$\vec{\kappa} \cdot \vec{\eta} = 0 \tag{A.1b}$$

since $k_0 = \omega/c$ is purely real. In this discussion we only consider waves in free space but what follows can be easily generalized to any homogeneous material, lossless or lossy. The only significant difference is that a lossy material will have an imaginary component in the dispersion relation in Eq. (A.1b) that requires $\vec{\kappa} \cdot \vec{\eta} \neq 0$.

In the absence of sources, Maxwell's equations require that the electric and magnetic fields obey the transverse and curl conditions as,

$$\vec{k} \cdot \vec{\mathcal{E}} = 0 \tag{A.2a}$$

$$\vec{k} \times \vec{k} \times \vec{\mathcal{E}} = -k_0{}^2\vec{\mathcal{E}} \tag{A.2b}$$

where $\vec{\mathcal{E}}$ is the electric field in the complex representation. Note that Eq. (A.2a) and (A.2b) applies equally to the magnetic field. These two conditions admit two degrees of freedom for the field polarization state that can be satisfied by appealing to the familiar $\hat{s}$ and $\hat{p}$ unit vectors.

When considering complex wavevectors, we do not need to introduce any extraneous vectors to define our basis set. To construct $\hat{s}$ and ensure it is orthogonal to $\vec{k}$, we utilize both $\vec{\kappa}$ and $\vec{\eta}$ independently as,

$$\hat{s} = \frac{\vec{\kappa} \times \vec{\eta}}{|\vec{\kappa} \times \vec{\eta}|} = \mathrm{i}\frac{\vec{k} \times \vec{k}^*}{|\vec{k} \times \vec{k}^*|} \tag{A.3}$$

and since $\vec{\kappa}$, $\vec{\eta}$ and $\vec{\kappa} \times \vec{\eta}$ are all mutually orthogonal, these three vectors actually form a new electromagnetic triplet set. Next we will show that the $\hat{p}$ polarization is simply a linear combination of $\vec{\kappa}$ and $\vec{\eta}$ unit vectors. We construct $\hat{p}$ by choosing the only vector orthogonal to both $\hat{s}$ and $\vec{k}$ which is simply,

$$\hat{p} = \frac{\vec{k} \times \hat{s}}{|\vec{k}|} = \mathrm{i}\, \frac{\vec{k} \times (\vec{k} \times \vec{k}^*)}{|\vec{k}||\vec{k} \times \vec{k}^*|}. \tag{A.4}$$

where $|\vec{k}|^2 = \vec{k}^* \cdot \vec{k}$ is the L^2 norm and should not be confused with the dispersion relation, $\vec{k} \cdot \vec{k}$. These two quantities are not equivalent for complex wavevectors.

Up until this point, the definitions for $\hat{s}$ and $\hat{p}$ have actually been entirely consistent for situations when $\vec{\kappa} \cdot \vec{\eta} \neq 0$ which is why their form is intuitive. Another convenience of this basis representation is that all the complex components are encapsulated in the $\hat{p}$ polarization which we will see constitutes the spin of an evanescent wave. In this case, the $\hat{s}$ vector can be thought of as the "spin direction" because it points out of the plane.

If we restrict ourselves to orthogonal $\vec{\kappa}$ and $\vec{\eta}$ which would be the case for free space or a lossless medium, we can expand out the term in Eq. (A.4) as,

$$\hat{p} = \mathrm{i}\left[\frac{\eta}{|\vec{k}|}\left(\frac{\vec{\kappa}}{\kappa}\right) + \mathrm{i}\frac{\kappa}{|\vec{k}|}\left(\frac{\vec{\eta}}{\eta}\right)\right] \tag{A.5}$$

and as expected, the $\hat{p}$ polarization state is simply a specific linear combination of $\vec{\kappa}$ and $\vec{\eta}$ unit vectors which means we have fully described any evanescent wave in terms of our

electromagnetic triplet set. For waves in free space, the following identities can also be proven,

$$\vec{k} \times \hat{p} = -\frac{{k_0}^2}{|\vec{k}|}\hat{s} \tag{A.6a}$$

$$\vec{k^*} \times \hat{p} = \vec{k} \times \hat{p}^* = -|\vec{k}|\hat{s} \tag{A.6b}$$

which confirm that the conditions in Eq. (A.2a) and (A.2b) are satisfied.

A.0.2 Propagating waves in the $\eta \to 0$ limit

Here we show that the evanescent basis defined in Eq. (A.3) and (A.4) for $\hat{s}$ and $\hat{p}$ reduces to the well known plane wave vector basis for propagating waves near an interface. Before we outline the steps, we must clarify an important distinction. We first make note that evanescent waves and free propagating waves are fundamentally different. The existence of decay ($\vec{\eta}$) for evanescent waves breaks up the symmetry of the problem and allows us to represent $\hat{s}$ and $\hat{p}$ in a *coordinate independent* form using the wavevectors exclusively. This is why our basis is universal because it can represent *any* evanescent wave in a homogeneous medium. Conversely, for free propagating waves there is no preferred basis and any set that satisfies $\vec{k} \cdot \vec{\mathcal{E}} = 0$ is equally valid. For a propagating wave, it is the existence of an interface which leads to the definition of $\hat{s}$ and $\hat{p}$.

The reasoning for how the basis sets are related is subtle because it would seem at first glance that as $\eta \to 0$, the polarization vectors would be undefined. However, taking the unique limit and retaining the interface in the problem shows that this is not the case. When we introduce an interface to the problem, we can define the decay as $\vec{\eta} = \eta\hat{m}$, with $\hat{m}$ being the unit vector normal to the interface. Substituting this in,

$$\hat{s} = \frac{\vec{\kappa} \times \hat{m}}{|\vec{\kappa} \times \hat{m}|} \tag{A.7a}$$

$$\hat{p} = \frac{\vec{\kappa} + \mathrm{i}\vec{\eta}}{|\vec{\kappa} + \mathrm{i}\vec{\eta}|} \times \frac{\vec{\kappa} \times \hat{m}}{|\vec{\kappa} \times \hat{m}|} \tag{A.7b}$$

and we see that nearly all the difficulties with taking the limit have been removed.

We consider the limiting case as an evanescent wave is transformed to a propagating wave near an interface. Doing this, we take $\eta \to 0$ so there is no decay (propagating wave), but the interface is fixed which means $\hat{m}$ is still defined as the unit vector normal to this interface. This implies $\vec{\kappa} \to \vec{k}$ and $|\vec{k}| \to k_0$ where $\vec{k}$ is now a purely real momentum vector and we arrive at,

$$\hat{s} = \frac{\vec{k} \times \hat{m}}{|\vec{k} \times \hat{m}|} \tag{A.8a}$$

$$\hat{p} = \frac{\vec{k}}{k_0} \times \frac{\vec{k} \times \hat{m}}{|\vec{k} \times \hat{m}|} \tag{A.8b}$$

which satisfies $\vec{k} \cdot \hat{s} = \vec{k} \cdot \hat{p} = 0$ and is indeed the standard basis set for a propagating wave interacting with an interface.

A.0.3 Complex n and ENZ

For completeness, we also include the polarization vectors for a general complex refractive index $n = |n| \exp(\mathrm{i}\phi_n)$ and show that everything is consistent by letting $\vec{k} \to n\vec{k}$. Where $\vec{k}$ is the complex wavevector inside the media and $\vec{k}$ is the wavevector in the free-space representation. Simply plugging this into Eq. (A.3) and (A.4) our basis vectors transform as,

$$\hat{s} \to \hat{s} \tag{A.9a}$$

$$\hat{p} \to \mathrm{i} \exp(\mathrm{i}\phi_n) \left[\frac{\eta}{|\vec{k}|} \left(\frac{\vec{\kappa}}{\kappa} \right) + \mathrm{i} \frac{\kappa}{|\vec{k}|} \left(\frac{\vec{\eta}}{\eta} \right) \right] \tag{A.9b}$$

and we see that our original orthogonal basis is actually preserved except for a phase factor, ϕ_n that rotates the $\hat{p}$ polarization in the plane of propagation. Note however, that the actual components of $\vec{k}$ inside the media are given as $\mathrm{Re}\vec{k} = |n| [\cos \phi_n \vec{\kappa} - \sin \phi_n \vec{\eta}]$ and $\mathrm{Im}\vec{k} = |n| [\cos \phi_n \vec{\eta} + \sin \phi_n \vec{\kappa}]$ so the branch cut is not particularly well-defined in this representation. In a practical problem where we have to consider phase-matching constraints at an interface, it would almost always be simpler to cast everything in terms of $\vec{k}$ from the outset.

We comment briefly how such circular polarization effects and unidirectional propagation can manifest itself in epsilon-near-zero (ENZ) and hyperbolic metamaterials. A detailed analysis follows from the equations of the main paper and will be presented elsewhere. It

has been demonstrated that waves can tunnel through narrow channels of ENZ media and lead to multiple interesting effects. We note here another intriguing aspect for a low loss ENZ material with $\varepsilon \approx 0$. This condition immediately implies from the dispersion relation $(\vec{k}\cdot\vec{k} = \varepsilon(\omega/c)^2)$ that all waves will be necessarily evanescent in such media since propagating solutions do not exist. Furthermore, these evanescent waves will have $\kappa = \eta$ (decay connected to phase) leading to a fundamental circular nature to the $\hat{p}$-polarization component of the evanescent wave. These are modes with an electric field vector perpendicular to the interface of a thin film. Such effects can be experimentally verified close to the plasma frequency in a plasmonic metal.

Formally, this can be inferred once again from the properties of our polarization basis. The $\hat{s}$ and $\hat{p}$ unit vectors for an ENZ medium can be expressed quite simply as,

$$\hat{s} = \mathrm{i}\hat{e} \times \hat{e}^* \tag{A.10a}$$

$$\hat{p} = \mathrm{i}\hat{e} \tag{A.10b}$$

and we come to an interesting result. Here $\hat{e} = \hat{e}_+ = \hat{e}_-^*$ is shorthand for the two $\pm$ independent circularly polarized solutions (i.e. opposite handedness) and the orthogonal components of $\hat{e}$ are governed by the direction of the momentum and decay. One can easily derive Eq. (A.10a) and (A.10b) by plugging in $\eta = \kappa$ and $|\vec{k}| = \sqrt{\kappa^2 + \eta^2} = \sqrt{2}\kappa$ into the polarization equations defined previously in Eq. (A.3) and (A.4). One sees immediately that $\hat{p} \cdot \hat{p} = 0$ which is the definition of a circular polarized state.

What this tells us is that all waves in ENZ materials (which are necessarily evanescent) are perfectly circularly polarized through $\hat{p}$, regardless of their corresponding phase velocity. Again, we emphasize that the handedness is flipped $\hat{e} \to \hat{e}^*$ when the wave propagates in the opposite direction. This phenomenon is quite interesting when we consider analogies with the quantum spin-Hall effect (QSHE) in electronics. In essence, these ENZ evanescent waves have directional dependent quantized transverse spin, which is a defining characteristic of the QSHE. Experimental realization of a quantized surface state would surely have important implications in the quantum optics and photonics field.

A.0.4 Inherent polarization

We now derive the Stokes parameters of a general planar evanescent wave using the familiar complex angle representation. This corresponds to a particular branch cut in the $\vec{k}$-complex plane and arises because of the symmetry breaking in the problem under consideration. Our complex wave vector $\vec{k} = \vec{\kappa} + i\vec{\eta}$ can be expressed in terms of trigonometric and hyperbolic functions as,

$$\vec{k} = k_0[(\cos\phi\hat{x} + \sin\phi\hat{y})\sin\theta + \cos\theta\hat{z}] \tag{A.11a}$$

$$\vec{\kappa} = k_0[(\cos\phi\hat{x} + \sin\phi\hat{y})\sin\alpha + \cos\alpha\hat{z}]\cosh\beta \tag{A.11b}$$

$$\vec{\eta} = k_0[(\cos\phi\hat{x} + \sin\phi\hat{y})\cos\alpha - \sin\alpha\hat{z}]\sinh\beta \tag{A.11c}$$

where we have allowed the complex rotation to be in the $\theta = \alpha + i\beta$ plane. One can also check that all of the properties in Eq. (A.1a) and (A.1b) are satisfied for any (real) value of α or β. We let $\alpha = \pi/2$, which in practice would correspond to an interface that breaks symmetry in the $\hat{z}$ direction. This is the conventional planar evanescent wave that has been reduced from the more general coordinate-independent representation.

Next we construct our $\hat{s}$ and $\hat{p}$ polarization vectors as prescribed in equations Eq. (A.3) and (A.4) which results in,

$$\hat{s} = \begin{bmatrix} -\sin\phi \\ \cos\phi \\ 0 \end{bmatrix} \tag{A.12a}$$

$$\hat{p} = i\left\{ \begin{bmatrix} \cos\phi \\ \sin\phi \\ 0 \end{bmatrix} \frac{\sinh\beta}{\sqrt{\cosh^2\beta + \sinh^2\beta}} + i \begin{bmatrix} 0 \\ 0 \\ -1 \end{bmatrix} \frac{\cosh\beta}{\sqrt{\cosh^2\beta + \sinh^2\beta}} \right\} \tag{A.12b}$$

The Stokes parameters that characterize the complex $\hat{p}$ state can be written strictly in terms of β. The Stokes parameters corresponding to the fraction of linear (S_1) and circular (S_3) polarization can be expressed as,

$$S_1 = \frac{1}{\cosh^2 \beta + \sinh^2 \beta} = \text{sech}(2\beta) \tag{A.13a}$$

$$S_3{}^\pm = \pm 2 \frac{\cosh \beta \sinh \beta}{\cosh^2 \beta + \sinh^2 \beta} = \pm \tanh(2\beta) \tag{A.13b}$$

where one can see that the $\hat{p}$-polarization state is variable with respect to β.

A.1 Universal behavior

A.1.1 Circular total internal reflection (golden ratio condition)

In general, the electric field at the boundary between two media must satisfy Maxwell's sourceless boundary conditions as,

$$\hat{n}_\parallel \cdot (\vec{E_1} - \vec{E_2}) = 0 \tag{A.14a}$$

$$\hat{n}_\perp \cdot (\varepsilon_1 \vec{E_1} - \varepsilon_2 \vec{E_2}) = 0 \tag{A.14b}$$

where $\hat{n}_\parallel$ and $\hat{n}_\perp$ are the unit vectors parallel and normal to the boundary respectively. As always, ε is the relative permittivity in the respective medium. If we restrict our attention to only $\hat{p}$-polarized evanescent fields, it is straightforward to show that the handedness of the evanescent field, which we take to be in region 2, will be imparted to the propagating wave, which we take to be in region 1.

Firstly, $\vec{\eta}$ must be in the same direction as $\hat{n}_\perp$ since from our causality requirement the wave must decay away from the boundary. This is equivalent to stating

$$\left(\frac{\vec{\eta}}{\eta} \right) = \hat{n}_\perp. \tag{A.15}$$

Also, since we are only considering $\hat{p}$-polarized fields we know that the direction of $\vec{\kappa}$ has to be in the plane of the electric field vector therefore,

$$\left(\frac{\vec{\kappa}}{\kappa}\right) = \hat{n}_{\parallel} \tag{A.16}$$

which is the direction parallel to the interface. Strictly speaking, $\vec{\kappa}$ can actually be parallel or anti-parallel to $\hat{n}_{\parallel}$ depending on the propagation direction because we have 2 possible solutions. This is implied when we discuss counter-propagating waves. Putting it all together, the field of an evanescent wave at the interface between two mediums must be proportional to,

$$\vec{E}_2 \propto (\eta_2 \hat{n}_{\parallel} + \mathrm{i}\kappa_2 \hat{n}_{\perp}) \exp(\mathrm{i}\vec{\kappa}_2 \cdot \vec{r}) \exp(-\vec{\eta}_2 \cdot \vec{r}). \tag{A.17}$$

When we equate boundary conditions in Eq. (A.14a) and (A.14b) for $\vec{E}_1 = (E_{\parallel})_1 \hat{n}_{\parallel} + (E_{\perp})_1 \hat{n}_{\perp}$ at the interface of the two mediums, this requires the phase between the two electric field components be related by,

$$\left[\frac{E_{\perp}}{E_{\parallel}}\right]_1 = \pm\mathrm{i}\frac{\varepsilon_2}{\varepsilon_1}\left[\frac{\kappa}{\eta}\right]_2 \qquad \text{@interface} \tag{A.18}$$

where the $\pm$ indicates oppositely travelling evanescent waves. Again, the spin-momentum locking of the evanescent wave requires a change in handedness when the momentum direction changes, and we see that this handedness is also imparted to any wave coupled to the evanescent field.

A.1.2 Directional quantum emitter coupling

Here we show the derivation for the chiral emitter placed inside a single mode optical fiber. Any arbitrary field within an optical fiber can be expressed as,

$$\vec{\mathcal{E}} = \sum_{\lambda} A_{\lambda}\vec{\mathcal{E}}_{\lambda} + \vec{\mathcal{E}}_{\mathrm{rad}} \tag{A.19a}$$

$$\vec{\mathcal{H}} = \sum_{\lambda} A_{\lambda}\vec{\mathcal{H}}_{\lambda} + \vec{\mathcal{H}}_{\mathrm{rad}} \tag{A.19b}$$

240

where $\vec{\mathcal{E}}_\lambda/\vec{\mathcal{H}}_\lambda$ are the guided modes of the fiber with A_λ being the expansion coefficients (coupling strength) of each mode. The explicit expressions for the guided modes can be found in the main manuscript. $\vec{\mathcal{E}}_{\text{rad}}/\vec{\mathcal{H}}_{\text{rad}}$ are the continuous collection of radiative modes that are not guided by the fiber so we will mostly ignore them. We use,

$$\int \nabla \cdot (\vec{\mathcal{E}} \times \vec{\mathcal{H}}_\lambda^* + \vec{\mathcal{E}}_\lambda^* \times \vec{\mathcal{H}}) \mathrm{d}V = -\int \vec{J}_{\text{E}}^* \cdot \vec{\mathcal{E}}_\lambda \mathrm{d}V - \int \vec{J}_{\text{H}}^* \cdot \vec{\mathcal{H}}_\lambda \mathrm{d}V \tag{A.20a}$$

$$\int (\vec{\mathcal{E}} \times \vec{\mathcal{H}}_\lambda^* + \vec{\mathcal{E}}_\lambda^* \times \vec{\mathcal{H}}) \cdot \mathrm{d}\vec{a} = \mathrm{i}\omega[\vec{p}^* \cdot \vec{\mathcal{E}}_\lambda(0) + \vec{m}^* \cdot \vec{\mathcal{H}}_\lambda(0)] \tag{A.20b}$$

and we only have to integrate the area element normal to the fiber axis $\mathrm{d}\vec{a} = \mathrm{d}a\hat{z}$. The modes are orthogonal so we can solve for A_λ. We have four degenerate modes for an HE_{11} fiber. Two propagating in the forward direction for $z > 0$ and two in the backward direction when $z < 0$. We label these $A_\lambda \to A_\beta^m$ where the $m = \pm 1$ indicates the two left and right orbital angular momentum modes propagating in the direction given by $\text{sign}(\beta)$. Here, β is the propagation constant with the same magnitude for the four degenerate modes, and $\text{sign}(\beta) = \pm 1$ depending on the direction of propagation. Inserting our dipoles for the chiral source and using unit magnitude field normalizations ($E_0 = 1$) for the waveguide modes we have,

$$A_\beta^m \int (\vec{\mathcal{E}}_\beta^m \times \vec{\mathcal{H}}_\beta^{m*} + \vec{\mathcal{E}}_\beta^{m*} \times \vec{\mathcal{H}}_\beta^m) \cdot \mathrm{d}\vec{a} = \mathrm{i}\sqrt{2}\left[\text{sign}(\beta)|\beta|\omega p_0 + m\frac{(\sigma_1)^2 m_0}{\mu_0 a}\right]. \tag{A.21}$$

The surface integrals are all the same and we do not care about overall phase factors or constants so we absorb it into the magnitudes $|A_\beta^m|^2$ as,

$$|A_\beta^m|^2 = C\left|\text{sign}(\beta)|\beta|\omega p_0 + m\frac{(\sigma_1)^2 m_0}{\mu_0 a}\right|^2 \tag{A.22}$$

where C is some positive proportionality constant. Do not confuse the angular momentum quantum number $m = \pm 1$, with the magnitude of the magnetic dipole $|\vec{m}| = m_0$. These are two very different but important quantities. Notice that we have differing coupling depending on both propagation direction and the circular polarization of the chiral source. For instance, the $+$ circular polarization source couples only into the $m = +1$ angular momentum modes

and will emit preferentially in the $\text{sign}(\beta) = +1$ propagation direction. Conversely, the $-$ circular polarization source couples only into the $m = -1$ angular momentum modes and will emit preferentially in the $\text{sign}(\beta) = -1$ propagation direction. Most importantly, note that the power along the fiber axis for a given mode is $P \propto |A_\beta^m|^2$. This will lead to *differing power* being emitted in different directions along the fiber.

B. QUANTUM GYROELECTRIC EFFECT: PHOTON SPIN-1 QUANTIZATION IN CONTINUUM TOPOLOGICAL BOSONIC PHASES [SUPPLEMENTAL MATERIAL]

From [T. Van Mechelen and Z. Jacob, "Quantum gyroelectric effect: Photon spin-1 quantization in continuum topological bosonic phases," *Phys. Rev. A*, vol. 98, p. 023842, 2 Aug. 2018]. © 2020 American Physical Society. [54]

B.1 2+1D electromagnetic Lagrangian

To understand the two dimensional behavior of photons [84], we start with the electromagnetic Lagrangian coupled to a conserved current $\partial_\mu J^\mu = 0$,

$$\mathcal{L} = -\frac{1}{4} F^{\mu\nu} F_{\mu\nu} - A_\mu J^\mu, \qquad F^{\mu\nu} = \partial^\mu A^\nu - \partial^\nu A^\mu, \tag{B.1}$$

which is exact in any space-time dimension. The conservation of charge ensures the action $S = \int d^d x dt \mathcal{L}$ is gauge invariant, where d is the spatial dimension. For $d = 2$, the motion of charge is restricted to the x-y plane,

$$J^\mu = (\rho, J_x, J_y), \qquad \dot{\rho} + \partial_i J^i = 0. \tag{B.2}$$

Similarly, planar currents restrict the spatial degrees of freedom of the gauge potential A^μ,

$$A^\mu = (\phi, A_x, A_y). \tag{B.3}$$

This implies there are only 2 components of the electric field and 1 for the magnetic field,

$$E_i = -\partial_i \phi - \dot{A}_i, \qquad B_z = \epsilon^{ij} \partial_i A_j = \partial_x A_y - \partial_y A_x, \tag{B.4}$$

such that exclusively transverse-magnetic (TM) waves propagate within a 2D material. This makes physical sense since the circulation of currents can only generate magnetic fields in a

single $\hat{z}$ direction. Note that $\epsilon_{ij} = -\epsilon_{ji}$ is the 2D antisymmetric matrix and should not be confused with the permittivity.

Varying the action with respect to A^μ, we arrive at the familiar equations of motion,

$$\partial_\mu F^{\mu\nu} = J^\nu, \qquad \tilde{F}^\mu = \frac{1}{2}\epsilon^{\mu\nu\rho} F_{\nu\rho}, \qquad \partial_\mu \tilde{F}^\mu = 0. \tag{B.5}$$

Notice the dual equation $\tilde{F}_\mu$ is slightly different in 2D, which arises from the fact there are only 3 unique components of the electromagnetic field. We can express the equations of motion directly in terms of E_i and B_z,

$$\partial_i E^i = \rho, \qquad \epsilon_{ij}\partial^j B_z - \dot{E}_i = J_i, \qquad \dot{B}_z + \epsilon^{ij}\partial_i E_j = 0. \tag{B.6}$$

These are precisely Maxwell's equations in 2D. We are most interested with the response of a bulk 2D material so it is convenient to represent the induced charges in terms of the polarization P_i and magnetization M_z densities,

$$\rho = -\partial_i P^i, \qquad J_i = \dot{P}_i + \epsilon_{ij}\partial^j M_z. \tag{B.7}$$

Substituting into the equations of motion, we define the electric D_i and magnetic B_z displacement fields as,

$$\dot{D}_i - \epsilon_{ij}\partial^j H_z = 0, \qquad \dot{B}_z + \epsilon^{ij}\partial_i E_j = 0, \tag{B.8}$$

which is simply the linear superposition of,

$$D_i = E_i + P_i, \qquad B_z = H_z + M_z. \tag{B.9}$$

The wave equation in Eq. (3.2) follows immediately after substituting for the linear response function $\mathcal{M}$ and defining the column vector $f = \begin{bmatrix} E_x & E_y & H_z \end{bmatrix}^\mathsf{T}$ for the TM state.

B.2 Electromagnetic Hamiltonian and polariton eigenstates

Here, we show that the response function $\mathcal{M}$ is derived form a first-order in time Hamiltonian. Utilizing the decomposition in Eq. (3.6), we expand in terms of 3-component oscillator variables ψ_α by defining,

$$\psi_\alpha = \frac{\mathcal{C}_{\alpha\mathbf{k}}f}{\omega - \omega_{\alpha\mathbf{k}}}, \qquad \omega\psi_\alpha = \omega_{\alpha\mathbf{k}}\psi_\alpha + \mathcal{C}_{\alpha\mathbf{k}}f, \tag{B.10}$$

which is first-order in time. Similarly, we back-substitute Eq. (3.6) into Eq. (3.2) to obtain,

$$\omega f = \left[\mathcal{H}_0(\mathbf{k}) + \sum_\alpha \omega_{\alpha\mathbf{k}}^{-1}\mathcal{C}_{\alpha\mathbf{k}}^\dagger\mathcal{C}_{\alpha\mathbf{k}}\right] f + \sum_\alpha \mathcal{C}_{\alpha\mathbf{k}}^\dagger\psi_\alpha. \tag{B.11}$$

The first term represents the vacuum equations and self-energy of the electromagnetic field, while the second is the linear coupling to the oscillators. By combining Eq. (B.10) and (B.11) into a single algebraic matrix, the complete electromagnetic Hamiltonian emerges,

$$H(\mathbf{k}) = \begin{bmatrix} \mathcal{H}_0(\mathbf{k}) + \sum_\alpha \omega_{\alpha\mathbf{k}}^{-1}\mathcal{C}_{\alpha\mathbf{k}}^\dagger\mathcal{C}_{\alpha\mathbf{k}} & \mathcal{C}_{1\mathbf{k}}^\dagger & \mathcal{C}_{2\mathbf{k}}^\dagger & \cdots \\ \mathcal{C}_{1\mathbf{k}} & \omega_{1\mathbf{k}} & 0 & \cdots \\ \mathcal{C}_{2\mathbf{k}} & 0 & \omega_{2\mathbf{k}} & \cdots \\ \vdots & \vdots & \vdots & \ddots \end{bmatrix}. \tag{B.12}$$

The Hermitian equation $Hu = \omega u$ characterizes the dynamics of the entire electromagnetic problem in a 2D material. u constitutes the cumulative state vector of the photon + all oscillator degrees of freedom,

$$u = \begin{bmatrix} f & \psi_1 & \psi_2 & \dots \end{bmatrix}^\mathsf{T}. \tag{B.13}$$

Notice that contraction of u naturally reproduces the energy density upon summation over all degrees of freedom,

$$u^\dagger u = f^\dagger f + f^\dagger \sum_\alpha \frac{\mathcal{C}_{\alpha\mathbf{k}}^\dagger\mathcal{C}_{\alpha\mathbf{k}}}{(\omega - \omega_{\alpha\mathbf{k}})^2} f = f^\dagger \bar{\mathcal{M}} f, \tag{B.14}$$

with $\bar{\mathcal{M}} = \partial_\omega(\omega\mathcal{M}) > 0$ always positive definite. Eigenstates of the Hamiltonian are collective excitations of oscillators coupled to the electromagnetic field,

$$H_\mathbf{k} u_{n\mathbf{k}} = \omega_{n\mathbf{k}} u_{n\mathbf{k}}, \tag{B.15}$$

and are manifestly bosonic quasiparticles. These are the n non-trivial roots of the characteristic equation,

$$\det\left[\mathcal{H}_0(\mathbf{k}) - \omega\mathcal{M}(\omega, \mathbf{k})\right] = 0, \qquad \omega = \omega_n(\mathbf{k}), \tag{B.16}$$

which generates the eigenenergies at any particular momenta. Normalization of each mode is given concisely as $1 = f_{n\mathbf{k}}^\dagger \bar{\mathcal{M}}(\omega_{n\mathbf{k}}, \mathbf{k}) f_{n\mathbf{k}}$.

B.3 Continuum regularization

To adequately describe a continuum topological field theory, the Hamiltonian must approach a directionally independent value in the asymptotic limit $\lim_{k\to\infty} H(\mathbf{k}) \to H(k)$, such that the system is connected at infinity [15]. This is the continuum equivalent of a periodic boundary condition since all limits at $k \to \infty$ are mapped into a single point (i.e. one-point compactification). We can prove the Chern number is quantized by analyzing the Berry phase over all momentum. Continuum regularization necessitates the following condition,

$$\oint_{k=\infty} \mathbf{A}_n \cdot d\mathbf{k} = -2\pi \sum_i p_i + \iint_{\mathbb{R}^2} F_n d^2\mathbf{k} = 2\pi p, \tag{B.17}$$

with p and $p_i \in \mathbb{Z}$ an integer. Here, $\mathbf{A}_n(\mathbf{k}) = -i u_{n\mathbf{k}}^\dagger \partial_\mathbf{k} u_{n\mathbf{k}}$ is the Berry connection of any particular eigenstate and $F_n(\mathbf{k}) = \hat{z} \cdot [\partial_\mathbf{k} \times \mathbf{A}_n(\mathbf{k})]$ is the Berry curvature. The path integral is performed over a closed loop at infinity $k = \infty$, which is equivalent to the Berry flux over all momentum space $\mathbb{R}^2$ minus any singular points in the connection. p_i label these singular points of the Berry connection $\mathbf{A}_n(\mathbf{k}_i)$ which contribute an integer unit of Berry flux at a particular momentum $\mathbf{k}_i$. The Chern number $C_n \in \mathbb{Z}$ is the summation over all such singularities,

$$C_n = p + \sum_i p_i = \frac{1}{2\pi} \iint_{\mathbb{R}^2} F_n d^2\mathbf{k}. \tag{B.18}$$

For Eq. (B.18) to hold, we see that the eigenstates must approach a directionally independent value in the asymptotic limit, up to a possible U(1) gauge,

$$\lim_{k \to \infty} u_n(\mathbf{k}) \to u_n(k) \exp\left[i\chi_n(\mathbf{k})\right]. \tag{B.19}$$

When this is the case, the closed loop at infinity $k = \infty$ is determined purely by the gauge,

$$\oint_{k=\infty} \mathbf{A}_n \cdot d\mathbf{k} = \oint_{k=\infty} \partial_{\mathbf{k}}\chi_n \cdot d\mathbf{k} = \chi_n|_0^{2\pi} = 2\pi p, \tag{B.20}$$

which is guaranteed to be an integer multiple of 2π. Hence, Chern numbers are quantized. For completeness, we note that the Berry connection can be simplified slightly to,

$$\mathbf{A}_n(\mathbf{k}) = -i f_{n\mathbf{k}}^\dagger \bar{\mathcal{M}}(\omega_{n\mathbf{k}}, \mathbf{k}) \partial_{\mathbf{k}} f_{n\mathbf{k}} + f_{n\mathbf{k}}^\dagger \boldsymbol{\mathcal{A}}(\omega_{n\mathbf{k}}, \mathbf{k}) f_{n\mathbf{k}}, \tag{B.21}$$

where $\boldsymbol{\mathcal{A}}$ is the Berry connection arising from the oscillators,

$$\boldsymbol{\mathcal{A}}(\omega, \mathbf{k}) = -i \sum_\alpha \frac{\mathcal{C}_{\alpha\mathbf{k}}^\dagger \partial_{\mathbf{k}} \mathcal{C}_{\alpha\mathbf{k}}}{(\omega - \omega_{\alpha\mathbf{k}})^2}. \tag{B.22}$$

C. NONLOCAL TOPOLOGICAL ELECTROMAGNETIC PHASES OF MATTER [SUPPLEMENTAL MATERIAL]

From [T. Van Mechelen and Z. Jacob, "Nonlocal topological electromagnetic phases of matter," *Phys. Rev. B*, vol. 99, p. 205146, 20 May 2019]. © 2020 American Physical Society. [164]

C.1 Symmetry-protected topological fermionic phases

For completeness, we examine the SPT fermionic phases associated with each point group C_N and highlight their essential differences from bosons. The most important distinction is how they transform under rotations; half-integer particles are antisymmetric $\mathcal{R}(2\pi) = -1$. In terms of discrete rotations $\hat{\mathcal{R}}_N$ about the z-axis, the eigenstates of a Bloch spinor particle satisfy,

$$\hat{\mathcal{R}}_N|\Psi_{\mathbf{k}_p}\rangle = \zeta_N(\mathbf{k}_p)|\Psi_{\mathbf{k}_p}\rangle, \tag{C.1}$$

where the eigenvalues at HSPs are related by,

$$\zeta_N(\mathbf{k}_p) = \exp\left[i\frac{2\pi}{N}m_N(\mathbf{k}_i)\right], \qquad (\zeta_N)^N = -1. \tag{C.2}$$

$m_N(\mathbf{k}_i) \in \mathbb{Z}_N + 1/2$ is a modulo half-integer and labels the N possible spin-½ eigenvalues. Notice that ζ_N represents the Nth roots of *negative* unity which is characteristic of a fermionic field. The single-particle fermionic classification for C_2, C_3, C_4 and C_6 respectively is [100], [185],

$$\exp\left(i\frac{2\pi}{2}\mathfrak{C}\right) = \zeta_2(\Gamma)\zeta_2(X)\zeta_2(Y)\zeta_2(M), \tag{C.3a}$$

$$\exp\left(i\frac{2\pi}{3}\mathfrak{C}\right) = -\zeta_3(\Gamma)\,\zeta_3(K)\,\zeta_3(K)\,, \tag{C.3b}$$

$$\exp\left(i\frac{2\pi}{4}\mathfrak{C}\right) = -\zeta_4(\Gamma)\,\zeta_4(M)\,\zeta_2(Y)\,, \tag{C.3c}$$

$$\exp\left(i\frac{2\pi}{6}\mathfrak{C}\right) = -\zeta_6(\Gamma)\,\zeta_3(K)\,\zeta_2(M)\,. \tag{C.3d}$$

Although the classification appears similar, the SPT fermionic phases constitute very different physics than their bosonic counterparts, which is alluded to by the antisymmetric phase factors $\mathcal{R}(2\pi) = -1$. We illustrate this with an example in C_4. Applying the logarithm - the classification for the SPT fermionic phase $\nu = \mathfrak{C} \mod 4$ can be expressed as,

$$\nu = m_4(\Gamma) + m_4(M) + 2m_2(Y) + 2 \mod 4, \tag{C.4}$$

where $m_4(\Gamma)$ & $m_4(M) \in \mathbb{Z}_4 + {}^1\!/_2$ are modulo 4 half-integers and $m_2(Y) \in \mathbb{Z}_2 + {}^1\!/_2$ is a modulo 2 half-integer.

C.2 Example of a continuum topological electromagnetic phase

We consider the long wavelength (continuum) limit $k \approx 0$ and ignore all higher order $\mathbf{g} \neq \mathbf{0}$ spatial harmonics [54], [116], [167]. The simplest response function showing a topologically nontrivial electromagnetic phase is described by the permittivity tensor ε_{ij},

$$\varepsilon_{ij}(\omega, k) = \varepsilon(\omega, k)\delta_{ij} + ig(\omega, k)\epsilon_{ij}. \tag{C.5}$$

$\epsilon_{ij} = -\epsilon_{ji}$ is the antisymmetric tensor and should not be confused with the permittivity ε_{ij}. This is simply the Drude model biased under an applied magnetic field. ε is the scalar permittivity (diagonal part),

$$\varepsilon(\omega, k) = 1 + \frac{\omega_p^2(k)}{\omega_c^2(k) - \omega^2}, \tag{C.6}$$

while g is the gyrotropic coefficient (off-diagonal part) which breaks both parity and time-reversal symmetry,

$$g(\omega, k) = \frac{\omega_c(k)\omega_p^2(k)}{\omega(\omega_c^2(k) - \omega^2)}. \tag{C.7}$$

Notice we have added nonlocal (momentum-dependent) corrections to both the plasma ω_p and cyclotron ω_c frequencies. As we will see, nonlocality is imperative to describe a topo-

logically nontrivial phase. In terms of coupling matrices $\mathcal{C}$, the permittivity tensor can be expressed as,

$$\varepsilon_{ij} = \delta_{ij} - \frac{[\mathcal{C}_+]_{il}[\mathcal{C}_+]_j^l}{\omega(\omega - \omega_c)} - \frac{[\mathcal{C}_-]_{il}[\mathcal{C}_-]_j^l}{\omega(\omega + \omega_c)}, \tag{C.8}$$

where repeated indices imply summation and,

$$[\mathcal{C}_\pm]_{ij} = \frac{\omega_p}{2}(\delta_{ij} \pm i\epsilon_{ij}). \tag{C.9}$$

The corresponding Hamiltonian $\omega u = Hu$ governing the total light-matter interaction is therefore,

$$H = \begin{bmatrix} \mathcal{H}_0 & \mathcal{C}_+ & \mathcal{C}_- \\ \mathcal{C}_+ & \omega_c & 0 \\ \mathcal{C}_- & 0 & -\omega_c \end{bmatrix}, \qquad u = \begin{bmatrix} f \\ \psi_+ \\ \psi_- \end{bmatrix}, \tag{C.10}$$

where $\psi_\pm$ are the positive and negative energy matter oscillations. To be properly regularized, the nonlocaity (spatial dispersion) must be at least quadratic in k,

$$\omega_p(k) = \omega_{p0} + \omega_{p2}k^2, \qquad \omega_c(k) = \omega_{c0} + \omega_{c2}k^2. \tag{C.11}$$

Physicallty, the quadratic nonlocality arises from high-momentum corrections to the effective mass, since the electronic bands are not perfectly parabolic,

$$\frac{1}{M^*} = \frac{1}{\hbar^2}\frac{\partial^2 E}{\partial k^2} = \frac{1}{M_0} + \frac{1}{M_2}(ka)^2 + \dots \tag{C.12}$$

which gives,

$$\omega_{c0} = \frac{eB_0}{M_0}, \qquad \omega_{c2} = \frac{eB_0}{M_2}a^2. \tag{C.13}$$

a is the lattice constant in this case. Inserting into the wave equation, we obtain the dispersion relation,

$$\omega^2\left(\varepsilon - \frac{g^2}{\varepsilon}\right) = k^2, \tag{C.14}$$

which has two (positive energy) eigenmode branches,

$$\omega_\pm^2 = \frac{1}{2}\left[2\omega_p^2 + \omega_c^2 + k^2 \pm \sqrt{4\omega_p^2\omega_c^2 + (\omega_c^2 - k^2)^2}\right]. \tag{C.15}$$

After a bit of work, it can be shown that the Chern number for each band is determined by the spin eigenvalues at $k_i = 0$ and $k_i = \infty$,

$$C_\pm = m_\pm(0) - m_\pm(\infty) = \mp[\mathrm{sgn}(\omega_{c0}) - \mathrm{sgn}(\omega_{c2})]. \tag{C.16}$$

Alternatively, the Chern number can be expressed in terms of the relative sign of the effective masses, M_0 and M_2, and the applied magnetic field B_0,

$$C_\pm = \mp[\mathrm{sgn}(M_0) - \mathrm{sgn}(M_2)]\mathrm{sgn}(B_0). \tag{C.17}$$

If the cyclotron frequency switches sign with momentum $\omega_{c0}\omega_{c2} < 0$, the topological phase is nontrivial $|C_\pm| = 2$. This implies there is an inflection point in the electronic band, $1/M^* = \partial^2 E/\partial k^2 = 0$ such that the curvature changes. More precisely, if there are an odd number of inflection points, the curvature changes an odd number of times, which always produces a nontrivial phase $|C_\pm| = 2$.

D. UNIDIRECTIONAL MAXWELLIAN SPIN WAVES [SUPPLEMENTAL MATERIAL]

From [T. V. Mechelen and Z. Jacob, "Unidirectional maxwellian spin waves," *Nanophotonics*, vol. 8, no. 8, pp. 1399–1416, Aug. 2019]. © 2020 De Gruyter. [167]

D.1 Dirac Jackiw-Rebbi edge states

For completeness, we provide a brief review of Jackiw-Rebbi states that arise in two-dimensional condensed matter systems. The simplest realization is described by the 2D Dirac equation $H\Psi = E\Psi$,

$$H = v(k_x \sigma_x + k_y \sigma_y) + \Lambda \sigma_z, \tag{D.1}$$

where $[\sigma_i, \sigma_j] = 2i\epsilon_{ijk}\sigma_k$ are the Pauli matrices. v is the Fermi velocity and Λ is a two-dimensional Dirac mass.

We consider an interface of two Dirac particles with opposite masses $\Lambda \to \Lambda \mathrm{sgn}(x)$. Similar to the photonic problem [Sec. 6.5], there is now mirror symmetry about $x = 0$. The unidirectional (chiral) edge solution is well known [93] and assumes a surprisingly simple form,

$$\Psi(x) = \Psi_0 \begin{bmatrix} 1 \\ i\, s_{k_y} \end{bmatrix} \mathrm{e}^{-\eta|x|}, \tag{D.2}$$

where $s_{k_y} = \mathrm{sgn}(k_y) = \pm 1$ is the sign of the momentum and Ψ_0 is a normalization constant. This follows from the characteristic equation,

$$\eta = \frac{|\Lambda|}{v}, \qquad E^2 = v^2 k_y^2. \tag{D.3}$$

If $\Lambda > 0$, the Dirac edge wave propagates strictly in the $k_y > 0$ direction and vice verse for $\Lambda < 0$. It is clear that Ψ is an eigenstate of both the helicity operator $\hat{k} \cdot \vec{S} = \sigma_y/2$ and the mirror operator $\mathcal{P}_x = \sigma_y$ which are identical in this case,

$$\sigma_y \Psi(-x) = \sigma_y \Psi(x) = s_{k_y} \Psi(x). \tag{D.4}$$

Indeed, the Dirac Jackiw-Rebbi edge states are helically quantized and behave identically to a massless (Weyl) fermion. This should be contrasted with their photonic (spin-1) equivalent in Eq. (6.53).

D.2 Robustness of PQH and PJR edge states

Although the PQH and PJR states are not topologically-protected, they can still exhibit robust transport – ie. immunity to small perturbations in the gyrotropic coefficient g. Let us assume $g \to g(x)$ is a function of x but take ε as a constant in space. In reality, this is only approximately true since g and ε cannot be completely independent functions. In the Drude model for instance, a field gradient $B_0 \to B_0(x)$ creates a spatially dependent cyclotron frequency $\omega_c \to \omega_c(x)$ which alters both the resonance frequency and the relative magnitude of the gyrotropy. Hence, both g and ε will generally vary with x. However, this simplifying assumption illustrates the point very well and holds for relatively small perturbations in the gyrotropy.

When only $g(x)$ varies with x, the Schrödinger-like wave equation [Eq. (6.42)] for the PQH state becomes,

$$ -\partial_x^2 E_y + \left[\frac{k_y}{\varepsilon} \partial_x g(x) + \omega^2 \frac{g^2(x)}{\varepsilon} \right] E_y = (\omega^2 \varepsilon - k_y^2) E_y. \tag{D.5} $$

Due to the mirror boundary condition, $g(-x) = -g(x)$ is an odd function of x. However, we can still allow a jump discontinuity at $x = 0$, such that $g(0^-) = -g(0^+)$. Far from the boundary $|x| \to \infty$, the gyrotropy approaches the uniform bulk $g(x \to \pm\infty) = \pm g_0$. A unidirectional edge state always exists and is immune to perturbations in g. To prove this, we choose an integrating factor of the form,

$$ E_y(x) = E_y(0) \exp\left[\frac{k_y}{\varepsilon} \int_{-\infty}^{x} g(x) dx \right], \tag{D.6} $$

which satisfies,

$$ \partial_x E_y(x) = \frac{k_y}{\varepsilon} g(x) E_y(x), \tag{D.7} $$

and,

$$\partial_x^2 E_y(x) = \left[\frac{k_y}{\varepsilon}\partial_x g(x) + \frac{k_y^2}{\varepsilon^2}g^2(x)\right] E_y(x). \tag{D.8}$$

Clearly, if the edge dispersion is fulfilled $k_y^2 = \omega^2\varepsilon$, Eq. (D.5) is satisfied regardless of the particular form of $g(x)$. The exact same integrating solution exists for the PJR states, with $E_y(x) = 0$, except the momentum is reversed $k_y \to -k_y$. As an example, let $g(x) = g_0 \tanh(x/a)$, where a is some characteristic transition length that interpolates between $g(0) = 0$ and $g(x \to \pm\infty) = \pm g_0$. The integral of which is $\int g(x)dx = ag_0 \log[\cosh(x/a)]$. The spatial profile then becomes,

$$E_y(x) = E_y(0)[\cosh(x/a)]^{(k_y a g_0/\varepsilon)}. \tag{D.9}$$

In the limit of an infinitesimally narrow transition width $a \to 0$, the solution reduces to the idealized case $[\cosh(x/a)]^{(k_y a g_0/\varepsilon)} \to \exp(-\eta|x|)$ with $\eta = -k_y g_0/\varepsilon$.

D.3 Temporal dispersion

Temporal dispersion, or the frequency dependence of linear response, arises whenever light couples to matter,

$$\mathcal{M}(\omega) = \begin{bmatrix} \varepsilon_{xx} & \varepsilon_{xy} & \chi_x \\ \varepsilon_{xy}^* & \varepsilon_{yy} & \chi_y \\ \chi_x^* & \chi_y^* & \mu \end{bmatrix}, \qquad \begin{aligned} & D_i = \varepsilon_{ij}E^j + \chi_i H_z, \\ & \\ & B_z = \chi_i^* E^i + \mu H_z. \end{aligned} \tag{D.10}$$

Temporal dispersion is always present because it characterizes the relative coupling at a particular energy to the material degrees of freedom – the electronic modes. These are the physical objects that generate the linear response theory to begin with. Moreover, due to the reality condition of the electromagnetic field (particle-antiparticle symmetry), the real and imaginary components of $\mathcal{M}$ cannot be arbitrary functions of ω,

$$\mathcal{M}^*(-\omega) = \mathcal{M}(\omega). \tag{D.11}$$

This implies $\mathrm{Re}\,[\mathcal{M}(-\omega)] = \mathrm{Re}\,[\mathcal{M}(\omega)]$ must be even in ω while $\mathrm{Im}\,[\mathcal{M}(-\omega)] = -\mathrm{Im}\,[\mathcal{M}(\omega)]$ is odd. Hence, it is physically impossible to break time-reversal ($\mathcal{T}$) symmetry without dispersion. In this case, we imply breaking $\mathcal{T}$ symmetry nontrivially (Hermitian response). In the rare circumstance of strong magnetoelectricity $\chi_i \neq 0$, it is conceptually possible to break time-reversal without dispersion but these generally vanish due to rotational symmetry. Adding loss (antiHermitian response) breaks $\mathcal{T}$ symmetry in a trivial way because it does not alter the dynamics of the field – it simply adds a finite lifetime.

Besides the reality condition, $\mathcal{M}$ must satisfy three additional physical constraints. The first being transparency at high frequency,

$$\lim_{\omega \to \infty} \mathcal{M}(\omega) \to \mathbb{1}_3, \tag{D.12}$$

where $\mathbb{1}_3$ is the 3×3 identity. The second being Kramers-Kronig (causality),

$$\oint_{\mathrm{Im}\,[\omega] \geq 0} \frac{\mathcal{M}(\omega) - \mathbb{1}_3}{\omega - \omega} d\omega = 0. \tag{D.13}$$

This ensures the response function is analytic in the upper complex plane and decays at least as fast as $|\omega|^{-1}$. The last condition requires a positive definite energy density,

$$\bar{\mathcal{M}}(\omega) = \partial_\omega[\omega \mathcal{M}(\omega)] > 0. \tag{D.14}$$

By combining all the aforementioned constraints and assuming Hermitian (lossless) systems $\mathcal{M}^\dagger = \mathcal{M}$, we can always expand $\mathcal{M}$ via a partial fraction decomposition [74],

$$\mathcal{M}(\omega) = \mathbb{1}_3 - \sum_\alpha \frac{\mathcal{C}_\alpha^\dagger \mathcal{C}_\alpha}{\omega_\alpha(\omega - \omega_\alpha)}. \tag{D.15}$$

The poles of the response function $\omega = \omega_\alpha$ represent resonances of the material degrees of freedom. From an electronic band structure point of view, $\omega_\alpha = (E_\alpha - E_0)/\hbar$ represents the energy difference between the ground state and an excited state. $\mathcal{C}_\alpha$ is the coupling strength (matrix element) of the excitation.

D.4 Spatial dispersion (nonlocality)

Spatial dispersion, or the momentum dependence of linear response, dictates how the light-matter interaction changes with wavelength (scale). Nonlocality becomes relevant at the nanoscale and governs the deep subwavelength physics. Perhaps more importantly, nonlocality is fundamentally necessary to describe topological phenomena. As has been proven in Ref. [54], [116], Chern numbers are only quantized when $\mathcal{M}$ is *regularized* which inherently requires spatial dispersion. This is the only way for the electromagnetic theory to be consistent with the tenfold way [15], which describes all possible continuum topological theories. Technically, the photon belongs to Class D, the same universality class as the p-wave topological superconductor [243]. Class D possesses an integer topological invariant (Chern number) in two dimensions.

Spatial dispersion is easily introduced by letting $\omega_\alpha \to \omega_{\alpha\mathbf{k}}$ and $\mathcal{C}_\alpha \to \mathcal{C}_{\alpha\mathbf{k}}$ be functions of $\mathbf{k}$,

$$\mathcal{M}(\omega, \mathbf{k}) = \mathbb{1}_3 - \sum_\alpha \frac{\mathcal{C}_{\alpha\mathbf{k}}^\dagger \mathcal{C}_{\alpha\mathbf{k}}}{\omega_{\alpha\mathbf{k}}(\omega - \omega_{\alpha\mathbf{k}})}. \tag{D.16}$$

The $\mathbf{k}$ dependence cannot be completely arbitrary because the response function must satisfy the generalized reality condition,

$$\mathcal{M}^*(-\omega, -\mathbf{k}) = \mathcal{M}(\omega, \mathbf{k}). \tag{D.17}$$

The reality condition (particle-antiparticle symmetry) implies there is a negative energy resonance $-\omega_{\alpha-\mathbf{k}}$ associated with each positive energy $\omega_{\alpha\mathbf{k}}$. The wave equation of the 2D photon coupled to matter is thus,

$$\mathcal{H}_0(\mathbf{k})f = \omega \mathcal{M}(\omega, \mathbf{k})f. \tag{D.18}$$

However, this is still not a first-order eigenvalue problem since $\mathcal{M}$ depends on the eigenvalue ω itself. Moreover, the electromagnetic field f is not the complete eigenvector of this system. A simple reason is because the number of eigenmodes n should match the dimensionality of the eigenvector $\dim[u] = n$. This clearly does not hold $\dim[f] = 3$ when temporal dispersion is present since there can be many modes that satisfy the wave equation [Eq. (D.18)].

D.4.1 Electromagnetic Hamiltonian

To convert Eq. (D.18) into a first-order Hamiltonian, we define the auxiliary variables ψ_α that describe the internal polarization and magnetization modes of the medium,

$$\psi_\alpha = \frac{\mathcal{C}_{\alpha\mathbf{k}}f}{\omega - \omega_{\alpha\mathbf{k}}}, \qquad \omega\psi_\alpha = \omega_{\alpha\mathbf{k}}\psi_\alpha + \mathcal{C}_{\alpha\mathbf{k}}f. \tag{D.19}$$

Back-substituting into Eq. (D.18) and using the partial fraction expansion,

$$\frac{\omega}{\omega_\alpha(\omega - \omega_\alpha)} = \frac{1}{\omega_\alpha} + \frac{1}{\omega - \omega_\alpha}, \tag{D.20}$$

we obtain the first-order wave equation,

$$H(\mathbf{k})u = \omega u, \qquad u = \begin{bmatrix} f & \psi_1 & \psi_2 & \ldots \end{bmatrix}^{\mathsf{T}}. \tag{D.21}$$

u accounts for the electromagnetic field f and all internal polarization modes ψ_α describing the linear response. $H(\mathbf{k})$ is the Hamiltonian matrix that acts on this generalized state vector u,

$$H(\mathbf{k}) = \begin{bmatrix} \mathcal{H}_0(\mathbf{k}) + \sum_\alpha \omega_{\alpha\mathbf{k}}^{-1}\mathcal{C}_{\alpha\mathbf{k}}^\dagger\mathcal{C}_{\alpha\mathbf{k}} & \mathcal{C}_{1\mathbf{k}}^\dagger & \mathcal{C}_{2\mathbf{k}}^\dagger & \ldots \\ \mathcal{C}_{1\mathbf{k}} & \omega_{1\mathbf{k}} & 0 & \ldots \\ \mathcal{C}_{2\mathbf{k}} & 0 & \omega_{2\mathbf{k}} & \ldots \\ \vdots & \vdots & \vdots & \ddots \end{bmatrix}. \tag{D.22}$$

This decomposition makes intuitive sense. The dimensionality of the Hamiltonian matches the number of distinct eigenmodes and eigenenergies of the problem. The complete set of eigenvectors is thus,

$$H(\mathbf{k})u_{n\mathbf{k}} = \omega_{n\mathbf{k}}u_{n\mathbf{k}}. \tag{D.23}$$

Constructing the total Hamiltonian $H(\mathbf{k})$ is a very important procedure when nonlocality is present. This is because we have to start imposing boundary conditions on the oscillators ψ_α themselves when we consider interface effects.

Utilizing the linear response theory, the electromagnetic eigenstates of the medium $f_{n\mathbf{k}}$ are solutions of the self-consistent wave equation,

$$\det\left[\omega\mathcal{M}(\omega,\mathbf{k})-\mathcal{H}_0(\mathbf{k})\right]=0,\qquad \omega=\omega_{n\mathbf{k}}, \tag{D.24}$$

which determines all possible polaritonic bands. These bands are normalized to the energy density as,

$$u_{n\mathbf{k}}^\dagger u_{n\mathbf{k}} = f_{n\mathbf{k}}^\dagger\bar{\mathcal{M}}(\omega_{n\mathbf{k}},\mathbf{k})f_{n\mathbf{k}} = 1, \tag{D.25}$$

where,

$$\bar{\mathcal{M}}(\omega,\mathbf{k}) = \partial_\omega[\omega\mathcal{M}(\omega,\mathbf{k})] = \mathbb{1}_3 + \sum_\alpha \frac{\mathcal{C}_{\alpha\mathbf{k}}^\dagger\mathcal{C}_{\alpha\mathbf{k}}}{(\omega-\omega_{\alpha\mathbf{k}})^2}. \tag{D.26}$$

Due to the constraints on $\mathcal{M}$, these bands are continuous and real-valued for all $\mathbf{k}$.

D.4.2 Nonlocal regularization

A well known requirement of any continuum topological theory, is that the Hamiltonian must approach a *directionally independent* value in the asymptotic limit [15],

$$\lim_{k\to\infty} H(\mathbf{k}) = H(k). \tag{D.27}$$

This ensures the Hamiltonian is connected at infinity and is the continuum equivalent of a periodic boundary condition. Mathematically, this means the momentum space manifold is compact and can be projected onto the Riemann sphere $\mathbb{R}^2 \to S^2$. Alternatively, if the response function is regularized, the wave equation approaches a directionally independent value in the asymptotic limit,

$$\lim_{k\to\infty}\left[\omega\mathcal{M}(\omega,\mathbf{k})-\mathcal{H}_0(\mathbf{k})\right] \to \omega\mathcal{M}(\omega,k). \tag{D.28}$$

This places constraints on the asymptotic behavior of the response parameters,

$$\lim_{k\to\infty}\mathcal{C}_{\alpha\mathbf{k}} \to \mathcal{C}_{\alpha q}k^q, \qquad \lim_{k\to\infty}\omega_{\alpha\mathbf{k}} \to \omega_{\alpha q}k^q, \tag{D.29}$$

where $\mathcal{C}_{\alpha q}$ and $\omega_{\alpha q}$ are constants of the qth order k expansion. Consequently, $\mathcal{C}_{\alpha \mathbf{k}}$ and $\omega_{\alpha \mathbf{k}}$ require quadratic order nonlocality at minimum $q \geq 2$ to be properly regularized. We will show that this is a necessary and sufficient condition for Chern number quantization.

It is important to remember that continuum models are long wavelength theories $k \approx 0$ and are only valid approximations within a small range of k. The asymptotic behavior $k \to \infty$ is defined to ensure the Taylor expansion is well-behaved at the order of the approximation $O(k^q)$. In reality, the wave always approaches a Bragg condition $ka = \pi$, at a very large but finite momentum $k \neq \infty$, which maps the $\mathbf{k}$-space into itself. This designates a torus $\mathbb{T}^2 = S^1 \times S^1$ in two dimensions – a compact manifold. Waves constrained to a compact manifold is the fundamental origin of Chern number quantization and topological phenomena. When the $k \approx 0$ expansion is well-behaved, the torus is topologically equivalent to the plane $\mathbb{T}^2 \simeq S^2 \simeq \mathbb{R}^2$, such that the $\mathbf{k}$-space remains compact. The limit at $k \to \infty$ guarantees this and means topological physics descends to the long wavelength theory.

D.5 Continuum electromagnetic Chern number

The Berry connection is found by varying the complete eigenvectors $u_{n\mathbf{k}}$ with respect to the momentum $\mathbf{A}_n(\mathbf{k}) = -\mathrm{i} u_{n\mathbf{k}}^\dagger \partial_{\mathbf{k}} u_{n\mathbf{k}}$. This can be simplified to,

$$\mathbf{A}_n(\mathbf{k}) = -\mathrm{i} f_{n\mathbf{k}}^\dagger \bar{\mathcal{M}}(\omega_{n\mathbf{k}}, \mathbf{k}) \partial_{\mathbf{k}} f_{n\mathbf{k}} + f_{n\mathbf{k}}^\dagger \boldsymbol{\mathcal{A}}(\omega_{n\mathbf{k}}, \mathbf{k}) f_{n\mathbf{k}}, \tag{D.30}$$

where $\boldsymbol{\mathcal{A}}$ is the Berry connection arising from the material degrees of freedom,

$$\boldsymbol{\mathcal{A}}(\omega, \mathbf{k}) = -\mathrm{i} \sum_\alpha \frac{\mathcal{C}_{\alpha \mathbf{k}}^\dagger \partial_{\mathbf{k}} \mathcal{C}_{\alpha \mathbf{k}}}{(\omega - \omega_{\alpha \mathbf{k}})^2}. \tag{D.31}$$

It is straightforward to prove that nonlocal regularization guarantees Chern number quantization. In the asymptotic limit, the electromagnetic modes approach a directionally independent value, up to a possible U(1) gauge,

$$\lim_{k \to \infty} f_n(\mathbf{k}) \to f_n(k) \exp\left[\mathrm{i} \chi_n(\mathbf{k})\right]. \tag{D.32}$$

The closed loop at $k = \infty$ is therefore a pure gauge, which is necessarily a unit Berry phase $\gamma_n = 1$,

$$\exp\left[i \oint_{k=\infty} \mathbf{A}_n(\mathbf{k}) \cdot d\mathbf{k}\right] = \exp\left[i \int_{\mathbb{R}^2} F_n(\mathbf{k}) d^2\mathbf{k}\right] = \exp\left[i\chi_n|_0^{2\pi}\right] = 1. \tag{D.33}$$

$F_n(\mathbf{k}) = \hat{z} \cdot [\partial_\mathbf{k} \times \mathbf{A}_n(\mathbf{k})]$ is the Berry curvature and we have utilized Stokes' theorem to convert the line integral to a surface integral over the entire planar momentum space $\mathbb{R}^2$. Since the total Berry flux must come in multiples of 2π, the Chern number C_n is guaranteed to be an integer,

$$C_n = \frac{1}{2\pi} \int_{\mathbb{R}^2} F_n(\mathbf{k}) d^2\mathbf{k} \in \mathbb{Z}. \tag{D.34}$$

C_n counts the number of singularities in the gauge potential $\mathbf{A}_n(\mathbf{k})$ as it evolves over the momentum space. We will now discuss the role of symmetries on the electromagnetic Chern number – specifically rotational symmetry.

D.6 Rotational symmetry and spin

If the unit cell of the atomic crystal possesses a center (at least threefold cyclic) the response function is rotationally symmetric about z,

$$\mathcal{R}^{-1}\mathcal{M}(\omega, R\mathbf{k})\mathcal{R} = \mathcal{M}(\omega, \mathbf{k}). \tag{D.35}$$

R is the SO(2) matrix acting on the coordinates $\mathbf{k}$. $\mathcal{R}$ is the action of SO(2) acting on the fields f, which induces rotations in the x-y plane,

$$R = \begin{bmatrix} \cos\theta & \sin\theta \\ -\sin\theta & \cos\theta \end{bmatrix}, \qquad \mathcal{R} = \exp(i\theta\hat{S}_z) = \begin{bmatrix} R & 0 \\ 0 & 1 \end{bmatrix}. \tag{D.36}$$

$\mathcal{R}$ is simply the SO(3) matrix along $\hat{z}$ which rotates the polarization state of the electromagnetic field. E_i transforms as vector in 2D while H_z transforms as scalar. Clearly the representation is single-valued (bosonic) and describes a spin-1 particle,

$$\mathcal{R}(2\pi) = \mathbb{1}_3. \tag{D.37}$$

Infinitesimal rotations on the coordinates $\mathbf{k}$ gives rise to the orbital angular momentum (OAM) $\hat{L}_z = -\mathrm{i}\partial_\phi$ while infinitesimal rotations on the polarization state gives rise to the spin angular momentum (SAM) $\hat{S}_z = -\mathrm{i}\epsilon_{ijz}$. Consequently, the total angular momentum (TAM) $\hat{J}_z$ is conserved, at all frequencies and wave vectors,

$$[\hat{J}_z, \mathcal{M}(\omega, \mathbf{k})] = 0, \qquad \hat{J}_z = \hat{L}_z + \hat{S}_z. \tag{D.38}$$

Equation (D.35) and (D.38) are equivalent statements in this context. Moreover, this implies the electromagnetic field is a simultaneous eigenstate of $\hat{J}_z$,

$$\hat{J}_z f_{n\mathbf{k}} = j_n f_{n\mathbf{k}}, \qquad j_n \in \mathbb{Z}. \tag{D.39}$$

j_n is necessarily an integer for photons. Note though, j_n is only uniquely defined up to a gauge since we can always add an arbitrary OAM to the state $f_{n\mathbf{k}} \to f_{n\mathbf{k}} \exp(\mathrm{i}l_n\phi)$ such that $j_n \to j_n + l_n$.

D.6.1 Stationary (high-symmetry) points

At an arbitrary momentum $\mathbf{k}$, the SAM and OAM are not good quantum numbers – only the TAM is well defined (up to a gauge). However, at stationary points $k = k_p$, also known as high-symmetry points (HSPs), the electromagnetic field is a simultaneous eigenstate of $\hat{S}_z$ and $\hat{L}_z$. In the continuum limit there are two such HSPs, $k_p = 0$ and $k_p = \infty$. At these specific momenta, the response function is rotationally invariant – it commutes with $\mathcal{R}$,

$$[\mathcal{R}, \mathcal{M}(\omega, k_p)] = [\hat{S}_z, \mathcal{M}(\omega, k_p)] = [\hat{L}_z, \mathcal{M}(\omega, k_p)] = 0. \tag{D.40}$$

Since $\mathcal{M}$ is a continuous function of $\mathbf{k}$, it cannot depend on the azimuthal coordinate ϕ at HSPs, otherwise $\mathcal{M}$ would be multivalued. Hence, the electromagnetic field is an eigenstate of both $\hat{S}_z$ and $\hat{L}_z$ at k_p,

$$\hat{S}_z f_{n\mathbf{k}_p} = m_n(k_p) f_{n\mathbf{k}_p}, \qquad \hat{L}_z f_{n\mathbf{k}_p} = l_n(k_p) f_{n\mathbf{k}_p}. \tag{D.41}$$

$m_n(k_p) = \pm 1, 0$ is the SAM eigenvalue at k_p of the nth band and $l_n(k_p) \in \mathbb{Z}$ is the OAM eigenvalue. Importantly, only the SAM is gauge invariant because it represents the eigenvalue of a matrix – ie. it only depends on the polarization state. This immediately implies the eigenmode can be factored into a spin and orbital part at HSPs,

$$f_{n\mathbf{k}_p} \propto [\vec{e}_m(k_p)]_n \exp\left[\mathrm{i}l_n(k_p)\phi\right]. \tag{D.42}$$

$[\vec{e}_m(k_p)]_n$ is the particular spin eigenstate at k_p for the nth band. There are three possible eigenstates $\vec{e}_m$ corresponding to three quantized spin-1 vectors,

$$\mathcal{R}\vec{e}_m = \vec{e}^{\,\mathrm{i}m\theta}\vec{e}_m, \qquad \hat{S}_z\vec{e}_m = m\vec{e}_m, \tag{D.43}$$

where $m = \pm 1, 0$ labels the quantum of spin for each state,

$$\vec{e}_\pm = \frac{1}{\sqrt{2}}\begin{bmatrix} 1 \\ \pm\mathrm{i} \\ 0 \end{bmatrix}, \qquad \vec{e}_0 = \begin{bmatrix} 0 \\ 0 \\ 1 \end{bmatrix}. \tag{D.44}$$

$\vec{e}_\pm$ are right and left-handed states respectively and represent electric resonances $E_y = \pm\mathrm{i}E_x$ with $H_z = 0$. The spin-0 state $\vec{e}_0$ is a magnetic resonance $E_x = E_y = 0$ with $H_z \neq 0$.

D.6.2 Spin spectrum

To determine the spin state of a particular band n, we need to solve the wave equation at HSPs. At these points, only three parameters are permitted by symmetry,

$$\mathcal{M}(\omega, k_p) = \begin{bmatrix} \varepsilon & \mathrm{i}g & 0 \\ -\mathrm{i}g & \varepsilon & 0 \\ 0 & 0 & \mu \end{bmatrix}. \tag{D.45}$$

ε and μ are the scalar permittivity and permeability respectively. g is the gyrotropic coefficient which breaks both time-reversal ($\mathcal{T}$) and parity ($\mathcal{P}$) symmetry but preserves rotational

$(\mathcal{R})$ symmetry. Assuming a regularized response function, nontrivial solutions of the wave equation simultaneously satisfy,

$$\det\left[\mathcal{M}(\omega, k_p)\right] = 0, \qquad \omega = \omega_n(k_p) \neq 0. \tag{D.46}$$

There are three possible conditions that satisfy Eq. (D.46). The first two generate right or left-handed states $\vec{e}_\pm$,

$$m_n(k_p) = \frac{g(\omega_n(k_p), k_p)}{\varepsilon(\omega_n(k_p), k_p)} = \pm 1. \tag{D.47}$$

The last generates the the spin-0 state $\vec{e}_0$,

$$m_n(k_p) = \mu(\omega_n(k_p), k_p) = 0. \tag{D.48}$$

Note, since m_n is a discrete quantum number, it cannot vary continuously if rotational symmetry is preserved. It can only be changed at a topological phase transition which requires an accidental degeneracy at a HSP.

D.6.3 Symmetry-protected topological (SPT) phases

Remarkably, the electromagnetic Chern number is determined entirely from the spin eigenvalues at the HSPs k_p. The proof is surprisingly simple. Due to rotational symmetry, the Berry curvature $F_n(k) = \partial_k A_n^\phi(k)$ depends only on the magnitude of k since F_n is a scalar. Integrating the Berry curvature over all space $\mathbb{R}^2$, we arrive at,

$$C_n = A_n^\phi(\infty) - A_n^\phi(0) = l_n(\infty) - l_n(0). \tag{D.49}$$

This follows because $f_{n\mathbf{k}_p}$ is an eigenstate of the OAM at HSPs $k_p = 0$ and $k_p = \infty$. The OAM at k_p is not gauge invariant, however the difference at the two stationary points is gauge invariant because the TAM is conserved $j_n = m_n(0) + l_n(0) = m_n(\infty) + l_n(\infty)$. Substituting for m_n we obtain,

$$C_n = m_n(0) - m_n(\infty). \tag{D.50}$$

Hence, the spin eigenstate must change at HSPs $m_n(0) \neq m_n(\infty)$ to acquire a nontrivial phase $C_n \neq 0$. It is also clear that a purely gyrotropic medium $\mu = 1$ always has Chern numbers of $|C_n| = 2$ since $m_n(k_p) = \pm 1$ only assumes two values. $|C_n| = 1$ is much more exotic as it requires both gyrotropy and magnetism.

E. VISCOUS MAXWELL-CHERN-SIMONS THEORY FOR TOPOLOGICAL ELECTROMAGNETIC PHASES OF MATTER [SUPPLEMENTARY MATERIAL]

From [T. Van Mechelen and Z. Jacob, "Viscous Maxwell-Chern-Simons theory for topological electromagnetic phases of matter," *Phys. Rev. B*, vol. 102, p. 155425, 15 Oct. 2020]. © 2020 American Physical Society. [246]

Supplementary information for "Viscous Maxwell-Chern-Simons theory for topological electromagnetic phases of matter". Here, we derive a general bulk-boundary correspondence for the viscous MCS theory. We follow a very similar procedure as Mong [Phys. Rev. B 83, 125109 (2011)] which analyzed the Dirac equivalent.

E.1 Gauge theory and dual fields

We emphasize that the topological field theory for electromagnetic fields can be constructed equivalently in terms of a gauge theory A_μ or the dual fields $\tilde{F}_\mu$. Indeed, Lagrangians $\mathcal{L}_A$ and $\mathcal{L}_F$ produce the exact same equations of motion when one varies the action with respect to A_μ or $\tilde{F}_\mu$. The subtle difference is that $\mathcal{L}_F$ is manifestly gauge invariant, while $\mathcal{L}_A$ is only gauge invariant up to a total divergence. The total divergence has no effect in the bulk but will generate gauge-breaking boundary terms that need to be carefully accounted for [273]. To avoid this complication, we prefer to work with the dual fields $\tilde{F}_\mu$ since the boundary theory is automatically gauge invariant.

E.2 Equivalence with Hoyos and Son action

In flat space time, the Hoyos and Son action [255] that describes the viscous component of the Hall response is,

$$\mathcal{S} = \int dV \mathcal{L}, \qquad \mathcal{L} = \xi E^i \partial_i B, \tag{E.1}$$

where ξ is the effective Hall visosity. The Hoyos and Son action assumes that $\mathbf{E} = -\boldsymbol{\nabla}\phi$ is longitudinal and therefore neglects the transverse component of the response. It is straight-

forward to show that our action reduces to the Hoyos and Son action under the substitution $\mathbf{E} = -\boldsymbol{\nabla}\phi$ and two integration by parts,

$$
\begin{aligned}
\mathcal{L} &= -\frac{\xi}{4}\epsilon^{\mu\nu\rho}A_\mu\nabla^2 F_{\nu\rho} = \frac{\xi}{2}(\phi\nabla^2 B + \epsilon_{ij}A^i\nabla^2\partial^j\phi) = \frac{\xi}{2}[\phi\nabla^2 B - \epsilon_{ij}A^i\partial_j(\boldsymbol{\nabla}\cdot\mathbf{E})] \\
&\to \frac{\xi}{2}(-\partial^i\phi\partial_i B - B\boldsymbol{\nabla}\cdot\mathbf{E}) \to \frac{\xi}{2}(-\partial^i\phi\partial_i B + \partial^i B E_i) = \xi E^i\partial_i B.
\end{aligned}
\tag{E.2}
$$

Hence, our formulation is a generalization of the Hoyos and Son action to include transverse fields in flat space time.

E.3   Gauss's law and electrostatics

For time-dependent fields $\omega \neq 0$, the Maxwell Hamiltonian automatically enforces Gauss's law from the definition of the cross product,

$$
\vec{d}\cdot\vec{F} = \partial_i E^i - (\kappa + \xi\nabla^2)B_z = 0.
\tag{E.3}
$$

As we can see, the MCS mass (Hall conductivity) ties electric charge to the magnetic field B_z. However, an important difference between the Maxwell Hamiltonian (H) and Schrödinger/Dirac Hamiltonians is that $\det[H] = 0$ is manifestly singular (noninvertible). This is because the equations of motion for gauge theories are inherently redundant. Electrostatic $\omega = 0$ (time-independent) potentials always exist $\vec{F}_0 = \vec{d}\phi$ which are trivial solutions of $H\vec{F}_0 = 0$. Elimination of these "zero modes" requires Gauss's law as an additional constraint at zero frequency,

$$
\vec{d}\cdot\vec{F}_0 = \vec{d}\cdot\vec{d}\phi = [\nabla^2 - (\kappa + \xi\nabla^2)^2]\phi = 0.
\tag{E.4}
$$

These scalar potentials ϕ do not enter the free field theory since they do not possess a plane wave representation.

E.4 Topologically-protected spin-1 edge states

E.4.1 Natural boundary condition

To see that the normal Poynting vector vanishes as implied by the boundary term of the MCS Lagrangian, it is useful to first derive the velocity operator v_i,

$$v_i = \frac{\partial H}{\partial p_i} = S_i - 2\xi p_i S_z, \tag{E.5}$$

which has an additional kinetic term when $\xi \neq 0$. The Poynting vector is simply the expectation value of $P_i = \vec{F}^* \cdot v_i \vec{F}$. Clearly, if $\vec{F}$ is a null state of v_x at $x = 0$,

$$v_x \vec{F}|_{x=0} = 0, \tag{E.6}$$

then the normal component $P_x|_{x=0} = 0$ vanishes identically. Equation (E.6) is equivalent to the Lagrangian variation of the main text, just expressed in a more enlightening form.

E.4.2 Bulk-boundary correspondence for spin-1 Maxwell Hamiltonian

Now we show that the boundary of the nontrivial phase $|C_{em}| = 2$ hosts chiral photons that minimize the surface action $\delta \mathcal{S}_s = 0$. This is the bulk-boundary correspondence (BBC) of the viscous MCS theory which applies to spin-1 systems. We follow a very similar proof as Mong (Ref. [224]) that exhaustively analyzed the spin-½ Dirac counterpart. Here we present the proof for the continuum model since it is particularly intuitive. The proof and results for the lattice theory are essentially identical.

We consider a half-space truncated at $x = 0$ with the topological medium in the $x > 0$ space. Due to quadratic nonlocality in the photonic mass $\Lambda(k) = \kappa - \xi k^2$, there are generally two characteristic wavelengths for a given momentum k_y,

$$\vec{F}(x) = c_1 \vec{f_1} e^{i\zeta_1 x} + c_2 \vec{f_2} e^{i\zeta_2 x}, \tag{E.7}$$

where $\vec{f_1}$ and $\vec{f_2}$ are polarization states to be determined. The constraint that $\text{Im}(\zeta_{1,2}) > 0$ lie in the upper complex plane ensures $\vec{F}(x \to \infty) \to 0$ are decaying waves. To fulfill

Dirichlet $\vec{F}(0) = 0$ or Neumann $\partial_x \vec{F}(0) = 0$ type boundary conditions at $x = 0$ (or any linear combination), the polarization states $\vec{f_1} \propto \vec{f_2}$ must share an eigenvector. Assuming dynamical fields $\omega \neq 0$, this implies the wave equation is satisfied for arbitrary choices of c_1 and c_2,

$$\det \left[(c_1 + c_2)\omega - c_1 \vec{d}(\zeta_1) \cdot \vec{S} - c_2 \vec{d}(\zeta_2) \cdot \vec{S} \right] = 0, \tag{E.8}$$

which produces a system of equations,

$$\omega^2 = \vec{d}(\zeta_1) \cdot \vec{d}(\zeta_1) = \vec{d}(\zeta_2) \cdot \vec{d}(\zeta_2) = \vec{d}(\zeta_1) \cdot \vec{d}(\zeta_2). \tag{E.9}$$

By direct inspection, the system of equations [Eq. (E.9)] is only fulfilled if,

$$\omega^2 = k_y^2, \qquad \zeta_1 - i\Lambda_1 = \zeta_2 - i\Lambda_2 = 0, \tag{E.10}$$

or,

$$\omega^2 = k_y^2, \qquad \zeta_1 + i\Lambda_1 = \zeta_2 + i\Lambda_2 = 0, \tag{E.11}$$

where $\Lambda_{1,2} = \kappa - \xi(k_y^2 + \zeta_{1,2}^2)$. Imposing the constraint $\text{Im}(\zeta_{1,2}) > 0$, only one of these conditions can be true for a given k_y. The other corresponds to an exponentially growing wave. Plugging the two ζ roots back into the wave equation, the solution with a degenerate eigenvector requires $E_y(x) = 0$,

$$\vec{f_1} \propto \vec{f_2} \propto \begin{bmatrix} 1 \\ 0 \\ \mp i \end{bmatrix}, \tag{E.12}$$

which are eigenvectors of $S_y \vec{f}_{1,2} = \pm \vec{f}_{1,2}$.

E.4.3 Massless chiral edge states

Curiously, we find a single chiral edge state in the nontrivial regime $\kappa\xi > 0$, even though the Chern number is $|C_{em}| = 2$, which usually suggests two edge states from conventional wisdom. In any case, the general solution is a linearly dispersing (massless) photon,

$$\vec{F}(x) = \begin{bmatrix} 1 \\ 0 \\ -\mathrm{i}s_\kappa \end{bmatrix} \left(c_1 \mathrm{e}^{-\eta_1 x} + c_2 \mathrm{e}^{-\eta_2 x} \right), \qquad \omega = s_\kappa k_y, \tag{E.13}$$

where we have redefined $\zeta = \mathrm{i}\eta$ to emphasize that the edge state decays at $x \to \infty$. The direction of propagation $s_\kappa = \mathrm{sgn}(\kappa)$ is dictated by the relative sign of $\mathrm{sgn}(\kappa) = \mathrm{sgn}(\xi) = \pm 1$, giving $C_{em} = \pm 2$. The edge state is completely unidirectional (chiral) as $k_y \to -k_y$ is never a simultaneous solution. Interestingly, the edge state is also an eigenstate of the spin-1 helicity operator $S_y \vec{F} = s_\kappa \vec{F}$, which represents a completely transverse electromagnetic (TEM) wave $E_y(x) = 0$. The decay constants $\eta_{1,2}$ are the two roots of the secular equation,

$$s_\kappa \eta = \Lambda(\eta) = \kappa - \xi k_y^2 + \xi \eta^2, \tag{E.14}$$

which gives,

$$\eta_{1,2} = \frac{1}{2|\xi|} \left[1 \pm \sqrt{1 + 4\xi(\xi k_y^2 - \kappa)} \right]. \tag{E.15}$$

It is also clear that the edge state is gapless, as the momentum k_y intersects the bulk (massive) spectrum at $k_y = k_c = \sqrt{\kappa/\xi}$, precisely where the MCS mass passes through zero $\Lambda(k_c) = 0$. At this point, one of the decay constants vanishes $\eta(k_c) = 0$ and the edge wave joins the bulk continuum.

Depending on the choice of $c_{1,2}$, the edge state can satisfy either of the two boundary conditions that minimize the action $\delta \mathcal{S}_s = 0$. For Dirichlet we have an antisymmetric combination,

$$\vec{F}(0) = 0, \qquad c_1 = -c_2, \tag{E.16}$$

while the natural boundary condition is a symmetric combination,

$$v_x \vec{F}(0) = 0, \qquad c_1 = c_2. \tag{E.17}$$

It is important to emphasize that both boundary conditions are satisfied irrespective of the contacting medium in the $x < 0$ half-space. The photonic edge states will exist at the boundary of vacuum.

E.5 Lattice theory

In the lattice theory, we do not assume that space is continuous but instead discretized into a square lattice ; a is the lattice spacing. In this case, the space coordinates can be expressed as $x = n_x a$ and $y = n_y a$, with $n_{x,y} \in \mathbb{Z}$. However, time remains continuous. First-order derivatives are converted to,

$$\partial_x \vec{F} \rightarrow \frac{\vec{F}(x+a) - \vec{F}(x-a)}{2a}, \tag{E.18}$$

while second-order derivatives are,

$$\partial_x^2 \vec{F} \rightarrow \frac{\vec{F}(x+a) - 2\vec{F}(x) + \vec{F}(x-a)}{a^2}, \tag{E.19}$$

with similar expressions for y. The continuum limit $a \rightarrow 0$ is obtained from standard calculus assuming the fields are at least twice differentiable. Transferring to the momentum space $\vec{F} = \mathrm{e}^{\mathrm{i}\mathbf{k}\cdot\mathbf{r}} \vec{F}_{\mathbf{k}}$; linear terms in the Hamiltonian are replaced with,

$$p_x \vec{F} \rightarrow \frac{1}{a} \sin(k_x a) \vec{F}_{\mathbf{k}}, \tag{E.20}$$

and similarly for quadratic terms arising from the Hall viscosity $\xi \neq 0$,

$$p_x^2 \vec{F} \rightarrow \frac{4}{a^2} \sin^2\left(\frac{k_x a}{2}\right) \vec{F}_{\mathbf{k}}. \tag{E.21}$$

The quadratic terms are essential to realize nontrivial topology [271].

E.5.1 Lattice edge states

Topologically-protected edge states in the lattice theory assume a nearly identical form as the continuum limit [54], [116], with only slight modifications to the dispersion. To uncover the edge states, we terminate the lattice at $x = 0$ and introduce a half-space in the $x > 0$ domain. In this case, $|k_y| \leq \pi/a$ is still a good quantum number, which we Fourier transform over, but the lattice has now been truncated at $x = n_x a = 0$. Hence, we solve for the field at every discrete lattice point $n_x \geq 0$ which is labelled by $\vec{F}(n_x a)$ and the stipulation that the field is decaying $\vec{F}(n_x a) \to 0$ as $n_x \to \infty$. To satisfy an open $\vec{F}(0) = 0$ or mixed $v_x \vec{F}(0) = 0$ boundary condition, the edge state must possess a degenerate eigenvector for two decay constants $\eta_{1,2}$. After a bit of work, the edge state can be expressed as,

$$
\vec{F}(n_x a) = \begin{bmatrix} 1 \\ 0 \\ -s_C i \end{bmatrix} \left[c_1 \exp^{n_x}(-\eta_1 a) + c_2 \exp^{n_x}(-\eta_2 a) \right], \tag{E.22}
$$

where $s_C = \mathrm{sgn}(C_{em})$ is the sign of the Chern number and $c_{1,2}$ are proportionality constants that are set by the boundary condition. The dispersion relation reads,

$$
\omega a = s_C \sin(k_y a). \tag{E.23}
$$

For small $k_y a \approx 0$ the dispersion is linear $\omega \approx s_C k_y$ and the edge state propagates near the effective speed of light in the material $|\partial \omega / \partial k_y| = 1$. Interestingly, $S_y \vec{F}_{n_x} = s_C \vec{F}_{n_x}$ is also an eigenstate of the spin-1 helicity operator (SO(3)) with quantized spin along $\hat{y}$.

The proportionality constants $c_{1,2}$ can be chosen to satisfy Dirichlet (open) $\vec{F}(0) = 0$ or mixed (natural) boundary conditions $v_x \vec{F}(0) = 0$ at $x = n_x a = 0$. The Dirichlet condition represents an antisymmetric combination $c_1 = -c_2$ while the natural condition is a symmetric combination $c_1 = c_2$. The decay constants $\eta_{1,2}$ are found from the characteristic equation, with $k_x = i\eta$,

$$
\frac{s_C}{a} \sinh(\eta a) = \Lambda(\eta), \tag{E.24}
$$

which has two decaying roots $\mathrm{Re}(\eta_{1,2}) > 0$ strictly in the nontrivial regime $|C_{em}| = 2$. Solving the secular equation we obtain,

$$\exp(-\eta_{1,2}a) = \frac{1}{2q_+}\left(-p \pm \sqrt{w^2 - 4q_+ q_-}\right) \tag{E.25}$$

where,

$$p = \kappa - \left(\frac{2}{a}\right)^2 \xi \left[\sin^2\left(\frac{k_y a}{2}\right) + \frac{1}{2}\right], \quad q_\pm = \frac{s_C}{2a} \pm \frac{\xi}{a^2}. \tag{E.26}$$

The regimes where $\mathrm{Re}(\eta) > 0$ define the allowed parallel k_y vectors of the edge state. When one of $\eta = 0$, the edge state is no longer confined and joins the continuum of bulk states. This occurs precisely when k_y intersects the bulk bands; i.e. the edge state is gapless.

VITA

TODD VAN MECHELEN

EDUCATION

Ph.D. in Fields and Optics 2016 – 2020

School of Electrical and Computer Engineering, Purdue University, West Lafayette, IN

M.Sc. in Quantum Optics 2014 – 2015

Department of Physics and Astronomy, University of Toronto, Toronto, ON

B.Sc. in Engineering Physics 2009 – 2014

Department of Electrical and Computer Engineering, University of Alberta, Edmonton, AB

AWARDS & HONORS

Dimiti N Chorafas finalist for best PhD dissertation 2020

NSERC Postgraduate Scholarship – Doctoral (PGS D) 2017 – 2020

Purdue Graduate Student Government Travel Grant 2017

SPIE Optics and Photonics Education Scholarship 2016

NSERC Undergraduate Student Research Awards (USRA) 2013 – 2014

Louise McKinney Scholarship 2013

Jason Lang Scholarship 2010 – 2012

GRANTS & FELLOWSHIPS

Research Assistantship: Purdue University 2016 – 2020

Teaching Assistantship: University of Toronto 2014 – 2015

TEACHING

Purdue University, ECE 695 Topological Electrodynamics: Co-Instructor 2020

University of Toronto, PHY250 Electricity and Magnetism: Seminar Instructor 2015

University of Toronto, PHY132 Introduction to Physics II: Lab Instructor 2015

University of Toronto, PHY131 Foundations of Physics I: Lab Instructor 2014

PUBLICATIONS

12. **Van Mechelen, T.**, and Jacob, Z., "Viscous Maxwell-Chern-Simons theory for topological electromagnetic phases of matter [editors' suggestion]," *Phys. Rev. B* **102**, 155425 (2020).

11. Sengupta, P., Khandekar, C., **Van Mechelen, T.**, Rahman, R., and Jacob, Z., "Electron g-factor engineering for nonreciprocal spin photonics," *Phys. Rev. B* **101**, 035412 (2019).

10. Khosravi, F., **Van Mechelen, T.**, and Jacob, Z., "Dirac wire: Fermionic waveguides with longitudinal spin," *Phys. Rev. B* **100**, 155105 (2019).

9. Jacob, Z., Khandekar, C., **Van Mechelen, T.**, and Khosravi, F., "Spin photonics: from Dirac monopoles to unidirectional heat flow (Conference Presentation)", *Proc. SPIE 11081, Active Photonic Platforms XI, 110810Q (9 September 2019)*

8. **Van Mechelen, T.**, and Jacob, Z., "Unidirectional Maxwellian spin waves [editors' suggestion]," *Nanophotonics* **8**(8), pp. 1399-1416 (2019).

7. **Van Mechelen, T.**, and Jacob, Z., "Nonlocal topological electromagnetic phases of matter [editors' suggestion]," *Phys. Rev. B* **99**, 205146 (2019).

6. **Van Mechelen, T.**, and Jacob, Z., "Photonic Dirac monopoles and skyrmions: spin-1 quantization [invited]," *Opt. Mater. Express* **9**, 95-111 (2019).

5. El Gawhary, O., **Van Mechelen, T.**, and Urbach, H. P., "Role of Radial Charges on the Angular Momentum of Electromagnetic Fields: Spin-¾ Light," *Phys. Rev. Lett.* **121**, 123202 (2018).

4. **Van Mechelen, T.**, and Jacob, Z., "Dirac-Maxwell correspondence: Spin-1 bosonic topological insulator," *Proceedings of the 2018 Conference on Lasers and Electro-Optics (CLEO)* (IEEE, San Jose, CA, 2018), pp. 1–2 (2018).

3. Pendharker, S., Kalhor, F., **Van Mechelen, T.**, Jahani, S., Nazemifard, N., Thundat, T., and Jacob, Z., "Spin photonic forces in non-reciprocal waveguides," *Optics Express* **26**, 23898-23910 (2018).

2. **Van Mechelen, T.**, and Jacob, Z., "Quantum gyroelectric effect: Photon spin-1 quantization in continuum topological bosonic phases," *Phys. Rev. A* **98**, 023842 (2018).

1. **Van Mechelen, T.**, and Jacob, Z., "Universal spin-momentum locking of evanescent waves," *Optica* **3**, 118-126 (2016).